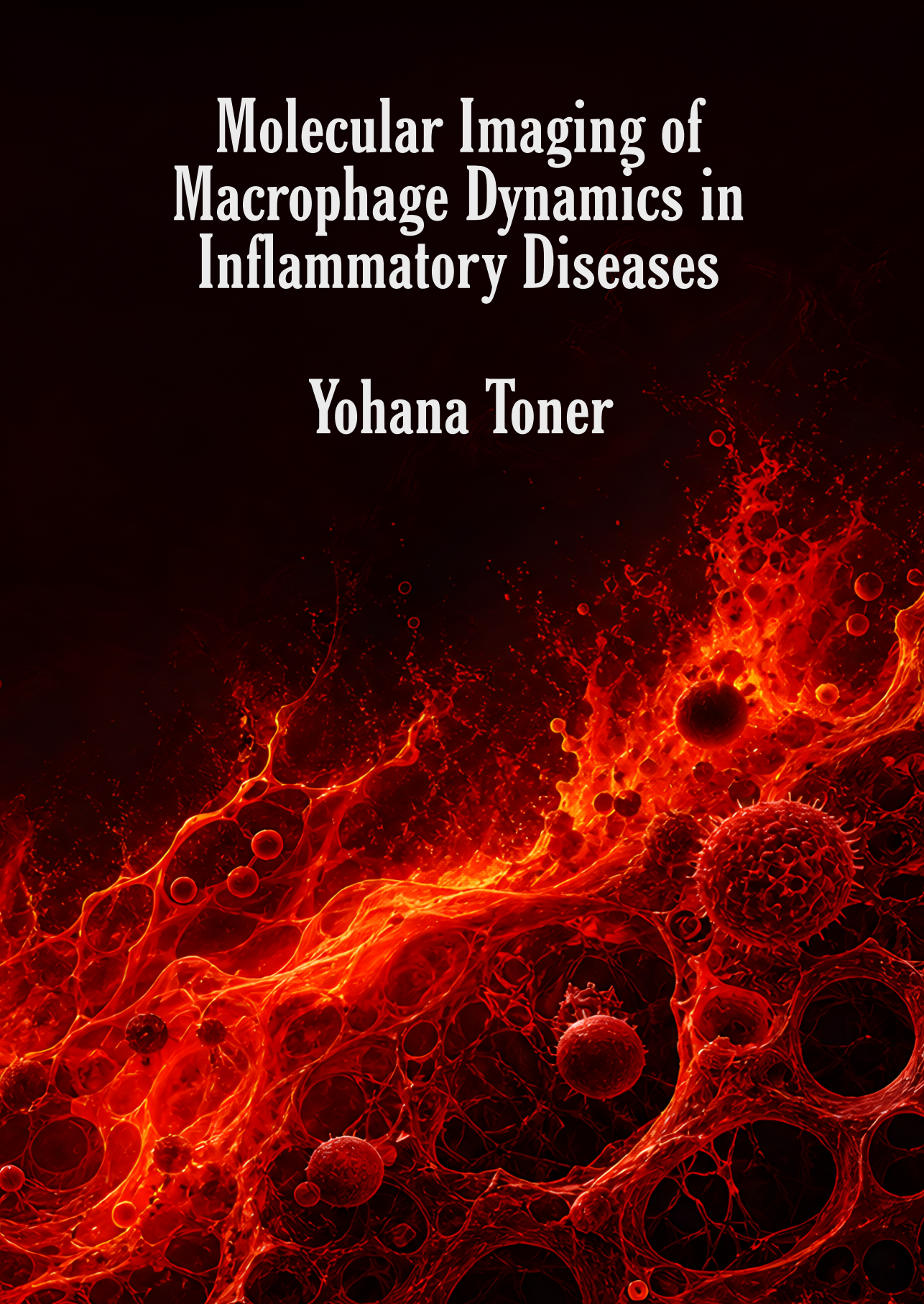
Molecular Imaging of Macrophage Dynamics in Inflammatory Diseases

Yohana Toner



Propositions

Accompanying the dissertation

Molecular Imaging of Macrophage Dynamics in Inflammatory Diseases

Yohana C. Toner

1. The value of an imaging biomarker lies not in its ability to produce statistically significant differences but also in recognizing tracer pharmacokinetics, tissue perfusion, and disease stage.
   This dissertation

2. The bone marrow and spleen should be considered active therapeutic targets in inflammation, not merely background organs in imaging studies.
   This dissertation

3. Longitudinal imaging is most powerful not because it generates more images, but because it reveals whether a biological process is changing direction.
   This dissertation

4. In molecular imaging, novelty is frequently defined by the finding new tracers, rather than by the experimental question it is meant to answer.
   This dissertation

5. Public confidence in animal research is earned by demonstrating that animal use is necessary, minimized, and scientifically rigorous.

6. The modern scarcity of idle time and the administrative burden in academia are genuine threats to scientific creativity.

7. Reproducibility in preclinical research will improve more through rigorous experimental design and transparent reporting than through increasing animal-group sizes alone.

8. The strength of mouse models lies not in their resemblance to patients, but in their ability to test molecular tracers within a controlled biological environment.

9. Current AI-generated hypotheses are only as original as the evidence, assumptions, and omissions embedded in their training data. It increases, rather than decreases, the responsibility of scientists to verify every claim.

10. Many shortcuts around animal research are based on the premise that biology will behave exactly as predicted, which is precisely the bet I would advise against.

Molecular Imaging of Macrophage Dynamics in Inflammatory Diseases

Molecular Imaging of Macrophage Dynamics in Inflammatory Diseases

Yohana C. Toner

Molecular Imaging of Macrophage Dynamics in Inflammatory Diseases
Yohana C. Toner
Eindhoven University of Technology, The Netherlands

Copyright © 2026, Y.C. Toner, Eindhoven, the Netherlands.

All rights reserved. No part of this thesis may be reproduced, stored, or transmitted in any form or by any means, without prior permission of the author.

A catalogue record is available from the Eindhoven University of Technology Library
ISBN: 978-90-386-6810-9
Cover: Yohana Camila Toner
Layout: ProefschriftMaken || proefschriftmaken.nl
Printed and published by: ProefschriftMaken || proefschriftmaken.nl

The work described in this thesis was financially supported by NIH grants, the American Heart Association, the European Research Council and grants from The Netherlands Organization for Scientific Research (NWO).

Molecular Imaging of Macrophage Dynamics in Inflammatory Diseases

PROEFSCHRIFT

ter verkrijging van de graad van doctor aan de Technische Universiteit Eindhoven,
op gezag van de rector magnificus prof. dr. S.K. Lenaerts,
voor een commissie aangewezen door het College van Promoties, in het openbaar te
verdedigen op vrijdag 13 november 2026 om 11:00 uur.

Door

Yohana Camila Toner

Geboren te Curitiba, Brazilië

Dit proefschrift is goedgekeurd door de promotoren en de samenstelling van de promotiecommissie is als volgt:

Voorzitter:	prof. dr. ir. L. Brunsveld
1e promotor:	prof. dr. W.J.M. Mulder
2de promotor:	dr. R. van der Meel
Leden:	dr. L. Albertazzi
	prof. dr. ir. R.G.P. Lopata
	prof. dr. J.W.M. Bulte (Johns Hopkins University)
	prof. dr. S. Middeldorp (Radboud universitair medisch centrum)

Het onderzoek dat in dit proefschrift wordt beschreven is uitgevoerd in overeenstemming met de TU/e Gedragscode Wetenschapsbeoefening.

TABLE OF CONTENTS

Chapter I General introduction and outline 11

Part I. *In vivo* imaging to study inflammation kinetics in cardiovascular disease.

Chapter II Systematically evaluating DOTATATE and FDG as PET immuno-imaging tracers of cardiovascular inflammation 23

Chapter III Multiparametric immunoimaging maps inflammatory signatures in murine myocardial infarction models 69

Part II. New imaging probes for cardiovascular disease imaging

Chapter IV Imaging cardiovascular and lung macrophages with the positron emission tomography sensor ^{64}Cu-macrin in mice, rabbits, and pigs 113

Chapter V Macrophage PET imaging in mouse models of cardiovascular disease and cancer with an apolipoprotein-inspired radiotracer 167

Chapter VI Probing myeloid cell dynamics in ischaemic heart disease by nanotracer hot-spot imaging 207

Part III. *In vivo* imaging to evaluate anti-inflammatory nanotherapy

Chapter VII Targeting myelopoiesis prevents organ inflammation 243

Chapter VIII Imaging-assisted nanoimmunotherapy for atherosclerosis in multiple species 291

Chapter IX	Epilogue	329
Appendices	Summary	340
	Nederlandse Samenvatting	342
	Curriculum Vitae	345
	List of Publications	346
	Dankwoord	354



1

General introduction and outline

Introduction

The association between sickness and the immune system dates to the zenith of the Roman Empire, when the encyclopedist Celsus formally characterized the cardinal signs of inflammation as a pathological marker[1]. Indeed, modern research confirms that most diseases have an inflammatory component[2], with effects that are rarely confined to a single tissue and instead extend to multiple organ systems. Thus, despite its crucial role in tissue regeneration and fighting infections, the immune response is also the primary driver of pathology in sepsis, cardiovascular malignancies, tumor growth, and other chronic illnesses[3–6].

Because inflammatory pathways are highly conserved across species[7,8] and observed in a broad spectrum of medical disorders, they provide a unique opportunity for developing imaging agents. Therefore, the molecular and cellular mediators of inflammation serve not only as therapeutic targets but also as endogenous biomarkers, allowing disease processes to be visualized and monitored *in vivo*[9,10]. This dual utility gives rise to a groundbreaking imaging modality: immunoimaging. This technique leverages these cells and molecules as biological indicators of disrupted immune homeostasis during an inflammatory reaction, enabling the temporospatial tracking of disease dynamics, progression, and therapeutic response[11].

Among the many biological processes accessible to immunoimaging, the trafficking of innate immune cells has emerged as a particularly compelling target. It is well established that following stimuli such as trauma or infections, damaged tissues rapidly release danger signals, known as cytokines and chemokines. These messengers travel through the bloodstream, distally inducing emergency myelopoiesis in the bone marrow and spleen and expanding the production of myeloid progenitors. This process ultimately replenishes the circulating pools of mature neutrophils and monocytes, which are subsequently mobilized to the affected organs[12]. Thus, hematopoietic organs constitute active leukocyte reservoirs that can be recruited to injured

tissues on demand, emphasizing the systemic framework of the immune response[13].

Once recruited, monocytes regulate the initial stages of inflammation. They respond to chemotactic gradients and can further differentiate into macrophages or dendritic cells[14]. Both cell types act as antigen-presenting cells that migrate to lymphoid tissues to activate T cells, thereby bridging innate and adaptive immunity[15]. Macrophages, in particular, play a central role in both acute injury and chronic disease by phagocytosing debris and apoptotic cells, as well as producing the pro- and anti-inflammatory mediators necessary for damage repair. During the resolution stages, they are also involved in angiogenesis and orchestrating communication with resident cells[16].

Despite being intrinsically involved in tissue remodeling, repair, and fibrosis, dysregulated and prolonged myeloid activation can sustain cytokine production. This establishes a self-propagating inflammatory loop with deleterious consequences[16]. For instance, in cardiovascular diseases, monocytes, macrophages, and related innate immune populations are key players in vascular inflammation and ischemic injury[17]. In atherosclerosis, recruited monocytes differentiate into macrophages within developing plaques, where they drive lipid accumulation and extracellular matrix remodeling, ultimately influencing plaque stability[18,19]. Similarly, following a myocardial infarction, recruited monocytes and macrophages can contribute to maladaptive fibrosis and impair vascular repair, compromising tissue perfusion and functional recovery[20,21].

During infection, macrophages act as the first responders, recognizing pathogens through pattern recognition receptors and coordinating anti-microbial defenses. Following pathogen control, macrophages receive signals to undergo a coordinated shift toward reparative states that support increased efferocytosis and a reduction in inflammatory cell recruitment[22]. However, excessive cytokine production or failure to transition toward restorative programs can lead to tissue damage and even organ dysfunction,

as seen in sepsis[23]. More importantly, this double-edged sword role of myeloid cells and macrophages also extends to other conditions, including auto-immune diseases and cancer[24].

Various modalities of non-invasive molecular imaging probes have been developed to visualize macrophages and myeloid cells. Of particular interest are positron emission tomography (PET) tracers, which combine quantitative whole-body imaging with high sensitivity[25]. Unlike conventional anatomical imaging, PET addresses biological function, enabling the mechanistic characterization of diseases[26]. A key strength of PET imaging is its intrinsic versatility. By leveraging specific molecular targets, PET probes can be designed to capitalize on distinct aspects of cellular physiology, including metabolism, receptor or target expression, and phagocytosis[27,28]. For instance, ^{18}F-FLT measures cell proliferation by targeting thymidine metabolism during DNA synthesis, while nanoparticle-based probes take advantage of the macrophage's phagocytic activity and lipid handling[27].

However, developing an optimal inflammatory PET tracer requires more than molecular versatility; it demands balancing immune-cell specificity with clinical feasibility. To date, available PET tracers remain limited in their ability to achieve both objectives simultaneously[25]. Among existing approaches, ^{18}F-FDG is currently the gold-standard benchmark for PET imaging of inflammation. ^{18}F-FDG is a glucose analog taken up by metabolically active cells through competitive uptake with endogenous glucose. During inflammatory processes, activated immune cells undergo metabolic reprogramming toward increased glycolysis, leading to enhanced ^{18}F-FDG accumulation[29]. First used in humans in 1979[30], ^{18}F-FDG is a clinically approved PET tracer for diagnosing a range of tumors, infections, and myocardial viability[31]. However, ^{18}F-FDG uptake is highly non-specific; it is also taken up by other cells with substantial glycolytic activity, such as skeletal muscle cells, cardiomyocytes, and brain tissue. This lack of precision carries several implications, including the need for complex dietary preparation prior to imaging, high physiological background signal (particularly in

cardiovascular imaging), and limited sensitivity for detecting specific illnesses[29].

Consequently, several alternative tracers have been developed. TSPO tracers, such as 11C-PK11195 and 18F-DPA-714, capitalize on the upregulation of a translocator protein in many activated immune cell types and are widely used to diagnose neuroinflammation[32]. Recent work has also explored broadening the use of such tracers for peripheral inflammation[33,34]. However, in addition to limited cell-type specificity, TSPO gene polymorphisms lead to variable affinity binders. In the absence of genotyping, this can be a confounding factor for quantification and inter-individual comparison[35,36]. Conversely, radiolabeled white blood cells, originally popular in the SPECT/CT modality, are now being adapted to PET/CT use. Yet, despite their leukocyte specificity, their manufacturing requires laborious *ex vivo* cell isolation and reinfusion, posing a significant logistical challenge for scalability[37].

Addressing these hurdles requires imaging approaches that capture the complexity of immune dynamics while remaining compatible with clinical translation. With that in mind, the work described in this thesis is situated at the intersection of molecular imaging, immunology, and disease biology, with the overarching aim of understanding how inflammatory processes can be visualized *in vivo*. By focusing on myeloid cells, particularly macrophages as central orchestrators of inflammation, we evaluated current and emerging PET tracers along with their limitations. While ^{18}F-FDG served as the most widely used reference tracer in this thesis, additional PET platforms were utilized to probe different dimensions of macrophage biology, ranging from metabolism and receptor expression to nanoparticle uptake. Beyond disease characterization, these imaging strategies were also employed to monitor therapeutic responses, enabling a longitudinal assessment of how interventions modulate immune-cell behavior *in vivo*. In several studies, integrating complementary tracers through multiparametric imaging provided a more comprehensive characterization of disease biology, enabling the simultaneous assessment of distinct cellular and molecular

processes that a single biomarker cannot capture. Ultimately, this work aims to advance molecular imaging from a general indicator of inflammation toward a mechanistically informative and clinically translatable tool for monitoring immune responses *in vivo*.

References

1. Cavaillon, J.-M. Once upon a time, inflammation. *Journal of Venomous Animals and Toxins including Tropical Diseases* https://doi.org/10.1590/1678-9199-jvatitd-2020-0147 (2021) doi:10.1590/1678-9199-jvatitd-2020-0147.
2. Swann, J. W., Olson, O. C. & Passegué, E. Made to order: emergency myelopoiesis and demand-adapted innate immune cell production. *Nat. Rev. Immunol.* **24**, 596–613 (2024).
3. Agrati, C. *et al.* The immune response as a double-edged sword: The lesson learnt during the <scp>COVID</scp> -19 pandemic. *Immunology* **167**, 287–302 (2022).
4. Greten, F. R. & Grivennikov, S. I. Inflammation and Cancer: Triggers, Mechanisms, and Consequences. *Immunity* **51**, 27–41 (2019).
5. Libby, P. The changing landscape of atherosclerosis. *Nature* **592**, 524–533 (2021).
6. Rock, K. L., Latz, E., Ontiveros, F. & Kono, H. The Sterile Inflammatory Response. *Annu. Rev. Immunol.* **28**, 321–342 (2010).
7. Bernheim, A., Cury, J. & Poirier, E. Z. The immune modules conserved across the tree of life: Towards a definition of ancestral immunity. *PLoS Biol.* **22**, e3002717 (2024).
8. Silva, R. C. M. C. & Gomes, F. M. Evolution of the Major Components of Innate Immunity in Animals. *J. Mol. Evol.* **92**, 3–20 (2024).
9. MacRitchie, N. *et al.* Molecular imaging of inflammation - Current and emerging technologies for diagnosis and treatment. *Pharmacol. Ther.* **211**, 107550 (2020).
10. Hammoud, D. A. Molecular Imaging of Inflammation: Current Status. *Journal of Nuclear Medicine* **57**, 1161–1165 (2016).
11. Mayer, A. T. & Gambhir, S. S. The Immunoimaging Toolbox. *Journal of Nuclear Medicine* **59**, 1174–1182 (2018).
12. Kelly, L. S., Darden, D. B., Fenner, B. P., Efron, P. A. & Mohr, A. M. The Hematopoietic Stem/Progenitor Cell Response to Hemorrhage, Injury, and Sepsis: A Review of Pathophysiology. *Shock* **56**, 30–41 (2021).
13. Boes, K. M. & Durham, A. C. Bone Marrow, Blood Cells, and the Lymphoid/Lymphatic System. in *Pathologic Basis of Veterinary Disease* 724-804.e2 (Elsevier, 2017). doi:10.1016/B978-0-323-35775-3.00013-8.
14. Yang, J., Zhang, L., Yu, C., Yang, X.-F. & Wang, H. Monocyte and macrophage differentiation: circulation inflammatory monocyte as biomarker for inflammatory diseases. *Biomark. Res.* **2**, 1 (2014).
15. Collin, M. & Bigley, V. Monocyte, Macrophage, and Dendritic Cell Development: the Human Perspective. *Microbiol. Spectr.* **4**, (2016).
16. Oishi, Y. & Manabe, I. Macrophages in inflammation, repair and regeneration. *Int. Immunol.* **30**, 511–528 (2018).
17. Chen, R. *et al.* Macrophages in cardiovascular diseases: molecular mechanisms and therapeutic targets.

Signal Transduct. Target. Ther. **9**, 130 (2024).
18. Moore, K. J., Sheedy, F. J. & Fisher, E. A. Macrophages in atherosclerosis: a dynamic balance. *Nat. Rev. Immunol.* **13**, 709–721 (2013).
19. Libby, P. *et al.* Macrophages and atherosclerotic plaque stability. *Curr. Opin. Lipidol.* **7**, 330–335 (1996).
20. Kubota, A. & Frangogiannis, N. G. Macrophages in myocardial infarction. *American Journal of Physiology-Cell Physiology* **323**, C1304–C1324 (2022).
21. Peet, C., Ivetic, A., Bromage, D. I. & Shah, A. M. Cardiac monocytes and macrophages after myocardial infarction. *Cardiovasc. Res.* **116**, 1101–1112 (2020).
22. Rodríguez-Morales, P. & Franklin, R. A. Macrophage phenotypes and functions: resolving inflammation and restoring homeostasis. *Trends Immunol.* **44**, 986–998 (2023).
23. Huang, T., Cheng, H., Zhao, Q. & Li, M. Macrophage reprogramming and functional plasticity in sepsis. *Front. Immunol.* **17**, (2026).
24. Sica, A. & Massarotti, M. Myeloid suppressor cells in cancer and autoimmunity. *J. Autoimmun.* **85**, 117–125 (2017).
25. Patel, N., Bergstrom, M., Murphy, P. S. & Maynard, J. PET in the characterization of immune diseases and development of therapeutics. *Oxf. Open Immunol.* **6**, (2025).
26. Signore, A. *et al.* Current Status of Molecular Imaging in Inflammatory and Autoimmune Disorders. *Curr. Pharm. Des.* **24**, 743–753 (2018).
27. Mason, C., Gimblet, G. R., Lapi, S. E. & Lewis, J. S. Novel Tracers and Radionuclides in PET Imaging. *Radiol. Clin. North Am.* **59**, 887–918 (2021).
28. Weissleder, R., Nahrendorf, M. & Pittet, M. J. Imaging macrophages with nanoparticles. *Nature Materials* vol. 13 125–138 Preprint at https://doi.org/10.1038/nmat3780 (2014).
29. Pijl, J. P. *et al.* Limitations and Pitfalls of FDG-PET/CT in Infection and Inflammation. *Semin. Nucl. Med.* **51**, 633–645 (2021).
30. Reivich, M. *et al.* The [18F]fluorodeoxyglucose method for the measurement of local cerebral glucose utilization in man. *Circ. Res.* **44**, 127–137 (1979).
31. Ashraf, M. A. & Goyal, A. *Fludeoxyglucose (18F).* (2026).
32. Chauveau, F., Becker, G. & Boutin, H. Have (R)-[11C]PK11195 challengers fulfilled the promise? A scoping review of clinical TSPO PET studies. *Eur. J. Nucl. Med. Mol. Imaging* **49**, 201–220 (2021).
33. Uzuegbunam, B. C., Rummel, C., Librizzi, D., Culmsee, C. & Hooshyar Yousefi, B. Radiotracers for Imaging of Inflammatory Biomarkers TSPO and COX-2 in the Brain and in the Periphery. *Int. J. Mol. Sci.* **24**, 17419 (2023).
34. Torrado-Carvajal, A. & Loggia, M. L. Towards a Whole-Body Assessment of Pain Using the 18 <scp>kDa</scp> Translocator Protein (<scp>TSPO</scp>) as a Broad-Spectrum Imaging Marker of Inflammation. *European Journal of Pain* **30**, (2026).
35. Owen, D. R., Guo, Q., Rabiner, E. A. & Gunn, R. N. The impact of the rs6971 polymorphism in TSPO for quantification and study design. *Clin. Transl. Imaging* **3**, 417–422 (2015).
36. Cumbers, G. A., Harvey-Latham, E. D., Kassiou, M., Werry, E. L. & Danon, J. J. Emerging TSPO-PET Radiotracers for Imaging Neuroinflammation: A Critical Analysis. *Semin. Nucl. Med.* **54**, 856–874 (2024).
37. Salmanoglu, E., Kim, S. & Thakur, M. L. Currently Available Radiopharmaceuticals for Imaging Infection and the Holy Grail. *Semin. Nucl. Med.* **48**, 86–99 (2018).

Outline and scope of the thesis

The overarching goal of this thesis is to deploy myeloid cell-targeting PET tracers as vessels for imaging inflammation and its kinetics across different disease models and multiple species. In **Part I**, we establish a comprehensive framework of tracers that can be employed to study the dynamics of inflammation in cardiovascular disease. In **Part II**, we develop, characterize, and validate new probes for inflammation imaging. Finally, in **Part III**, we utilize myeloid cell imaging for quantitative analysis of therapy response.

Following a brief introduction in **Chapter I**, we compare the somatostatin receptor 2-based imaging agent DOTATATE to gold standard ^{18}F-FDG in **Chapter II**. This comparison is used to image macrophage-driven inflammation in small and large animal models of cardiovascular disease. In **Chapter III**, we employ a diverse range of imaging tracers and readouts to compare permanent and temporary coronary occlusion models of myocardial infarction, revealing their distinct inflammatory signatures and systemic implications.

In **Chapter IV**, we fully validate and characterize macrin, a novel and versatile PET-based tracer. This nanoparticle-based imaging agent is tested across multiple pathological conditions, ranging from myocardial infarction to pneumonia, and animal species (mice, rabbits and pigs). The use of large animals in this study demonstrates strong translational potential. In **Chapter V**, we leverage the natural affinity of apolipoprotein A1 and HDL for macrophages to systemically characterize inflammation in cancer and myocardial infarction. By using an apolipoprotein A1 mimetic, we successfully reduce the complexity associated with traditional nanoparticle approaches. In **Chapter VI**, we probe ^{19}F-HDL to image systemic myeloid cell mobilization and trafficking following myocardial infarction with magnetic resonance, PET, and other optical imaging modalities. This work demonstrates how nanotracers can be used to study immunology and egression of immune cells from hematopoietic organs in cardiovascular disease models.

Lastly, in **Chapters VII and VIII**, molecular imaging is deployed to guide and monitor therapeutic interventions. In **Chapter VII**, we study the effects of mTOR inhibition in *in vitro* and in mouse models of dysregulated immune responses. We leverage our myeloid cell-targeting platform to deliver an mTOR inhibitor drug, suppressing pathological inflammation while preserving immune homeostasis. We finalize with **Chapter VIII**, which bridges pre-clinical and precision medicine. In this concluding chapter, we scale up the production of HDL-based nanoimmunotherapy agents to overcome translational barriers in nanomedicine advancements. We integrate clinically relevant imaging modalities to track therapeutic response in large animal models, simultaneously tracking myeloid cells through ^{19}F-MRI, PET, optical imaging, and flow cytometry to monitor the efficacy of our nanodrug and predict its anti-atherosclerotic effect.

Part 1

In vivo imaging to study inflammation kinetics in cardiovascular disease.



2

Systematically evaluating DOTATATE and FDG as PET immuno-imaging tracers of cardiovascular inflammation

Published in Scientific Reports, 2022.

Toner, Y.C.*, Ghotbi, A.A.*, Naidu, S., Sakurai, K., van Leent, M.M.T., Jordan, S., Ordikhani, F., Amadori, L., Sofias, A.M., Fisher, E.L., Maier, A., Sullivan, N., Munitz, J., Senders, M.L., Mason, C., Reiner, T., Soultanidis, G., Tarkin, J.M., Rudd, J.H.F., Giannarelli, C., Ochando, J., Pérez-Medina, C., Kjaer, A., Mulder, W.J.M., Fayad, Z.A., Calcagno, C

.

* These authors contributed equally to this work.

Toner, Y.C. planned and performed the mouse experiments, including pharmacokinetics, biodistribution, blood separation assays, PET/CT imaging and samples preparation for flow cytometry. She was also responsible for the mouse models of atherosclerosis and myocardial infarction (including the LAD ligation surgery), subsequent data analysis and writing of the manuscript.

Abstract

In recent years, cardiovascular immuno-imaging by positron emission tomography (PET) has undergone tremendous progress in preclinical settings. Clinically, two approved PET tracers hold great potential for inflammation imaging in cardiovascular patients, namely FDG and DOTATATE. While the former is a widely applied metabolic tracer, DOTATATE is a relatively new PET tracer targeting the somatostatin receptor 2 (SST2). In the current study, we performed a detailed, head-to-head comparison of DOTATATE-based radiotracers and [^{18}F]F-FDG in mouse and rabbit models of cardiovascular inflammation. For mouse experiments, we labeled DOTATATE with the long-lived isotope [^{64}Cu]Cu to enable studying the tracer's mode of action by complementing *in vivo* PET/CT experiments with thorough *ex vivo* immunological analyses. For translational PET/MRI rabbit studies, we employed the more widely clinically used [^{68}Ga]Ga-labeled DOTATATE, which was approved by the FDA in 2016. DOTATATE's pharmacokinetics and timed biodistribution were determined in control and atherosclerotic mice and rabbits by *ex vivo* gamma counting of blood and organs. Additionally, we performed *in vivo* PET/CT experiments in mice with atherosclerosis, mice subjected to myocardial infarction and control animals, using both [^{64}Cu]Cu-DOTATATE and [^{18}F]F-FDG. To evaluate differences in the tracers' cellular specificity, we performed ensuing *ex vivo* flow cytometry and gamma counting. In mice subjected to myocardial infarction, *in vivo* [^{64}Cu]Cu-DOTATATE PET showed higher differential uptake between infarcted (SUV_{max} 1.3, IQR, 1.2-1.4, N=4) and remote myocardium (SUV_{max} 0.7, IQR, 0.5-0.8, N=4, p=0.0286), and with respect to controls (SUV_{max} 0.6, IQR, 0.5-0.7, N=4, p=0.0286), than [^{18}F]F-FDG PET. In atherosclerotic mice, [^{64}Cu]Cu-DOTATATE PET aortic signal, but not [^{18}F]F-FDG PET, was higher compared to controls (SUV_{max} 1.1, IQR, 0.9-1.3 and 0.5, IQR, 0.5-0.6, respectively, N=4, p=0.0286). In both models, [^{64}Cu]Cu-DOTATATE demonstrated preferential accumulation in macrophages with respect to other myeloid cells, while [^{18}F]F-FDG was taken up by macrophages and other leukocytes. In a translational PET/MRI study in atherosclerotic rabbits,

we then compared [^{68}Ga]Ga-DOTATATE and [^{18}F]F-FDG for the assessment of aortic inflammation, combined with *ex vivo* radiometric assays and near-infrared imaging of macrophage burden. Rabbit experiments showed significantly higher aortic accumulation of both [^{68}Ga]Ga-DOTATATE and [^{18}F]F-FDG in atherosclerotic (SUV_{max} 0.415, IQR, 0.338-0.499, N=32 and 0.446, IQR, 0.387-0.536, N=27, respectively) compared to control animals (SUV_{max} 0.253, IQR, 0.197-0.285, p=0.0002, N=10 and 0.349, IQR, 0.299-0.423, p=0.0159, N=11, respectively). In conclusion, we present a detailed, head-to-head comparison of the novel SST2-specific tracer DOTATATE and the validated metabolic tracer [^{18}F]F-FDG for the evaluation of inflammation in small animal models of cardiovascular disease. Our results support further investigations on the use of DOTATATE to assess cardiovascular inflammation as a complementary readout to the widely used [^{18}F]F-FDG.

Introduction

Cardiovascular disease is the principal cause of morbidity and mortality worldwide [1]. In the past two decades, pre-clinical and clinical studies [2–6] have uncovered inflammation's critical role in atherosclerotic plaque formation and the onset of cardio- and cerebrovascular events. As cardiovascular inflammation is rapidly developing into a therapeutic target, quantitative positron emission tomography (PET) inflammation imaging of the heart and vasculature is rapidly gaining momentum.

Originally developed as a cancer PET tracer, [^{18}F]F-fluorodeoxyglucose ([^{18}F]F-FDG) is also the most commonly used inflammation tracer in cardiovascular disease, both in the context of atherosclerosis and cardiac ischemia [7,8]. Nevertheless, several limitations are associated with [^{18}F]F-FDG's use for cardiovascular inflammation imaging. First and foremost, being a glucose analog, [^{18}F]F-FDG is taken up by metabolically active cells and is not necessarily specific for inflammatory cells. In fact, *in vitro* [9] and recent *in vivo* atherosclerosis studies [10] indicate that vascular [^{18}F]F-FDG signal might also originate from cells other than plaque macrophages, including non-immune cells. In the context of cardiac imaging, the absence of [^{18}F]F-FDG signal is indicative of cardiomyocyte loss after myocardial infarction[11]. Unfortunately, high [^{18}F]F-FDG background signal in the healthy heart makes it challenging to visualize inflammation in the coronaries or in the infarct itself [12–14].

To surpass these limitations, alternative, inflammatory cell-specific PET tracers are being actively investigated for use in cardiovascular disease [12,15–17]. [^{68}Ga]Ga- or [^{64}Cu]Cu-labeled DOTATATE is a somatostatin receptor type 2 (SST2)-binding, FDA approved, PET radiotracer used to identify and monitor SST2-positive neuroendocrine tumors [18,19]. Since SST2 receptors are also expressed on macrophages[20], DOTATATE-based tracers have recently gained significant interest for the quantification of inflammation in cardiovascular disease mouse models [21], in human plaques [20,22] and, more recently, in myocardial infarction [23,24]. However, the advantages and

challenges of using DOTATATE-based radioligands to characterize and quantify cardiovascular inflammation, especially in comparison with the validated and widely used [^{18}F]F-FDG, have yet to be elucidated.

Here, we use the combination of *in vivo* PET imaging and extensive *ex vivo* radio-immunological assays to study the immunological behavior of [^{68}Ga]Ga- and [^{64}Cu]Cu-DOTATATE compared to [^{18}F]F-FDG, in mouse and rabbit models of cardiovascular inflammation. To facilitate its rigorous evaluation in mice, DOTATATE was labeled with [^{64}Cu]Cu. [^{64}Cu]Cu's relatively long radioactive half-life (12.7 hours) allows quantitatively studying [^{64}Cu]Cu-DOTATATE's pharmacokinetics, timed biodistribution, quantification of cardiovascular inflammation and cellular specificity over a course of 2 days. Additionally, we performed translational experiments in rabbits on a clinical PET/MRI scanner using [^{68}Ga]Ga-DOTATATE (radioactive half-life 68 minutes), approved by the FDA in 2016, and widely used in humans.

Collectively, our data in several small animal models of cardiovascular disease suggest a valuable complementary role of DOTATATE-based tracers and [^{18}F]F-FDG for the assessment of cardiovascular inflammation, supporting the use of DOTATATE in this field.

Results

Study design

This study's aim was to thoroughly characterize and compare DOTATATE-based radiotracers and [^{18}F]F-FDG for the evaluation of inflammation in mouse and rabbit small animal models of cardiovascular disease (Fig. 1). We designed unique mode of action mouse studies using DOTATATE radiolabeled with the long half-life radioisotope [^{64}Cu]Cu (12.7 hours). This allows complementing *in vivo* PET/CT imaging with extensive (and time consuming) *ex vivo* radiometric and immunological assays. For translational PET/MRI rabbit studies, we used [^{68}Ga]Ga-labeled DOTATATE (half-life 68 minutes), a radiotracer approved by the FDA since 2016, and of high translational relevance due to its use in clinical settings. We investigated

DOTATATE's pharmacokinetics and timed organ biodistribution in mice by *ex vivo* gamma counting of blood and organs (Supplementary Fig. S1A). In mice with atherosclerosis, mice subjected to myocardial infarction and control animals, we used *in vivo* PET/CT, together with *ex vivo* autoradiography and fluorescence activated cell sorting (FACS), to compare the quantification of cardiovascular inflammation and uptake by immune cells between [^{64}Cu]Cu-DOTATATE and [^{18}F]F-FDG (Supplementary Fig. S1B). Pharmacokinetics and biodistribution were also studied in rabbits (Supplementary Fig. S2A). Subsequently, translational rabbit experiments were performed on a clinical PET/MRI scanner. Atherosclerotic rabbits were imaged with both [^{68}Ga]Ga-DOTATATE and [^{18}F]F-FDG at different time points after Western diet (WD) initiation and compared to non-atherosclerotic controls. PET/MR data was validated with *ex vivo* near-infrared imaging of macrophage burden in the aorta (Supplementary Fig. S2B).

[^{64}Cu]Cu-DOTATATE's *in vivo* behavior in mice

In both control and atherosclerotic mice, [^{64}Cu]Cu-DOTATATE rapidly cleared from the blood, with a weighted blood half-life of, respectively, 4.8 and 6.8 minutes (Fig. 2A and Supplementary Table S1, C57Bl/6 N=7 and *Apoe*$^{-/-}$ N=6). In both groups, separation of blood fractions revealed that most of the tracer was in the plasma, which contained on average 83.4 ± 0.6 and 88.7 ± 0.9 % of the radioactivity at 120 minutes after radiotracer injection, respectively (Fig. 2B, N=5 per group). Density gradient separation of blood cells indicated that the tracer was taken up by mononuclear cells at early time-points, with progressive increase in polynuclear cells in control and atherosclerotic animals over the 120 minutes after injection (Fig. 2C, N=5 per group). In both C57Bl/6 and *Apoe*$^{-/-}$ mice, gamma counting of clearance organs substantiated the fast removal of [^{64}Cu]Cu-DOTATATE from the bloodstream. Shortly after injection, kidneys, bladder and liver cleared up most of the tracer. [^{64}Cu]Cu-DOTATATE exhibited affinity for organs rich in neuroendocrine cells, such as the pancreas, adrenal gland, stomach and intestines (Fig. 2D and Supplementary Fig. S3A, N=5 per group; Supplementary Table S2 and S3).

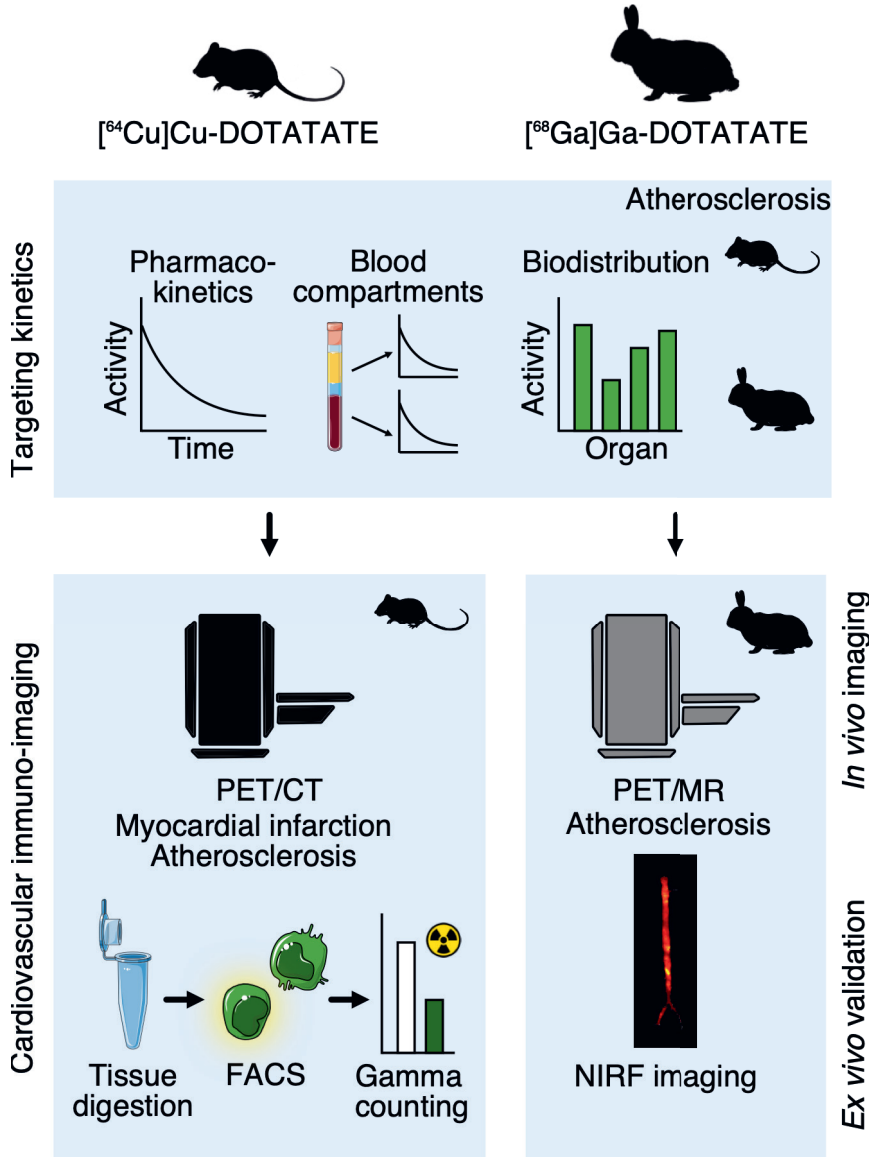


Figure 1. Study design. DOTATATE biodistribution and pharmacokinetics were obtained by *ex vivo* gamma counting of organs, blood and blood fractions in healthy and atherosclerotic mice and rabbits. In mice, comparison of [^{64}Cu]Cu-DOTATATE and [^{18}F]F-FDG in models of myocardial infarction and atherosclerosis was performed by *in vivo* PET/CT, while tracers' cellular uptake was determined by fluorescence activated cell sorting (FACS) of digested heart and aortic tissue followed by gamma counting. In rabbits, animals were imaged by *in vivo* PET/MRI using [^{68}Ga]Ga-DOTATATE and [^{18}F]F-FDG. Results were validated by *ex vivo* gamma counting and near-infrared fluorescence imaging.

To investigate [^{64}Cu]Cu-DOTATATE's suitability for use in cardiovascular disease studies, we evaluated myocardial and aortic uptake over time. In atherosclerotic mice, median heart signal at 120 minutes was 1.4 (IQR, 1.2-1.4) %ID/g, which was significantly higher compared to 0.7 %ID/g in time-matched controls (IQR, 0.7-0.8, p=0.0159, Fig. 2E and Supplementary Fig. S3A; Supplementary Table S2 and S3, C57Bl/6 N=5 and *Apoe*$^{-/-}$ N=4), most likely due to atherosclerosis-driven chronic inflammation. Two hours after injection, signal in the thoracic aorta was also significantly higher in atherosclerotic compared to control mice with medians of 2.1 (IQR, 2-2.4) and 1 (IQR, 0.7-1.1) %ID/g, respectively (p=0.0079, Fig. 2F and Supplementary Fig. S3A; Supplementary Table S2 and S3, N=5 per group).

[^{64}Cu]Cu-DOTATATE and [^{18}F]F-FDG PET imaging of cardiac inflammation in infarcted mice

Three days after myocardial infarct (MI) induction in C57Bl/6 mice, we performed *in vivo* PET/CT with either [^{64}Cu]Cu-DOTATATE or [^{18}F]F-FDG to quantify myocardial inflammation (Supplementary Fig. S1B). [^{64}Cu]Cu-DOTATATE PET images showed lower uptake throughout the body, particularly in the muscles (Fig. 3A-C), when compared to [^{18}F]F-FDG (Fig. 3D-F). In the infarcted heart, *in vivo* [^{64}Cu]Cu-DOTATATE SUV_{max} was significantly higher (median SUV_{max} 1.3, IQR, 1.2-1.4) compared to both the hearts of control animals (median SUV_{max} 0.6, IQR, 0.5-0.7, p=0.0286), and to the remote (non-infarcted) myocardium (median SUV_{max} 0.7, IQR, 0.5-0.8, p=0.0286, Fig. 3B, N=4 per group), as confirmed by *ex vivo* gamma counting and autoradiography (Fig. 3C and Supplementary Fig. S3B, N=4 per group). In contrast, quantification of [^{18}F]F-FDG uptake in control and infarcted hearts showed no significant difference (median SUV_{max} 3.4, IQR 2.6-3.7 and 4.2, IQR 3.3-4.6, respectively, p=0.2571, Fig. 3E, controls N=4 and infarcted N=6).

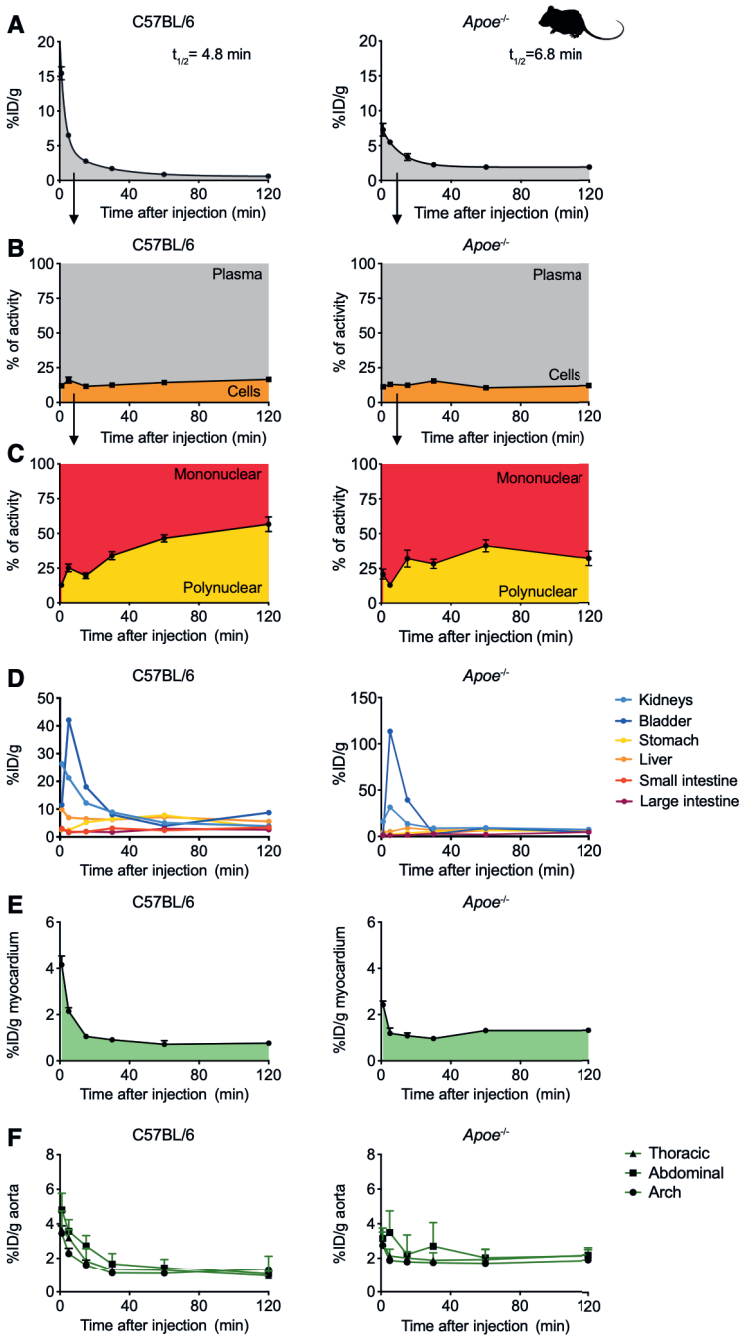

A
C57BL/6
$t_{1/2}$= 4.8 min
Apoe-/-
$t_{1/2}$=6.8 min
%ID/g
Time after injection (min)
B
C57BL/6
Apoe-/-
Plasma
Cells
% of activity
Time after injection (min)
C
Mononuclear
Polynuclear
D
Kidneys
Bladder
Stomach
Liver
Small intestine
Large intestine
E
%ID/g myocardium
F
%ID/g aorta
Thoracic
Abdominal
Arch

Figure 2. [^{64}Cu]Cu-DOTATATE pharmacokinetics and biodistribution in mice. A) Blood time-activity curve for intravenously infused [^{64}Cu]Cu-DOTATATE in C57Bl/6 (left) and *Apoe*$^{-/-}$ (right) mice. Data are presented as mean ± standard error of the mean. C57Bl/6 N=7 and *Apoe*$^{-/-}$ N=6. B) [^{64}Cu]Cu-DOTATATE radioactivity distribution in blood fractions as measured by gamma counting. Graphs show the percentage of activity associated with cells or plasma. Data are presented as mean ± standard error of the mean. N=5 per group. C) Percentage of activity associated with blood mononuclear or polynuclear cells. Data are presented as mean ± standard error of the mean. N=5 per group. D) Time-activity curves for [^{64}Cu]Cu-DOTATATE in clearance organs. N=5 per group. E) Gamma counting of [^{64}Cu]Cu-DOTATATE activity in the myocardium over time. Data are presented as median (interquartile range). C57Bl/6 N=5 and *Apoe*$^{-/-}$ N=4. F) Time-activity curves for [^{64}Cu]Cu-DOTATATE in the arch, thoracic and abdominal aorta. Data are presented as median (interquartile range). N=5 per group. ID: injected dose; $t_{1/2}$: half-life.

Within the heart of infarcted animals, we observed a difference in [^{18}F]F-FDG uptake in the infarcted myocardium when compared to remote myocardium (2.1, IQR, 2-3.8, p=0.0411, Fig. 3E, N=6) as described in the literature [25,26], but these findings could not be confirmed by *ex vivo* gamma counting (Fig. 3F, controls N=4 and infarcted N=6). By autoradiography, the ratio between the signal in infarcted and remote myocardium was approximately 2 for [^{64}Cu]Cu-DOTATATE, but close to 1 for [^{18}F]F-FDG (Supplementary Fig. S3B, N=4 per group), indicating better infarct/remote myocardium delineation using [^{64}Cu]Cu-DOTATATE.

We postulate that [^{64}Cu]Cu-DOTATATE's affinity for SST2-expressing cells, particularly macrophages, is responsible for the improved specificity compared to [^{18}F]F-FDG. To verify this hypothesis, we harvested the infarcted myocardium and cell-sorted CD11b^{+}CD11c^{-}F4/80^{+} (macrophages), CD11b^{+} (myeloid cells excluding macrophages) and CD11b^{-} (non-myeloid cells) populations after PET imaging (Fig. 3G, Supplementary Fig. S3C and Supplementary Table S4). Cell suspensions were gamma counted and radiotracer activity was normalized to the number of cells per sample. The ratio of activity in CD11b^{+} (myeloid) versus CD11b^{-} (non-myeloid leukocytes) cells was 6-fold higher for [^{64}Cu]Cu-DOTATATE compared to [^{18}F]F-FDG (p=0.0286, Fig. 3H, N=4 per group), indicating higher accumulation of [^{64}Cu]Cu-DOTATATE in the myeloid cell fraction. Within CD11b^{+} myeloid cells, [^{64}Cu]Cu-DOTATATE was found to accumulate 3-fold more in

macrophages with respect to [^{18}F]F-FDG, although these differences did not reach statistical significance (p=0.0571, Fig. 3H, N=4 per group).

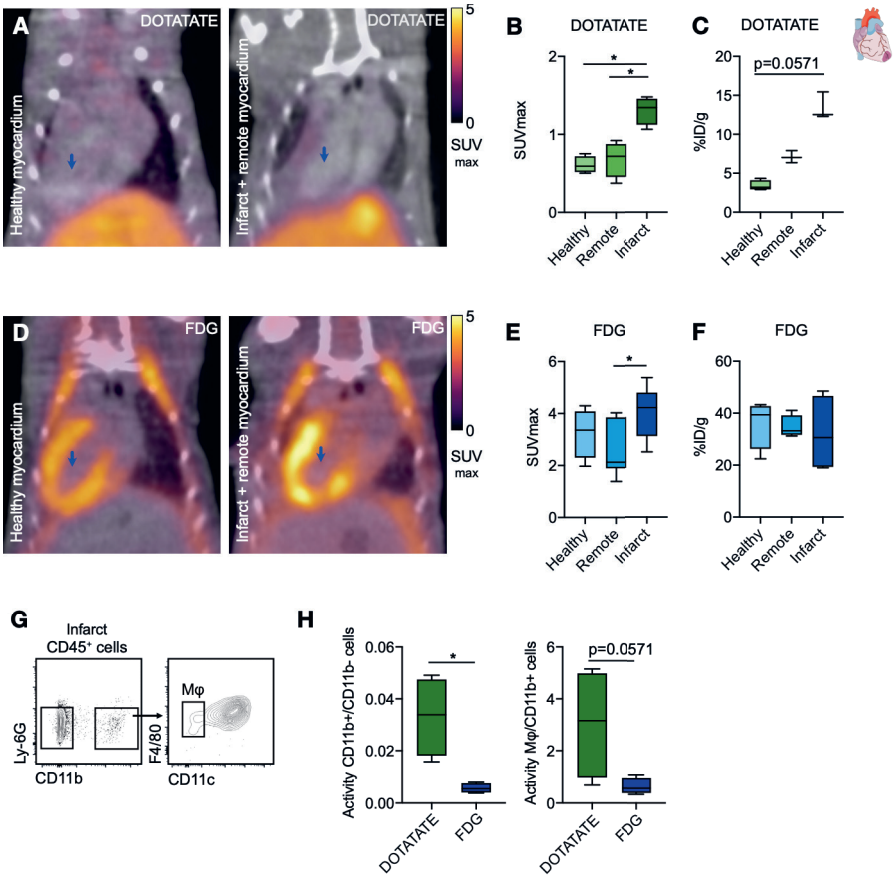


Figure 3. [^{64}Cu]Cu-DOTATATE PET imaging of murine myocardial infarction. A) Representative fused [^{64}Cu]Cu-DOTATATE PET/CT 3D-rendered images of healthy (left) and LAD-ligated (right) animals. Blue arrows represent region of infarct. B) [^{64}Cu]Cu-DOTATATE SUV_{max} (*in vivo*) and C) %ID/g (*ex vivo*) in the heart of C57Bl/6 healthy animals (myocardium) and LAD-ligated mice (remote and infarct). N=4 per group. D) Representative fused [^{18}F]F-FDG PET/CT 3D-rendered images of healthy (left) and LAD-ligated (right) animals. Blue arrows represent region of infarct. E) [^{18}F]F-FDG SUV_{max} (*in vivo*) and F) %ID/g (*ex vivo*) in the heart of C57Bl/6 healthy animals (myocardium) and LAD-ligated mice (remote and infarct). Controls N=4 and infarcted N=6/ G) Representative flow cytometry plots identifying $CD11b^-$, $CD11b^+$ and macrophage cell populations in the myocardium. H) Quantification of activity per cell in the infarcted myocardium. Data are expressed as ratio of $CD11b^+/CD11b^-$ (left) and **Mφ**/$CD11b^+$ cell activity (right). N=4 per group. DOTATATE: [^{64}Cu]Cu-DOTATATE; FDG: [^{18}F]F-FDG; infarct: infarcted region of the myocardium; ID: injected dose; **Mφ**: macrophages; Myocardium: healthy C57Bl/6 myocardium; remote: remote myocardium (non-infarcted); SUV_{max}: maximum standardized uptake value.

CD11b^{+} cells represent CD11b^{+}CD11c^{hi}, excluding macrophage population. *p<0.05. Data are presented as median (interquartile range).

[^{64}Cu]Cu-DOTATATE and [^{18}F]F-FDG PET imaging of vascular inflammation in atherosclerotic mice

Encouraged by its macrophage specificity in the heart, we set out to investigate the application of [^{64}Cu]Cu-DOTATATE PET imaging in aortic plaques of *Apoe*$^{-/-}$ atherosclerotic mice. *In vivo* PET showed significantly higher [^{64}Cu]Cu-DOTATATE SUV_{max} in the ascending aorta of *Apoe*$^{-/-}$ mice with median of 1.1 (IQR, 0.9-1.3) compared to healthy (non-atherosclerotic) C57Bl/6 mice where median SUV_{max} was 0.5 (IQR, 0.5-0.6, p=0.0286, Fig. 4A and 4B, N=4 per group). This finding was in agreement with the overall trend of *ex vivo* gamma counting, which, however, did not reach statistical significance, with median %ID/g values of 7.4 (IQR, 3.6-9.9) and 3.5 (IQR, 2.7-4, p=0.2, Fig. 4C, N=4 per group) in atherosclerotic and control mice, respectively. In atherosclerotic mice, *ex vivo* autoradiography demonstrated 2-fold higher signals in atherosclerotic plaques compared to healthy (no plaque) areas of the aorta (Supplementary Fig. S3D, N=4). [^{18}F]F-FDG SUV_{max} in the ascending aorta showed no significant difference between *Apoe*$^{-/-}$ mice with median of 1.2 (IQR, 1.1-1.5) and C57Bl/6 control animals with median of 1.7 (IQR, 1.4-2.2, p =0.2, Fig. 4D and 4E, N=4 per group), as also observed by *ex vivo* gamma counting (Fig. 4F, N=4 per group). In line with our observations in the myocardial infarction model, in atherosclerotic mice there was a non-significant trend for greater uptake of [^{64}Cu]Cu-DOTATATE in CD11b^{+} cells over CD11b^{-} cells (2-fold higher when compared to [^{18}F]F-FDG), and specifically in macrophages (1.5-fold increase when compared to [^{18}F]F-FDG, p=0.2, Fig. 4G and 4H, Supplementary Fig. S3C and Supplementary Table S4, N=4 per group).

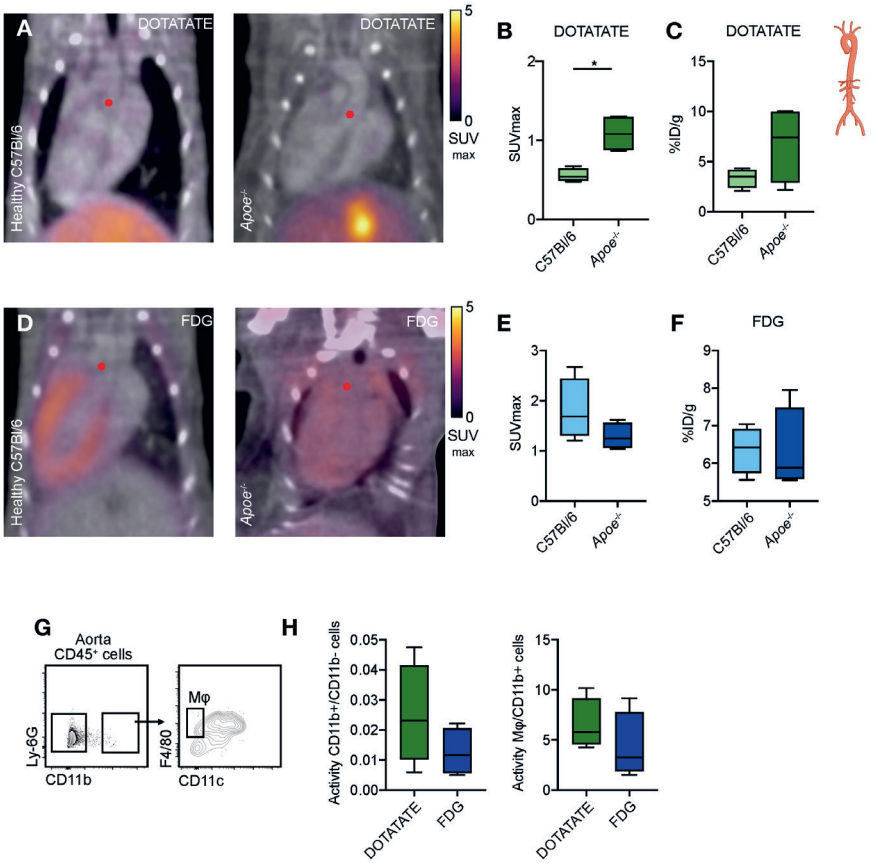


Figure 4. [^{64}Cu]Cu-DOTATATE PET imaging of murine atherosclerosis. A) Representative fused PET/CT image of [^{64}Cu]Cu-DOTATATE-infused C57Bl/6 (left) and *Apoe*$^{-/-}$mice after 12 weeks on WD (right). Red dot represents origin of ascending aorta. B) *In vivo* [^{64}Cu]Cu-DOTATATE SUV_{max} of the ascending aorta. N=4 per group. C) *Ex vivo* %ID/g of the whole aorta. N=4 per group. D) Representative fused PET/CT 3D-rendered image of [^{18}F]F-FDG-infused *Apoe*$^{-/-}$ mice. Red dot represents origin of ascending aorta. E) [^{18}F]F-FDG SUV_{max} of ascending aorta. N=4 per group. F) %ID/g of the whole aorta. N=4 per group. G) Representative flow cytometry plots identifying CD11b^{+} and macrophage cell populations in the aorta. H) Quantification of activity per cell in the aorta. Data are expressed as ratio of CD11b^{+}/CD11b^{-} (left) and M**φ**/CD11b^{+} cell activity (right). N=4 per group. DOTATATE: [^{64}Cu]Cu-DOTATATE; FDG: [^{18}F]F-FDG; ID: injected dose; M**φ**: macrophages; SUV_{max}: maximum standardized uptake value. CD11b^{+} cells represent CD11b^{+}CD11c^{hi}, excluding macrophage population. *p<0.05. Data are presented as median (interquartile range).

[^{68}Ga]Ga-DOTATATE's *in vivo* behavior in rabbits

In the next stage of our workflow, we evaluated DOTATATE labeled with the short-lived isotope [^{68}Ga]Ga in a translational rabbit model of atherosclerosis (aortic endothelium denudation in combination with western diet[27]) on a clinical PET/MR scanner. [^{68}Ga]Ga-DOTATATE pharmacokinetics was assessed in atherosclerotic animals 4 months after diet initiation (athero$_{4mo}$) and non-atherosclerotic (control) New Zealand White (NZW) rabbits (Supplementary Fig. S2A). [^{68}Ga]Ga-DOTATATE weighted half-life was 53.7 minutes in atherosclerotic rabbits and 21.2 minutes in control animals (Fig. 5A and Supplementary Table S1, controls N=2 and athero$_{4mo}$ N=3). In line with findings in mice, the majority of [^{68}Ga]Ga-DOTATATE was detected in plasma, rather than cells (Supplementary Fig. S4A, controls N=2 and athero$_{4mo}$ N=3). [^{68}Ga]Ga-DOTATATE behaved similarly to [^{64}Cu]Cu-DOTATATE, showing renal clearance and high accumulation in the stomach and other gastrointestinal organs (Fig. 5B and Supplementary Fig. S4B; Supplementary Table S5, controls N=6 and athero$_{4mo}$ N=9). In atherosclerotic rabbits [^{68}Ga]Ga-DOTATATE median %ID/g in the thoracic and abdominal aorta were, respectively, 0.015 (IQR, 0.011-0.018) and 0.017 (IQR, 0.014-0.022), while, in controls median [^{68}Ga]Ga-DOTATATE %ID/g was 0.004 (IQR, 0.002-0.006;–p=0.0028) in the thoracic aorta and 0.006 (IQR, 0.003-0.02; p=0.1483) in the abdominal aorta (Fig. 5C and Supplementary Fig. S4B; Supplementary Table S5, controls N=6 and athero$_{4mo}$ N=9).

Translational [^{68}Ga]Ga-DOTATATE PET/MR imaging of inflammatory atherosclerosis in rabbits

Encouraged by the mouse data, we performed an extensive PET imaging study to quantify vascular inflammation by [^{68}Ga]Ga-DOTATATE's and [^{18}F]F-FDG in an atherosclerosis rabbit model. Atherosclerotic rabbits 4 and 7 months after Western diet initiation (athero$_{4mo}$ and athero$_{7mo}$, respectively) and healthy controls were imaged with both [^{68}Ga]Ga-DOTATATE and [^{18}F]F-FDG on separate days (Supplementary Fig. S2B). Based on pharmacokinetic analyses and dynamic imaging experiments (Supplementary Fig. S4C, N=3

per group), we allowed [^{68}Ga]Ga-DOTATATE to circulate for 120 minutes and [^{18}F]F-FDG for 180 minutes, as previously validated [28], before PET imaging.

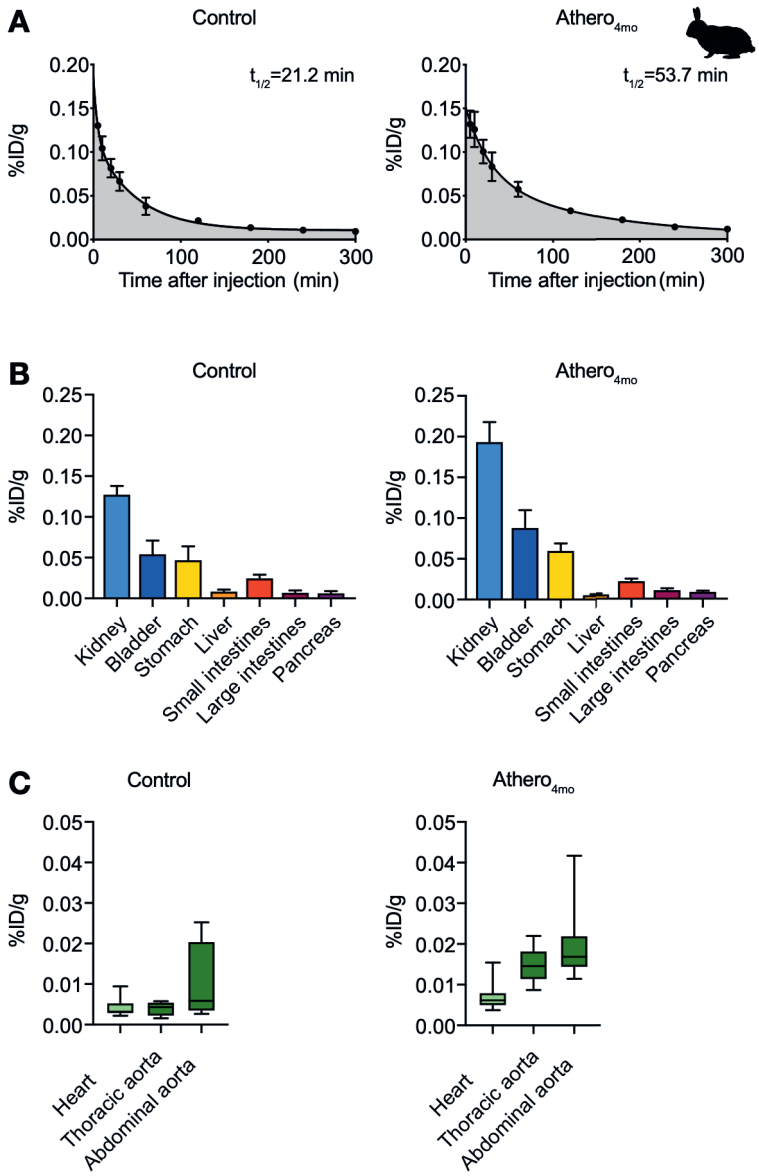


Figure 5. [^{68}Ga]Ga-DOTATATE pharmacokinetics and biodistribution in rabbits. A) Blood time-activity curve of [^{68}Ga]Ga-DOTATATE-infused control (left) and athero$_{4mo}$ (right) rabbits. Controls N=2 and athero$_{4mo}$ N=3. Data are presented as mean ± standard error of the mean. B) *Ex vivo* quantification of [^{68}Ga]Ga-DOTATATE uptake in urinary and digestive organs of rabbits at 200

minutes after tracer injection, as determined by gamma counting. Data are presented as mean ± standard error of the mean. Controls N=6 and athero$_{4mo}$ N=9. C) *Ex vivo* quantification of [^{68}Ga]Ga-DOTATATE uptake in the heart, thoracic and abdominal aorta 200 minutes after tracer injection, as determined by *ex vivo* gamma counting. Controls N=6 and athero$_{4mo}$ N=9. Data are presented as median (interquartile range). ID: injected dose; $t_{1/2}$: half-life.

Using [^{68}Ga]Ga-DOTATATE (Fig. 6A), we found a 1.6-fold higher SUV_{max} in atherosclerotic aortas of athero$_{4mo}$ animals as compared to controls, with medians of 0.415 (IQR, 0.338-0.499) and 0.253 (IQR, 0.197-0.285), respectively (p=0.0002) (Fig. 6B, controls N=10 and athero$_{4mo}$ N=32, excluded rabbits N=5). However, based on [^{68}Ga]Ga-DOTATATE PET, we did not detect a further increase in tracer accumulation in rabbits kept on Western Diet for 7 months (athero$_{7mo}$, p> 0.9999, Fig. 6C, N=7, excluded rabbits N=2). Similar to previous studies [29], we found 1.2-fold higher [^{18}F]F-FDG SUV_{max} in the abdominal aorta of athero$_{4mo}$ rabbits, with median 0.446 (IQR, 0.387-0.536), as compared to controls, with median 0.349 (IQR, 0.299-0.423, p=0.0159, Fig. 6D and 6E, controls N=11 and athero$_{4mo}$ N=27, excluded rabbits N=9). [^{18}F]F-FDG SUV_{max} also increased to a median of 0.515 (IQR, 0.409-0.602) over 3 additional months of Western diet (athero$_{7mo}$, p=0.0312, Fig. 6F, N=7, excluded rabbits N=2). Analysis of *ex vivo* near-infrared fluorescence imaging of Cy5.5-labeled HDL in the aorta (a validated marker of macrophage burden [30]) was in line with [^{68}Ga]Ga-DOTATATE results: while a significant difference was found in maximum radiant efficiency median values between control $1.67x10^8$ (IQR, $1.29x10^8$ – $1.94x10^8$) and atherosclerotic athero$_{4mo}$ animals $4.89x10^9$ (IQR, $3.36x10^9$ - $6.79x10^9$, p<0.0001), no increase in fluorescent HDL signal was observed when comparing athero$_{4mo}$ and athero$_{7mo}$, suggesting no increase in macrophage burden over time (p=0.5584, Fig. 6G, controls N=11, athero$_{4mo}$ N=15 and athero$_{7mo}$ N=8). A weak, but significant (r=0.3522; p=0.0141), correlation was found between [^{18}F]F-FDG and [^{68}Ga]Ga-DOTATATE aortic SUV_{max}, reflecting the partially overlapping cellular specificity of the two tracers (Supplementary Fig. S4D).

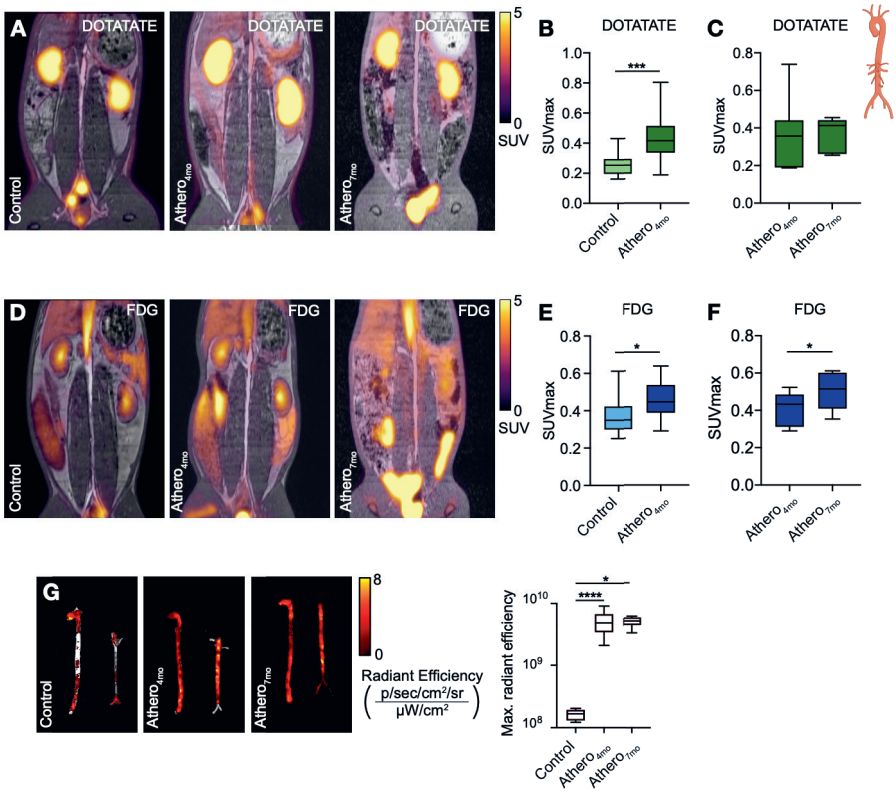


Figure 6. *In vivo* and *ex vivo* imaging of atherosclerosis in rabbits. A) Representative fused PET/MR image of [^{68}Ga]Ga-DOTATATE-infused control (left), athero$_{4mo}$ (middle) and athero$_{7mo}$ (right) rabbits. B) [^{68}Ga]Ga-DOTATATE SUV$_{max}$ of abdominal aorta in control and athero$_{4mo}$ animals. Controls N=10 and athero$_{4mo}$ N=32. C) Paired analysis of [^{68}Ga]Ga-DOTATATE SUV$_{max}$ of abdominal aorta in athero$_{4mo}$ and athero$_{7mo}$ animals. N=7 per group. D) Representative fused PET/MR image of [^{18}F]F-FDG-infused control (left), athero$_{4mo}$ (middle) and athero$_{7mo}$ (right) rabbits. E) [^{18}F]F-FDG SUV$_{max}$ of abdominal aorta in control and athero$_{4mo}$ animals. controls N=11 and athero$_{4mo}$ N=27. F) Paired analysis of [^{18}F]F-FDG SUV$_{max}$ of abdominal aorta in athero$_{4mo}$ and athero$_{7mo}$ animals. N=7 per group. G) Near-infrared fluorescence imaging of Cy5.5-HDL in the aorta of rabbits. Controls N=11, athero$_{4mo}$ N=15 and athero$_{7mo}$ N=8. DOTATATE: [^{64}Cu]Cu-DOTATATE; FDG: [^{18}F]F-FDG; SUV$_{max}$: maximum standardized uptake value. *p<0.05, ***p<0.001, ****p<0.0001. Data are presented as median (interquartile range).

Discussion

The use of SST2-specific PET radiotracers, and predominantly DOTATATE-based ligands, is rapidly gaining momentum for cardiovascular inflammation imaging [8,26,31]. In pre-clinical settings, visible uptake of SST2-specific PET radiotracers [15,21] including, but not limited to, DOTATATE has been previously demonstrated in mice with atherosclerosis. Yet, in selected studies, *in vivo* vascular imaging findings were confounded by concomitant uptake in nearby organs. Following successful retrospective analyses in cancer patients [32,33], DOTATATE vascular uptake has been shown in the vasculature of patients with coronary and carotid atherosclerosis [20,34], although other studies have question DOTATATE's ability to discriminate symptomatic lesions in humans [35]. Studies in patients with myocardial infarction [23] and a case report on cerebral stroke[36] have demonstrated significant uptake of DOTATATE in the infarcted, with respect to non-infarcted, tissue.

However, the strengths and weaknesses of DOTATATE, especially with respect to the validated metabolic tracer [^{18}F]F-FDG, in evaluating cardiovascular inflammation still need to be fully elucidated. In this study, we sought to thoroughly characterize the *in vivo* immune behavior of the SST2-specific [^{68}Ga]Ga- and [^{64}Cu]Cu-DOTATATE in comparison with the widely used metabolic tracer [^{18}F]F-FDG in experimental models of cardiovascular disease. Previous studies suggest that [^{64}Cu]Cu-DOTATATE and [^{68}Ga]Ga-DOTATATE have similar imaging performance for detection of neuroendocrine tumors. In the literature, dosimetric data indicates that differences in DOTATATE's tumor effective dose for both tracers is negligeable [37,38] and further image analysis in animal models showed similar results [39].

In mechanistic mouse experiments, we labeled DOTATATE with [^{64}Cu]Cu. The longer physical half-life of this radioisotope allowed complementing *in vivo* PET imaging with extensive *ex vivo* assays, including flow cytometry, gamma counting, and autoradiography, to investigate the tracer pharmacokinetics,

timed organ biodistribution, cellular specificity and ability to report on cardiovascular inflammation. In translational PET/MRI rabbit studies, we instead used *in vivo* PET imaging with [^{68}Ga]Ga-DOTATATE to assess aortic inflammation, in comparison with [^{18}F]F-FDG.

Our pharmacokinetic studies in mice confirmed rapid clearance of [^{64}Cu]Cu-DOTATATE from the bloodstream (similar to [^{18}F]F-FDG, which has a 5.1 minutes half-life) [40]. This feature is important when performing *in vivo* imaging and especially in the vasculature, whose signal can be easily contaminated by the blood pool because of partial volume errors. Timed biodistribution analysis in the mouse confirmed fast accumulation in the kidneys and gastrointestinal organs [41], and, as expected, targeting of SST2-expressing organs, such as pancreas and adrenal gland. We further used the combination of *in vivo* PET/CT imaging and *ex vivo* radiometric and immunological assays to investigate [^{64}Cu]Cu-DOTATATE as an inflammation tracer in mice with atherosclerosis and mice subjected to myocardial infarction. For the myocardial infarction model, mice were imaged 3 days after LAD ligation surgery. This timeline was chosen to capture the peak of SST2-expressing inflammatory macrophage infiltration in the infarcted myocardium [26], since SST2 is upregulated in inflammatory macrophages/LPS-stimulated macrophages, while expression in other leukocytes is negligible [20,42,43]. A previous preclinical study [24] that investigated the use of [^{68}Ga]Ga-DOTATATE in mouse models of cardiac ischemia did not show significant radiotracer accumulation in the infarct. While we also generally observed low myocardial signal, our data suggests improved infarct delineation from healthy myocardium with [^{64}Cu]Cu-DOTATATE in comparison with [^{18}F]F-FDG, as confirmed by *in vivo* SUVmax measurements. The difference between our findings and previous studies employing [^{68}Ga]Ga-DOTATATE may be due to the lower positron range of [^{64}Cu]Cu (1 mm) with respect to [^{68}Ga]Ga (4 mm), which intrinsically lowers the occurrence of partial volume artifacts from the blood stream, while offering intrinsic better signal-to-noise and spatial resolution [19,22,44]. Our results are also in agreement with findings from a recent clinical study [23],where focal, infarct-related [^{68}Ga]Ga-DOTATATE signal in patients with MI was well-visualized thanks to the tracer very low

physiological background tracer uptake, and was significantly higher than in the remote myocardium. In line with several clinical studies, as well as previous *ex vivo* autoradiography and *in vivo* analysis in *Apoe*$^{-/-}$ mice using [^{68}Ga]Ga-DOTATATE [20–22,33,34,41,45], we confirmed accumulation of [^{64}Cu]Cu-DOTATATE in mouse aortic plaques. Pre-clinical studies applying different SST2-specific PET radiotracers, such as the antagonist [^{111}In]In-DOTA-JR11, in atherosclerotic *Apoe*$^{-/-}$ mice have also demonstrated visible tracer accumulation in plaques. However, the interpretation of *in vivo* imaging findings was hampered by thymus uptake [15], making it challenging to use these different tracers in pre-clinical research settings. Our atherosclerosis mouse model also showed that [^{64}Cu]Cu-DOTATATE uptake was higher in the ascending aorta of atherosclerotic versus control animals, while no differences were detected for [^{18}F]F-FDG. While other studies in mice showed higher [^{18}F]F-FDG accumulation in atherosclerotic versus control animals [46,47], a recent report indicated that the specific anesthesia regimen used, and periaortic fat uptake may significantly affect [^{18}F]F-FDG plaque signal [48]. [^{64}Cu]Cu-DOTATATE blood half-life was longer in atherosclerotic mice (and rabbits) compared to controls, a factor that may potentially confound vessel wall readings because of higher blood background signal. We hypothesize that this phenomenon may be attributed to lower renal clearance (due to impaired kidney function) in diseased animals. However, *ex vivo* gamma counting validated the higher aortic tracer accumulation in atherosclerotic versus healthy animals, thereby mitigating these concerns.

Unlike a recently published *in vitro* analysis that employed macrophages differentiated from an immortalized THP-1 cell line [49], flow cytometry in both mouse models from our study confirmed higher affinity of DOTATATE for myeloid CD11b^{+} cells, with respect to [^{18}F]F-FDG, particularly for the macrophage fraction. This discrepancy might be attributed to methodological differences between the two studies, such as our studies being conducted *in vivo*, in mouse models, as opposed to *in vitro*, in cells derived from human blood, as well as the different cell isolation protocols. Our results are in line with a recent clinical study that confirmed high expression of SST2 in human M1 inflammatory macrophages, in comparison

with other myeloid and immune cells. However, glucose transporters 1 and 3 (GLUT1 and GLUT3) were found to be highly expressed by all immune cells, corroborating the lower cellular specificity of [^{18}F]F-FDG [20].

In addition to the extensive mechanistic mouse work, we evaluated [^{68}Ga]Ga-DOTATATE in a rabbit model of atherosclerosis. *Ex vivo* quantification of aortic HDL accumulation (a marker of macrophage burden) by near-infrared fluorescence imaging was in line with the *in vivo* [^{68}Ga]Ga-DOTATATE readout, indicating no increased macrophage burden during atherosclerosis progression. These findings strengthen the notion that the two tracers report on inter-related but intrinsically different processes.

To summarize, in this study we present a detailed, head-to-head comparison of the novel SST2-specific tracer DOTATATE and the validated metabolic tracer [^{18}F]F-FDG for the immune evaluation of inflammation in small animal models of cardiovascular disease. Our encouraging results support DOTATATE's use to assess cardiovascular inflammation, as a complementary readout to the widely used [^{18}F]F-FDG PET.

Methods

Radiolabeling of DOTA-(Tyr^3)-Octreotate with Copper-64 [^{64}Cu]Cu

DOTA-(Tyr^3)-Octreotate (DOTATATE) acetate salt was purchased from Bachem (Bubendorf, Switzerland). [^{64}Cu]Cu was produced using a CS15 cyclotron located at Washington University by the [^{64}Ni]Ni(p,n)[^{64}Cu]Cu nuclear reaction. Activity measurements were made using a Capintec CRC-15R Dose Calibrator (Capintec, Florham Park, NJ). [^{64}Cu]Cu was chelated to DOTATATE by adjusting the pH of a [^{64}Cu]Cu solution to 5, using a buffer containing 0.1 M NH_4OAc. Subsequently, 20 µg of DOTATATE were added to the solution and the reaction mixture was heated at 80 °C for approximately 45 minutes. The labeling reaction yielded [^{64}Cu]Cu-DOTATATE with a radiochemical purity of >98%, as determined by RadioHPLC, and a representative specific activity of 10 MBq/nmol. [^{68}Ga]Ga-DOTATATE was

purchased from Advanced Accelerator Applications (Millburn, NJ), with a representative specific activity of 1.01 MBq/nmol.

High-performance liquid chromatography (HPLC) and radio-HPLC.

High-performance liquid chromatography (HPLC) was performed on a Shimadzu (Kyoto, Japan) HPLC system equipped with two LC-10AT pumps and an SPD-M10AVP photodiode array detector. Radio-HPLC was performed using a Lablogic (Tampa, FL) Scan-RAM Radio-TLC/HPLC detector. Reverse phase chromatography was performed using a Waters Atlantis T3 column, 100, 5 µm, 4.6 mm x 250 mm (Waters, Milford, MA) with an acetonitrile to water gradient from 5-95% acetonitrile over 20 minutes at a flow rate of 1.0 mL min^{-1}.

Animal experiments

All animal experiments were performed in accordance with protocols approved by the Institutional Animal Care and Use Committee at the Icahn School of Medicine at Mount Sinai and followed National Institutes of Health guidelines for animal welfare. This study is reported in accordance with ARRIVE guidelines.

Mouse model

Animals were housed under a constant room temperature at 25 ± 2 °C and 50 ± 5% humidity with a 12-hour daylight period and 12-hour darkness period, with free access to water. For the mouse atherosclerosis model, 8-weeks old female *Apoe*$^{-/-}$ mice (N=51) were purchased from Jackson Laboratories (Bar Harbor, ME) and, after a 48 hours acclimatization period, were fed a Western Diet (42% Kcal from fat TD88137, Envigo, Huntingdon, UK) for 12 weeks. 16-20 weeks old female C57Bl/6 controls (N=67) were kept on regular chow diet. The myocardial infarction group consisted 16-20 weeks old female C57Bl/6 mice (N=18) purchased from Jackson Laboratories and subjected to ligation of the left anterior descending artery, as previously described [50].

Rabbit model

For the rabbit atherosclerosis model, 3 months old male New Zealand White (NZW) rabbits (N=47) were purchased from Charles River Laboratories (Wilmington, MA) and placed on Western diet (initial 8 weeks on regular chow enriched with 0.3% cholesterol and 4.7% coconut oil, and the remaining time period on 0.15% enriched cholesterol diet from Research diets, Inc. Brunswick, NJ). Randomly assigned control rabbits (N=11) were kept on chow diet and imaged with PET/MR. Among these some animals were euthanized for biodistribution assays (N=6) or used for time-activity characterization of aorta signal (N=3). In order to induce atherosclerotic lesions, the remaining rabbits (N=36) were subjected to two endothelial denudations of the aorta through the right and left femoral artery at 2 and 6 weeks after diet initiation, respectively, as described previously [27]. Briefly, femoral artery angioplasty was performed under fluoroscopic guidance using a 4F-Fogarty embolectomy catheter. Once catheter is inserted, catheter is positioned in the thoracic descending aorta region. The balloon was then inflated to 2 atm. Catheter is then pulled back over the entire length of the aorta down to the iliac bifurcation, and the pullback procedure is repeated for two additional times. Catheter is then removed, and femoral artery is ligated. Rabbits with atherosclerosis were imaged 4 months after diet initiation (N=36). Among these animals some were euthanized for *ex vivo* biodistribution analyses (N=9), used for time-activity characterization of aorta signal (N=3) or near infra-red imaging (N=27). The remaining atherosclerotic rabbits were fed a Western diet for an additional 3 months (N=9) to advance atherosclerosis. At the end of the 3-month period, these rabbits were imaged and euthanized.

Myocardial infarction surgery in mice

Myocardial infarction in mice was induced by permanent ligation of the left anterior descending (LAD) coronary artery of female C57Bl/6 mice (N=18). Briefly, animals were anesthetized with xylazine (10 mg/Kg) and ketamine (100 mg/Kg) and intubated using an endotracheal intubation kit from Braintree Scientific (Braintree, MA). Left-sided thoracotomy and pericardial incision were performed. A 7-0 Silk suture was used to occlude the LAD.

Incisions were closed with a 5-0 Silk suture. Infarcted animals were treated with 0.1 mg/Kg of buprenorphine every 12 hours and used 3 days after the surgery.

[^{64}Cu]Cu-DOTATATE biodistribution, pharmacokinetics and blood separation analysis in mice

For biodistribution, pharmacokinetics and blood separation analysis in mice we used [^{64}Cu]Cu-labeled DOTATATE due to this isotope's longer physical half-life compared to [^{68}Ga]Ga (12.7 vs 1.1 hours), which allowed us to perform extensive *ex vivo* validation assays. Wild-type and atherosclerotic animals were injected with approximately 1.85 MBq of [^{64}Cu]Cu-DOTATATE and euthanized at either 1, 5, 15, 30, 60 or 120 minutes after injection (Supplementary Fig. S1A) to evaluate the tracer's biodistribution. After euthanasia, an insulin syringe was used to collect blood samples from the left ventricle. Blood samples were used for the establishment of pharmacokinetics profile. Mice were then perfused with 20 mL of phosphate-buffered saline (PBS) and tissues of interest (heart, aorta, bone marrow, spleen, liver, stomach, bladder, kidneys, intestines, lungs, adrenal gland, muscles and pancreas) were harvested. Tissues were blotted for gamma counting on a Wizard2 2480 automatic gamma counter (Perkin Elmer, Waltham, MA). Values were corrected for decay and normalized to tissue weight to express radioactivity concentration as percentage injected dose per gram (%ID/g). Blood half-life was calculated by measuring blood radioactivity over time for 120 minutes and data were fitted using a two-phase decay non-linear regression using GraphPad Prism v8.4.3 (Supplementary Table S1). To investigate the tracer's distribution within different blood compartments, after gamma counting, 100 µL of blood were spun down at 2000g for 15 minutes at 4°C. Plasma (supernatant) and cells (pellet) were gamma counted and expressed as percentage of total activity. The remainder of the blood was separated using Lymphoprep density gradient medium (Nycomed Pharma, Zurich, Switzerland) following manufacturer's instructions. Percentage of activity in mononuclear and polynuclear cells was calculated.

In vivo PET/CT imaging in mice

For the PET/CT experiments, mice were fasted for 12 hours before radiotracer injection and anesthetized with xylazine (10 mg/kg) and ketamine (100 mg/kg) through intraperitoneal injection prior to radiotracer administration. Subsequently they were injected via the lateral tail vein with approximately 22.2 MBq of [^{18}F]F-FDG or 5.55 MBq of [^{64}Cu]Cu-DOTATATE. Tracers were allowed to circulate for 60 minutes. Immediately before imaging, mice were placed under 1% isoflurane (BaxterHealthcare, Deerfield, IL), and subsequently imaged on a high resolution (700 µm) Mediso nanoScan PET/CT scanner (Mediso, Budapest, Hungary). CT scan was acquired at 50 kVp and 300 ms exposure per projection. eXIA160 (Binitio, Ontario, Canada) was used as a contrast agent to improve imaging of the vasculature by intravenous administration of 100 µl per mouse 5 minutes prior to CT acquisition [51]. PET acquisition time was 40 minutes. Reconstruction was performed using TeraTomo 3D reconstruction engine, for 8 iterations and 6 subsets per iteration for both tracers. The voxel size was isotropic at 0.3 mm. Immediately after the PET/CT scan, animals were euthanized for *ex vivo* assays.

Flow cytometry

After PET imaging, mouse hearts and aortas were harvested and collected in PBS-filled tubes. Aortas were minced and digested with an enzymatic digestion solution containing liberase TH (4 U/ml) (Roche, Basel, Switzerland), DNase I (40 U/ml) and hyaluronidase (60 U/ml) in PBS. Heart tissue was minced and digested using an enzymatic digestion solution containing DNase I (60 U/ml), collagenase type I (450 U/ml), collagenase type XI (125 U/ml) and hyaluronidase (60 U/ml) in PBS. Samples were treated with the respective enzymatic solution for 60 minutes at 37 °C. All enzymes were purchased from Sigma-Aldrich (St. Louis, MO). Samples were then passed through a 70 µm filter, washed and prepared for antibody staining and flow sorting. Cellular fragments and debris were gated out of the analysis by utilizing forward and side angle light scatter signal. Macrophages were identified as Ly6G$^-$ (Clone 1A8, PE/Cy7), CD11b$^+$ (Clone M1/70, PE), CD11c$^-$

(Clone N418, PerCP/Cy5.5) and F4/80^{+} (Alexa Fluor® 647, Clone BM8) from Biolegend (San Diego, CA). The remaining CD11b^{+} cells were identified as Ly6G^{lo}, CD11b^{hi}, CD11c^{hi}. Data were acquired on a FACS Aria flow sorter (BD Biosciences, East Rutherford, NJ) and analyzed using FlowJo v10.0.7 (Tree Star, Ashland, OR). Sorted cells were gamma counted and activity per cell values were calculated.

Autoradiography

Tissues (heart and aorta) were placed in a film cassette against a phosphorimaging plate (BASMS-2325, Fujifilm) at −20 °C to determine the regional radioactivity distribution. Exposure time was optimized to dose, tracer, and tissue uptake differences. Tissues from the heart of [^{18}F]F-FDG injected animals were exposed for 5 minutes, [^{18}F]F-FDG infused aortas were exposed for 30 minutes and tissues from animals in the [^{64}Cu]Cu-DOTATATE group were exposed for 60 minutes. The plates were read at a pixel resolution of 25 µm with a Typhoon 7000IP plate reader (GE Healthcare, Pittsburgh, PA). Images were analyzed using ImageJ software v1.52 (Madison, WI).

[^{68}Ga]Ga-DOTATATE biodistribution, pharmacokinetics and blood separation analysis in rabbits

Adopting a translational approach, the rabbit studies were performed with the [^{68}Ga]Ga-labeled tracer, which is already being used in the clinic. [^{68}Ga]Ga-DOTATATE was purchased from Advanced Accelerator Applications (AAA, Millburn, NJ, USA). To determine its pharmacokinetics, three atherosclerotic rabbits and two healthy controls were injected with approximately 190 MBq of [^{68}Ga]Ga-DOTATATE. Venous blood was sampled at 1, 5, 10, 15, 20, 30, 60, 120, 180, 240 and 300 minutes after injection through the ear vein. Samples were weighed and gamma counted. Blood half-life data were fitted using a two-phase decay non-linear regression using GraphPad Prism v8.4.3 (Supplementary Table S1). To investigate the tracer blood distribution, blood samples were centrifuged at 2000g for 15 minutes at 4 °C to determine the radioactivity concentration in the plasma and cellular fractions. To analyze [^{68}Ga]Ga-DOTATATE biodistribution, all rabbits were

euthanized after the last imaging time-point using an injection of pentobarbital 100 mg/kg and exsanguination of the portal vein. Rabbits were extensively perfused with 1000 mL of saline. Following, tissues (blood, heart, aorta, liver, kidney, skeletal muscle, small and large intestine, fat, stomach, pancreas and bladder) were harvested, weighed and gamma counted.

In vivo PET/MR imaging in rabbits

In vivo imaging in rabbits was performed on a 3 Tesla Biograph mMR (Siemens, Erlangen, Germany) Positron Emission Tomography/Magnetic Resonance Imaging (PET/MRI) clinical scanner. To establish the optimal imaging time-point for [^{68}Ga]Ga-DOTATATE aortic imaging in this animal model, 5 rabbits underwent dynamic PET imaging for 3 hours immediately after injection of approximately 190 MBq of the tracer. Rabbits where injected intravenously via the ear vein with approximately 190 MBq of either [^{18}F]F- FDG or [^{68}Ga]Ga-DOTATATE. Rabbits undergoing [^{18}F]F-FDG scans were fasted for 3-4 hours before injection to avoid tracer uptake in the bowels, as previously validated [52]. After injection, [^{18}F]F-FDG was allowed to circulate for 3 hours, as per previously described [28], while, based on results of dynamic analyses, [^{68}Ga]Ga-DOTATATE was left to circulate for 2 hours. At the end of the circulation time, rabbits were anesthetized with ketamine (20 mg/kg) and xylazine (5mg/kg) i.m. Animals were then placed in supine position under 1.5% isoflurane inhalation on the PET/MR scanner. After scout scans, PET imaging was initiated for 30 minutes for [^{18}F]F-FDG and 60 minutes for [^{68}Ga]Ga-DOTATATE. 3D non contrast enhanced time-of-fight (TOF) images were acquired to visualize the abdominal aorta and renal arteries, with the following imaging parameters: repetition time (TR), 23 ms; echo time (TE), 2.8 ms; flip angle, 20 degrees; spatial resolution, 0.35 mm^2 (interpolated); slice thickness, 1 mm. PET images were reconstructed offline. Attenuation correction of PET images was performed by using a vendor built-in Dixon MR- based attenuation map (MR-AC) with 2 (soft tissue, air). Images were reconstructed using a 3D ordinary Poisson ordered subsets expectation maximization (OP-OSEM) algorithm with point-spread-function (PSF) resolution modeling, using 3 iterations and 21 subsets and filtered with a 4

mm Gaussian filter. Animals were then euthanized, perfused and aortas were collected for gamma counting.

[^{64}Cu]Cu-DOTATATE, [^{68}Ga]Ga-DOTATATE and [^{18}F]F-FDG PET image analysis

Using OsiriX v5.6 software (OsiriX Foundation, Geneva, Switzerland), regions of interest (ROIs) were drawn to determine organ radioactivity concentration. In mice, for healthy and infarcted myocardium, ROIs were traced manually in the apex of the heart in the axial view. For remote myocardium, analysis was performed in myocardium 180° from the infarcted zone. In the mice aorta, sequential ROIs were drawn in the ascending aorta based on consecutive tomographic (CT) slices beginning from the root up to the brachiocephalic branch, merging point with the aortic arch. Voxel counts were converted to maximum standardized uptake values (SUV_{max}). In rabbits, PET images were fused with time-of-flight bright blood MRI angiography and ROIs were manually drawn on the infrarenal abdominal aorta in TOF images. The slice-by-slice maximum standard uptake values (SUV_{max}) were averaged across the whole aorta. When prominent image artifacts, such as spill over artefacts into the abdominal aorta from neighbouring tissues, were present, rabbits were excluded from image analysis, as detailed in the Results section. To ensure blinding, investigator involved in the imaging analysis was not aware of the group distribution in the imaging slices.

Near infrared fluorescence imaging in of rabbit aortas

Ex vivo near infrared fluorescence imaging of rabbit aortas was performed on a Xenogen IVIS Spectrum Preclinical Imaging System (Perkin Elmer, Waltham, MA). Approximately 24 hours before euthanasia, animals were injected with Cy5.5-labeled high-density lipoprotein (HDL), which was used to determine macrophage burden. Fluorescence images were obtained with the following excitation and emission band-pass filter parameters: **λ** excitation = 640 ± 18 nm, **λ** emission = 720 ± 10 nm. Images were subsequently analyzed by dividing the infrarenal abdominal aorta into 8 ROIs of the same size. Max

radiant efficiency [(p/s/cm^2/sr)/(μW/cm^2)] for each ROI were recorded as a measure Cy5.5-HDL deposition in the aorta.

Statistics

All results are presented as mean ± standard error of the mean (SEM) or median and interquartile range (IQR). After running appropriate tests for normality, non-parametric statistical tests were deemed appropriate. Unpaired data were analyzed with non-parametric Mann-Whitney tests. Analysis of longitudinal imaging studies were performed using Wilcoxon matched-pairs signed rank tests. Correlation of [^{68}Ga]Ga-DOTATATE maximum standardized uptake value (SUV_{max}) and [^{18}F]F-FDG SUV_{max} was calculated by computing a nonparametric Spearman coefficient. For all tests, α<0.05 represents statistical significance. Levels of significance were indicated as follows: * p<0.05, **p<0.01, ***p<0.001, ****p<0.0001.

Data availability

The datasets generated during and/or analysed during the current study are available from the corresponding author on reasonable request.

Sources of funding:

AAG was supported by The Lundbeck Foundation R251-2017-870. FO was supported by an Institutional Research Training Grant T32CA078207. AM was supported by Deutsche Forschungsgemeinschaft MA7059/1. TR was supported by MSK Cancer Center P30 P30 CA008748. JMT was supported by the Wellcome Trust (211100/Z/18/Z). JHFR is part-supported by the NIHR Cambridge Biomedical Research Centre, the British Heart Foundation, Higher Education Funding Council for England, the Engineering and Physical Sciences Research Council and the Wellcome Trust. CG was supported by NIH-NHLBI R01 HL153712-01, NIH-NCATS UH3TR002067, American Heart Association 20SFRN35210252 and Chan Zuckerberg Initiative NFL-2020-218415. ZAF was supported by NIH/NHLBI R01 HL135878.

Competing interests

Andreas Kjaer is an inventor on a patent/holds IPR regarding the use of [^{64}Cu]Cu-DOTATATE in neuroendocrine tumor patients. The other authors report no Relationship with Industry and Other Entities. No other potential conflicts of interest relevant to this article exist.

References

1. Virani, S. S. *et al. Heart disease and stroke statistics—2020 update: A report from the American Heart Association. Circulation* (2020). doi:10.1161/CIR.0000000000000757.
2. Dutta, P. *et al.* Myocardial infarction accelerates atherosclerosis. *Nature* **487**, 325–329 (2012).
3. Tomas, L. *et al.* Altered metabolism distinguishes high-risk from stable carotid atherosclerotic plaques. *Eur. Heart J.* **39**, 2301–2310 (2018).
4. Fernandez, D. M. *et al.* Single-cell immune landscape of human atherosclerotic plaques. *Nat. Med.* **25**, 1576–1588 (2019).
5. Ridker, P. M. *et al.* Antiinflammatory therapy with canakinumab for atherosclerotic disease. *N. Engl. J. Med.* **377**, 1119–1131 (2017).
6. Tardif, J. *et al.* Efficacy and Safety of Low-Dose Colchicine after Myocardial Infarction To cite this version : HAL Id : hal-02368804. (2020).
7. Kircher, M. & Lapa, C. Novel Noninvasive Nuclear Medicine Imaging Techniques for Cardiac Inflammation. *Curr. Cardiovasc. Imaging Rep.* **10**, (2017).
8. Ćorović, A., Wall, C., Mason, J. C., Rudd, J. H. F. & Tarkin, J. M. Novel Positron Emission Tomography Tracers for Imaging Vascular Inflammation. *Curr. Cardiol. Rep.* **22**, (2020).
9. Maschauer, S., Prante, O., Hoffmann, M., Deichen, J. T. & Kuwert, T. Characterization of 18F-FDG uptake in human endothelial cells in vitro. *J. Nucl. Med.* **45**, 455–460 (2004).
10. Al-Mashhadi, R. H. *et al.* 18Fluorodeoxyglucose Accumulation in Arterial Tissues Determined by PET Signal Analysis. *J. Am. Coll. Cardiol.* **74**, 1220–1232 (2019).
11. Kobylecka, M. *et al.* Myocardial viability assessment in 18FDG PET/CT study (18FDG PET myocardial viability assessment). *Nucl. Med. Rev.* **15**, 52–60 (2012).
12. Manabe, O. *et al.* Radiopharmaceutical tracers for cardiac imaging. *J. Nucl. Cardiol.* **25**, 1204–1236 (2018).
13. Inglese, E. *et al.* Spatial and temporal heterogeneity of regional myocardial uptake in patients without heart disease under fasting conditions on repeated whole-body 18F-FDG PET/CT. *J. Nucl. Med.* **48**, 1662–1669 (2007).
14. Gropler, R. J. *et al.* Nonuniformity in myocardial accumulation of fluorine-18-fluorodeoxyglucose in normal fasted humans. *J. Nucl. Med.* **31**, 1749–1756 (1990).
15. Meester, E. J. *et al.* Imaging

inflammation in atherosclerotic plaques, targeting SST2 with [111In]In-DOTA-JR11. *J. Nucl. Cardiol.* (2020) doi:10.1007/s12350-020-02046-y.

16. Senders, M. L. *et al.* Probing myeloid cell dynamics in ischaemic heart disease by nanotracer hot-spot imaging. *Nat. Nanotechnol.* **15**, 398–405 (2020).
17. Heo, G. S., Sultan, D. & Liu, Y. Current and novel radiopharmaceuticals for imaging cardiovascular inflammation. *Q. J. Nucl. Med. Mol. Imaging* **64**, 4–20 (2020).
18. Gipharma S.r.l. NETSPOT (kit for the preparation of gallium Ga 68 dotatate injection). 1–13 (2016).
19. Johnbeck, C. B. *et al.* Head-to-Head Comparison of 64Cu-DOTATATE and 68Ga-DOTATOC PET/CT: A prospective study of 59 patients with neuroendocrine tumors. *J. Nucl. Med.* **58**, 451–457 (2017).
20. Tarkin, J. M. *et al.* Detection of Atherosclerotic Inflammation by 68Ga-DOTATATE PET Compared to [18F]FDG PET Imaging. *J. Am. Coll. Cardiol.* **69**, 1774–1791 (2017).
21. Li, X. *et al.* Specific somatostatin receptor II expression in arterial plaque: 68Ga-DOTATATE autoradiographic, immunohistochemical and flow cytometric studies in apoE-deficient mice. *Atherosclerosis* **230**, 33–39 (2013).
22. Malmberg, C. *et al.* 64Cu-DOTATATE for noninvasive assessment of atherosclerosis in large arteries and its correlation with risk factors: Head-to-head comparison with 68Ga-DOTATOC in 60 patients. *J. Nucl. Med.* **56**, 1895–1900 (2015).
23. Tarkin, J. M. *et al.* 68Ga-DOTATATE PET Identifies Residual Myocardial Inflammation and Bone Marrow Activation After Myocardial Infarction. *J. Am. Coll. Cardiol.* **73**, 2489–2491 (2019).
24. Thackeray, J. T. *et al.* Targeting post-infarct inflammation by PET imaging: comparison of 68Ga-citrate and 68Ga-DOTATATE with 18F-FDG in a mouse model. *Eur. J. Nucl. Med. Mol. Imaging* **42**, 317–327 (2015).
25. Lee, W. W. *et al.* PET/MRI of inflammation in myocardial infarction. *J. Am. Coll. Cardiol.* (2012) doi:10.1016/j.jacc.2011.08.066.
26. Thackeray, J. T. & Bengel, F. M. Molecular Imaging of Myocardial Inflammation With Positron Emission Tomography Post-Ischemia: A Determinant of Subsequent Remodeling or Recovery. *JACC Cardiovasc. Imaging* **11**, 1340–1355 (2018).
27. Binderup, T. *et al.* Imaging-assisted nanoimmunotherapy for atherosclerosis in multiple species. *Sci. Transl. Med.* **11**, (2019).
28. Tawakol, A. *et al.* Noninvasive in

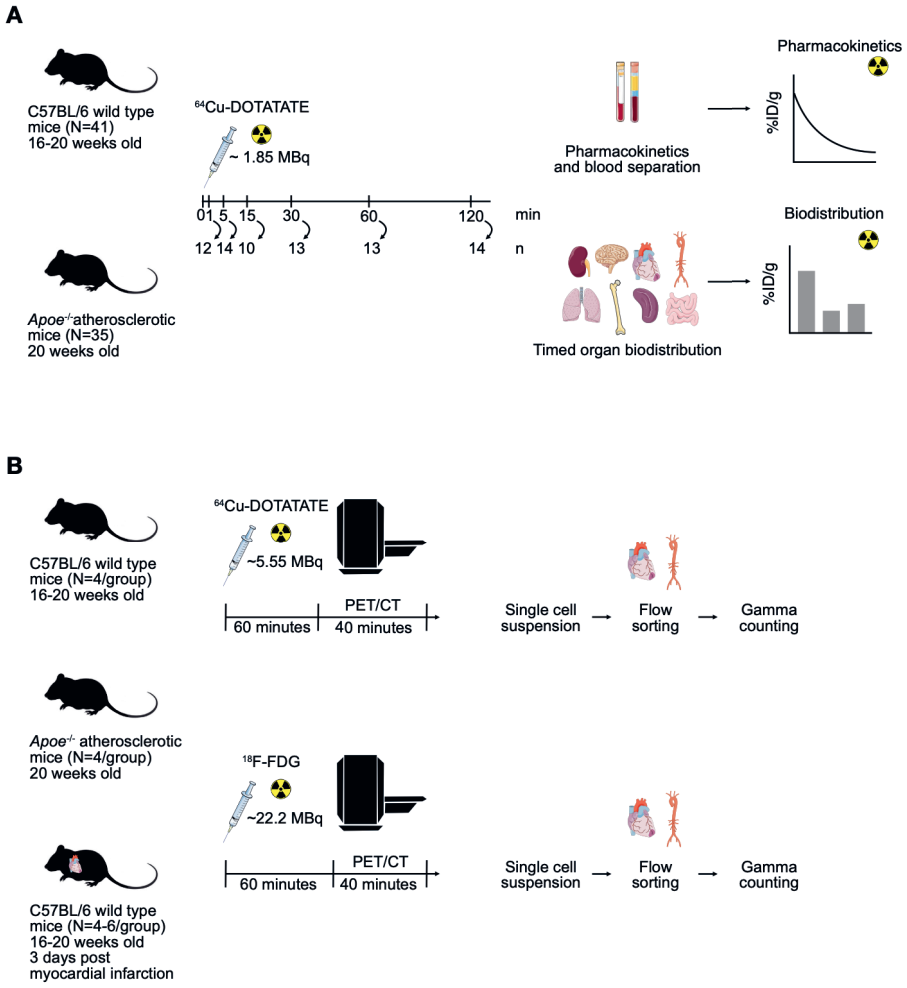
vivo measurement of vascular inflammation with F-18 fluorodeoxyglucose positron emission tomography. *J. Nucl. Cardiol.* **12**, 294–301 (2005).
29. Zhao, Q. ming *et al.* Detection of Vulnerable Atherosclerotic Plaque and Prediction of Thrombosis Events in a Rabbit Model Using 18F-FDG -PET/CT. *PLoS One* **8**, 1–9 (2013).
30. Pelosi, G. *et al.* Inflammation blood and tissue factors of plaque growth in an experimental model evidenced by a systems approach. *Front. Genet.* **5**, 1–6 (2014).
31. Tarkin, J. M., Joshi, F. R. & Rudd, J. H. F. PET imaging of inflammation in atherosclerosis. *Nat. Rev. Cardiol.* **11**, 443–457 (2014).
32. Li, X. *et al.* 68Ga-DOTATATE PET/CT for the detection of inflammation of large arteries: Correlation with 18F-FDG, calcium burden and risk factors. *EJNMMI Res.* **2**, 1–10 (2012).
33. Rominger, A. *et al.* In vivo imaging of macrophage activity in the coronary arteries using 68Ga-DOTATATE PET/CT: Correlation with coronary calcium burden and risk factors. *J. Nucl. Med.* **51**, 193–197 (2010).
34. Pedersen, S. F. *et al.* 64Cu-DOTATATE PET/MRI for detection of activated macrophages in carotid atherosclerotic plaques: Studies in patients undergoing endarterectomy. *Arterioscler. Thromb. Vasc. Biol.* **35**, 1696–1703 (2015).
35. Wan, M. Y. S. *et al.* PET/CT imaging of unstable carotid plaque with 68Ga-labeled somatostatin receptor ligand. *J. Nucl. Med.* **58**, 774–780 (2017).
36. Vallée, É., Paquet, N., Buteau, J. P. & Turcotte, É. 68Ga-DOTATATE Uptake in Ischemic Stroke. *Clin. Nucl. Med.* **43**, 46–47 (2018).
37. Sandström, M. *et al.* Comparative biodistribution and radiation dosimetry of 68Ga-DOTATOC and 68Ga-DOTATATE in patients with neuroendocrine tumors. *J. Nucl. Med.* **54**, 1755–1759 (2013).
38. Pfeifer, A. *et al.* Clinical PET of neuroendocrine tumors using 64Cu-DOTATATE: First-in-humans study. *J. Nucl. Med.* **53**, 1207–1215 (2012).
39. Andersen, T. L., Baun, C., Olsen, B. B., Dam, J. H. & Thisgaard, H. Improving contrast and detectability: Imaging with [55Co]Co-DOTATATE in comparison with [64Cu]Cu-DOTATATE and [68Ga]Ga-DOTATATE. *J. Nucl. Med.* **61**, 228–235 (2020).
40. Liu, R. S. *et al.* Biodistribution, pharmacokinetics and PET Imaging of [18F]FMISO, [18F]FDG and [18F]FAc in a sarcoma- and inflammation-bearing mouse model. *Nucl. Med. Biol.* **36**, 305–312 (2009).
41. Rinne, P. *et al.* Comparison of Somatostatin Receptor 2-

Targeting PET Tracers in the Detection of Mouse Atherosclerotic Plaques. *Mol. Imaging Biol.* **18**, 99–108 (2016).

42. Perez, J. *et al.* Somatostatin binds to murine macrophages through two distinct subsets of receptors. *J. Neuroimmunol.* **138**, 38–44 (2003).
43. Dalm, V. A. S. H. *et al.* Expression of somatostatin, cortistatin, and somatostatin receptors in human monocytes, macrophages, and dendritic cells. *Am. J. Physiol. - Endocrinol. Metab.* **285**, 344–353 (2003).
44. Fani, M., André, J. P. & Maecke, H. R. 68Ga-PET: A powerful generator-based alternative to cyclotron-based PET radiopharmaceuticals. *Contrast Media Mol. Imaging* **3**, 53–63 (2008).
45. Mojtahedi, A. *et al.* Assessment of vulnerable atherosclerotic and fibrotic plaques in coronary arteries using (68)Ga-DOTATATE PET/CT. *Am. J. Nucl. Med. Mol. Imaging* **5**, 65–71 (2015).
46. Hag, A. M. F. *et al.* 18F-FDG PET Imaging of Murine Atherosclerosis: Association with Gene Expression of Key Molecular Markers. *PLoS One* **7**, (2012).
47. Hellberg, S. *et al.* Effects of atorvastatin and diet interventions on atherosclerotic plaque inflammation and [18F]FDG uptake in Ldlr−/−Apob100/100 mice. *Atherosclerosis* **263**, 369–376 (2017).
48. Toczek, J. *et al.* Periaortic brown adipose tissue as a major determinant of [18F]-fluorodeoxyglucose vascular uptake in atherosclerosis-prone, ApoE-/- mice. *PLoS One* **9**, 1–9 (2014).
49. Borchert, T. *et al.* Dissecting the target leukocyte subpopulations of clinically relevant inflammation radiopharmaceuticals. *J. Nucl. Cardiol.* (2019) doi:10.1007/s12350-019-01929-z.
50. Tarnavski, O. *et al.* Mouse cardiac surgery: Comprehensive techniques for the generation of mouse models of human diseases and their application for genomic studies. *Physiol. Genomics* **16**, 349–360 (2004).
51. Xing, R. *et al.* Contrast-enhanced micro-CT imaging in murine carotid arteries: A new protocol for computing wall shear stress. *Biomed. Eng. Online* **15**, 621–636 (2016).
52. Lederman, R. J. *et al.* Detection of atherosclerosis using a novel positron-sensitive probe and 18-fluorodeoxyglucose (FDG). *Nucl. Med. Commun.* **22**, 747–753 (2001

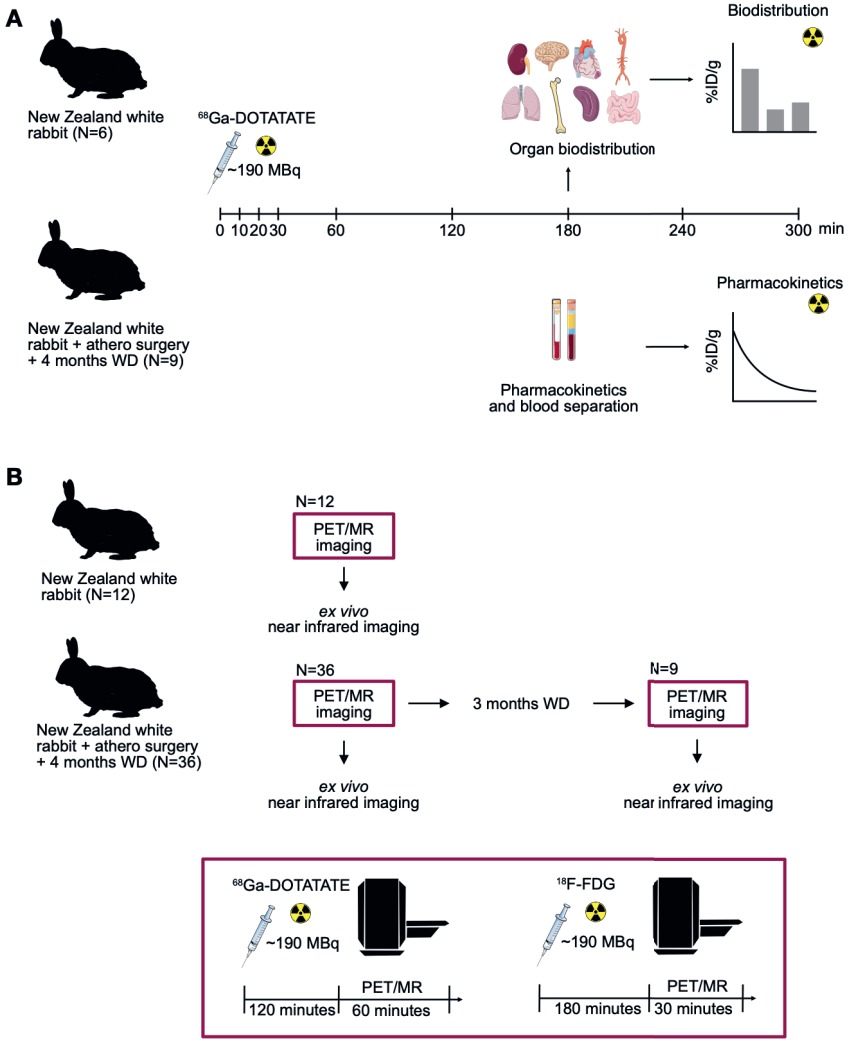
Supplementary materials

Supplementary figures



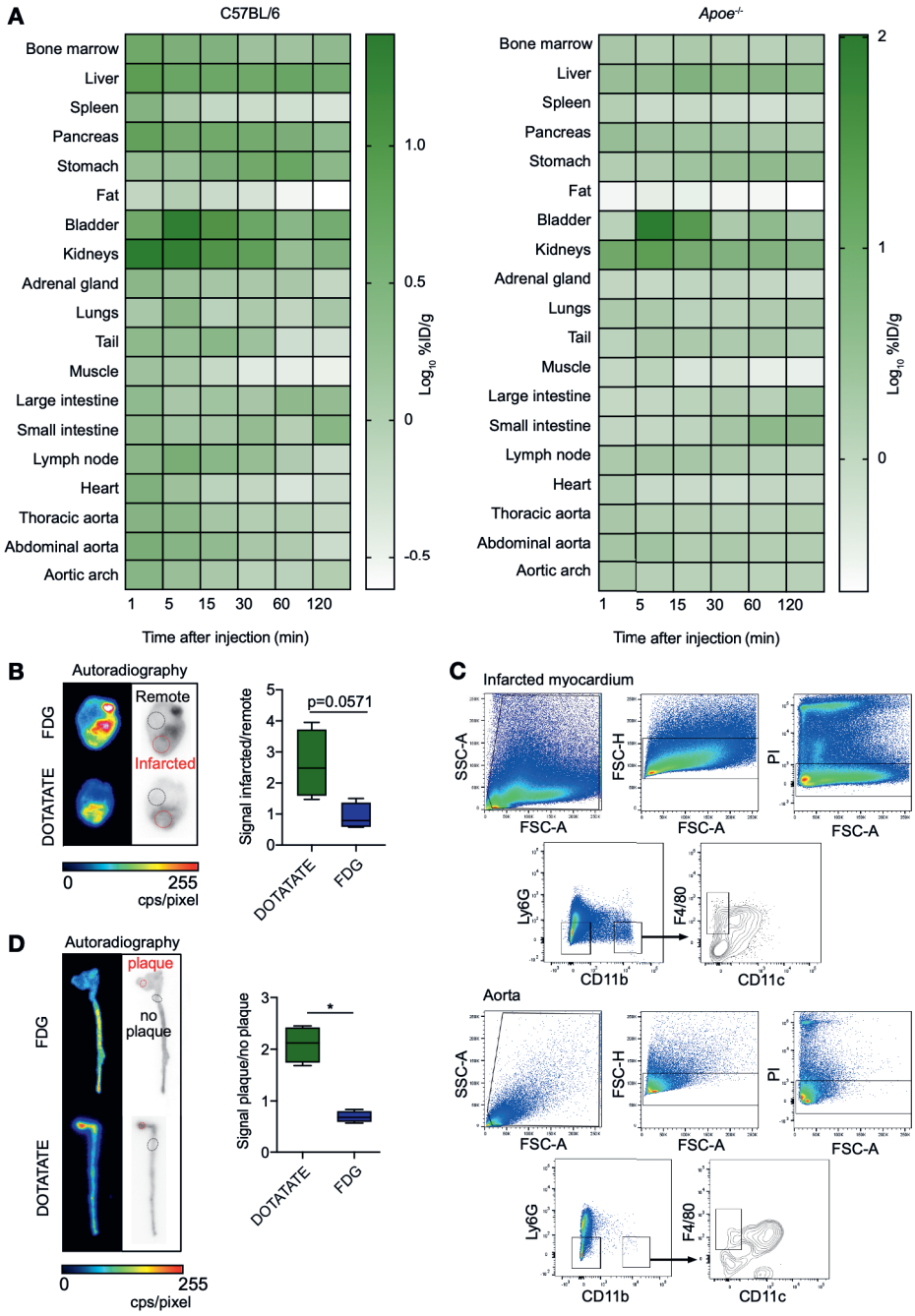
Supplementary Figure S1. Flowchart of the experimental design in mice. A) C57Bl/6 and *Apoe*$^{-/-}$ mice at 16-20 weeks of age were injected with [^{64}Cu]Cu-DOTATATE and euthanized at different time-points. Animals were perfused and organs of interest were gamma-counted. Blood was processed for plasma, mononuclear and polynuclear cell separation. Results were plotted as %ID/g. B) Healthy and MI (3 days after infarct) C57Bl/6 mice, and *Apoe*$^{-/-}$ mice were injected with either [^{18}F]F-FDG or [^{64}Cu]Cu-DOTATATE. Tracer was allowed to circulate for 60 minutes. Animals were injected with eXIA™160 contrast agent (Binitio Biomedical Inc, Ontario, Canada). PET/CT acquisition was performed for 40 minutes. Mice were then sacrificed and perfused. Aorta and

heart, the organs of interest, were collected and flow sorted. After sorting, cells were gamma-counted and activity per cell ratio was calculated. ID: injected dose.



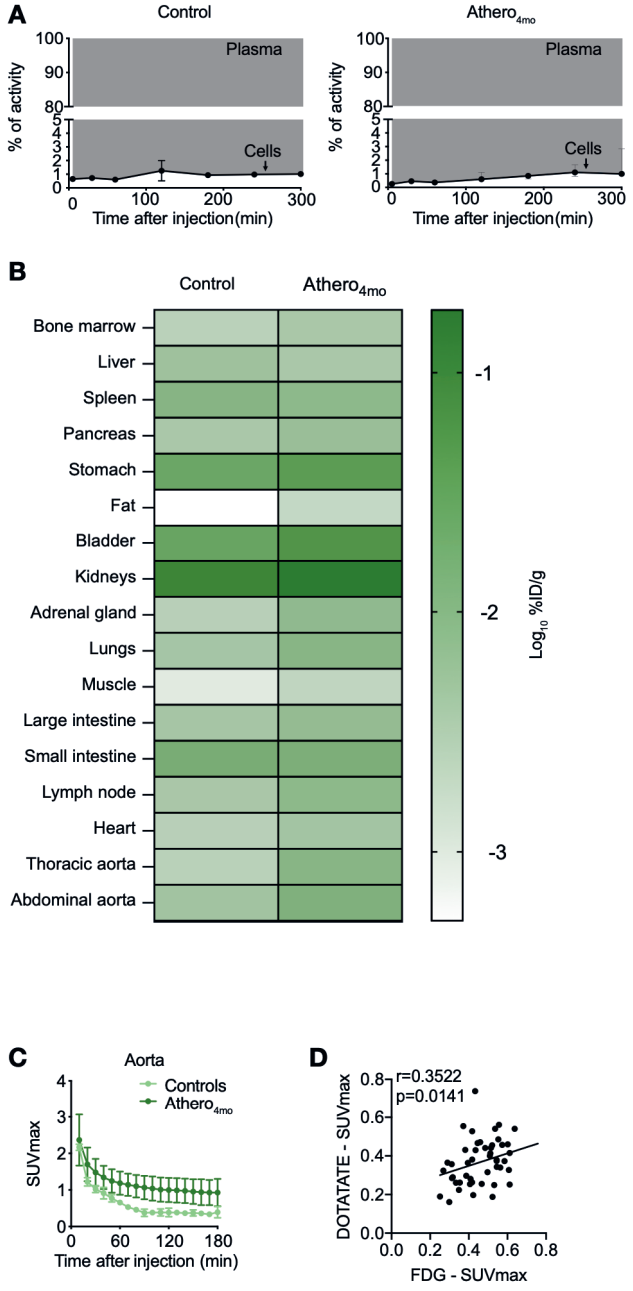
Supplementary Figure S2. Flowchart of the experimental design in rabbits. A) Healthy and atherosclerotic (athero$_{4mo}$) New Zealand White rabbits were injected with [^{68}Ga]Ga-DOTATATE and pharmacokinetics profile was determined by blood sampling at different time-points. Blood was processed for plasma and cell separation. At 180 minutes, animals were sacrificed and perfused. Organs of interest were gamma-counted. Results were plotted as %ID/g. B) Healthy and atherosclerotic (athero$_{4mo}$) New Zealand White rabbits were injected with either [^{68}Ga]Ga-

DOTATATE or [^{18}F]F-FDG. Tracer was allowed to circulate for 120 ([^{68}Ga]Ga-DOTATATE) and 180 minutes ([^{18}F]F-FDG), after which, rabbits were imaged with PET/MR for 60 or 30 minutes, respectively. Control animals and athero$_{4mo}$ were then sacrificed and perfused. Organs of interest were gamma counted and aortas were imaged with near infrared. A group of 8 atherosclerotic animals (athero$_{7mo}$) was kept and fed with Western Diet for additional 3 months, after which animals were imaged again with [^{68}Ga]Ga-DOTATATE and [^{18}F]F-FDG, sacrificed and perfused for aorta harvesting. Aortas were imaged with near infrared. Athero surgery: balloon denudation surgery; ID: injected dose; WD: Western Diet.



Supplementary Figure S3. [^{64}Cu]Cu-DOTATATE uptake in mice and autoradiography of [^{64}Cu]Cu-DOTATATE and [^{18}F]F-FDG in cardiovascular disease animal models. A) Heatmap

visualization of [^{64}Cu]Cu-DOTATATE distribution at different timepoints in healthy C57Bl/6 (left) and atherosclerotic *Apoe*$^{-/-}$ (right) mice (N=5 per group). Data was obtained by *ex vivo* gamma counting of blotted organs. B) Representative autoradiography images showing radioactivity distribution in the myocardium of MI mice injected with [^{18}F]F-FDG or [^{64}Cu]Cu-DOTATATE. Regions of interest (ROI) represented in red (infarcted myocardium) and black (non-infarcted remote myocardium). Quantification of signal was plotted as ratio between infarcted and remote myocardium. (N=4 per group) C) Representative plot of gating strategy for flow sorting of heart (top) and aorta (bottom) tissues D) Representative autoradiography images showing radioactivity distribution in the aorta of C57Bl/6 mice and *Apoe*$^{-/-}$ mice injected with [^{18}F]F-FDG or [^{64}Cu]Cu-DOTATATE. Regions of interest (ROI) represented in red (plaque) and black (no plaque). Quantification of signal was plotted as ratio between plaque and no plaque signal. (N=4 per group). cps: counts per second; DOTATATE: [^{64}Cu]Cu-DOTATATE; FDG: [^{18}F]F-FDG; ID: injected dose. Data are presented as median (interquartile range).



Supplementary Figure S4. Analysis of [^{68}Ga]Ga-DOTATATE biodistribution in rabbits and [^{18}F]F-FDG and [^{68}Ga]Ga-DOTATATE aortic uptake comparison. A) [^{68}Ga]Ga-DOTATATE radioactivity distribution in blood fractions of control (left) and athero$_{4mo}$ (right) rabbits as determined by

gamma counting. Graphs show the percentage of activity associated with cells or plasma over time. Controls N=2 and athero$_{4mo}$ N=3 B) Heatmap visualization of [^{68}Ga]Ga-DOTATATE distribution at different timepoints in healthy (left) and athero$_{4mo}$ rabbits (right) Controls N=6 and athero$_{4mo}$ N=9. Data was obtained by *ex vivo* gamma counting of blotted organs. C) [^{68}Ga]Ga-DOTATATE SUV$_{max}$ of abdominal aorta in control and athero$_{4mo}$ animals over the first 3 hours after injection, acquired by dynamic PET/MR imaging. N=3 per group. Data are presented as mean ± standard error of the mean. D) Correlation between [^{18}F]F-FDG and [^{64}Cu]Cu-DOTATATE aortic uptake in control, athero$_{4mo}$ and athero$_{7mo}$ animals. N=57. DOTATATE: [^{64}Cu]Cu-DOTATATE; FDG: [^{18}F]F-FDG; ID: injected dose; SUV$_{max}$: maximum standardized uptake value.

Supplementary Table S1. Blood circulation half-lives of DOTATATE-based radiotracers in mice and rabbits.

	Mice		Rabbits	
	C57Bl/6	*Apoe*$^{-/-}$	Control	Athero$_{4mo}$
%fast	79.14	11.27	39.7	53.17
$t_{1/2}$ fast (minutes)	1.939	0.557	3.419	19.17
%slow	20.86	88.73	60.3	46.83
$t_{1/2}$ slow (minutes)	15.81	7.627	32.86	92.82
Weighed $t_{1/2}$ (minutes)	4.83	6.83	21.17	53.66

Supplementary Table S2. Tissue radioactivity distribution of [^{64}Cu]Cu-DOTATATE in female C57BL/6 mice in %ID/g.

WT	1 min	5 min	15 min	30 min	60 min	120 min
Bone marrow	6.5 (5.4-7.1)	4.3 (3.6-5.6)	3.5 (3-5.6)	1.9 (1.7-2.9)	2.1 (1.6-2.5)	2.5 (2.1-4.1)
Liver	10 (8.5-11.1)	7.1 (6.1-7.7)	6.5 (6.1-7)	6.4 (6-6.4)	6.9 (6.7-7.8)	5.4 (4.8-6.4)
Spleen	3.7 (3.2-4.2)	1.5 (1.2-2)	0.9 (0.8-0.9)	0.7 (0.7-0.8)	0.6 (0.6-0.8)	0.5 (0.5-0.7)
Pancreas	8.7 (7.5-9.3)	5.3 (4.7-6.3)	6.1 (5.7-6.4)	5.8 (5.2-6.2)	4.8 (4.5-5)	2.6 (2.5-3.4)
Stomach	2.3 (2.2-3.1)	2.4 (1.7-3.2)	5 (3.5-7)	7.8 (3.6-8.7)	8 (4.8-10.8)	3.2 (2.7-3.6)
Fat	1.1 (0.5-1.5)	1.3 (1.1-1.5)	0.8 (0.6-0.9)	0.5 (0.4-0.8)	0.3 (0.2-0.4)	0.2 (0.2-0.5)

Bladder	4.6 (2.5-24)	36.4 (8.2-78.9)	7.9 (6.1-34.9)	6.8 (4-12.6)	3.3 (1.9-6.6)	10.4 (1.5-15.2)
Kidneys	26.8 (19.1-33.4)	20.5 (18.7-24.2)	11.5 (11.3-13.6)	8.2 (7.3-10.9)	6.1 (3-6.7)	3.7 (3.3-4.6)
Adrenal gland	3.3 (2.9-3.5)	2.2 (2.1-2.5)	1.7 (1.4-2.2)	1.6 (1.5-1.7)	1.6 (1.5-1.8)	0.6 (0.6-1.7)
Lungs	1.8 (1.2-2.1)	3.2 (2.7-4)	0.9 (0.7-2)	1.3 (1.1-2.2)	1.1 (0.8-1.1)	1.8 (1.2-2.6)
Tail	3.5 (2-4.9)	2.7 (1.6-4)	3.6 (2.9-3.7)	1.8 (1.6-2.9)	1.6 (0.6-1.7)	0.6 (0.5-0.7)
Muscle	2 (1.7-2.5)	1.6 (1.5-2.1)	0.9 (0.7-0.9)	0.5 (0.3-0.6)	0.3 (0.3-0.6)	0.3 (0.2-0.7)
Large intestine	2.7 (2.3-3.7)	1.6 (1.4-1.9)	1.9 (1.7-2.2)	1.7 (1.3-2.1)	3 (2.5-3.3)	3.1 (1.8-3.5)
Small intestine	3 (2.3-3.6)	2 (1.6-2.1)	1.7 (1.3-2.4)	2.6 (1.6-4.4)	2.4 (0.9-3.7)	3.3 (3.1-3.8)
Lymph node	3 (2.8-3.8)	4.7 (4.5-5.5)	3.2 (2.8-3.9)	2.2 (1.5-4.7)	1.3 (1.2-1.7)	0.6 (0.4-1.8)
Heart	3.8 (3.6-4.9)	2.1 (1.9-2.5)	1.1 (0.9-1.2)	0.9 (0.8-1)	0.8 (0.4-0.9)	0.7 (0.7-0.8)
Thoracic aorta	3.2 (2.9-4.6)	3.1 (2.9-3.5)	1.6 (1.4-2.4)	1.3 (1.2-1.4)	1.2 (1.2-1.4)	1 (0.7-1.1)
Abdominal aorta	5.1 (4.1-5.3)	3.8 (3-4)	2.4 (2.4-3.2)	1.7 (1.3-2.1)	1.3 (1.1-1.8)	0.7 (0.3-1.9)
Aortic arch	2.8 (2.7-4.5)	2.2 (1.8-2.9)	1.3 (1.2-2.1)	1.1 (1-1.2)	1.1 (1-1.1)	1.2 (1.2-1.6)

(N=3-7 per time-point). Data are presented as median (interquartile range).

Supplementary Table S3. Tissue radioactivity distribution of [^{64}Cu]Cu-DOTATATE in female *Apoe*$^{-/-}$ mice 12 weeks on Western Diet represented in %ID/g.

Apoe-/-	1 min	5 min	15 min	30 min	60 min	120 min
Bone marrow	3.1 (2.2-3.5)	2.3 (1-4)	2.6 (2.1-3.2)	1.8 (1.5-3.1)	1.9 (1.2-2.4)	2.7 (2-3)
Liver	4.4 (4.1-4.9)	4.9 (4.1-6.5)	8.6 (6.4-12.6)	6.9 (6.6-7.4)	6.9 (5.9-8.7)	6.3 (5.6-7.5)
Spleen	2 (1.6-2.5)	1.1 (0.8-1.3)	1.2 (0.8-1.6)	1.1 (0.8-1.2)	0.8 (0.6-1.2)	1.2 (1.1-1.3)
Pancreas	4.7 (3.9-6)	4.1 (3-4.4)	3.5 (2.9-4.2)	3.4 (3.1-3.8)	2.7 (2.3-3.5)	2.6 (1.9-3.2)
Stomach	2.1 (1.6-2.6)	2.4 (1.8-3.2)	3.3 (3.1-4.7)	5.4 (4.1-6.7)	5.4 (4.1-9.4)	5 (4-6.8)

Fat	0.3 (0.3-0.3)	0.4 (0.3-0.7)	0.4 (0.3-0.5)	0.3 (0.2-0.6)	0.2 (0.2-0.7)	0.2 (0.2-0.4)
Bladder	1.7 (1.6-2.1)	98.7 (69.1-165)	38.9 (16-63.1)	2.9 (1.8-3.6)	4.7 (2.5-17.5)	2.4 (1.4-10.2)
Kidneys	15.6 (15.1-17.5)	22.9 (18.7-48.4)	13.2 (11.9-16)	8.8 (7.3-10.5)	11.2 (6-11.6)	7.1 (7-8.1)
Adrenal gland	1.4 (1.2-1.5)	1.2 (1-1.5)	1.4 (1.2-1.7)	1.5 (1.4-1.9)	1.4 (1.1-1.6)	1.1 (0.7-1.5)
Lungs	2.1 (2.1-3.3)	2.6 (2.2-3)	1.9 (0.9-2.7)	1.6 (1.3-2.5)	2.5 (1.6-3.1)	2.8 (2.2-3.5)
Tail	1.8 (1-2.7)	2.5 (1.7-4.5)	2.5 (1.6-4.7)	3.1 (1.6-3.3)	2 (1.5-5.9)	2.7 (1.3-3.4)
Muscle	1.2 (1.1-1.5)	1.4 (1.3-2.2)	0.6 (0.5-0.9)	0.7 (0.5-1.4)	0.4 (0.3-0.6)	0.3 (0.3-0.7)
Large intestine	1.3 (1-1.5)	1.3 (1.1-1.6)	1.8 (1.1-2.3)	2.8 (1.4-3.9)	2.2 (1.1-3.1)	3.8 (3.6-6.5)
Small intestine	1.4 (0.7-3)	1.2 (1-1.7)	1.8 (1-2)	3.1 (1.8-5.6)	7.1 (4.7-7.8)	7.2 (4.4-9.5)
Lymph node	2.6 (1.8-3.8)	3.2 (2.5-4)	3 (2.2-4.1)	2.4 (1.6-4.6)	2.1 (1.3-2.7)	1.8 (1.4-2.6)
Heart	2.3 (2.1-2.8)	1.4 (0.7-1.6)	1.1 (0.8-1.3)	0.9 (0.8-1.2)	1.3 (1.1-1.5)	1.4 (1.2-1.4)
Thoracic aorta	2.9 (2.5-3.2)	2.1 (1.9-2.4)	2 (1.8-2.3)	1.8 (1.6-2.3)	2.1 (1.6-2.2)	2.1 (2-2.4)
Abdominal aorta	3.1 (2.9-3.6)	3.2 (2.6-4.6)	2.1 (1.7-3)	2.5 (1.9-3.6)	2.2 (1.7-2.3)	2.1 (1.9-2.5)
Aortic arch	2.9 (2.4-3)	1.9 (1.9-1.9)	1.7 (1.6-2)	1.7 (1.5-2.1)	1.8 (1.3-2)	1.9 (1.9-1.9)

(N=3-8 per time-point). Data are presented as median (interquartile range).

Supplementary Table S4. Number of cells analyzed by flow cytometry.

Tissue	Cells	Mouse 1	Mouse 2	Mouse 3	Mouse 4
Infarcted myocardium C57Bl/6 (FDG)	Macrophages	13644	3871	3591	1400
	Other CD11b positive	55751	12479	7031	18511
	CD11b negative	403562	182839	264546	145387
	Total	472957	199189	275168	165298
Infarcted myocardium C57Bl/6 (DOTA)	Macrophages	22882	5168	7279	6314
	Other CD11b positive	65733	39530	35666	30890
	CD11b negative	602928	225498	466014	255403
	Total	691543	270196	508959	292607
Aorta *Apoe*$^{-/-}$ (FDG)	Macrophages	6414	3288	2275	1429
	Other CD11b positive	24293	15900	22842	9988
	CD11b negative	435993	855828	405410	191276

	Total	466700	875016	430527	202693
Aorta *Apoe*$^{-/-}$ (DOTA)	Macrophages	4281	3370	7270	6917
	Other CD11b positive	22812	21362	44521	40724
	CD11b negative	513480	179121	392296	321097
	Total	540573	203853	444087	368738

Supplementary Table S5. Tissue radioactivity distribution of [^{68}Ga]Ga-DOTATATE in male control rabbits and athero$_{4mo}$ in %ID/g.

	Controls Median (interquartile range)	Athero$_{4mo}$ Median (interquartile range)
Bone marrow	0.003 (0.002-0.009)	0.006 (0.003-0.012)
Liver	0.009 (0.005-0.013)	0.006 (0.004-0.007)
Spleen	0.015 (0.007-0.035)	0.012 (0.011-0.013)
Pancreas	0.005 (0.004-0.009)	0.009 (0.007-0.011)
Stomach	0.036 (0.022-0.071)	0.053 (0.041-0.079)
Fat	0 (0-0.001)	0.002 (0.002-0.005)
Bladder	0.053 (0.014-0.1)	0.075 (0.038-0.155)
Kidneys	0.128 (0.108-0.148)	0.157 (0.141-0.263)
Adrenal gland	0.003 (0.003-0.005)	0.012 (0.009-0.017)
Lungs	0.005 (0.003-0.012)	0.015 (0.012-0.02)
Muscle	0.001 (0.001-0.002)	0.003 (0.002-0.006)
Large intestine	0.005 (0.004-0.012)	0.01 (0.007-0.015)
Small intestine	0.025 (0.016-0.033)	0.021 (0.016-0.029)
Lymph node	0.005 (0.005-0.007)	0.013 (0.01-0.019)
Heart	0.003 (0.003-0.005)	0.006 (0.005-0.008)
Thoracic aorta	0.004 (0.002-0.006)	0.015 (0.011-0.018)
Abdominal aorta	0.006 (0.003-0.02)	0.017 (0.014-0.022)

(N=6-9 per group). Data are presented as median (interquartile range).



3

Multiparametric immunoimaging mapsinflammatory signatures in murine myocardial infarction models

Published in JACC: Basic to Translational Science, 2023.

Maier, A., **Toner, Y.C.**, Munitz, J., Sullivan, N.A.T., Sakurai, K., Meerwaldt, A.E., Brechbühl, E.E.S., Prévot, G., van Elsas, Y., Maas, R.J.F., Ranzenigo, A., Soultanidis, G., Rashidian, M., Pérez-Medina, C., Heo, G.S., Gropler, R.J., Liu, Y., Reiner, T., Nahrendorf, M., Swirski, F.K., Strijkers, G.J., Teunissen, A.J.P., Calcagno, C., Fayad, Z.A., Mulder, W.J.M., van Leent, M.M.T.

Toner, Y.C., in collaboration with Maier, A., helped perform the in vivo studies, including PET/CT imaging, and subsequent sample preparation for flow cytometry, histology, and biodistribution. Together with Maier, A., she was also responsible for the mouse models in this study, including the LAD permanent ligation and ischemia reperfusion surgeries.

Abstract

Background: In the past two decades, research on atherosclerotic cardiovascular disease has uncovered inflammation to be a key driver of the pathophysiological process. A pressing need therefore exists to quantitatively and longitudinally probe inflammation, in preclinical models and in cardiovascular disease patients, ideally using non-invasive methods and at multiple levels.

Objectives: To develop and employ *in vivo* multiparametric imaging approaches to thoroughly investigate the immune response following myocardial infarction.

Methods: The myocardial infarction models encompassed either transient (40 min) or permanent left anterior descending coronary artery occlusion in C57BL/6 and Apoe$^{-/-}$ mice.

Results: We found that immune cell influx in the infarct was more pronounced in the permanent occlusion model, as assessed by nanotracer-based fluorine magnetic resonance imaging and positron emission tomography (PET) imaging using a CD11b-specific nanobody and a C-C motif chemokine receptor 2-binding probe. Further, using ^{18}F-fluorothymidine and ^{18}F-fluorodeoxyglucose PET, we detected increased hematopoietic activity after myocardial infarction, with no difference between the models. Finally, we observed persistent systemic inflammation and exacerbated atherosclerosis in *Apoe*$^{-/-}$ mice, regardless of which infarction model was used.

Conclusions: Taken together, we showed the strengths and capabilities of multiparametric imaging in detecting inflammatory activity in cardiovascular disease, which augments the development of clinical readouts.

Key Words: Imaging, Inflammation, Immunology, Atherosclerosis, MI

Condensed Abstract

We developed and employed multimodal, multiparametric imaging protocols to characterize the immune response in the heart, bone marrow and spleen following transient and permanent coronary artery occlusion in mice. While cardiac function was more severely affected in the permanent occlusion model, both types of myocardial infarction provoked a similar immune reaction of the bone marrow and spleen and accelerated atherosclerosis.

Highlights

- Preclinical PET and MR imaging methods can be used to characterize the immune response in the heart, bone marrow and spleen following myocardial infarction.
- Permanent coronary artery occlusion triggers the infiltration of more inflammatory cells into the myocardium as compared to the ischemia and reperfusion model.
- Bone marrow and spleen immune responses are similar in ischemia-reperfusion and permanent occlusion.
- Atherosclerosis accelerates in both types of myocardial infarction.

Abbreviations

MI – Myocardial infarction
PO – Permanent occlusion
IR – Ischemia Reperfusion
MRI – Magnetic resonance imaging
PET – Positron emission tomography
LAD – Left anterior descending coronary artery
LGE – Late gadolinium enhancement
CT – Computed tomography
FDG – Fluorodeoxyglucose
FLT – Fluorothymidine

Introduction

The immune reaction to acute myocardial infarction comprises a complex interplay between inflammation and repair. Either insufficient or overly active immune responses can be harmful, negatively impacting patient recovery and prognosis [1,2]. For instance, inadequate activation of reparative programs can lead to infarct expansion, which increases the risk of subsequent heart failure [3,4], while an exacerbated immune response can cause harm systemically. In the context of cardiovascular disease, excessive monocytosis after myocardial infarction accelerates atherosclerosis development [5]. A detailed understanding of these processes is therefore of substantial clinical importance.

Our view of the complex immune mechanisms that follow myocardial infarction is primarily built on research that employs a murine model of permanent coronary artery occlusion [6]. While this model can enable important insights, it may not mimic the clinically more relevant cardiac ischemia and reperfusion scenario. Animal models of temporary coronary artery occlusion, however, do simulate blood flow restoration by percutaneous coronary intervention – the standard of care for patients who experience a myocardial infarction. So far, research using temporary occlusion models has mainly focused on the paradoxically deteriorating effects of reperfusion on the myocardium, but not on systemic and immunological processes [7]. Longitudinal readouts that provide systemic information must be developed to comprehensively profile immune responses following temporal coronary artery occlusion and assess differences from those after permanent occlusion [8]. While conventional *ex vivo* snapshot techniques offer vital information, they do not yield this level of insight. *In vivo* imaging methods such as magnetic resonance imaging (MRI) and positron emission tomography (PET) have the ability to fill this void[9].

In the current study, we developed, validated and applied multiparametric imaging methods to investigate the immune response following permanent

and transient coronary artery occlusion. Specifically, we used different imaging modalities to profile distinct facets of the immune response after myocardial ischemia. We explored systemic immune activation and local leukocyte recruitment into the myocardium using a combination of contrast-enhanced and fluorine MRI. In addition, we applied PET imaging approaches that report on immune cell metabolism, proliferation and migration. Finally, we evaluated how different models of myocardial ischemia impact atherosclerotic plaque progression and cardiac function in mice.

Results

Ischemia-reperfusion and permanent LAD occlusion result in distinct myocardial injury and cardiac function profiles

We profiled the immune responses to cardiac ischemia using two different myocardial infarction models (see Supplementary Fig. S1A for an overview of the entire study). Male C57BL/6 mice underwent either 40-minute occlusion of the LAD, followed by reperfusion (ischemia-reperfusion, IR), or permanent ligation (permanent occlusion, PO) of the same coronary artery (Fig. 1A).

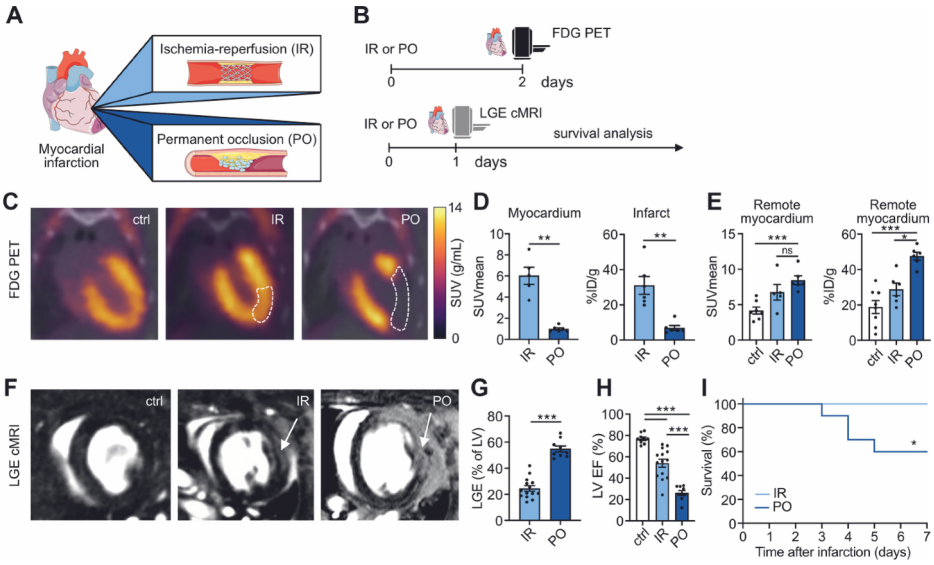


Figure 1. IR and PO Result in Distinct Myocardial Injury and Cardiac Function Profiles

A) This study compared mouse models of ischemia -reperfusion (IR) injury, with 40 minutes of ischemia, and permanent left anterior descending coronary artery occlusion (PO). B) We performed ^{18}F-fluorodeoxyglucose (FDG) PET imaging 2 days after IR or PO surgery. Late gadolinium enhancement (LGE) cardiac MRI was performed 1 day after IR or PO surgery, followed by survival analysis for 1 week. C) FDG PET/CT 2 days after surgery allowed accurate delineation of the infarct zone. **Dashed lines** highlight the infarct area. D)^{18}F-FDG uptake as mean standardized uptake values (SUVs) of the infarct area and as % injected dose (ID)/g infarct tissue (n = 5-6; P = 0.004 for SUVmean; P = 0.002 for %ID/g; 2-tailed Mann-Whitney test). E)^{18}F-FDG uptake in the remote myocardium of mice with PO and IR and the corresponding healthy myocardium of control mice (SUVmean: n = 5-7, P = 0.001 control vs PO, P = 0.132 IR vs PO; %ID/g: n = 5-8, P = 0.025 IR vs PO, P < 0.001 control vs PO; Kruskal-Wallis test). F) Representative LGE cardiac MRI; **arrows** indicate infarct area. G) LGE area in % of left ventricle (n = 9-14; P < 0.001; 2-tailed Student's t-test). H) Left ventricular ejection fraction (LVEF) in % for control, IR, and PO mice (n = 9-14; P < 0.001 for IR vs PO, ctrl vs IR, control vs PO; 1-way ANOVA). I) Simple survival analysis for IR and PO mice for 1 week after myocardial infarction induction (n = 26-29; log-rank test: P = 0.015). Data are presented as mean ± SEM, unless otherwise specified. $*P$ <0.05; $**P$ <0.01; $***P$ <0.001. ANOVA = analysis of variance; MRI =magnetic resonance imaging.

First, we used *in vivo* imaging to investigate differences in cardiac pathology between the IR and PO models. Specifically, we used ^{18}F-FDG PET to assess cardiac viability and MRI to evaluate cardiac function and infarct size (Fig. 1B). Two days after cardiac ischemia, mice with permanent LAD occlusion showed significantly less ^{18}F-FDG uptake in the ischemic myocardium than mice with temporary LAD occlusion, as assessed by *in vivo* PET imaging and *ex vivo* gamma counting (Fig. 1C and 1D). We observed compensatory higher ^{18}F-FDG uptake in the remote myocardium of mice with permanent coronary artery occlusion, compared with mice with IR injury and control mice (Fig. 1E). LGE cardiac MRI 1 day after the ischemic event delineated cardiac function and necrosis with high accuracy (Fig. 1F). We observed ~2.5-fold larger infarcts after PO compared with IR (Fig. 1G), resulting in strongly impaired LVEF in mice with PO. In contrast, mice with IR had relatively preserved LVEF (Fig. 1H). These results were consistent on day 6 after the ischemic event (Supplementary Fig. S1B to S1D). Consequently, mice with reperfusion intervention had better survival than mice without reperfusion salvage (Fig. 1I). Collectively, and in line with previous studies, [17-19] our experiments

detected profound differences in myocardial injury and cardiac function between the two myocardial infarction models.

Ischemia severity correlates with immune cell accumulation in the infarcted myocardium

We next studied whether these substantially different cardiac outcomes are accompanied by distinct leukocyte infiltration profiles in the infarcted tissue (Fig. 2A). To this end, we first used lipoprotein-based nanomaterials, which can be used as *in vivo* immune cell tracers owing to their inherent propensity for myeloid cell uptake,[20] which we loaded with perfluorocarbons (Supplementary Fig. S2A). Perfluorocarbons are biologically inert and can be imaged by ^{19}F-MRI with high specificity owing to a negligible *in vivo* background signal. [21-23] We used the perfluorocarbon PERFECTA, a compound that has 36 equivalent fluorine atoms and thus enables highly sensitive ^{19}F-MRI applications.[11] We intravenously injected our PERFECTA nanotracer 1 day after myocardial infarction and performed ^{19}F-MRI of the myocardium the following day to investigate myeloid cell recruitment to the infarct (Fig. 2B). Mice with IR and PO had significantly higher ^{19}F signal compared with control mice ($P = 0.021$ control vs IR; $P < 0.001$ control vs PO) (Fig. 2C), suggesting myeloid cell influx. We observed a weak inverse correlation between ^{19}F infarct signal and cardiac function (Supplementary Fig. S2B).

To investigate inflammatory monocyte recruitment to the infarct area, we applied ^{64}Cu-DOTA-ECL1i PET imaging of C-C motif chemokine receptor 2 (CCR2) (Fig. 2G). Expression of this receptor is required for monocyte migration to inflammatory lesions.[28] This radiotracer has previously been used to image CCR2 expression in several preclinical animal models as well as in patients with pulmonary fibrosis. [29-31] CCR2 PET imaging of the two myocardial infarction models revealed increased signal in the infarct area of mice subjected to PO compared with control mice ($P = 0.021$) (Fig. 2H). In addition, *ex vivo* gamma counting showed more activity in the infarct zones

of both myocardial infarction models than in myocardium of control mice (P = 0.011 control vs IR; P < 0.001 control vs PO) (Fig. 2I).

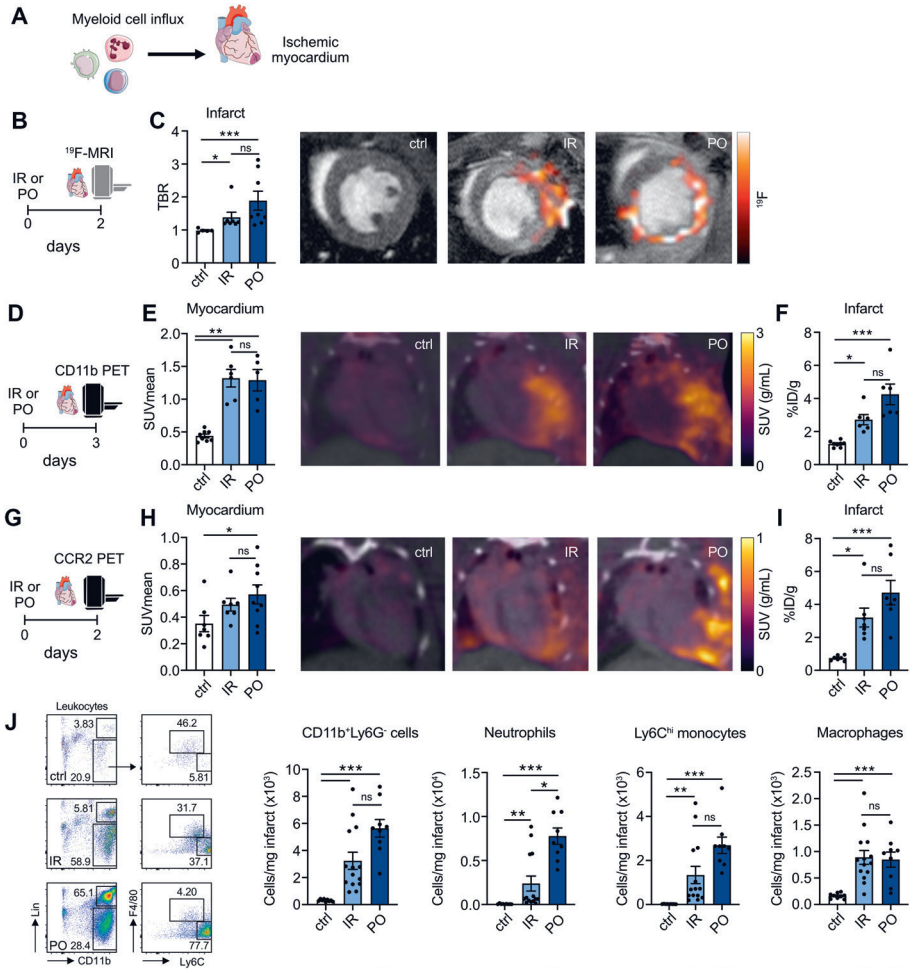


Figure 2. Ischemia Severity Dictates Myeloid Cell Influx Into the Ischemic Myocardium. A) Myeloid cell influx to the ischemic myocardium assessed by multimodal imaging. B)^{19}F-MRI of the heart 2 days after IR/PO surgery and 1 day after PERFECTA nanotracer injection. C)^{19}F concentration in the infarct zone of PO mice compared with IR and control mice, expressed as target-to-background ratio (TBR; n = 5-8; P = 0.021 for control vs IR; P < 0.001 for ctrl vs PO; P = 0.22 IR vs PO; Kruskal-Wallis test). Fused ^{19}F-MRI with fluorine uptake in the infarct zone. D) CD11b PET was performed 3 days after IR/PO surgery and 2 days after tracer injection. E) CD11b PET signal quantification expressed as SUVmean (n = 5-8; P = 0.002 control vs IR; P = 0.002 control vs PO; P = 0.91 IR vs PO; Kruskal-Wallis test) and fused PET/CT images of the heart. F) *Ex vivo* quantification showed higher tracer uptake for mice with IR and PO injury

compared to control mice (n = 6-8; $P = 0.019$ control vs IR; $P < 0.001$ control vs PO; $P = 0.14$ IR vs PO; Kruskal-Wallis test). G) CCR2 PET to image inflammatory monocytes was performed 2 days after IR/PO surgery. The scan occurred during the first 60 minutes after ^{64}Cu-DOTA-ECL1i injection. H)^{64}Cu-DOTA-ECL1i PET signal quantification expressed as SUVmean (n = 7-9; $P = 0.083$ control vs IR; $P = 0.021$ control vs PO; $P = 0.64$ IR vs PO; Kruskal-Wallis test) and representative images of control, IR, and PO mice. I) *Ex vivo* quantification of tracer uptake by gamma-counting (n = 7; $P = 0.011$ control vs IR; $P < 0.001$ control vs PO; $P = 0.21$ IR vs PO; Kruskal-Wallis test). J) Flow cytometry of the infarct zone 2 days after myocardial infarction. **(Left)** Representative flow plots for control, IR and PO hearts, gated on leukocytes. **(Right)** Quantification of $CD11b^+/Ly6G^-$ cells (n = 9-14; $P < 0.001$ control vs IR; $P < 0.001$ control vs PO; $P = 0.092$ IR vs PO; Kruskal-Wallis test), neutrophils (n = 9-14; $P = 0.002$ control vs IR; $P < 0.001$ control vs PO; $P = 0.028$ IR vs PO; Kruskal-Wallis test), $Ly6C^{high}$ monocytes (n = 9-14; $P = 0.001$ control vs IR; $P < 0.001$ control vs PO; $P = 0.069$ IR vs PO; Kruskal-Wallis test), and macrophages (n = 9-14; $P < 0.001$ control vs IR; $P < 0.001$ control vs PO; $P = 0.87$ IR vs PO; Kruskal-Wallis test) in the infarct. Data are presented as mean ± SEM, unless otherwise specified. $*P < 0.05$; $**P < 0.01$; $***P < 0.001$. Abbreviations as in Figure 1.

Two days after infarction, we performed flow cytometry analysis of the infarcted myocardium in both models to further validate our imaging findings. In agreement with the imaging findings, we found significantly increased $CD11b^+$ cell numbers in the myocardial infarction models than in control mice ($P < 0.001$ control vs IR; $P < 0.001$ control vs PO; $P = 0.092$ IR vs PO) (Fig. 2J, Supplementary Fig. S3A). When comparing the two infarction models, we found more neutrophils in the infarct zone after PO than after IR ($P = 0.027$). In addition, we observed a trend toward elevated $Ly6C^{high}$ monocyte numbers in the PO group ($P = 0.069$), whereas macrophage numbers were similar in both models 2 days after infarction. Seven days after inducing cardiac ischemia, we detected a difference between PO and IR regarding macrophage burden in the infarct (Supplementary Fig. S3B). Overall, flow cytometry data for the infarct area align with our imaging results and indicate distinct differences in immune response severity.

Next, we investigated the relationship between cardiac function (as assessed by cMR) and myeloid cell burden in the infarct area (as measured by flow cytometry), and we noted a strong inverse correlation between these parameters (Supplementary Fig. S3C). Taken together, these results

demonstrate that the two models of cardiac ischemia differ in their degree of inflammatory cell infiltration into the infarct zone and that these infiltration levels negatively correlate with cardiac function.

Bone marrow responses are similar in ischemia-reperfusion and permanent occlusion

The immune cells that infiltrate the heart are produced in the bone marrow and spleen and are quickly deployed from these organs.[3] In response to the inflammatory factors and damage-associated molecular patterns generated and released after myocardial ischemia, the proliferation of inflammatory immune cell progenitors profoundly increases before leukocyte release from the hematopoietic organs, a process called emergency hematopoiesis.[32] We used multimodal imaging to investigate potential differences in emergency hematopoiesis by measuring proliferation and metabolic activity in the bone marrow and myeloid cell egress from the hematopoietic tissues (Fig. 3A).

We first assessed proliferation with the use of ^{18}F-fluorothymidine (FLT) PET 2 days after infarction (Fig. 3B).^{18}F-FLT uptake in the bone marrow was significantly higher in both myocardial infarction mouse models compared with control animals, but there was no difference between the two models (Figs. 3C and 3D). We complemented these findings with the use of flow cytometry to evaluate BrdU incorporation in bone marrow LSK hematopoietic stem and progenitor cells 3 days after infarction. We found significantly more BrdU-positive LSK cells in both myocardial infarction models compared with naïve control mice (Fig. 3E, Supplementary Fig. S4A). These data suggest that the increased hematopoietic proliferation does not depend on the type of cardiac ischemia.

Post–myocardial infarction emergency hematopoiesis is an energy-demanding process. We therefore used ^{18}F-FDG PET to investigate metabolic activity (Fig. 3F). In line with data on proliferation, mice with either type of myocardial infarction displayed significantly higher ^{18}F-FDG accumulation in the bone marrow compared with control mice, although we

observed no significant difference between IR and PO mice by means of either *in vivo* PET imaging or *ex vivo* gamma counting (Figs. 3G and 3H). Correspondingly, we found more LSK cells in the bone marrow of the myocardial infarction groups compared with control mice ($P = 0.003$ control vs IR; $P = 0.052$ control vs PO) (Fig. 3I), whereas there was no difference between IR and PO models.

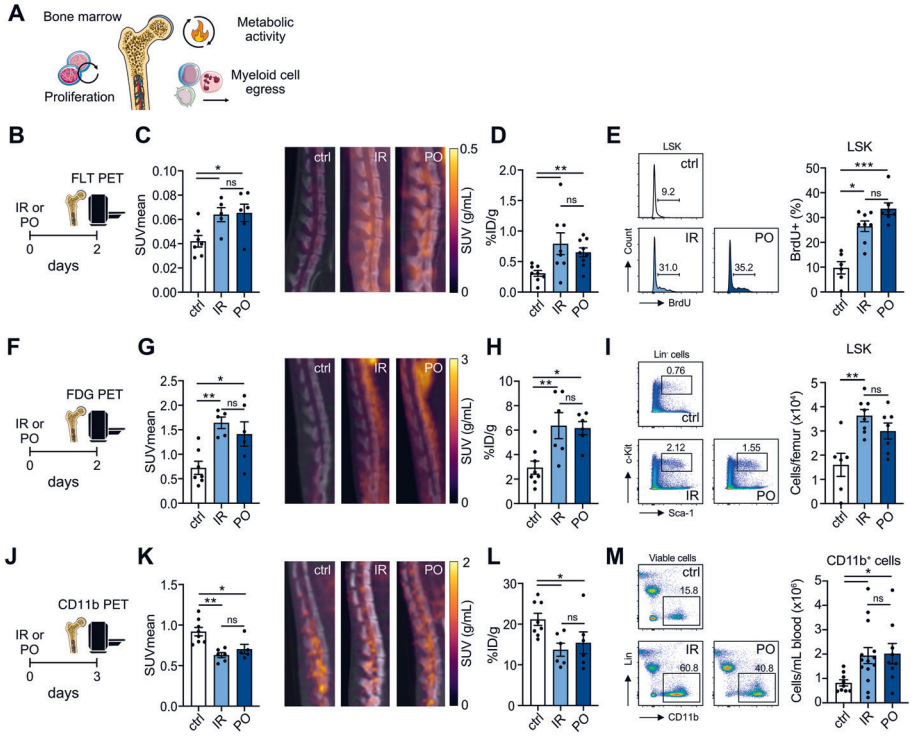


Figure 3. Bone Marrow Activity After Cardiac Ischemia-Reperfusion and Permanent Left Anterior Descending Coronary Artery Occlusion Are Similar. A) Cardiac ischemia induces proliferation, metabolic activation, and myeloid cell egress in/from the bone marrow. We probed these processes via molecular imaging. B)^{18}F-fluorothymidine (FLT) PET/CT was performed 2 days after IR/PO surgery. ^{18}F-FLT was injected 90 minutes before the scan. C) Quantification of ^{18}F-FLT signal in the lumbar vertebrae (n = 5-7; $P = 0.032$ control vs IR; $P = 0.018$ control vs PO; $P = 0.92$ IR vs PO; Kruskal-Wallis test) and representative ^{18}F-FLT PET/CT images showing higher activity for both IR and PO mice. D) *Ex vivo* gamma counting of ^{18}F-FLT uptake in the bone marrow (n = 8-9; $P = 0.006$ control vs IR; $P = 0.006$ control vs PO; $P = 0.92$ IR vs PO; Kruskal-Wallis test). E) Flow cytometry analysis of bone marrow cells 3 days after IR/PO. Representative histograms of BrdU expression in Lin$^-$Sca-1$^+$cKit$^+$ (LSK) cells and quantification of BrdU-positive

cells. BrdU (1 mg) was injected i.*P*. 24 hours before analysis (n = 6-8, *P* = 0.014 control vs IR; *P* < 0.001 control vs PO; *P* = 0.18 IR vs PO; Kruskal-Wallis test). F)^{18}F-FDG PET/CT was performed 2 days after IR/PO surgery. ^{18}F-FDG was injected 30 minutes before imaging. G) Quantification of ^{18}F-FDG signal in the lumbar vertebrae (n = 5-7; *P* = 0.005 control vs IR; *P* = 0.025 control vs PO; *P* = 0.52 IR vs PO; Kruskal-Wallis test) and representative images showing higher activity in IR and PO mice compared with control mice. H) *Ex vivo* gamma counting of ^{18}F-FDG uptake in the bone marrow (n = 6-8; *P* = 0.008 control vs IR; *P* = 0.011 control vs PO; *P* = 0.92 IR vs PO; Kruskal-Wallis test). I) Number of LSK cells in the bone marrow 3 days after IR/PO (n = 6-8; *P* = 0.003 control vs IR; *P* = 0.052 control vs PO; *P* = 0.33 IR vs PO; Kruskal-Wallis test) with representative plots. J) CD11b PET was performed 3 days after myocardial infarction. The ^{89}Zr-labeled CD11b-specific nanobody was injected 2 days after myocardial infarction. K) Quantification of PET signal in the lumbar vertebrae (n = 5-8; *P* = 0.001 control vs IR; *P* = 0.032 control vs PO; *P* = 0.41 IR vs PO; Kruskal-Wallis test) and representative images showing lower signal in mice with IR or PO surgery compared with control. L) *Ex vivo* gamma counting of tracer uptake in the bone marrow (n = 6-8; *P* = 0.017 control vs IR; *P* = 0.039 control vs PO; *P* = 0.77 IR vs PO; Kruskal-Wallis test). M) Representative flow plots of blood samples, gated on viable cells. Significantly higher numbers of CD11b$^+$ cells were observed in the blood of IR and PO animals 2 days after infarction (n = 9-14; *P* = 0.021 control vs IR; *P* = 0.025 control vs PO; *P* = 0.87 IR vs PO; 1-way ANOVA). Data are presented as mean ± SEM, unless otherwise specified. ∗*P* <0.05; ∗∗*P* <0.01, ∗∗∗*P* <0.001. Abbreviations as in Figures 1 and 2.

We also used the CD11b PET imaging data to explore myeloid cell dynamics in the bone marrow. The radiotracer was injected 2 days after myocardial infarction, and imaging was performed 1 day later (ie, 3 days after cardiac ischemia) (Fig. 3J). We found significantly lower bone marrow signal in the IR and PO mouse models than in control mice (*P* = 0.001 control vs IR; *P* = 0.032 control vs PO) (Figs. 3K and 3L), suggesting myeloid cell egress. Corroboratively, we found increased CD11b$^+$ cells in the circulation in both myocardial infarction models compared with naïve control mice (*P* = 0.021 control vs IR; *P* = 0.025 control vs PO) (Fig. 3M, Supplementary Fig. S4B), mainly driven by an expansion in circulating neutrophils (*P* = 0.001 control vs IR; *P* = 0.003 control vs PO) (Supplementary Fig. S4C). We did not detect a difference in CCR2 expression in the bone marrow after myocardial infarction (Supplementary Figs. S4D to S4F). Although more CCR2+ inflammatory cells are produced after myocardial infarction, their immediate departure from the bone marrow could explain the lack of alterations in PET signal. [33]

We also pursued multiparametric immunoimaging of the spleen. In line with the bone marrow data, we found slightly increased ^{18}F-FLT uptake in the spleen of PO mice compared with control mice (P = 0.042), and we observed no difference between the two myocardial infarction models (Supplementary Figs. S5A to S5C). FDG PET imaging did not indicate altered metabolic activity in the spleen (Supplementary Figs. S5D to S5F). After PERFECTA–nanotracer injection, ^{19}F-MRI signal decreased in the spleen only in PO mice, compared with control, suggesting myeloid cell egress (P = 0.004 control vs PO; P = 0.015 IR vs PO) (Supplementary Figs. S5G and S5H). However, when we used ^{89}Zr-CD11b nanobodies to probe myeloid cell dynamics in the spleen, we found lower signal in both models than in control mice (P = 0.041 control vs PO; P = 0.046 control vs PO) (Supplementary Figs. S5I to S5K). *Ex vivo* gamma counting revealed slightly elevated CCR2 expression in the spleens in both myocardial infarction models, compared with naïve controls (P = 0.039 control vs IR; P = 0.039 control vs PO) (Supplementary Figs. S5l to S5N). Taken together, these data show that there is little difference in splenic activity between the two myocardial infarction models, as assessed by multimodal imaging.

Correlation between tracer uptake in the hematopoietic organs and the infarcted myocardium

We subsequently evaluated the correlations between tracer uptake in the infarct, spleen, and bone marrow (Fig. 4, Supplementary Fig. S6). For ^{89}Zr-CD11b-specific nanobody, ^{18}F-FLT, and ^{18}F-FDG, we found significant correlations between tracer uptake in the bone marrow and spleen. This correlation was weaker for ^{64}Cu-DOTA-ECL1i. However, we detected a significant correlation between ^{64}Cu-DOTA-ECL1i accumulation in the hematopoietic organs and the infarct. These findings highlight the importance of evaluating multiple tissues simultaneously.

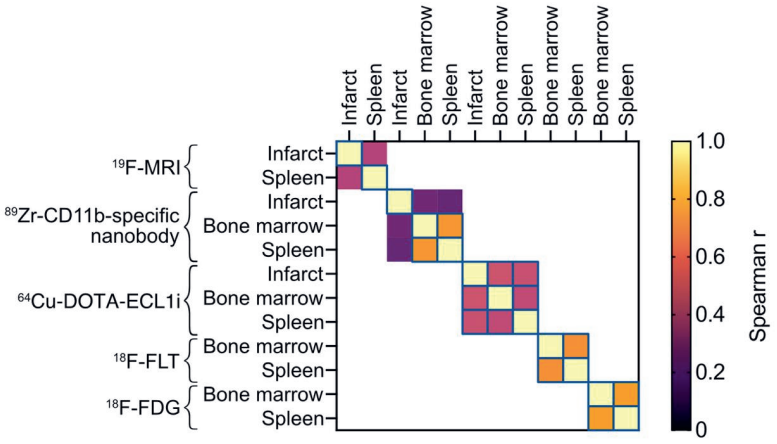


Figure 4. Heatmap of Correlations Between Tracer Uptake in Tissues of Interest. Heatmap showing correlations between tracer uptake in the infarct, spleen, and bone marrow. For ^{19}F-MRI, *in vivo* TBRs were used. For the PET tracers, *ex vivo* gamma counting data were used. Colors represent Spearman's *r*, and significant correlations are outlined by a **blue line**. For simplicity, inverse correlations were converted to positive values. See Supplementary Figure S6 for individual graphs.

Atherosclerosis accelerates in both types of myocardial infarction

Systemic inflammation after IR and PO was mainly caused by myocardial ischemia; we did not detect higher numbers of circulating inflammatory immune cells after sham surgery (Supplementary Fig. S4C). Seven days after infarction, circulating neutrophils were still elevated, with no differences between the models (Supplementary Fig. S7), indicating ongoing inflammatory activity and leukocyte supply from the hematopoietic organs. We therefore tested the long-term impact of these two types of cardiac ischemia on atherosclerosis. We know that PO results in accelerated atherosclerosis,[5] but whether IR has the same impact is unknown. To explore this, we exposed atherosclerosis-prone *Apoe*$^{-/-}$ mice to a Western diet for 6 weeks before inducing IR or PO. We performed cardiac MRI 2 days after ischemia to assess infarct size and cardiac function. Four weeks later, we investigated the effects on plaque and systemic inflammation (Fig. 5A). We found larger infarcts and greater reduction in LVEF in *Apoe*$^{-/-}$ PO mice

compared with *Apoe*$^{-/-}$ IR mice ($P < 0.001$) (Figs. 5C to 5D). In addition, atherosclerotic mice subjected to PO had worse survival than their littermates subjected to IR (Fig. 5E). These patterns are similar to our findings in wild-type mice (Figs. 1F to 1I).

Flow cytometric analyses 4 weeks after infarction disclosed more Ly6C^{hi} monocytes in the femurs of mice subjected to PO as compared to controls ($P = 0.035$), while splenic Ly6C^{hi} monocyte numbers increased in both cardiac ischemia models ($P < 0.001$ control vs IR; $P = 0.003$ control vs PO) (Fig. 5F). In addition, we found elevated numbers of CD11b^{+} myeloid cells in the spleens of IR and PO mice ($P = 0.063$ control vs IR; $P = 0.071$ control vs PO) (Supplementary Fig. S8A). We subsequently assessed the impact of the different myocardial ischemia types on plaque size and myeloid cell content. Flow cytometry analysis performed 4 weeks after infarction showed significantly higher CD11b^{+} cell numbers in the aortas of IR and PO mouse models, compared with atherosclerotic mice that were not subjected to myocardial infarction ($P < 0.001$ control vs IR; $P = 0.018$ control vs PO) (Supplementary Fig. S8B). This higher count was mainly due to raised macrophage numbers ($P < 0.001$ control vs IR; $P = 0.030$ control vs PO). In addition, we found expanded Ly6C^{high} monocyte numbers in the aortic plaque in both myocardial ischemia models compared with control mice ($P = 0.002$ control vs IR; $P = 0.021$ control vs PO) (Fig. 5G). We observed a larger mac3^{+} area in the aortic root of PO mice compared with mice without infarction ($P = 0.093$ control vs IR; $P = 0.011$ control vs PO) (Figs. 5H and 5I). Also, aortic root lesions were significantly larger in mice subjected to PO and trended toward larger in IR mice ($P = 0.079$ control vs IR; $P = 0.010$ control vs PO). Furthermore, we found an inverse correlation between plaque size and cardiac function (Fig. 5J).

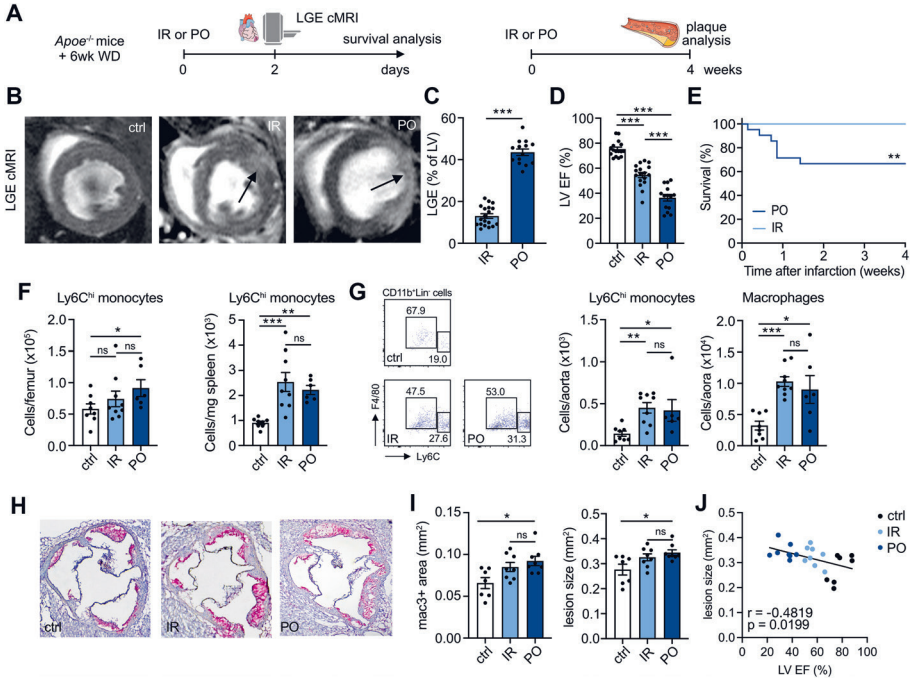


Figure 5. Ischemia-Reperfusion and Permanent Occlusion Similarly Accelerate Atherosclerosis. A) Eight-week-old *Apoe*$^{-/-}$ mice were fed a Western diet (WD) for 6 weeks before IR or PO surgery. Two days after cardiac ischemia, ILGE cardiac MRI was performed. Mice were followed for survival. Plaque analyses were performed 4 weeks after IR/PO surgery. B) Representative LGE cMR images; **arrows** indicate infarct area. C) LGE area in % of the left ventricle (n = 14-19; ***P <0.001; 2-tailed Student's t-test). D) LVEF of control, IR, and PO *Apoe*$^{-/-}$ mice (n = 14–17; P < 0.001 for IR vs PO, control vs IR, and control vs PO; 1-way ANOVA). E) *Apoe*$^{-/-}$ mice with IR injury had better survival than those with PO surgery (n = 23-25; log-rank test: P = 0.006). F) Ly6C^{high} monocyte numbers in the bone marrow (n = 6-9; P = 0.50 control vs IR; P = 0.035 control vs PO; P = 0.12 IR vs PO; Kruskal-Wallis test) and spleen (n = 6-9; P < 0.001 control vs IR; P = 0.003 control vs PO; P = 0.90 IR vs PO; Kruskal-Wallis test) of *Apoe*$^{-/-}$ mice 4 weeks after IR/PO surgery. G) Ly6C^{high} monocyte (n = 6-9; P = 0.002 control vs IR; P = 0.021 control vs PO; P = 0.66 IR vs PO; Kruskal-Wallis test) and macrophage (n = 6-9; P < 0.001 control vs IR; P = 0.030 control vs PO; P = 0.31 IR vs PO; Kruskal-Wallis test) numbers in aortas of *Apoe*$^{-/-}$ mice 4 weeks after IR/PO surgery, with representative flow cytometry plots. H) Representative images of mac3/hematoxylin–stained aortic roots 4 weeks after IR/PO surgery. I) Mac3^{+} area (n = 6-9; P = 0.093 control vs IR; P = 0.011 control vs PO; P = 0.38 IR vs PO; Kruskal-Wallis test) and lesion size (n = 6-9; P = 0.079 control vs IR; P = 0.010 control vs PO; P = 0.40 IR vs PO; Kruskal-Wallis test) were both significantly larger in PO mice compared with control mice. IR mice had a trend toward larger macrophage area and lesion size in aortic roots. J) Correlation between LVEF and lesion size. Data are presented as mean ± SEM, unless otherwise specified. *P <0.05; **P <0.01; ***P <0.001. Abbreviations as in Figures 1 and 2.

These data show that: 1) IR and PO myocardial infarction induce distinct cardiac phenotypes in mice with atherosclerosis, similar to outcomes seen in wild-type mice; 2) myocardial infarction accelerates atherosclerosis, as previously shown;[5] and 3) this happens regardless of which model of myocardial infarction is used.

Discussion

In this study, we characterized the inflammatory response after myocardial infarction in permanent and temporary LAD occlusion models by means of multiple PET and MRI approaches to probe myeloid cell dynamics and hematopoietic activity. Our data show that these two murine models of myocardial infarction induce similar systemic inflammation profiles and exacerbate atherosclerosis. At the same time, the models have notably different effects on cardiac function, with more favorable outcomes in the reperfusion model.

As our findings show, the reperfusion model generates smaller infarcts, accompanied by better cardiac function and improved survival rates, compared with the permanent coronary artery occlusion model. These data align with results from previous studies.[18,19] Recent work by Pluijmert et al[17] observed reduced inflammatory leukocyte influx into the infarct zone of mice with temporal coronary artery occlusion compared with permanent occlusion. We expand on this research by revealing systemic immune activation patterns in the hematopoietic organs (ie, spleen and bone marrow) after both temporal and permanent coronary artery occlusion. Moreover, we found that both models accelerate atherosclerotic plaque inflammation via enhanced systemic supply of leukocytes.

A pressing need exists for clinical readouts of inflammatory activity in cardiovascular disease. Therefore, developing and applying systemic noninvasive imaging techniques is critical. The present study deployed molecular imaging protocols with innovative radiotracers to assess immune

cell dynamics locally—in the infarcted myocardium—as well as systemically—in the bone marrow and spleen. In addition to ^{18}F-FDG PET, ^{18}F-FLT PET, ^{64}Cu-DOTA-ECL1i PET, and LGE-MRI, which are currently being used in the clinic or evaluated in clinical trials, we used CD11b-specific nanobody PET and nanotracer-based ^{19}F-MRI, which are now preclinical research methods. [22,23,27]

In the context of cardiovascular disease, ^{18}F-FDG PET imaging is increasingly applied to gauge (chronic) inflammatory activity in spleen, bone marrow, and atherosclerotic plaque. Recent studies showed that patients with atherosclerotic cardiovascular disease have enhanced ^{18}F-FDG uptake in spleen and bone marrow, corresponding with higher hematopoietic activity levels.[34] Moreover, ^{18}F-FDG uptake in the spleen independently predicts risk of subsequent cardiovascular events.[35] Elevated ^{18}F-FDG uptake in the bone marrow was even found to be an early indicator of atherosclerosis.[36] Our study successfully used this imaging method to detect the acute inflammatory response after myocardial infarction. We obtained similar findings through ^{18}F-FLT PET imaging, which could therefore serve as an alternate approach.[37]

The CD11b PET imaging method is based on an ^{89}Zr-labeled CD11b-binding nanobody, which, unlike ^{18}F-FDG and ^{18}F-FLT PET, is cell type specific. Nanobodies are the smallest antigen-binding derivative obtainable from naturally occurring antibodies.[25] Several nanobody-based tracers have been developed for other targets and are presently being evaluated in preclinical and clinical settings.[38] In the present study, we effectively used CD11b-specific nanobodies to capture myeloid cell influx into the ischemic myocardium. We also detected a reduction tracer signal in bone marrow after myocardial infarction. Although there is enhanced myelopoiesis at this stage, we think that the drop in PET signal is caused by ^{89}Zr-labeled CD11b^{+} cell egress from the bone marrow during the 24 hours between tracer administration and imaging. Detecting this phenomenon could be informative for preclinical studies. However, for clinical applications, labeling with a shorter-lived isotope (eg, ^{18}F) would be preferable. This would shorten

the interval between tracer administration and imaging, thereby reducing the opportunity to capture myeloid cell egress.

The PET tracer ^{64}Cu-DOTA-ECL1i targets CCR2-expressing inflammatory monocytes and macrophages. The tracer effectively detects inflammation in mouse models of aortic aneurysm and myocardial infarction.[16,30] It also binds inflammatory lesions in human tissue specimens taken from patients with myocardial infarction and chronic ischemic heart disease.[15] Moreover, this tracer has had promising results in patients with lung fibrosis[29,31] and is currently being tested in patients with myocardial infarction (NCT05107596). Here, we successfully used this radiotracer to visualize CCR2$^+$ cell recruitment to the infarcted myocardium in both infarction models; however, CCR2 PET was less informative for systemic inflammation. Although this imaging method and CD11b PET imaging similarly detect immune cell influx into the myocardium, the two approaches differ. On one hand, ^{64}Cu-DOTA-ECL1i does not bind to, for example, CCR2$^-$ resident macrophages, resulting in more specific detection of inflammatory activity. On the other hand, CD11b PET might be the preferred method for including neutrophils, which are important players in the immediate response to myocardial infarction.[26,29]

We have previously demonstrated the value of ^{19}F-MRI in assessing cardiac inflammation and myeloid cell migration from the spleen.[22] Here, we applied PERFECTA nanomaterials to investigate the immune response after myocardial infarction in two different mouse models. Perfluorocarbons (PFCs) are considered biologically inert, providing favorable characteristics for clinical applications. For example, they are already used as oxygen carriers in blood substitutes.[39] Nienhaus et al[40] demonstrated that human monocyte function and viability were maintained after PFC uptake. In line with our previous work,[22] we observed decreased ^{19}F-MRI signal in the spleen after permanent LAD ligation. However, we did not see this phenomenon in the IR mouse model: In those animals, ^{19}F-MRI signal in the spleen was similar to that in naïve mice. This difference could not be attributed to distinct patterns of myeloid cell migration from the spleen to the circulation, because we detected similar levels of CD11b$^+$ cells in the peripheral blood of both

myocardial infarction groups. Furthermore, ^{89}Zr-CD11b-specific nanobody and ^{64}Cu-DOTA-ECL1i accumulated similarly in the spleen in both models. Further research is needed to explain the varied ^{19}F-MRI signal in the spleen. Potentially, PERFECTA nanotracer behavior could be more susceptible to cardiac function differences between the models, given its larger size and longer circulation time compared with the two radiotracers.

Methods

Mice

Ten-week-old male C57BL/6J mice and 8-week-old male *Apoe*$^{-/-}$ mice (B6.129P2-*Apoetm*^{1Unc}/J) were purchased from The Jackson Laboratory. *Apoe*$^{-/-}$ mice were fed a Western diet (Harlan Teklad TD.88137, 42% of calories from fat) for 10 weeks. All animal experiments were performed in accordance with protocols approved by the Institutional Animal Care and Use Committee of the Icahn School of Medicine at Mount Sinai and followed the National Institutes of Health guidelines for animal welfare.

Myocardial infarction surgeries

Age-matched mice underwent permanent or temporary ligation of the left anterior descending coronary artery (LAD) to induce myocardial infarction. Anesthesia was induced with ketamine (100 mg/kg) and xylazine (10 mg/kg) intraperitoneally and maintained with isoflurane after intubation. Body temperature was held at 37 °C. Analgesia was provided with buprenorphine (0.1 mg/kg) before and 12 hours after surgery. After thoracotomy of the left fourth intercostal space, a retractor was used to keep the surgical field exposed. Next, pericardiotomy was performed, and the LAD was identified and then ligated with an 8-0 Prolene suture. Temporary ligation was maintained for 40 minutes via a small tube between the ligation suture and the LAD.[10] Sham procedure was executed the same way but without ligation of the LAD. Mice were extubated after the thoracotomy, and the skin was closed with sutures. C57BL/6J survival analysis included 29 mice with permanent LAD occlusion and 26 mice with temporary LAD

occlusion. *Apoe*$^{-/-}$ survival analysis included 23 with permanent LAD occlusion and 25 with temporary LAD occlusion.

Functional and late gadolinium enhancement cardiac MRI

Cardiac function and infarct size in isoflurane-anesthetized (4% for induction, 1% for maintenance) mice were assessed by means of cardiac MRI, using a 7.0-T small-animal scanner (Bruker BioSpec 70/30) equipped with a 40-mm-diameter $^{1}H/^{19}F$ volume coil (MR Coils). Cardiac MRI was performed 1 day after surgery for C57BL/6J mice and 2 days after surgery for *Apoe*$^{-/-}$ mice. Before being placed in the MRI scanner, mice were intraperitoneally injected with 0.4 mL/kg gadolinium contrast (Gadovist, Bayer). After survey scans to plan a cardiac short-axis orientation, 7 short-axis slices covering the heart from apex to base were scanned with a self-gated Cine 2D Flash sequence. This scan could be used to assess cardiac function and late gadolinium enhancement (LGE) infarct size. Sequence parameters were: repetition time (TR) = 10.5 ms; echo time (TE) = 1.9 ms; flip-angle = 20°; field-of-view (FOV) = 30 × 30 mm^2; slice thickness = 1 mm; acquisition matrix = 192 × 192; reconstruction matrix = 256 × 256; number of cardiac frames = 12; acquisition time = 4 minutes, 13 seconds per slice. The area of LGE uptake in percentage of the left ventricle and the left ventricular ejection fraction (LVEF) were analyzed with the use of Osirix MD (v12.0, Pixmeo) with the MRheart plugin in 5 to 7 cardiac short-axis slices, from apical to basal.

^{19}F-MRI

Formulating the PERFECTA nanotracer

PERFECTA, or 1,3-bis[[1,1,1,3,3,3-hexafluoro-2-(trifluoromethyl)propan-2-yl]oxy]-2,2-bis[[1,1,1,3,3,3-hexafluoro-2-2(trifluoromethyl)propan-2-yl]oxymethyl]propane, was synthesized as previously reported.[11] 1,2-Dimyristoyl-*sn*-glycero-3-phosphocholine (59 mg, 87 µmol; Avanti Polar Lipids) and 1-myristoyl-2-hydroxy-*sn*-glycero-3-phosphocholine (41 mg, 58 µmol; Avanti Polar Lipids) were dissolved in chloroform (2 mL). The solution was added dropwise to hot phosphate-buffered saline solution (PBS) (10 mL, 80 °C) and the obtained off-white suspension was stirred for

5 minutes before being allowed to cool to room temperature. If needed, additional PBS was added to attain a total volume of 10 mL. The resulting lipid suspension was stored at 4 °C for no more than 2 weeks. A mixture of the lipid suspension (0.5 mL), PBS (4.5 mL), and PERFECTA (100 mg, 0.10 mmol) was heated to approximately 80 °C in a glass vial by means of a microwave oven and directly afterward sonicated for 15 minutes with the use of a 150 V/T ultrasonic homogenizer equipped with a microtip working at 30% power output. The milky solution was allowed to cool to room temperature. Apolipoprotein-A1 (0.5 mg, purified in house from human high-density-lipoprotein obtained from Bioresource Technology) was added, and the mixture was incubated at room temperature for 12 to 16 hours. The mixture was shaken and subsequently left undisturbed for 30 seconds. Any precipitate was discarded, and the remaining suspension was transferred to a centrifugal filtration tube (1 MDa molecular weight cutoff; Vivaspin Sartorius Stedim Biotech). The tube was spun at 4,000*g* and 4 °C until concentrated to approximately 0.5 mL. Any precipitate was resuspended by repeatedly drawing the suspension up and down a pipette. PBS (5.0 mL) was added, and the solution was again concentrated to 0.5 mL and resuspended to produce the finished PERFECTA nanotracer. The nanotracer was diluted with PBS and injected intravenously via the tail vein at a concentration of 0.5 mg/g body weight, with typical injection volumes being around 100 µL. If not used immediately, the nanotracers were stored in the dark at 4 °C for a maximum of 2 weeks.

Physicochemical characterization of PERFECTA nanotracers

To determine particle size, an aliquot (10 µL) of the PERFECTA nanotracer suspension was diluted in PBS (1.0 mL) and analyzed by dynamic light scattering (DLS) to determine the mean of its number and average size distribution. DLS measurements were performed on a NanoBrook ZetaPlus system (Brookhaven Instruments). The typical particle size was 182 ± 15 nm; n = 7. PERFECTA concentrations were determined by means of ^{19}F nuclear magnetic resonance spectroscopy (NMR). A suspension of nanotracers (90 vol%) and deuterium oxide (10 vol%) containing a predetermined amount of sodium trifluoroacetate as an internal standard was prepared. Samples of the

suspension were analyzed by means of ^{19}F-NMR with the use of a Bruker 600 Ultrashield magnet connected to a Bruker Avance 600 console. Data were processed with the use of Topspin v.3.5pl7. Typical PERFECTA nanotracer concentrations were around 150 mg/mL.

^{19}F-MRI protocol

In vivo ^{19}F-MRI was performed in the same scanning session and with the same setup described above for MRI of cardiac function and LGE. To obtain an anatomic background, we first acquired a ^{1}H whole-body 3D fast imaging with steady-state precession scan with the following parameters: TR = 8 ms; TE = 4 ms; flip-angle = 15°; FOV = 64 × 32 × 32 mm^2; acquisition matrix = 256 × 96 × 9six, reconstruction matrix = 256 × 128 × 128; number of signal averages (NSA) = 4; acquisition time = 4 minutes 54 seconds. Whole-body ^{19}F-MRI was performed with a 3D rapid acquisition with relaxation enhancement (RARE) sequence with the following parameters: TR = 1,000 ms; TE = 10.9 ms; RARE factor = 16; FOV = 64 × 32 × 32 mm^2; acquisition matrix = 128 × 64 × 64; reconstruction matrix = 128 × 64 × 64; NSA = 6; acquisition time = 25 minutes 36 seconds. Next, a higher-resolution 3D RARE ^{19}F scan of the heart was conducted in the same short-axis orientation as the ^{1}H Cine cardiac scans and with the following parameters: TR = 1,000 ms; TE = 8 ms; RARE factor = 16; FOV = 30 × 30 × 16 mm^2; acquisition matrix = 64 × 64 × 16; reconstruction matrix = 64 × 64 × 16; NSA = 32; acquisition time = 34 minutes 8 seconds.

Image analysis

The target-to-background ratio (TBR) was calculated, with the use of Osirix MD (v12.0, Pixmeo), for fluorine uptake in the infarct area and spleen. LVEF and LGE as percentage of the left ventricle were analyzed as described above. Fluorine uptake in the infarct area was calculated from the LGE area as target zone in all 5 to 7 cardiac short-axis slices and upper limb muscles as background. The spleen TBR was measured by using the whole spleen in the abdominal^{1}H coronal images as the target area and using the psoas muscle as the background area. After image fusion of ^{1}H/^{19}F, the TBR was calculated.

PET/CT imaging

Before the PET/computed tomographic (CT) scan, animals were anesthetized with an isoflurane (Baxter Healthcare)–oxygen gas mixture (4% for induction, 1% for maintenance) and subsequently imaged on a nano PET/CT scanner (Mediso). A tail vein catheter was inserted and contrast (Isovue-370; Bracco Diagnostics) was injected at a rate of 0.5 mL/min. A whole-body CT scan was performed (energy 50 kVp, current 180 μAs, isotropic voxel size 0.25 mm^3), followed by a PET scan. The coincidences were filtered with an energy window 400-600 keV. The voxel size was isotropic and 0.6 mm^3 in width, and the reconstruction was applied for 2 complete iterations, with 6 subsets per iteration. PET data were reconstructed using CT-based attenuation correction. Reconstruction was performed with the TeraTomo 3D reconstruction algorithm from Mediso Nucline software.

Fluorothymidine PET

^{18}F-Fluorothymidine (FLT) was synthesized as reported previously.[12] Briefly, ^{18}F was eluted in 4,7,13,16,21,24-hexaoxa-1,10-diazabicyclo[8.8.8]hexacosane, K_2CO_3, and MeCN. Solvents were removed azeotropically and 3-N-Boc-5′-O-dimethoxytrityl-3′-O-nosyl-thymidine in dry acetonitrile was added. N-Hydrochloric acid was then added to the mixture, followed by sodium acetate neutralization. Two days after myocardial infarction of C57BL/6 mice, ^{18}F-FLT (382 ± 20.3 μCi in 100 μL PBS) was administered via the tail vein and allowed to circulate for 90 minutes before PET imaging (30 minutes acquisition time).

Fluorodeoxyglucose PET

Two days after myocardial infarction, C57BL/6 mice were fasted overnight before ^{18}F-fluorodeoxyglucose (FDG) (340 ± 27.0 μCi in 100 μL PBS solution) injection, which was administered via the tail vein and allowed to circulate for 30 minutes before PET imaging (30 minutes acquisition time).

CD11b PET

CD11b-specific nanobodies were purified from *Escherichia coli* WK6 cells through immobilized metal affinity chromatography with the use of Ni-NTA beads, followed by functionalization with the chelator deferoxamine (DFO). The DFO-functionalized nanobody was then PEGylated, radiolabeled with ^{89}Zr in chelexed PBS and purified with the use of a PD-10 size exclusion cartridge. The purification and radiolabeling process is described elsewhere in more detail.[13] The radiochemical purity was >97%. Two days after myocardial infarction, C57BL/6 mice were injected with ^{89}Zr-labeled CD11b-specific nanobodies (200 ± 17.5 μCi in 100 μL PBS) via the tail vein. PET imaging was performed 24 hours later (30 minutes acquisition time).

C-C motif chemokine receptor 2 PET

^{64}Cu-1,4,7,10-tetraazacyclododecane-1,4,7,10-tetraacetic acid (DOTA)–extracellular loop 1 inverso (ECL1i) that allosterically binds to C-C motif chemokine receptor 2 (CCR2) was generously given to us by Dr Gropler (Washington University, St Louis, MO) as an intact radiotracer. ECL1i peptide was synthesized from D-form amino acids obtained from CPC Scientific, and maleimide-mono-amide-DOTA was purchased from Macrocyclics. The complete description of DOTA-ECL1i synthesis and radiolabeling with ^{64}Cu was reported previously.[14-16] The radiochemical purity was more than 95% (determined by radio-HPLC) before administration to mice. Two days after myocardial infarction, C57BL/6 mice received ^{64}Cu-DOTA-ECL1i (354 ± 65.8 μCi in 100 μL PBS) via tail vein injection and a 0- to 60-minute dynamic PET scan was performed.

Image analysis

Whole-body CT images of mice were fused with PET images (Osirix MD v12.0, Pixmeo) and analyzed along a coronal axis. Regions of interest (ROIs) were drawn on the CT image over tissues of interest, with 1 ROI drawn at every fourth coronal slice. After drawing ROIs, the remaining slices were interpolated with the use of OsirixMD's "generate missing ROIs" feature. The spleen and femur were drawn in their entirety, and samples of 3 lumbar

vertebrae were used for spinal bone marrow. For the (infarcted) myocardium, ROIs were drawn axially on the anterior wall of the left ventricle in every slice from the apex moving cranially to approximately three-fourths of the height of the left ventricle. For remote myocardium, ROIs were drawn axially on the left ventricle wall at the opposite side of the infarct. In noninfarcted animals, ROIs were drawn in the same locations. ROI mean standardized uptake values (SUVs) were calculated by transferring ROIs to the SUV-converted PET image. ROI SUVs of each organ were then exported to a CSV file, and SUVs were averaged for each organ.

Ex vivo gamma counting

Immediately after the PET scans, animals were euthanized and perfused with PBS, tissues of interest (remote myocardium, infarcted myocardium, corresponding myocardium of control animals, spleen, and femoral bone marrow) were collected and weighed in preweighed tubes. Radioactivity content was measured with the use of a Wizard2 2480 automatic gamma counter (Perkin Elmer). Tissue radioactivity concentration was calculated, decay corrected, and expressed as percentage of the injected dose per gram of tissue (%ID/g).

Flow cytometry

For flow cytometry analysis, blood was obtained by cardiac puncture and collected in an EDTA-coated tube. Mice were subsequently perfused through the left ventricle with 10 mL cold PBS. Femur and spleen were collected. The infarcted heart tissue was collected and weighed. In *Apoe*$^{-/-}$ mice, the aorta, from the aortic root to the iliac bifurcation, was also collected. Absolute cell counting was performed by adding CountBright beads (Invitrogen) to each sample and calculating the ratio of bead events to cell events. Data were acquired with an LSRFortessa flow cytometer (BD Biosciences) and were analyzed with the use of FlowJo v10.7.1.

Heart and aorta processing and analysis

The aorta was minced and digested by means of an enzymatic digestion solution containing liberase TH (4 U/mL; Roche), DNase I (40 U/mL; Sigma-Aldrich), and hyaluronidase (60 U/mL; Sigma-Aldrich) in PBS. Heart tissue was minced and digested with the use of an enzymatic digestion solution containing DNase I (60 U/mL), collagenase type I (450 U/mL), collagenase type XI (125 U/mL), and hyaluronidase (60 U/mL) (all from Sigma-Aldrich) in PBS. Aortas and heart tissues were incubated for 1 hour at 37 °C under agitation. Cells were filtered through a 70-µm cell strainer and washed with fluorescence-activated cell sorting (FACS) buffer (Dulbecco's PBS with 1% fetal calf serum, 0.5% bovine serum albumin, 0.1% NaN_3, and 1 mmol/L EDTA). Single-cell suspensions were stained with the following monoclonal antibodies: PE anti–mouse/human CD11b (clone M1/70, 1:200; BioLegend), PE-Cy7 anti–mouse F4/80 (clone BM8, 1:100; BioLegend), FITC anti–mouse Ly6C (clone AL-21, 1:400; BD Biosciences), BV510 anti–mouse CD45 (clone 30-F11, 1:200; BioLegend) and a lineage cocktail (Lin) containing eFluor 450 anti–mouse CD90.2 (clone 53-2.1, 1:200; eBioscience), eFluor 450 anti–mouse TER-119 (clone TER-119, 1:200; eBioscience), eFluor 450 anti–mouse NK-1.1 (clone PK136, 1:200; eBioscience), eFluor anti–mouse CD49b (clone DX5, 1:200; eBioscience), eFluor 450 anti-mouse/human CD45R/B220 (clone RA3-6B2, 1:200; eBioscience), eFluor 450 anti–mouse CD103 (clone 2E7, 1:200; eBioscience), and eFluor 450 anti–mouse Ly-6G (clone 1A8, 1:100; eBioscience); 10 µL DAPI was added for viability staining. CD11b+ cells were identified as $CD45^+$ $CD11b^+$, and $Lin.^-$ Monocytes were identified as CD45+, $CD11b^{high}$, $Lin^{-/low}$, and $Ly6C^{high/low}$. Neutrophils were identified as CD45+, $CD11b^{high}$, and Lin^+. Macrophages were identified as CD45+, $CD11b^{high}$, $Lin^{-/low}$, and $F4/80^{high}$.

Blood processing and analysis

Blood was incubated with red blood cell lysis buffer for 4 minutes and washed with FACS buffer; this was repeated twice more. Single-cell suspensions were stained with the following monoclonal antibodies: APC anti-CD115 (clone AFS98, 1:200; eBiosciences), PerCP-Cy5.5 anti-CD11b (clone M1/70, 1:200;

BioLegend), PE-Cy7 anti-Ly6C (clone Al-21, 1:200; BioLegend), eFluor 450 anti-Ly6G (clone 1A8, 1:100; eBioscience), anti-CD19 (clone 1D3, 1:400; BD Pharmingen) and anti-CD90.2 (clone 53-2.1, 1:400; BD Pharmingen); 10 µL DAPI was added for viability staining. $CD11b^+$ cells were identified as $CD11b^+$ and Lin^-. Neutrophils were identified as $CD11b^{high}$, $Lin^{-/low}$, $CD115^{low}$, and $Ly6G^{high}$. Monocytes were identified as $CD11b^{high}$, $Lin^{-/low}$, $CD115^{high}$, and $Ly6C^{high/low}$.

Progenitors and progenitor proliferation

For BrdU labeling, C57BL/6 mice were intraperitoneally injected with 1 mg BrdU (10 mg/mL in PBS) 2 days after myocardial infarction and euthanized 24 hours later. Bone marrow was flushed out of the femur with PBS, filtered through a 70-µm cell strainer, incubated with lysis buffer for 30 seconds, and washed with FACS buffer. Cells were stained with APC/Cy7 anti-CD48 (clone HM48-1, 1:80; BioLegend), PerCP/Cy5.5 anti-CD150 (clone TC15-12F12.2, 1:160; BioLegend), PE anti-CD117 (c-Kit, clone 2B8, 1:400; BioLegend), anti–Sca-1 (Ly6-A/E, clone E13-161.7, 1:160; BioLegend), and a lineage cocktail (1:10; BD Biosciences) containing anti-CD3**ε** (clone 500A2), anti-CD11b (clone M1/70), anti-CD45R/B220 (clone RA3-6B2), anti-Ly76 (clone TER-119), and anti-Ly6G/Ly6C (clone RB6-8C5). BrdU staining was performed with the use of the BrdU staining kit (BD FITC BrdU Flow Kit; Fisher Scientific), following the manufacturer's instructions. LSK cells were identified as Lin^-, $Sca\text{-}1^+$, and $c\text{-}Kit^+$.

Histology of aortic roots

Aortic roots were harvested from *Apoe*$^{-/-}$ mice, embedded in OCT (Sakura Finetek), and frozen. Sections 5 µm thick were stained with rat anti-MAC3 antibody (clone M3/84, 1:100; BD Biosciences) followed by a biotinylated antirat secondary antibody (1:300; Vector Laboratories). Vecta Stain ABC kit and ImmPact vector red (both from Vector Laboratories) were used for color development. Next, counterstaining with hematoxylin was carried out. Total plaque size and $mac3^+$ area were analyzed with the use of ImageJ

(v2.1.0/1.53c) by taking the average of 6 sections spaced ~30 µm apart, beginning at the base of the aortic root.

Statistics

Data are presented as mean ± SEM. Statistical analyses were performed with Prism 9 (GraphPad Software). First, normal distribution tests were carried out (d'Agostino and Pearson test, Anderson-Darling test, Shapiro-Wilk test, Kolmogorov-Smirnov test). Student's *t*-test for 2 groups or 1-way analysis of variance (ANOVA) for more than 2 groups was used if data passed the normal distribution tests. If data failed the normal distribution tests, the Mann-Whitney test for 2 groups or the Kruskal-Wallis test (uncorrected Dunn's test) for more than 2 groups was performed. We computed nonparametric Spearman correlations to evaluate the relation between tracer uptake in different tissues of interest. We used Pearson correlation coefficients for infarct ^{19}F-MRI TBR and LVEF. Survival evaluation was conducted by means of simple Kaplan-Meier analysis. Values of $P < 0.05$ were considered to be significant. Statistical tests and animal numbers for each graph are specified in the figure legends.

Sources of funding

This work was supported by National Institute of Health grants R01HL143814 (to Dr Fayad), P01HL131478 (Drs Fayad and Mulder), P41EB025815 (Drs Liu and Gropler), R35HL145212 (Dr Liu), and R35HL139598 (Dr Nahrendorf) and award K22CA226040 (Dr Rashidian). This work was also supported by an Innovation Research Fund Basic Research Award from the Dana-Farber Cancer Institute (Dr Rashidian). Dr Maier was supported by Deutsche Forschungsgemeinschaft grants (MA 7059/1 and MA 7059/3-1) and is part of SFB1425 funded by the Deutsche Forschungsgemeinschaft (project no. 422681845).

Competing interests

All other authors have reported that they have no relationships relevant to the contents of this paper to disclose.

References

1.Swirski F.K., Nahrendorf M., Etzrodt M., et al. Identification of splenic reservoir monocytes and their deployment to inflammatory sites. Science. 2009;325:612–616. doi: 10.1126/science.1175202.

2.van der Laan A.M., Ter Horst E.N., Delewi R., et al. Monocyte subset accumulation in the human heart following acute myocardial infarction and the role of the spleen as monocyte reservoir. Eur Heart J. 2014;35:376–385. doi: 10.1093/eurheartj/eht331.

3.Swirski F.K., Nahrendorf M. Leukocyte behavior in atherosclerosis, myocardial infarction, and heart failure. Science. 2013;339:161–166. doi: 10.1126/science.1230719.

4.Panizzi P., Swirski F.K., Figueiredo J.L., et al. Impaired infarct healing in atherosclerotic mice with Ly-6Chi monocytosis. J Am Coll Cardiol. 2010;55:1629–1638. doi: 10.1016/j.jacc.2009.08.089.

5.Dutta P., Courties G., Wei Y., et al. Myocardial infarction accelerates atherosclerosis. Nature. 2012;487:325–329. doi: 10.1038/nature11260.

6.Lavine K.J., Pinto A.R., Epelman S., et al. The macrophage in cardiac homeostasis and disease: JACC macrophage in CVD series (part 4) J Am Coll Cardiol. 2018;72:2213–2230. doi: 10.1016/j.jacc.2018.08.2149.

7.Yellon D.M., Hausenloy D.J. Myocardial reperfusion injury. N Engl J Med. 2007;357:1121–1135. doi: 10.1056/NEJMra071667.

8.Fayad Z.A., Swirski F.K., Calcagno C., Robbins C.S., Mulder W., Kovacic J.C. Monocyte and macrophage dynamics in the cardiovascular system: JACC macrophage in CVD series (part 3) J Am Coll Cardiol. 2018;72:2198–2212. doi: 10.1016/j.jacc.2018.08.2150.

9.Nahrendorf M., Frantz S., Swirski F.K., et al. Imaging systemic inflammatory networks in ischemic heart disease. J Am Coll Cardiol. 2015;65:1583–1591. doi: 10.1016/j.jacc.2015.02.034.

10.von Elverfeldt D., Maier A., Duerschmied D., et al. Dual-contrast molecular imaging allows noninvasive characterization of myocardial ischemia/reperfusion injury after coronary vessel occlusion in mice by magnetic resonance imaging. Circulation. 2014;130:676–687. doi: 10.1161/CIRCULATIONAHA.113.008157.

11.Tirotta I., Mastropietro A., Cordiglieri C., et al. A superfluorinated molecular probe for highly sensitive in vivo 19F-MRI. J Am Chem Soc. 2014;136:8524–8527. doi: 10.1021/ja503270n.

12.Kossatz S., Carney B., Schweitzer M., et al. Biomarker based PET imaging of diffuse intrinsic pontine glioma in mouse models. Cancer Res. 2017;77:2112–2123. doi: 10.1158/0008-5472.CAN-16-2850.

13.Priem B., van Leent M.M.T., Teunissen A.J.P., et al. Trained immunity-promoting nanobiologic therapy suppresses tumor growth and potentiates checkpoint inhibition. Cell. 2020;183:786–801.e19. doi: 10.1016/j.cell.2020.09.059.

14.Liu Y., Li W., Luehmann H.P., et al. Noninvasive imaging of CCR2+ cells in

ischemia-reperfusion injury after lung transplantation. Am J Transplant. 2016;16:3016–3023. doi: 10.1111/ajt.13907.

15.Heo G.S., Kopecky B., Sultan D., et al. Molecular imaging visualizes recruitment of inflammatory monocytes and macrophages to the injured heart. Circ Res. 2019;124:881–890. doi: 10.1161/CIRCRESAHA.118.314030.

16.Heo G.S., Bajpai G., Li W., et al. Targeted PET imaging of chemokine receptor 2–positive monocytes and macrophages in the injured heart. J Nucl Med. 2021;62:111–114. doi: 10.2967/jnumed.120.244673.

17.Pluijmert N.J., Bart C.I., Bax W.H., Quax P.H.A., Atsma D.E. Effects on cardiac function, remodeling and inflammation following myocardial ischemia-reperfusion injury or unreperfused myocardial infarction in hypercholesterolemic APOE∗3-Leiden mice. Sci Rep. 2020;10 doi: 10.1038/s41598-020-73608-w.

18.Michael L.H., Ballantyne C.M., Zachariah J.P., et al. Myocardial infarction and remodeling in mice: effect of reperfusion. Am J Physiol. 1999;277:H660–H668. doi: 10.1152/ajpheart.1999.277.2.H660.

19.de Celle T., Cleutjens J.P., Blankesteijn W.M., Debets J.J., Smits J.F., Janssen B.J. Long-term structural and functional consequences of cardiac ischaemia-reperfusion injury in vivo in mice. Exp Physiol. 2004;89:605–615. doi: 10.1113/expphysiol.2004.027649.

20.Mulder W.J.M., van Leent M.M.T., Lameijer M., Fisher E.A., Fayad Z.A., Pérez-Medina C. High-density lipoprotein nanobiologics for precision medicine. Acc Chem Res. 2018;51:127–137. doi: 10.1021/acs.accounts.7b00339.

21.Flögel U., Ding Z., Hardung H., et al. In vivo monitoring of inflammation after cardiac and cerebral ischemia by fluorine magnetic resonance imaging. Circulation. 2008;118:140–148. doi: 10.1161/CIRCULATIONAHA.107.737890.

22.Senders M.L., Meerwaldt A.E., van Leent M.M.T., et al. Probing myeloid cell dynamics in ischaemic heart disease by nanotracer hot-spot imaging. Nat Nanotechnol. 2020;1:398–405. doi: 10.1038/s41565-020-0642-4.

23.Schoormans J., Calcagno C., Daal M.R.R., et al. An iterative sparse deconvolution method for simultaneous multicolor 19F-MRI of multiple contrast agents. Magn Reson Med. 2020;83:228–239. doi: 10.1002/mrm.27926.

24.Rashidian M., Ingram J.R., Dougan M., et al. Predicting the response to CTLA-4 blockade by longitudinal noninvasive monitoring of CD8 T cells. J Exp Med. 2017;214:2243–2255. doi: 10.1084/jem.20161950.

25.Teunissen A.J.P., Abousaway O.B., Munitz J., et al. Employing nanobodies for immune landscape profiling by PET imaging in mice. STAR Protoc. 2021;2 doi: 10.1016/j.xpro.2021.100434.

26.Rashidian M., Keliher E.J., Bilate A.M., et al. Noninvasive imaging of immune responses. Proc Natl Acad Sci U S A. 2015;112:6146–6151. doi: 10.1073/pnas.1502609112.

27.Rashidian M., LaFleur M.W., Verschoor V.L., et al. Immuno-PET identifies the myeloid compartment as a key contributor to the outcome of the antitumor response under PD-1 blockade. Proc Natl Acad Sci U S A. 2019;116:16971–16980. doi: 10.1073/pnas.1905005116.

28.Tsou C.-L., Peters W., Si Y., et al. Critical roles for CCR2 and MCP-3 in monocyte mobilization from bone marrow and recruitment to inflammatory sites. J Clin Invest. 2007;117:902–909. doi: 10.1172/JCI29919.

29.Liu Y., Gunsten S.P., Sultan D.H., et al. PET-based imaging of chemokine receptor 2 in experimental and disease-related lung inflammation. Radiology. 2017;283:758–768. doi: 10.1148/radiol.2016161409.

30.English S.J., Sastriques S.E., Detering L., et al. CCR2 positron emission tomography for the assessment of abdominal aortic aneurysm inflammation and rupture prediction. Circ Cardiovasc Imaging. 2020;13 doi: 10.1161/CIRCIMAGING.119.009889.

31.Brody S.L., Gunsten S.P., Luehmann H.P., et al. Chemokine receptor 2–targeted molecular imaging in pulmonary fibrosis. a clinical trial. Am J Respir Crit Care Med. 2021;203:78–89. doi: 10.1164/rccm.202004-1132OC.

32.Dutta P., Sager H.B., Stengel K.R., et al. Myocardial infarction activates CCR2+ hematopoietic stem and progenitor cells. Cell Stem Cell. 2015;16:477–487. doi: 10.1016/j.stem.2015.04.008.

33.Leuschner F., Rauch P.J., Ueno T., et al. Rapid monocyte kinetics in acute myocardial infarction are sustained by extramedullary monocytopoiesis. J Exp Med. 2012;209:123–137. doi: 10.1084/jem.20111009.

34.van der Valk F.M., Kuijk C., Verweij S.L., et al. Increased haematopoietic activity in patients with atherosclerosis. Eur Heart J. 2017;38:425–432. doi: 10.1093/eurheartj/ehw246.

35.Emami H., Singh P., MacNabb M., et al. Splenic metabolic activity predicts risk of future cardiovascular events: demonstration of a cardiosplenic axis in humans. J Am Coll Cardiol Img. 2015;8:121–130. doi: 10.1016/j.jcmg.2014.10.009.

36.Devesa A., obo-González M., Martínez-Milla J., et al. Bone marrow activation in response to metabolic syndrome and early atherosclerosis. Eur Heart J. 2022;43:1809–1828. doi: 10.1093/eurheartj/ehac102.

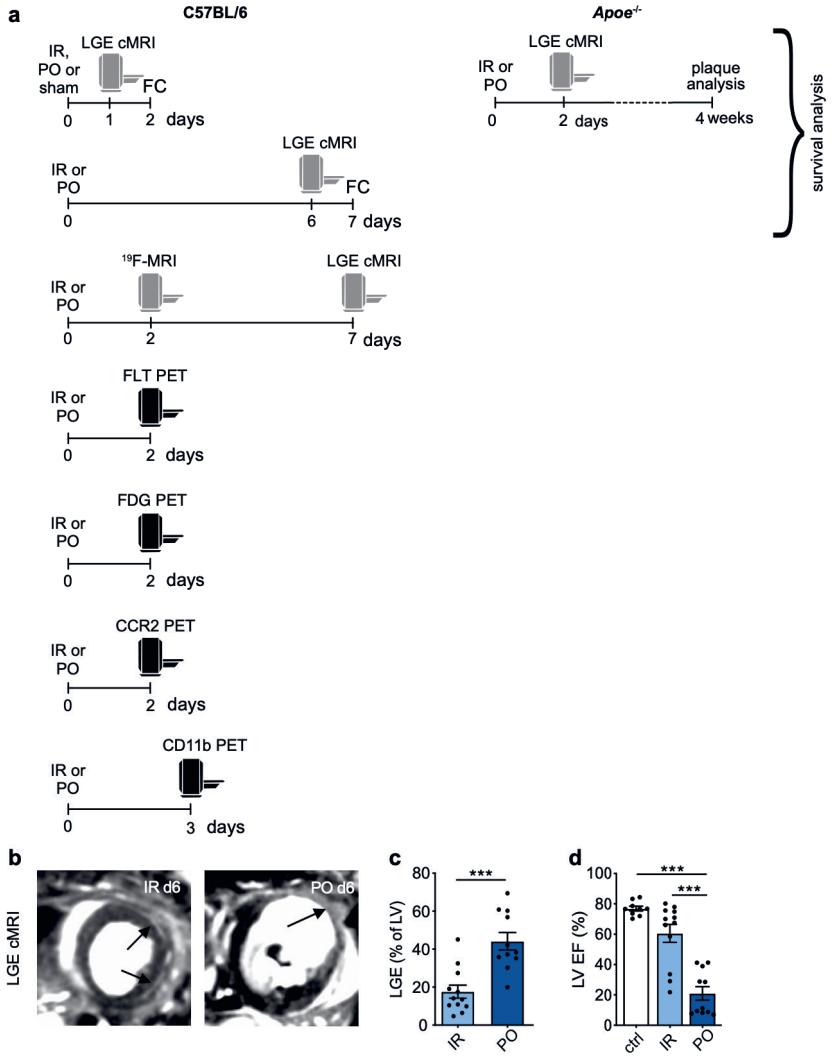
37.Ye Y.-X., Calcagno C., Binderup T., et al. Imaging macrophage and hematopoietic progenitor proliferation in atherosclerosis. Circ Res. 2015;117:835–845. doi: 10.1161/CIRCRESAHA.115.307024.

38.Berland L., Kim L., Abousaway O., et al. Nanobodies for medical imaging: about ready for prime time? Biomolecules. 2021;11:637. doi: 10.3390/biom11050637.

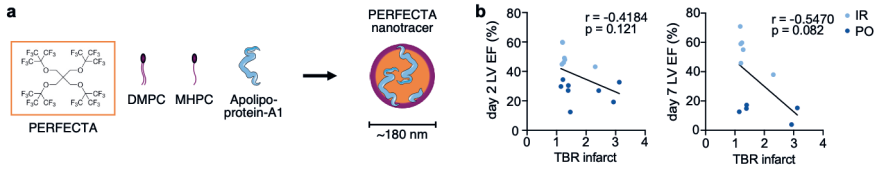
39.Spahn D.R. Blood substitutes. Artificial oxygen carriers: perfluorocarbon emulsions. Crit Care. 1999;3:R93–R97. doi: 10.1186/cc364.

40.Nienhaus F., Colley D., Jahn A., et al. Phagocytosis of a PFOB-nanoemulsion for 19F magnetic resonance imaging: first results in monocytes of patients with stable coronary artery disease and ST-elevation myocardial infarction. Molecules. 2019;24:2058. doi: 10.3390/molecules24112058.

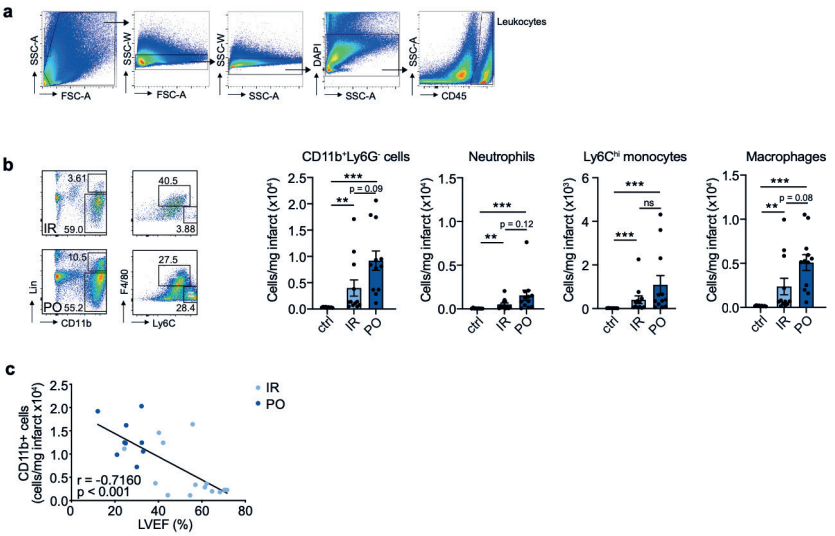
Supplementary Information



Supplementary figure 1. Study protocol and cardiac MRI 6 days after myocardial infarction. A) Study protocol for C57BL/6 and Apoe$^{-/-}$ mice and each imaging modality/tracer. FC = Flow cytometry. B) Representative LGE cMR images on day 6 after myocardial infarction; arrows indicate LGE area. C) LGE area in % of the left ventricle 6 days after surgery (n = 9-14, $p < 0.001$, two-tailed Student's t-test). D) Left ventricular ejection fraction (LVEF) 6 days after surgery (n = 9-12, $p < 0.001$ for ctrl vs. PO and IR vs. PO, $p = 0.058$ for ctrl. vs. IR, one-way ANOVA). Data are presented as mean +/- standard error of the mean, unless otherwise specified. Symbols used are specified as *$p < 0.05$, **$p < 0.01$ and ***$p < 0.001$.

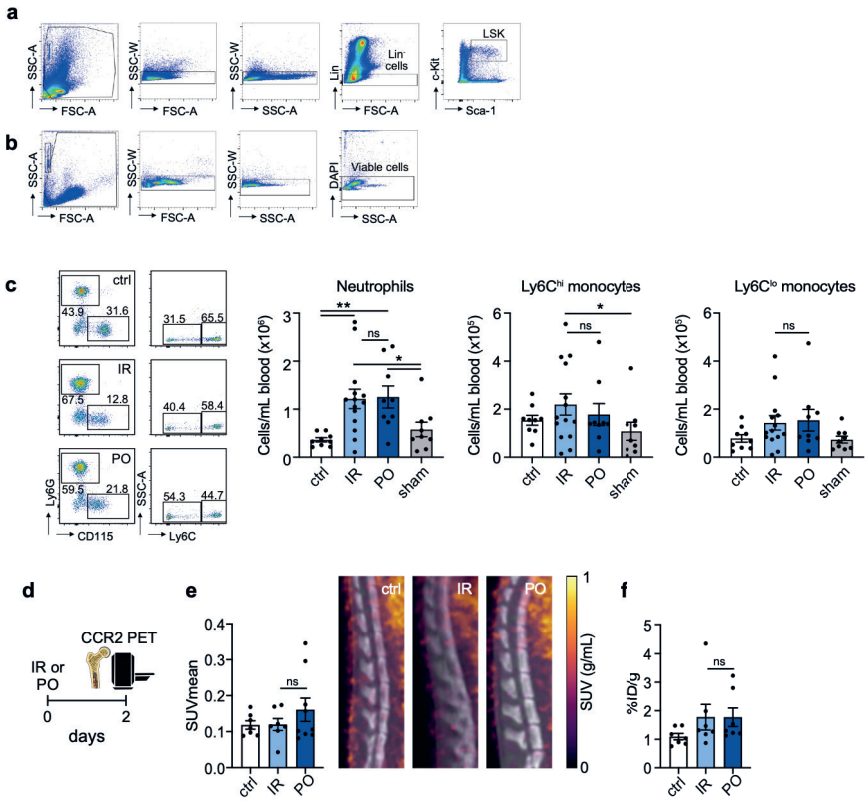


Supplementary figure 2. ^{19}F-MRI nanotracer and ^{19}F infarct/LVEF correlations A) Components and schematic representation of the PERFECTA nanotracer. The nanotracer consists of PERFECTA, DMPC, MHPC and Apolipoprotein A1. PERFECTA, 1,3-bis[[1,1,1,3,3,3-hexafluoro-2-(trifluoromethyl)propan-2-yl]oxy]-2,2-bis[[1,1,1,3,3,3-hexafluoro-2-2(trifluoromethyl)propan-2-yl]oxymethyl]propane; DMPC, 1,2-Dimyristoyl-*sn*-glycero-3-phosphocholine; MHPC, 1-myristoyl-2-hydroxy-*sn*-glycero-3-phosphocholine. B) PERFECTA target-to-background-ratio (TBR) in the infarct and left ventricular ejection fraction (LVEF) are inversely correlated on day 2 and 7 after IR/PO.



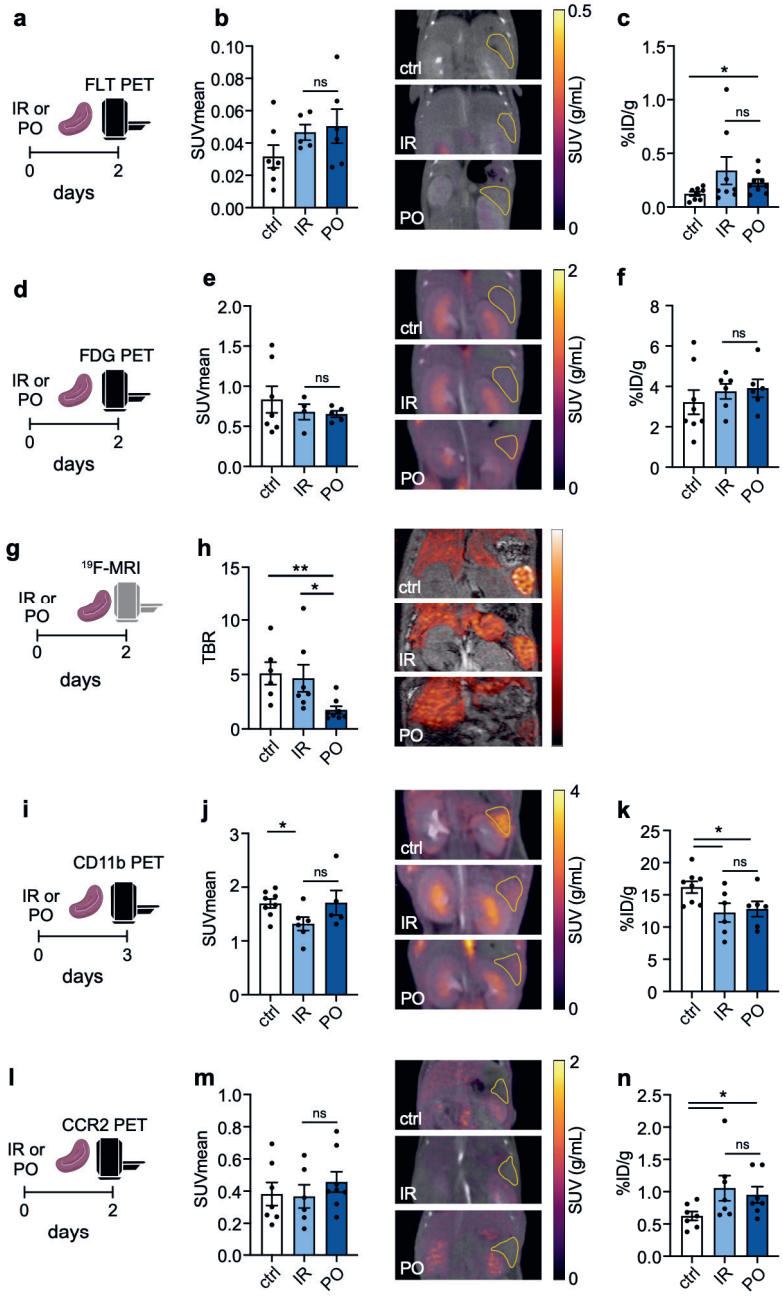
Supplementary figure 3. Myeloid cell numbers in the ischemic myocardium and correlation with left ventricle ejection fraction. A) The flow cytometry gating strategy used to identify leukocytes in the heart (infarct zone) and aorta. B) Representative flow cytometry plots of the IR and PO infarct areas 7 days after myocardial infarction. IR upper row, PO lower row. Following CD11b$^+$/Ly6G$^-$ (n = 9-12, p = 0.002 ctrl. vs. IR; p < 0.001 ctrl. vs. PO; p = 0.091 IR vs. PO, Kruskal-Wallis test), neutrophil (n = 9-12, p = 0.007 ctrl. vs. IR; p < 0.001 ctrl. vs. PO; p = 0.12 IR vs. PO, Kruskal-Wallis test), Ly6C^{hi} monocytes (n = 9-12, p < 0.001 ctrl. vs. IR; p < 0.001 ctrl. vs. PO; p = 0.28 IR vs. PO, Kruskal-Wallis test) and macrophage numbers (n = 9-12, p = 0.005 ctrl. vs. IR; p < 0.001 ctrl. vs. PO; p = 0.080 IR vs. PO, Kruskal-Wallis test). C) CD11b$^+$ cell numbers in the

infarct and left ventricular ejection fraction (LVEF) are inversely correlated on day 2 after IR/PO. Data are presented as mean +/- standard error of the mean, unless otherwise specified. Symbols used are specified as *p < 0.05, **p < 0.01 and ***p < 0.001.



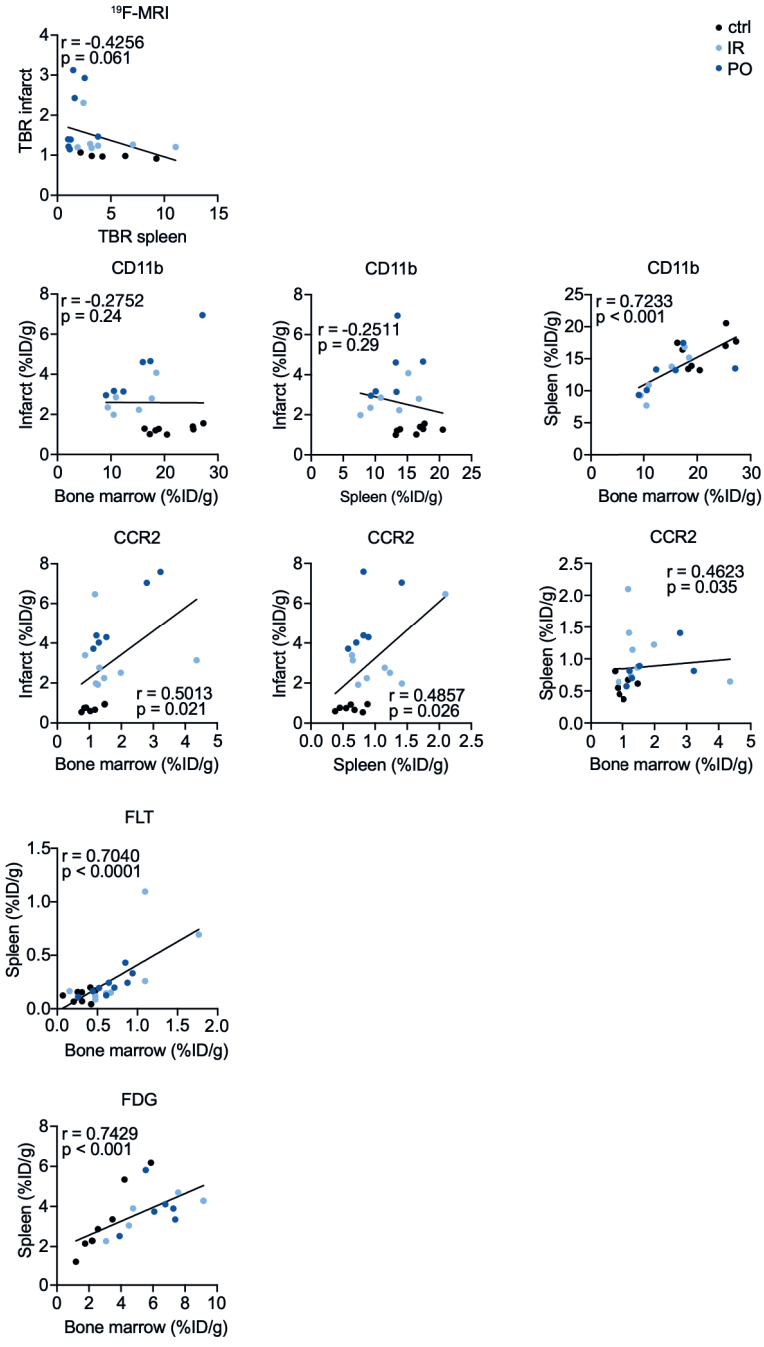
Supplementary figure 4. Blood myeloid cell numbers after IR/PO and CCR2 imaging of the bone marrow. A) Flow cytometry gating strategy for bone marrow progenitors. B) Gating strategy for viable cells in the blood. C) Neutrophils (n = 9-14, p = 0.002 ctrl. vs. IR; p = 0.003 ctrl. vs. PO; p = 0.39 ctrl. vs. sham; p = 0.87 IR vs. PO; p = 0.027 IR vs. sham; p = 0.032 PO vs. sham, Kruskal-Wallis test), Ly6C^{hi} monocytes (n = 9-14, p = 0.77 ctrl. vs. IR; p = 0.62 ctrl. vs. PO; p = 0.070 ctrl. vs. sham; p = 0.40 IR vs. PO; p = 0.021 IR vs. sham; p = 0.19 PO vs. sham, Kruskal-Wallis test) and Ly6C^{lo} monocytes (n = 9-14, p = 0.13 ctrl. vs. IR; p = 0.16 ctrl. vs. PO; p = 0.81 ctrl. vs. sham; p = 0.96 IR vs. PO; p = 0.076 IR vs. sham; p = 0.098 PO vs. sham, Kruskal-Wallis test) in the blood 2 days after myocardial infarction compared to naïve controls and sham controls. D) ^{64}Cu-DOTA-ECL1i PET/CT of the bone marrow was performed 2 days after IR/PO surgery. The scan was conducted during the first 60 minutes after injection. E) Quantification of ^{64}Cu-DOTA-ECL1i signal in the lumbar vertebrae and representative CCR2 PET images. The CCR2 tracer bone

marrow signal did not show significant differences between mice with IR/PO and controls (n = 7 – 9, p = 0.58 ctrl. vs. IR; p = 0.54 ctrl. vs. PO; p = 0.98 IR vs. PO, Kruskal-Wallis test). F) *Ex vivo* gamma counting of CCR2 tracer uptake in the bone marrow (n = 7, p = 0.12 ctrl. vs. IR; p = 0.070 ctrl. vs. PO; p = 0.80 IR vs. PO, Kruskal-Wallis test). Data are presented as mean +/- standard error of the mean, unless otherwise specified. Symbols used are specified as *p < 0.05, **p < 0.01 and ***p < 0.001.

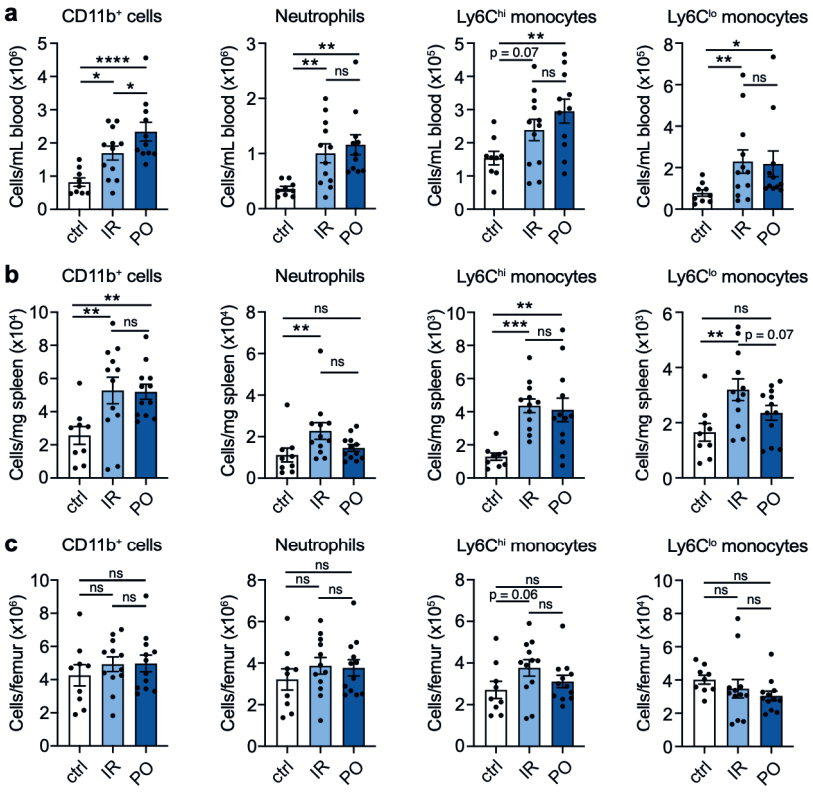


Supplementary figure 5. Multiparametric imaging of the spleen following ischemia-reperfusion and permanent LAD occlusion. A) ^{18}F-FLT PET/CT was performed 2 days after IR/PO surgery;

^{18}F-FLT was injected 90 minutes prior the scan. B) Quantification of ^{18}F-FLT signal in the spleen and representative ^{18}F-FLT PET/CT images ($p = 0.15$ ctrl. vs. IR; $p = 0.12$ ctrl. vs. PO; $p = 0.97$ IR vs. PO). C) *Ex vivo* gamma counting of ^{18}F-FLT uptake in the spleen ($n = 8$-9, $p = 0.14$ ctrl. vs. IR; $p = 0.042$ ctrl. vs. PO; $p = 0.62$ IR vs. PO, Kruskal-Wallis test). D) ^{18}F-FDG PET/CT was performed 2 days after IR/PO surgery. ^{18}F-FDG was injected 30 minutes before imaging. E) Quantification of ^{18}F-FDG signal in the spleen and representative ^{18}F-FDG PET/CT images. F) *Ex vivo* gamma counting of ^{18}F-FDG uptake in the spleen. Both showing no significant differences. G) ^{19}F-MRI of the spleen 2 days after IR/PO surgery and 1 day after PERFECTA nanotracer injection. H) Quantification of fluorine uptake in the spleen, expressed as target-to-background ratio ($n = 6$-8, $p = 0.58$ ctr. vs. IR; $p = 0.004$ ctrl. vs. PO; $p = 0.015$ IR vs. PO, Kruskal-Wallis test), and representative fused ^{19}F-MR images. I) ^{89}Zr-CD11b nanobody PET/CT was performed 3 days after IR/PO surgery. The nanobody was injected 2 days after surgery. J) Quantification of ^{89}Zr-CD11b nanobody signal in the spleen ($n = 5$-8, $p = 0.020$ ctrl. vs. IR; $p = 0.54$ ctr. vs. PO; $p = 0.13$ IR vs. PO, Kruskal-Wallis test) and representative ^{89}Zr-CD11b nanobody PET/CT images. K) *Ex vivo* gamma counting of ^{89}Zr-CD11b nanobody uptake in the spleen ($n = 6$-8, $p = 0.041$ ctrl. vs. IR; $p = 0.046$ ctrl. vs. PO; $p = 0.96$ IR vs. PO, Kruskal-Wallis test). L) ^{64}Cu-DOTA-ECL1i PET/CT of the spleen was performed 2 days after IR/PO surgery, during the first 60 minutes after injection. M) Quantification of CCR2 tracer signal in the spleen and representative ^{64}Cu-DOTA-ECL1i PET/CT images. N) *Ex vivo* gamma counting of CCR2 tracer uptake the spleen ($n = 7$, $p = 0.039$ ctrl. vs. IR; $p = 0.039$ ctrl. vs. PO; $p > 0.99$ IR vs. PO, Kruskal-Wallis test). Data are presented as mean +/- standard error of mean, unless otherwise specified. Symbols used are specified as $*p < 0.05$, $**p < 0.01$ and $***p < 0.001$.

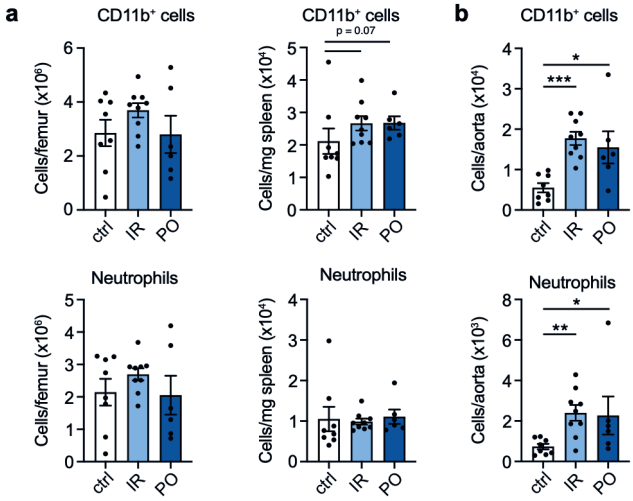

19F-MRI
r = -0.4256
p = 0.061
TBR infarct
TBR spleen
ctrl
IR
PO
CD11b
r = -0.2752
p = 0.24
Infarct (%ID/g)
Bone marrow (%ID/g)
CD11b
r = -0.2511
p = 0.29
Infarct (%ID/g)
Spleen (%ID/g)
CD11b
r = 0.7233
p < 0.001
Spleen (%ID/g)
Bone marrow (%ID/g)
CCR2
r = 0.5013
p = 0.021
Infarct (%ID/g)
Bone marrow (%ID/g)
CCR2
r = 0.4857
p = 0.026
Infarct (%ID/g)
Spleen (%ID/g)
CCR2
r = 0.4623
p = 0.035
Spleen (%ID/g)
Bone marrow (%ID/g)
FLT
r = 0.7040
p < 0.0001
Spleen (%ID/g)
Bone marrow (%ID/g)
FDG
r = 0.7429
p < 0.001
Spleen (%ID/g)
Bone marrow (%ID/g)

Supplementary figure 6. Correlations between tracer uptake in tissues of interest. Spearman's correlations between tracer uptake in the infarct, spleen and/or bone marrow. For ^{19}F-MRI, *in vivo* target-to-background ratios were used. For the PET tracers, *ex vivo* gamma counting data were used.



Supplementary figure 7. Myeloid cell numbers by flow cytometry of the blood, spleen and bone marrow 7 days after IR/PO. A) Blood. CD11b$^+$/Ly6G$^-$ cells (n = 9-12, p = 0.012 ctrl. vs. IR; p < 0.001 ctrl. vs. PO; p = 0.046 IR vs. PO, one-way ANOVA), Neutrophils (n = 9-12, p = 0.008 ctrl. vs. IR; p = 0.002 ctrl. vs. PO; p = 0.47 IR vs. PO, one-way ANOVA), Ly6C^{hi} monocytes (n = 9-12, p = 0.072 ctrl. vs. IR; p = 0.005 ctrl. vs. PO; p = 0.20 IR vs. PO, one-way ANOVA) and Ly6C^{lo} monocytes (n = 9-12, p = 0.010 ctrl. vs. IR; p = 0.016 ctrl. vs. PO; p = 0.90 IR vs. PO, Kruskal-Wallis test). B) Spleen. CD11b$^+$/Ly6G$^-$ cells (n = 9-12, p = 0.007 ctrl. vs. IR; p = 0.008 ctrl. vs. PO; p = 0.92 IR vs. PO, one-way ANOVA), Neutrophils (n = 9-12, p = 0.005 ctrl. vs. IR; p = 0.17 ctrl. vs. PO; p = 0.13 IR vs. PO, Kruskal-Wallis test), Ly6C^{hi} monocytes (n = 9-12, p < 0.001 ctrl. vs. IR; p = 0.001 ctrl. vs. PO; p = 0.73 IR vs. PO, one-way ANOVA) and Ly6C^{lo} monocytes (n = 9-12, p = 0.004 ctrl. vs. IR; p = 0.16 ctrl. vs. PO; p = 0.074 IR vs. PO, one-way ANOVA). C) Bone marrow. CD11b$^+$/Ly6G$^-$ cells (n = 9-12, p = 0.39 ctrl. vs. IR; p = 0.36 ctrl. vs. PO; p = 0.95 IR vs. PO, one-way ANOVA), Neutrophils (n = 9-12, p = 0.25 ctrl. vs. IR; p = 0.35 ctrl. vs. PO; p = 0.82 IR vs. PO,

Kruskal-Wallis test), Ly6C^{hi} monocytes (n = 9-12, p = 0.059 ctrl. vs. IR; p = 0.46 ctrl. vs. PO; p = 0.20 IR vs. PO, one-way ANOVA) and Ly6C^{lo} monocytes (n = 9-12, p = 0.37 ctrl. vs. IR; p = 0.12 ctrl. vs. PO; p = 0.45 IR vs. PO, one-way ANOVA). Data are presented as mean +/- standard error of mean, unless otherwise specified. Symbols used are specified as *p < 0.05, **p < 0.01 and ***p < 0.001.



Supplementary figure 8. Myeloid cell numbers in the bone marrow, spleen and aorta of *Apoe*$^{-/-}$ mice 4 weeks after IR/PO. A) Flow cytometry analysis of CD11b^{+}/Ly6G^{-} cells and neutrophils in the femur and spleen (n = 6-9, p = 0.063 ctrl. vs. IR; p = 0.071 ctrl. vs. PO for spleen CD11b^{+} cells, Kruskal-Wallis test) of *Apoe*$^{-/-}$ mice 4 weeks after IR/PO surgery. B) CD11b^{+}/Ly6G^{-} (n = 6-9, p < 0.001 ctrl. vs. IR; p = 0.018 ctrl. vs. PO; p = 0.34 IR vs. PO, Kruskal-Wallis test) and neutrophil (n = 6-9, p = 0.002 ctrl. vs. IR; p = 0.044 ctrl. vs. PO; p = 0.45 IR vs. PO, Kruskal-Wallis test) counts from the aortas of *Apoe*$^{-/-}$ mice 4 weeks after IR/PO surgery. Data are presented as mean +/- standard error of mean, unless otherwise specified. Symbols used are specified as *p < 0.05.

Part 2

New imaging probes for cardiovascular disease imaging



4

Imaging cardiovascular and lung macrophages with the positron emission tomography sensor ^{64}Cu-macrin in mice, rabbits, and pigs

Published in Circula0on Cardiovascular Imaging, 2020.

Nahrendorf, M., Hoyer, F.F., Meerwaldt, A.E., van Leent, M.M.T., Senders, M.L., Calcagno, C., Robson, P.M., Soultanidis, G., Pérez-Medina, C., Teunissen, A.J.P., **Toner, Y.C.**, Ishikawa, K., Fish, K., Sakurai, K., van Leeuwen, E.M., Klein, E.D., Sofias, A.M., Reiner, T., Rohde, D., Aguirre, A.D., Wojtkiewicz, G., Schmidt, S., Iwamoto, Y., Izquierdo-Garcia, D., Caravan, P., Swirski, F.K., Weissleder, R., Mulder, W.J.M.

Toner, Y.C. helped plan and perform the rabbit and pig experiments, including PET/MR imaging acquisition, tissue dissection, sample preparation for TTC staining, histology, autoradiography and biodistribution. In addition, she was responsible for the pneumonia model in mice and subsequent IVIS imaging acquisition. She also helped with the myocardial infarct surgeries in rabbits.

Abstract

Background

Macrophages, innate immune cells that reside in all organs, defend the host against infection and injury. In the heart and vasculature, inflammatory macrophages also enhance tissue damage and propel cardiovascular diseases.

Methods

We here use *in vivo* positron emission tomography (PET) imaging, flow cytometry and confocal microscopy to evaluate quantitative noninvasive assessment of cardiac, arterial and pulmonary macrophages using the nanotracer ^{64}Cu-Macrin, a 20 nm spherical dextran nanoparticle assembled from non-toxic polyglucose.

Results

PET imaging using ^{64}Cu-Macrin faithfully reported accumulation of macrophages in the heart and lung of mice with myocardial infarction, sepsis or pneumonia. Flow cytometry and confocal microscopy detected the near-infrared fluorescent version of the nanoparticle (^{VT680}Macrin) primarily in tissue macrophages. In 5-day-old mice, ^{64}Cu-Macrin PET imaging quantified physiologically more numerous cardiac macrophages. Upon intravenous administration of ^{64}Cu-Macrin in rabbits and pigs, we detected heightened macrophage numbers in the infarcted myocardium, inflamed lung regions and atherosclerotic plaques using a clinical PET/magnetic resonance imaging (MRI) scanner. Toxicity studies in rats and human dosimetry estimates suggest that ^{64}Cu-Macrin is safe for use in humans.

Conclusions

Taken together, these results indicate ^{64}Cu-Macrin could serve as a facile PET nanotracer to survey spatiotemporal macrophage dynamics during various physiological and pathological conditions. ^{64}Cu-Macrin PET imaging could stage inflammatory cardiovascular disease activity, assist disease management and serve as an imaging biomarker for emerging macrophage-targeted therapeutics.

Keywords: heart; macrophages; myocardial infarction; nanoparticles; pneumonia.

Abbreviations

CLP	cecal ligation and puncture
PET	positron emission tomography
MRI	magnetic resonance imaging
CT	X-ray computed tomography
TTC	triphenyltetrazolium chloride
GFP	green fluorescent protein
MFI	mean fluorescent intensity
SUV	standard uptake value

Clinical summary

Ushered in by high-dimensional diagnostic tools such as flow cytometry and single cell RNA-sequencing, the knowledge on the immune system's role in homeostasis and disease is rapidly expanding. The last decade has seen a considerable expansion of known immune cell subsets and their functions. Cardiovascular organs and cardiovascular disease are no exemption: for instance, we now understand that not only atherosclerotic plaques or ischemic, inflamed myocardium contains leukocytes, but that these cells are present in the steady-state heart and participate in organ development, homeostatic functions such as metabolism and conduction, tissue regeneration, matrix remodeling and recovery from disease. The field is on the verge of translating this insight into new cures; however, clinical tools to monitor the immune system, and more specifically immune cells, are still mostly limited to counting them in blood samples. This is a severe limitation as circulating immune cells do not necessarily correlate with the numbers and phenotypes of cells residing in tissues. Organ biopsies are likewise limited given their invasiveness and inherent sampling errors. We here provide insight into PET imaging agent development targeting macrophages. Based on small biodegradable nanoparticles derivatized with either a PET isotope of a fluorochrome, we characterize the utility of Macrin nanoparticles in several physiological and pathological settings. Since macrophages are emerging as high-value therapeutic targets, we anticipate that the described quantitative imaging tools will catalyze drug development and clinical trials.

Introduction

Tissue macrophages pursue heterogeneous functions[1,2] and populate organs with varying density in health and disease[3]. In the steady-state heart, arterial wall, lung and brain, among other organs, these cells suppress inflammation and contribute to tissue homeostasis. After sterile or infectious injuries, macrophages initiate and amplify immune responses to limit tissue damage and intercept bacterial intruders. While many macrophage functions protect the host, exuberant inflammatory actions and macrophage oversupply may compromise cardiovascular health[3].

Expanding macrophage populations are a characteristic system-wide feature in inflammatory cardiovascular conditions. At primary injury and remote disease sites[4], additional cells either derive from monocytes, i.e. they are recruited from hematopoietic organs, or they arise through local proliferation from macrophages that resided in the previously healthy tissue. Both processes co-exist in atherosclerotic plaque and in diseased myocardium, increasing macrophage numbers by orders of magnitude[3]. If macrophages become too abundant, they propagate inflammatory tissue destruction, cardiovascular disease progression and poor clinical outcomes. For instance, macrophage oversupply in acute myocardial infarction and in the remote myocardium leads to heart failure in mice[5], which is paralleled by the clinical association between systemic monocyte numbers and cardiovascular events[6–8]. Macrophages of varying phenotypes are also involved in heart regeneration; emerging data indicate that these cells support enhanced healing after myocardial infarction in newborn mice [9]. Finally, macrophages also sense remote injury and determine host resilience against infection. These functions may either propagate inflammatory complications and multi-organ failure or support elimination of bacteria[4].

For these reasons, macrophages and their inflammatory products are being investigated as highly promising therapeutic targets. One obstacle in this discovery process is the lack of noninvasive assays to quantify tissue

macrophages. Since macrophages rely on not only recruitment from the blood stream but also local proliferation in the tissue, circulating monocyte numbers are not always a suitable surrogate for tissue macrophage content. Biopsies are more reliable but only report on small specimen rather than entire organ systems, giving rise to sampling error. Biopsy of the myocardium and atherosclerotic plaques is not commonly pursued due to the threat of complications. Therefore, there is an unmet need for a noninvasive imaging assays that quantify tissue macrophages across the body.

Molecularly targeted imaging agents contribute to our insight into molecular and cellular mechanisms of inflammatory diseases, including coronary heart disease. Although numerous molecular imaging agents targeting inflammatory cells have been developed and validated in small animals[10], only a few are currently in clinical use. For example, ^{18}FDG[11] and ^{68}Ga-pentixafor[12] were used in patients with acute myocardial infarction, reporting on glucose uptake and the presence of the chemokine receptor CXCR4, respectively. These two targets are tightly related to inflammation; however, they are not specific for macrophages. Some promising macrophage imaging agents, for instance targeting these cells' surface receptors[13, 14], are advancing through development; however, given the heterogeneity of macrophages, such strategies may not report on certain cell subsets that do not express the targets.

To assay macrophages non-invasively, we developed a macrophage sensor called Macrin. This 20 nm spherical nanoparticle evolved through several iterations of adjusting physico- and radio-chemical properties to optimize pharmacokinetics and targeting of macrophages. Here we explored the utility of the latest-generation material[15] to quantify macrophages in physiological settings as well as cardiovascular and pulmonary inflammation. We examined the feasibility of ^{64}Cu-Macrin PET macrophage imaging in a basket trial of small and large animals with clinically relevant heart disease but also in the heart of newborn mice and in pneumonia (Fig. 1A, Online Table I) to test the assay in physiological settings and pathologies with various causes and degrees of inflammation. These experiments revealed the

sensitivity and versatility of Macrin PET across inflammatory conditions. We further report that rodent toxicity studies and human radiation dose estimates suggest that Macrin is safe for first-in-human studies.

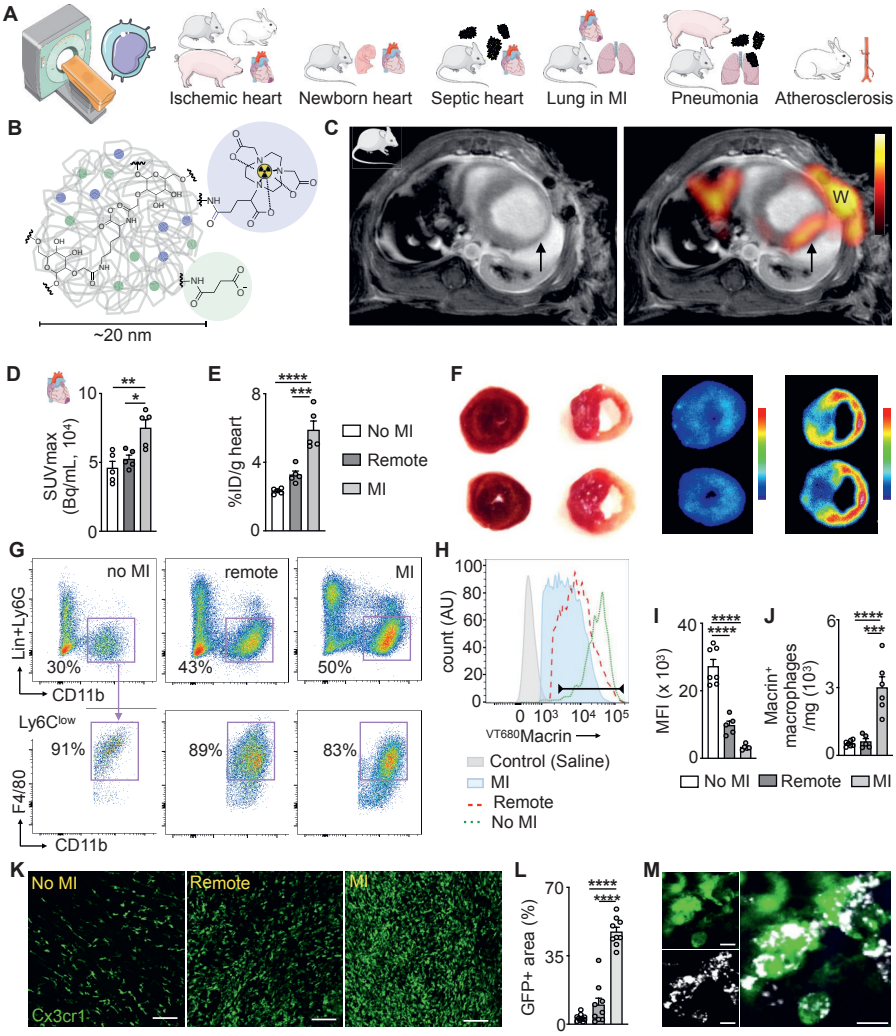


Figure 1. ^{64}Cu-Macrin PET imaging detects cardiac macrophage expansion following acute myocardial infarction in mice. A) Outline of macrophage imaging basket trial. B) Schematic view of ^{64}Cu-Macrin polyglucose nanoparticle. C) Short axis PET fused to MRI of mouse heart on day 5 after myocardial infarction (MI, arrow; W, surgical wound). Left image shows delayed enhancement MRI only, right is fused with PET. D) *In vivo* PET signal, calculated as SUVmax in naive controls (no MI) and in the infarct (MI) and non-infarcted myocardium of mice with MI

(remote). E) Macrin accumulation in heart tissue by *ex vivo* scintillation counting and expressed as a percent injected dose per gram tissue (%ID/g). F) TTC staining (left) and autoradiography (right) of mouse short axis rings from naive control and mouse with MI (right, infarct tissue is pale). G) Flow plots of cardiac macrophages from control mice and from remote and infarcted myocardium from mice with MI. Hearts were excised 24 h after IV injection of ^{VT680}Macrin. H) Histogram of ^{VT680}Macrin uptake by cardiac macrophages in saline-injected naive controls (shaded grey), control (no MI, dotted green line), ischemic myocardium (MI, red dashed line) and remote myocardium in mice with MI (shaded blue). I) ^{VT680}Macrin mean fluorescent intensity in cardiac macrophages and J) ^{VT680}Macrin^{+} macrophage numbers. K) Confocal microscopy of GFP expressing macrophages in Cx3cr1$^{GFP/+}$ mice on day 5 after MI (scale bar, 100 μm). L) Quantitation of GFP^{+} area in groups as depicted in **D**. M) High-magnification confocal image of ^{VT680}Macrin (grey) and green macrophages (scale bar, 10 μm). Data are mean ± SEM. **P*<0.05, ***P*<0.01, ****P*<0.001, *****P*<0.0001.

Results

Pharmacokinetic profile and biodistribution of ^{64}Cu-Macrin in mice, rabbits and pigs

We first recorded the *in vivo* biodistribution of ^{64}Cu-Macrin (Fig. 1B) in healthy C57BL/6J mice at 4 and 24 hours after intravenous administration. Representative PET images (Online Fig. IA) and signal quantification as SUV (Online Fig. IB) demonstrated ^{64}Cu-Macrin uptake in macrophage-rich organs of the mononuclear phagocyte system, i.e. liver and spleen, which was confirmed by *ex vivo* scintillation counting at 1, 4, 24 and 48 hours after ^{64}Cu-Macrin injection (Online Table II). Of note, low accumulation was detected in the brain (0.27 % injected dose/g) and bone (2.78 % injected dose/g) at 24 hours post injection. 50.5% of the injected ^{64}Cu-Macrin dose was detected in the kidneys, possibly due to renal excretion of the small-sized particles. The remaining whole-body radioactivity was 12.01% of the injected dose 24 hours post injection. The blood activity and the heart-to-blood signal ratio (Online Fig. II) indicated that 24 hours after injection is a suitable imaging time point. ^{64}Cu-Macrin pharmacokinetics in rabbits showed a blood half-life of 45.1±24.6 minutes based on a two-phase exponential decay model (Online Fig. IIIA). In rabbits and pigs, we likewise observed high ^{64}Cu-Macrin uptake in macrophage-rich organs such as liver and spleen (Online Fig. IIIB-C).

In vivo quantitation of cardiac macrophages in mice, rabbits and pigs with acute myocardial infarction

Acute MI elicits a strong systemic inflammatory response that increases the number of macrophages robustly. Cardiac macrophages, in particular the inflammatory response after MI, are emerging therapeutic targets[2], which is why we examined whether cardiac macrophage fluctuations could be quantitatively assessed using ^{64}Cu-Macrin. ^{64}Cu-Macrin was intravenously administered to mice on day 4 after MI, and PET/CT and MRI was performed 24 hours post injection. ^{64}Cu-Macrin accumulated in the infarcted myocardium (Fig. 1C), which showed a 1.6-fold higher SUVs in comparison to control mice without MI (Fig. 1D). *Ex vivo* scintillation counting confirmed these data (Fig. 1E). Short axis rings of heart tissue were then processed for triphenyltetrazolium chloride (TTC) staining and autoradiography, confirming ^{64}Cu-Macrin accumulation in the infarcted area *ex vivo* (Fig. 1F). To assess whether the infarct signal derives from the intra- or extracellular space, we performed *ex vivo* scintillation counting of infarct tissue followed by scintillation counting of cells isolated from the infarct on day 4 after MI. Macrin activity was 3.3-fold higher in the cell pellet compared to infarct tissue (Online Fig. IV).

We next examined the cellular distribution of ^{VT680}Macrin, a fluorescent analog of ^{64}Cu-Macrin, with flow cytometry (Fig. 1G-J, Online Fig. V). In the heart, ^{VT680}Macrin was predominantly taken up by macrophages (Fig. 1H), in particular by MHCII^{high} and CCR2^{high} macrophage subsets (Online Fig. VA-C). Fibroblasts, endothelial cells and other immune cells such as CD11C^{high} leukocytes and Ly6G^{high} neutrophils, showed negligible uptake (Online Fig. VD-F). The mean fluorescent intensity (MFI) per macrophage, i.e. their individual ^{VT680}Macrin uptake, declined in the MI (Fig. 1I) while the number of Macrin^{+} macrophages expanded (Fig. 1J). The correlation between Macrin accumulation in the heart and macrophage tissue density demonstrated that Macrin uptake was determined by cell density (Online Fig. VI).

To supplement quantitative FACS with anatomical distribution data, we investigated ^{VT680}Macrin cellular localization using confocal microscopy in Cx3cr1$^{GFP/+}$ mice, in which macrophages express high levels of green fluorescent protein (GFP)[18]. As expected, GFP^{+} macrophages expanded in infarcted myocardium (Fig. 1K-L). Confocal images demonstrated nanoparticle co-localization with GFP^{+} heart macrophages (Fig. 1M). Immunostaining of infarcted mouse hearts confirmed co-localization of Macrin with macrophages but not myocytes, endothelial cells or fibroblasts (Online Fig. VIIA-D).

Given the encouraging observations in mice with MI, we next used a clinical PET/magnetic resonance imaging (MRI) scanner to pursue imaging in large animals, a typical next step to evaluate whether a molecular imaging approach has clinical potential. Similar to mice, we observed a focal increase of PET signal in the infarcted myocardium (Fig. 2A) while MRI reported a decreased ejection fraction (Fig. 2B). The 27% increased SUVmax measured by PET (Fig. 2C) was confirmed by both *ex vivo* scintillation counting (Fig. 2D) and autoradiography exposure of rabbit heart slices (Fig. 2E). We obtained comparable results in pigs 3 days after ischemia reperfusion (Fig. 2F-J), which decreased the ejection fraction (Fig. 2G). Pig hearts were large enough to quantify ^{64}Cu-Macrin uptake in the 17 myocardial segments of the AHA circumferential polar plot used in clinical nuclear cardiology[19]. The 50% increased PET signal in infarcted segments (Fig. 2H) was corroborated by *ex vivo* tissue activity counting (Fig. 2I). Autoradiography exposure of excised pig hearts showed highest activity in the infarcted area (Fig. 2J). Hematoxylin and eosin (H&E) and immunohistochemistry staining for macrophages confirmed increased leukocyte and macrophage numbers in rabbit and pig infarcts (Online Fig. VIIE-J).

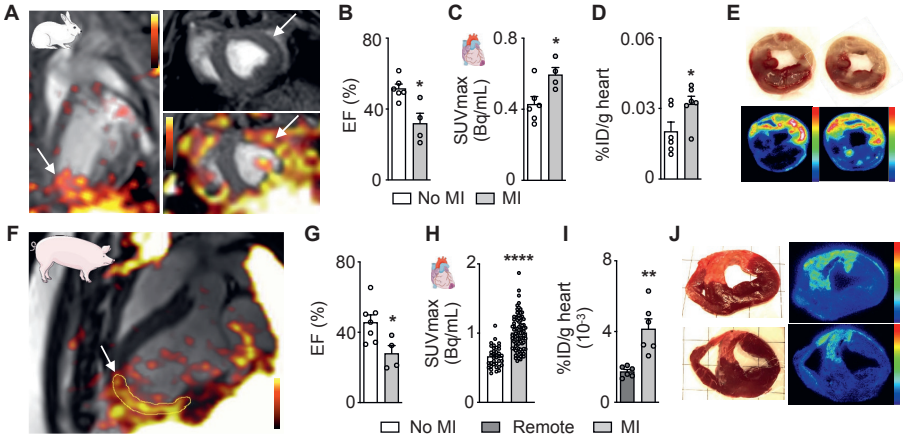


Figure 2. ^{64}Cu-Macrin PET imaging detects cardiac macrophage expansion following acute myocardial infarction in rabbits and pigs. A) PET/MR image of rabbit heart on day 3 after MI (arrows) and 24 h post injection of ^{64}Cu-Macrin. B) Left ventricular ejection fraction (EF), assessed by MRI (n=4-6 rabbits per cohort). C) *In vivo* ^{64}Cu-Macrin PET signal in rabbit hearts. D) *Ex vivo* ^{64}Cu-Macrin uptake in rabbit heart (%ID/g). E) TTC-stained rabbit heart tissue (upper row) shows pale infarcts with high activity on autoradiography exposure (bottom). F) Long axis PET/MR image of a pig 3 days after MI (arrow), 24 h post administration of ^{64}Cu-Macrin. G) EF in pigs assessed by MRI before and after MI (n=4-7 per cohort). H) PET signal in infarcted and non-infarcted control myocardium. Each dot represents a myocardial segment of the AHA circumferential polar plot (n=4-7 pigs per cohort). I) *Ex vivo* ^{64}Cu-Macrin uptake in pig hearts by scintillation counting (%ID/g). J) TTC images (left) and autoradiography exposure (right) of infarcted pig heart. Data are mean ± SEM. **P*<0.05, ***P*<0.01, ****P*<0.001, *****P*<0.0001.

^{64}Cu-Macrin PET detects physiological differences in cardiac macrophage content

Recent studies linked better recovery from myocardial injury to increased cardiac macrophages in very young mice[9, 20, 21], which motivated us to investigate cardiac macrophages from newborn mice using ^{64}Cu-Macrin PET imaging. Five-day-old mice weighed only 3.2±0.1g and had a heart weight of 18.6±0.7mg, which is 7- and 6-fold lighter than 10-week-old adult mice (Fig. 3A-B), respectively (Fig. 3C). Despite this, ^{64}Cu-Macrin PET imaging (Fig. 3D) detected 1.7-fold higher cardiac signal in newborn mice, which was corroborated by *ex vivo* scintillation counting (Fig. 3E-F). Flow cytometric analysis of young and adult mouse hearts confirmed predominant ^{VT680}Macrin accumulation in cardiac macrophages (Fig. 3G-H). Interestingly, cardiac

macrophages' phagocytic activity was higher in newborn mice (Fig. 3I), in which more cells had taken up the nanoparticle (Fig. 3J). Flow cytometry (Fig. 3K) and confocal microcopy of Cx3cr1$^{GFP/+}$ mice (Fig. 3L-M) confirmed higher macrophage numbers in the myocardium of 5-day-old mice when compared to 10-week-old adult mice (~22% difference by flow cytometry). Confocal images of GFP^{+} macrophages documented ^{VT680}Macrin uptake in young hearts (Fig. 3N).

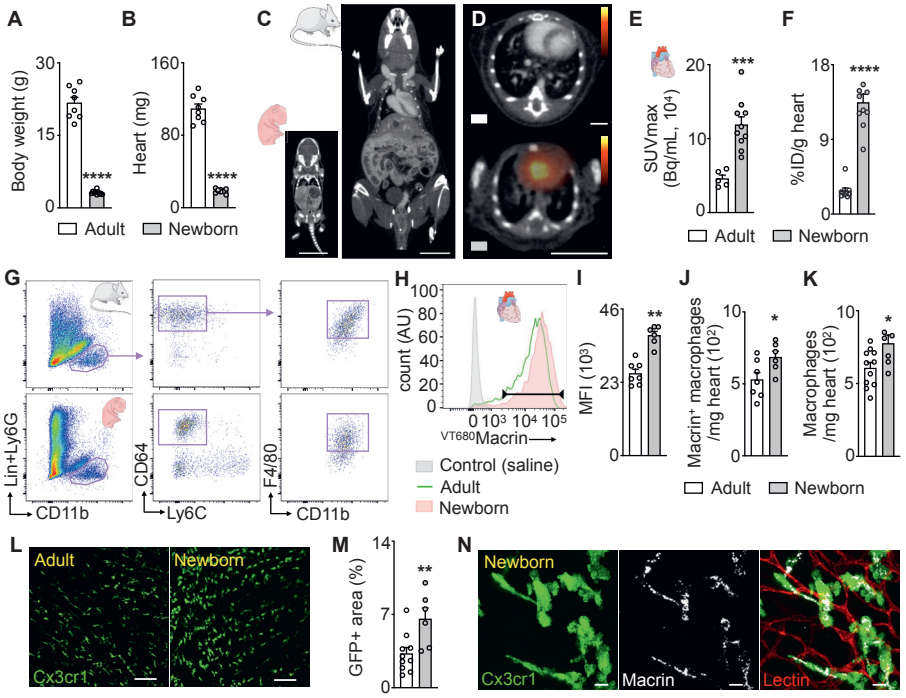


Figure 3. *In vivo* assessment of cardiac macrophages in newborn mice using ^{64}Cu-Macrin PET. A) Body and B) heart weight of adult (9-10 weeks) and 5-day-old mice. C) CT images of newborn and adult mouse (scale bar, 1cm). D) PET/CT images visualize ^{64}Cu-Macrin uptake in adult (top) and newborn mouse heart (scale bar, 1cm). E) ^{64}Cu-Macrin PET quantified as SUVmax and F) *ex vivo* scintillation counting. G) Flow cytometry gating for cardiac macrophages in adult and newborn mice. H) Histogram showing ^{VT680}Macrin uptake in cardiac macrophages. Controls injected with saline (shaded grey), adult (solid green) and newborn mice (shaded orange). I) Mean fluorescence intensity (MFI) in heart macrophages. J) Number of ^{VT680}Macri^{n+} macrophages in the heart. K) Macrophage numbers assessed by flow cytometry. L) Confocal images of myocardium in Cx3cr1$^{GFP/+}$ mice (scale bar, 100 µm). M) GFP^{+} area in hearts of Cx3cr1$^{GFP/+}$ mice by confocal microscopy. N) ^{VT680}Macrin (grey) co-localizes with GFP^{+} macrophages in the heart of a newborn Cx3cr1$^{GFP/+}$ mouse (scale bar, 10µm). Data are mean ± SEM. **P*<0.05, ***P*<0.01, ****P*<0.001, *****P*<0.0001.

^{64}Cu-Macrin PET senses systemic macrophage adaptions after remote injury

We next explored if ^{64}Cu-Macrin PET detects subtle systemic adaptions of the innate immune system that are remote from the site of injury or a septic focus, because our recent studies[4] indicate that tissue macrophages may play a role in remote organ resilience and complications. Sepsis can cause heart failure, and patients with myocardial infarction may develop edema and pneumonia. We thus tested whether ^{64}Cu-Macrin PET imaging can monitor heart macrophages in mice with peritonitis or lung macrophages after acute MI.

^{64}Cu-Macrin PET reported a 32% myocardial signal increase on day 5 after sepsis induction (Fig. 4A-B), which was corroborated by *ex vivo* scintillation counting of the heart (Fig. 4C). Flow cytometric analysis (Fig. 4D) revealed that ^{VT680}Macrin uptake decreased in individual cardiac macrophages after CLP (Fig. 4E-F); however, the total number of macrophages that incorporated the fluorescent nanoparticle increased (Fig. 4G). A sepsis-induced surge in cardiac macrophages was confirmed by confocal microscopy (Fig. 4H-I).

Recently, we discovered that acute MI primes lung macrophages via interferon-ɣ, which influenced bacterial clearance from mouse lungs[4]. We therefore employed ^{64}Cu-Macrin PET to study macrophages in the lungs of mice 5 days after MI. We observed patchy ^{64}Cu-Macrin uptake in the lung (Fig. 5A) and an 1.7-fold higher lung SUVmax after MI (Fig. 5B). Compared to mice without MI, ^{64}Cu-Macrin lung activity increased 2.4-fold by *ex vivo* scintillation counting (Fig. 5C). Flow cytometry documented an increased mean fluorescent intensity in alveolar macrophages after MI in mice injected with ^{VT680}Macrin (Fig. 5D-F). Also, the number of alveolar macrophages that had incorporated ^{VT680}Macrin expanded in mice after MI (Fig. 5G). Notably, ^{VT680}Macrin was not detectable in CD11c^{high}, MHCII^{high} and SiglecF^{low} lung leukocytes or Ly6G^{high} neutrophils (Online Fig. VG).

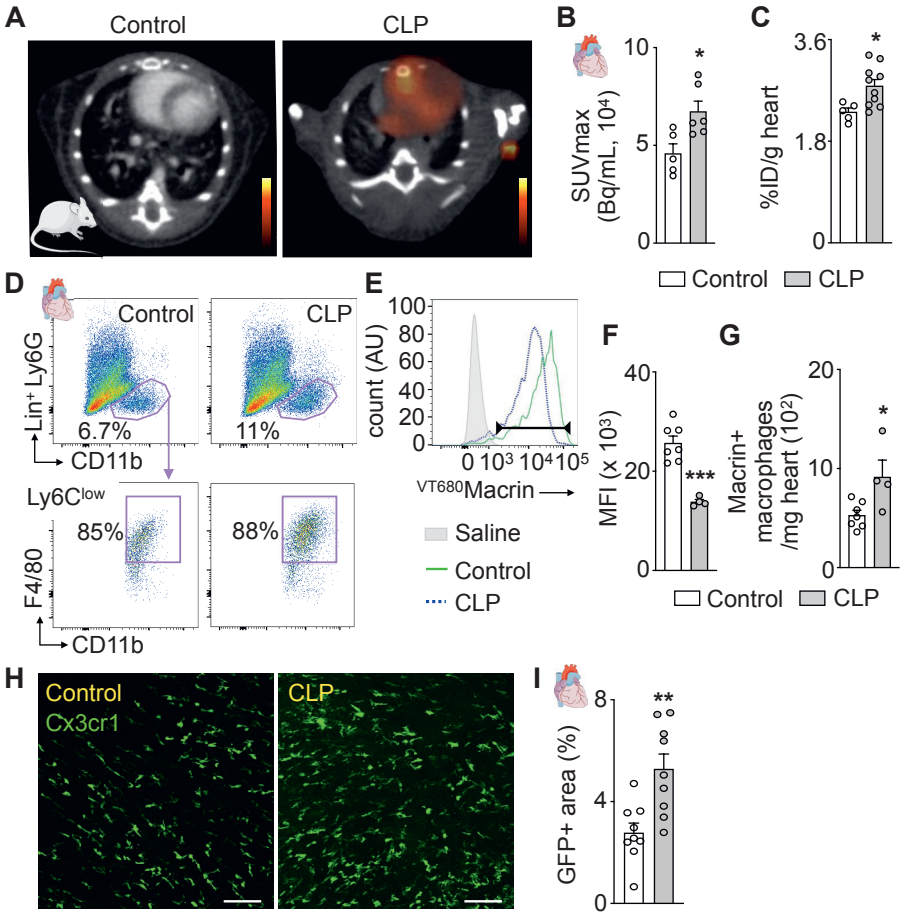


Figure 4. ^{64}Cu-Macrin PET detects cardiac macrophage dynamics in sepsis. A) PET/CT of the heart in a control mouse and a mouse after cecal ligation and puncture (CLP). B) ^{64}Cu-Macrin uptake in myocardium by *in vivo* PET and C) *ex vivo* scintillation counting. D) Flow cytometry of cardiac macrophages in controls and mice after CLP. E) Histogram of ^{VT680}Macrin uptake in cardiac macrophages. Saline-injected control group without CLP (shaded grey), control mice injected with ^{VT680}Macrin (solid green) and after CLP (dotted blue). F) ^{VT680}Macrin mean fluorescent intensity (MFI) in cardiac macrophages. G) Number of ^{VT680}Macrin^{+} cardiac macrophages. H) Confocal microscopy of control and after CLP in Cx3cr1$^{GFP/+}$ mice (scale bar, 100 µm). I) GFP-positive area in confocal heart images. Data are mean ± SEM. **P*<0.05, ***P*<0.01, ****P*<0.001.

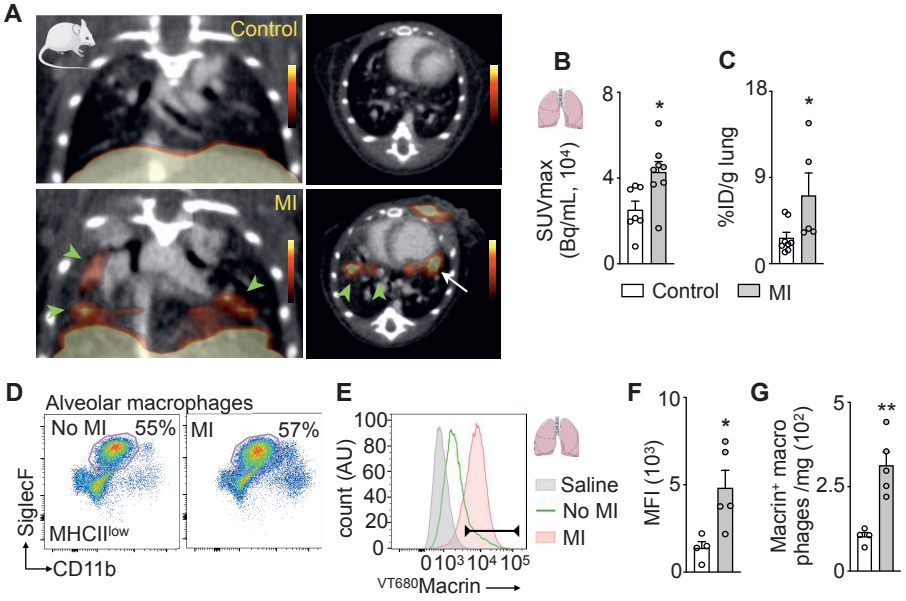


Figure 5. ^{64}Cu-Macrin PET detects lung macrophage dynamics after MI. A) Coronal and axial PET/CT images from control mouse (top) and mouse on day 5 after MI (bottom). Areas with high uptake in lung are indicated with arrowheads. Arrow indicates MI. B) ^{64}Cu-Macrin signal in lung quantified by PET and C) *ex vivo* scintillation counting. D) Flow plots of alveolar macrophages in controls and mice after MI. E) ^{VT680}Macrin fluorescence of alveolar macrophages; saline-injected controls (shaded grey), ^{VT680}Macrin injected control mice (solid green) and MI (shaded orange). F) ^{VT680}Macrin mean fluorescence intensity (MFI) in alveolar macrophages. G) Number of Macrin$^+$ alveolar macrophages. Data are mean ± SEM. **P*<0.05, ***P*<0.01, ****P*<0.001.

^{64}Cu-Macrin PET detects pulmonary inflammation in pigs and mice with pneumonia

When studying PET images obtained in ^{64}Cu-Macrin-injected pigs, we serendipitously observed lung areas with increased PET signal (Fig. 2F). This unexpected observation was also made in pigs without myocardial infarction (Fig. 6A). ^{64}Cu-Macrin distribution in pig lungs was heterogeneous, with higher uptake in inferior lung lobes. SUVmax obtained by PET differed significantly among lung regions, with high versus low uptake in individual animals (Fig. 6B), a finding that was replicated by *ex vivo* scintillation counting (Fig. 6C). Histological evaluation revealed increased macrophage content in alveoli and the interstitial space in certain lung regions (Fig. 6D-E), consistent with mild to moderate lung inflammation. A veterinarian pathologist noted

the presence of low-grade chronic pneumonia, consistent with *Mycoplasma hyopneumoniae*[22]. Two lung CTs obtained in pigs with increased PET signal were interpreted as normal by a clinical radiologist, ruling out severe lung disease.

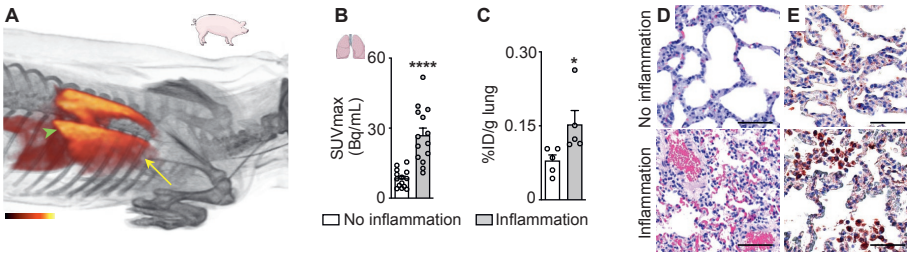


Figure 6. ^{64}Cu-Macrin PET imaging detects lung inflammation in pigs. A) 3-dimensional PET/MRI reconstruction of pig thorax 24 h post injection of ^{64}Cu-Macrin. Arrowhead indicates basal lung region with high PET signal; arrow indicates apical lung region with lower ^{64}Cu-Macrin uptake. B) ^{64}Cu-Macrin accumulation in lungs of n=8 pigs as analyzed by *in vivo* PET (SUVmax in multiple lung region of interests) and C) *ex vivo* scintillation counting of lung tissues. D) H&E histology and E) immunohistochemistry for macrophages from normal (top) and inflamed (bottom) pig lung regions (scale bar, 50 µm).

To follow up on these findings in pigs, we pursued ^{64}Cu-Macrin PET lung imaging using an experimental design that involved healthy control animals and mice infected with *Streptococcus pneumoniae*[23]. The bacterial burden in the lung (Fig. 7A-B) increased from day 3 to 4 after infection. Histological analysis revealed that mice with pneumonia had more lung macrophages (Fig. 7C-D). Gram-positive *S. pneumoniae* were identified in infected mouse lungs only (Fig. 7E). Based on these data, we chose days 3 and 4 after infection for PET imaging of the lung. Sagittal and coronal PET/CT views of lungs obtained in control mice and mice with pneumonia illustrate increased CT lung density and robust ^{64}Cu-Macrin uptake (Fig. 7F). *In vivo* PET, *ex vivo* scintillation counting and autoradiography exposure revealed higher ^{64}Cu-Macrin uptake in the lungs of mice with pneumonia (Fig. 7G-I). Interestingly, ^{64}Cu-Macrin accumulation had already increased ~2-fold on day 3 after bacterial inoculation compared to the healthy lung (Fig. 7G-H), a time when the bioluminescence was still rising (Fig. 7B).

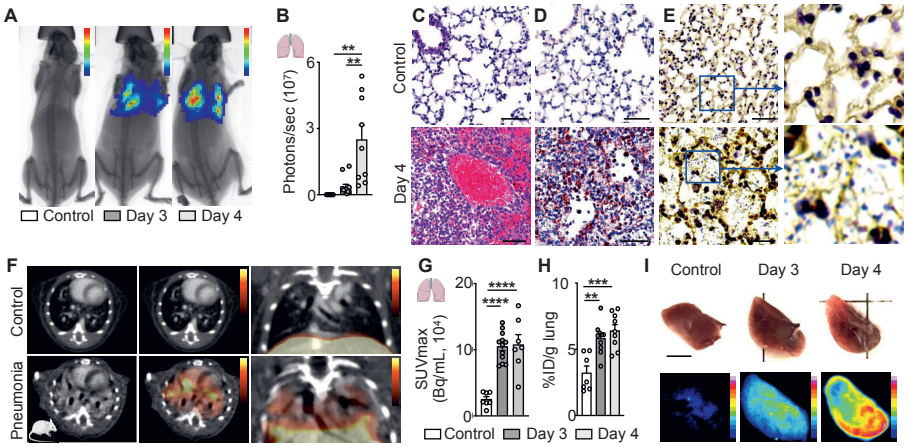


Figure 7. ^{64}Cu-Macrin PET imaging detects lung inflammation in mice. A) Bioluminescent / X-ray images of control mouse (left) and mice with pneumonia on days 3 and 4 after inoculation with bioluminescent Streptococcus pneumoniae. B) Bacterial burden assessed by bioluminescence. C-E) Lung histology from uninfected controls (top) and mice with pneumonia (bottom, day 4; scale bar, 50 μm), C) H&E, D) IHC for mouse macrophages (brown) and E) gram-staining for streptococcus pneumoniae (pale blue). F) PET/CT images from control mouse (top) and mouse with pneumonia (bottom, day 4 after infection). G) ^{64}Cu-Macrin lung uptake by *in vivo* PET and H) *ex vivo* scintillation counting. I) Visualization of ^{64}Cu-Macrin accumulation in mouse lungs by autoradiography (scale bar, 5 mm). Data are mean ± SEM. **P*<0.05, ***P*<0.01, ****P*<0.001, *****P*<0.0001.

^{64}Cu-Macrin identifies atherosclerotic plaque inflammation in rabbits

Macrophages are key protagonists propelling inflammation in the arterial wall[3]. Driven by expanding macrophage numbers and their inflammatory actions, atherosclerotic plaques may rupture or erode, leading to organ ischemia, especially MI and stroke. Given that recent clinical data[24] demonstrated the therapeutic benefits of inhibiting inflammation in patients with cardiovascular disease, there is considerable interest in imaging assays for plaque macrophages. We therefore explored ^{64}Cu-Macrin PET/MRI in rabbits with atherosclerosis induced by Western diet and balloon injury. Using a clinical PET/MRI scanner, we observed 1.4-fold increased ^{64}Cu-Macrin uptake in the injured segments of the rabbits' abdominal aorta (Fig. 8A-B). *Ex vivo* scintillation counting (Fig. 8C) and autoradiography (Fig. 8D) confirmed higher activity in the aorta of rabbits with atherosclerosis.

Immunohistochemical staining verified the presence of macrophages in rabbits' atherosclerotic lesions (Fig. 8E-F).

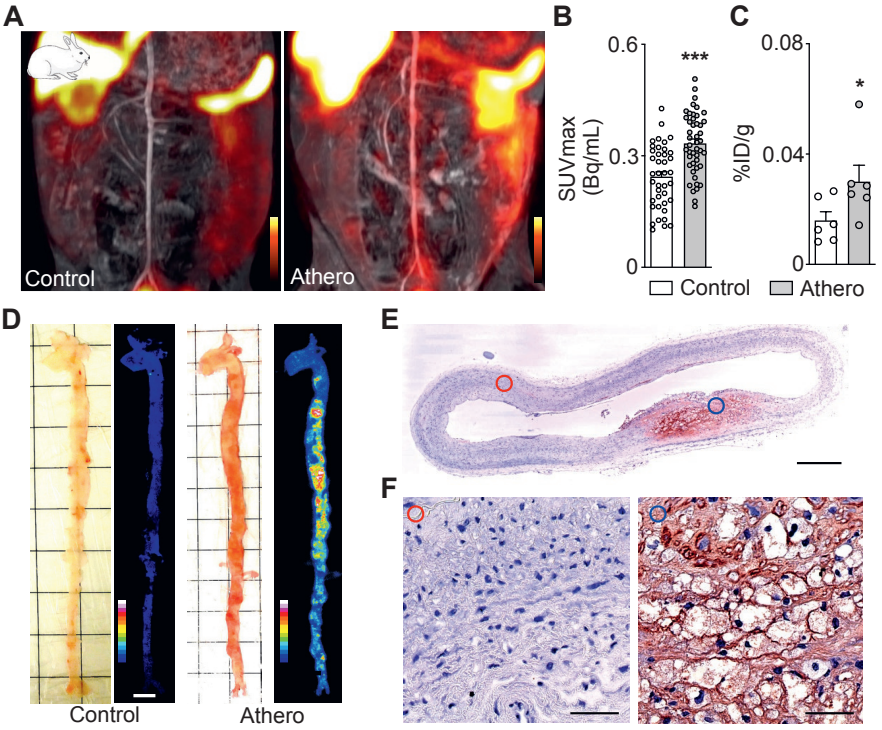


Figure 8. ^{64}Cu-Macrin PET imaging of atheromatous plaques in rabbits. (A) Coronal PET/MR images of the abdominal aorta in a control rabbit (left) and a rabbit with atherosclerosis (right) 24 h post injection. **(B)** *In vivo* ^{64}Cu-Macrin PET signal in aortic segments (n=6 rabbits per group). **(C)** ^{64}Cu-Macrin uptake in aortae as measured by *ex vivo* scintillation counting. **(D)** Bright-field image (left) and autoradiography (right) of dissected rabbit aortae (scale bar, 1 cm). **(E)** Immunohistochemical staining for macrophages in rabbit aortae (scale bar, 0.5 mm). **(F)** Images from normal region (left, red circle) and atherosclerotic lesion (right, blue circle) (scale bar, 50 μm). Data are mean ± SEM. **P*<0.05, ****P*<0.001.

Finally, we explored cellular Macrin uptake in mice with atherosclerosis (Online Fig. VIIIA) by quantitative flow cytometry, relying on the well-established surface markers for key plaque cell populations in the mouse. Among aortic cells, Macrin was exclusively found in macrophages but not in CD45^{-} cells, fibroblasts, endothelial cells, monocytes and lymphocytes.

Immunohistological examination of the mouse aortic root confirmed these FACS data (Online Fig. VIIIB).

Toxicity and dosimetry estimation

The documented sensitivity and specificity of the assay indicate its potential clinical usefulness. For first-in-human imaging, toxicity and dosimetry are warranted, which we report here. Standard toxicity evaluation showed no effect on body weight, food consumption, hematology blood counts, clinical chemistry or organ weights. No mortality or adverse clinical signs were observed up to 14 days after injection, when rats were sacrificed for autopsy and histopathology studies. The gross pathology and histopathology reports were normal, with no signs of toxicity.

Organ mass-adjusted extrapolation of the mouse biodistribution data (Online Table II) using the OLINDA/EXM dosimetry program yielded the human dose estimates shown in Table 1. The liver emerged as the dose-limiting organ with an effective dose of 0.143 ± 0.012 mSv/MBq. The organ with the second-highest uptake was the urinary bladder wall, followed by the kidneys. ^{64}Cu-Macrin uptake also occurred in the spleen. The average effective dose for ^{64}Cu-Macrin was 0.04 ± 0.001 mSv/MBq, which is higher than commonly used ^{18}F-FDG[25], but comparable to other copper-based PET tracers previously investigated in humans, including ^{64}Cu-ATSM (0.036 mSv/MBq)[26] and ^{64}Cu-Trastuzumab (0.036 mSv/MBq)[27], and considerably lower than an I-124 labeled nanoparticle, ^{124}I-cRGDY-PEG-C-dot (0.162 mSv/MBq), currently undergoing a phase 1 trial for melanoma and malignant brain tumor PET imaging[28].

Table 1. Human radiation dose estimates for ^{64}Cu-Macrin using Organ Level Internal Dose Assessment (OLINDA/EXM).

Organ	Adult male (mSv/MBq)	Adult female (mSv/MBq)	Adult (mSv/MBq)
Adrenals	0.018 ± 0.004	0.020 ± 0.004	0.019 ± 0.002
Brain	0.004 ± 0.001	0.004 ± 0.001	0.004 ± 0.001
Breast	0.010 ± 0.003	0.011 ± 0.003	0.011 ± 0.001
Gallbladder Wall	0.023 ± 0.004	0.024 ± 0.004	0.023 ± 0.001
LLI Wall	0.053 ± 0.016	0.058 ± 0.017	0.055 ± 0.004
Small Intestine	0.024 ± 0.002	0.026 ± 0.003	0.025 ± 0.002
Stomach Wall	0.019 ± 0.000	0.022 ± 0.000	0.021 ± 0.002
ULI Wall	0.046 ± 0.014	0.052 ± 0.015	0.049 ± 0.004
Heart Wall	0.013 ± 0.001	0.021 ± 0.002	0.017 ± 0.006
Kidneys	0.109 ± 0.095	0.109 ± 0.083	0.109 ± 0.000
Liver	0.135 ± 0.083	0.152 ± 0.098	0.143 ± 0.012
Lungs	0.017 ± 0.001	0.022 ± 0.001	0.019 ± 0.003
Muscle	0.007 ± 0.000	0.008 ± 0.000	0.008 ± 0.001
Ovaries	N/A	0.032 ± 0.019	0.032 ± 0.019
Pancreas	0.017 ± 0.000	0.019 ± 0.000	0.018 ± 0.001
Red Marrow	0.027 ± 0.004	0.029 ± 0.004	0.028 ± 0.002
Osteogenic Cells	0.029 ± 0.004	0.039 ± 0.004	0.034 ± 0.007
Skin	0.009 ± 0.003	0.010 ± 0.003	0.010 ± 0.001
Spleen	0.043 ± 0.009	0.048 ± 0.014	0.045 ± 0.004
Testes	0.053 ± 0.062	N/A	0.053 ± 0.062
Thymus	0.011 ± 0.003	0.012 ± 0.004	0.012 ± 0.001
Thyroid	0.010 ± 0.003	0.011 ± 0.004	0.010 ± 0.001
Urinary Bladder	0.097 ± 0.003	0.151 ± 0.003	0.124 ± 0.038
Uterus	N/A	0.026 ± 0.007	0.026 ± 0.007
Total Body	0.017 ± 0.000	0.019 ± 0.000	0.018 ± 0.002
Effective dose	0.040 ± 0.018	0.041 ± 0.011	0.040 ± 0.001

Estimated human organ dosimetry (mSv/MBq, mean ± SD) was extrapolated from the mouse biodistribution data (Table S1). LLI indicates lower large intestine; NA, not available; OLINDA/EXM, organ level internal dose assessment/exponential modeling; and ULI, upper large intestine.

Discussion

Despite advances in clinical care, cardiovascular disease is still the global leading cause of death. While some conditions such as hyperlipidemia can be treated effectively, the immune system's role in atherosclerosis and heart failure is currently not harnessed therapeutically. This unused opportunity exists despite an urgent clinical need for therapeutics that act orthogonally to the current standard of care. The past decade provided new insight into the life cycle and functions of innate immune cells[29, 30]. Among these cells, macrophages are the most numerous residents in healthy tissues and expand further in atherosclerotic plaques that are poised to cause organ ischemia. Unresolved inflammatory activity of cardiac macrophages following MI results in adverse cardiac remodeling, fibrosis, left ventricular dilation and heart failure[3]. An improved understanding of macrophages' roles in cardiovascular disease and cancer fuels the current interest in targeting these cells therapeutically[31, 32]. Quantitative measurements of macrophage population size and their spatiotemporal variation in human patients would catalyze development of macrophage-targeted therapeutics. However, to date there is no clinically viable, specific tool for imaging macrophages in patients.

We here describe the first use of ^{64}Cu-Macrin for PET imaging of macrophage dynamics spanning different amplitudes, physiological states and cardiopulmonary pathologies: in newborn, septic and ischemic myocardium, in the lung after acute MI, in atherosclerotic plaques, and in subclinical and clinical pneumonia. Our data suggest that ^{64}Cu-Macrin PET is capable to assay tissue macrophages non-invasively in all these settings. The nanotracer emerged from continuous efforts to develop macrophage imaging agents. A first-generation dextran-based nanoparticle, called monocrystalline iron oxide nanoparticle (MION), was employed to image patients with prostate

cancer[33], detecting the nanoparticles' iron oxide core by MRI. Similar materials were used to sense macrophages in atherosclerotic plaques[34] and acute myocardial infarction[35, 36]. The transition to nanoparticles derivatized with radioisotopes harnessed PET's higher sensitivity and quantitative capabilities[37]. Further optimization in size, surface chemistry and composition led to ^{89}Zr-labeled dextran nanoparticles made from the same coating material but without an iron oxide core[38]. To lower radiation burden and accelerate injection/imaging sequences, ultra-small 5 nm dextran nanoparticles were labeled with fluorine-18[39]. However, rapid renal clearance of these particles somewhat reduced macrophage uptake and sensitivity. This observation led to the current nanoparticle with ~20 nm diameter and a blood half-life of 45 min in rabbits. Macrin's favorable pharmacokinetic profile and high target cell avidity allowed macrophage detection in mice, rabbits and pigs with various inflammatory conditions. A previous study established its utility to detect tumor-associated macrophages in mice[15].

In addition to the dextran nanoparticle family, there are a number of alternatives for macrophage imaging; however, only a few have been evaluated in large animals and humans and none are in routine use (reviewed in[31, 40]). Noteworthy examples are small molecule-based imaging agents that bind the chemokine receptor CCR2[13, 41] or the macrophage colony-stimulating factor 1 receptor (CSF1R)[14]. In addition to the longer blood half life of ^{64}Cu-Macrin, which may augment signal to background ratio through longer systemic availability, the specific targeting profile for macrophage subsets may differ. For instance, we observed Macrin signal in cardiac resident macrophage subsets which express low levels of CCR2. While not explicitly examined here, we expect that Macrin enriches in resident macrophages of most healthy tissues. The uptake of nanoparticles in a tissue of interest may depend, in addition to the properties of the nanomaterial[40], on macrophage (subset) abundance, activity and phagocytic history. For instance, we observed that the per cell fluorescence, which indicates the amount of individual ^{VT680}Macrin uptake into a cell, was higher in neonatal heart and lower in infarct macrophages. Therefore, the choice of macrophage

imaging agent may depend on the specific application and currently emerging functions of macrophage subsets.

In addition to common inflammation imaging contexts such as atherosclerosis and myocardial infarction, we here employed ^{64}Cu-Macrin PET to image previously less well characterized biology. In newborn mice, which may still have active developmental pathways that facilitate better regeneration and scar-free infarct healing, ^{64}Cu-Macrin heart uptake was higher than in older mice. Flow cytometry of newborn hearts not only verified more cardiac macrophages per mg of myocardium but also documented a higher mean fluorescence intensity per cell, i.e. more Macrin nanoparticle uptake per individual macrophage. This observation indicates that the phenotype of cardiac macrophages in newborn hearts may be distinct, agreeing with a prior report that described a different, less inflammatory cardiac macrophage subset composition in neonatal mouse hearts[20]. A combination of enhanced macrophage functionalities needed for tissue repair, including phagocytosis, and lower inflammatory activity may contribute to the regenerative phenotype in the neonatal heart. In adult mice after MI, we observed higher Macrin uptake in primed alveolar macrophages, which then step up defenses against post-MI pneumonia, leading to better removal of bacteria from the alveolar space[4].

There is a growing need for assays to support macrophage-targeted drug development. Currently, the gold standards for macrophage quantification are flow cytometry and confocal microscopy, with extremely limited clinical utility. The ^{64}Cu-Macrin PET imaging applications tested here span conditions with large and subtle macrophage fluctuations, attesting to the dynamic range and utility of the assay. The large animal data, toxicity studies and human dosimetry estimates suggest that this latest-generation nanoparticle reporter is ready for first-in-human studies.

Methods

We confirm that the manuscript adheres to the Transparency and Openness Promotion (TOP) guidelines. The data that support the findings of this study are available from the corresponding author upon reasonable request. All experiments were approved by the Institutional Animal Care and Use Committee (IACUC) of the Massachusetts General Hospital or Icahn School of Medicine at Mount Sinai. **Online Table I** summarizes all experiments performed (including goals, model, interventions and animal numbers).

Mouse PET/CT

PET/CT (Inveon, Siemens, Munich, Germany) imaging was done 24 hours post injection of ^{64}Cu-Macrin (~230 µCi in 150 µL saline for adult mice via tail-vein injection and ~50 µCi in 30 µL saline for 5-day-old mice via retro-orbital injection). Primary end point was increased standard uptake value (SUV) in inflamed tissue, the only exclusion criterion was death prior imaging. High-resolution CT was acquired prior to serial 30-minute static PET with the following parameters: beam energy of 80 kVp, current 500 µA X-ray and exposure time of 425 ms over 360 projections. PET images were reconstructed using a 3D ordered-subset expectation maximization/maximum a posteriori (3D-OSEM/MAP). Voxel count rates in the reconstructed images were decay corrected and converted to SUV by system calibration factor from a cylindrical phantom. Regions of interest (ROI) analyses were guided by co-registered anatomic CT images to yield organ activity normalized by the body weight (g) and the residual activity at scan.

Mouse PET/MR

Mice were injected intravenously with ^{64}Cu-Macrin (218.3±41.1 µCi) via tail vein. PET/CT and MRI were conducted sequentially as described previously[16]. Under isoflurane anesthesia (2% in oxygen), mice were positioned on a custom-designed mouse bed compatible with both PET/CT and MRI. Mice were imaged with CT followed by static PET scans (30 minutes) ~24 hours after tracer administration on an Inveon small animal PET/CT scanner

(Siemens, Munich, Germany). MRI was performed on a 4.7 Tesla Bruker PharmaScan MRI scanner (Billerica, MA) with a cardiac coil in birdcage design (RAPID MR international, Columbus, OH). A fast low angle shot (FLASH) sequence was used with integrate cardiac and respiratory gating with the following parameters: TE=2.94, TR=10 ms, FA=18°, matrix size=200 x 200 x 1, voxel size=0.15 x 0.15 x 1 mm^3. Delayed enhancement was imaged 10 minutes post intravenous injection of gadolinium-diethylenetriamine pentaacetic acid (Gd-DTPA, 30 µL).

PET/MR rabbits

All rabbits were imaged with a clinical PET/MR system (Siemens 3T Biograph mMR). The rabbits received an intravenous injection of ^{64}Cu-Macrin (59.57-00.3 MBq) via marginal ear vein one day before imaging. Anesthesia was induced by intramuscular injection of ketamine (20 mg/kg) (Fort Dodge Animal Health) and xylazine (0.5 mg/kg) (Bayer). Rabbits were placed in a 6-channel body matrix coil, received isoflurane anesthesia at 1.5% by inhalation and were oxygenated for the remainder of the PET/MR imaging experiment while vital parameters were monitored. PET was acquired for thorax and abdomen, 60 minutes and 20 minutes, respectively, in caudocranial direction. During PET of the thorax, cardiac cine MR images were acquired for cardiac function measurement using retrospective gating and free breathing. Images were acquired using a fast low angle shot (FLASH) sequence, with the following imaging parameters: repetition time (TR) 64.64 ms, echo time (TE) 3.76 ms, flip angle 12°, number of averages 12, 14-15 interleaved slices with no gap, 15 cardiac frames, 3 mm slice thickness, reconstructed spatial resolution 0.729x0.729 mm^2. In parallel with abdominal PET, MR time-of-flight (TOF) non-contrast enhanced angiography images were acquired to delineate the abdominal aorta, with the following imaging parameters: TR 25 ms, TE 2.8 ms, flip angle 20°, number of averages 1, 200 slices, slice thickness 1 mm, reconstructed spatial resolution 0.35x0.35 mm^2. PET reconstruction was performed using Siemens E7 tools. Attenuation correction of PET images was performed using a vendor built-in Dixon MR-based attenuation map (MR-AC) with 2 (soft tissue, air). Images were reconstructed using a 3D ordinary Poisson ordered subsets expectation maximization (OP-OSEM)

algorithm with point-spread-function (PSF) resolution modeling, using 3 iterations and 21 subsets and filtered with a 4 mm Gaussian filter.

PET/MR pigs

Six Yucatan miniature pigs underwent imaging with a clinical PET/MR system (Siemens 3T Biograph mMR) before and after myocardial infarction. In addition, two Yorkshire pigs were included as controls and imaged once. All pigs received an intravenous injection of ^{64}Cu-Macrin (85.9 – 268.6 MBq) via marginal ear vein one day before each imaging session. Anesthesia was induced by intramuscular injection of tiletamine and zolazepam (6 – 10 mg/kg, Telazol, Zoetis). Pigs were intubated and placed on the scanner bed and were anesthetized with isoflurane at 1.5-2% supplemented with oxygen for the remainder of the PET/MR imaging experiment. Vital parameters were monitored. Six-channel body matrix coils were placed on the thorax and used for signal reception. Following scout scans, a multi-bed step-and-shoot PET was acquired within 20 mins (pelvis; abdomen) or 60 mins (thorax).

During thoracic PET/MR acquisition, cardiac cine and late gadolinium enhancement MR images were acquired for cardiac function and infarct detection, respectively. Cine short stack images were acquired using a True FISP sequence with retrospective ECG gating. Imaging parameters were: TR 46.62 ms, TE 1.51 ms, flip angle 45°, number of averages 1, 16-22 interleaved slices with no gap, 25 cardiac frames, 4mm slice thickness, reconstructed spatial resolution 1.875x1.875 mm^2. Late gadolinium (0.1 mmol/kg, Magnevist, Bayer) enhancement images were acquired using a FLASH sequence with prospective ECG triggering as follows: TR equivalent to 1 R-R period (mean 530.7, SD 112.4 ms), TE 2.21 ms, flip angle 20°, number of averages 1, 20 slices, slice thickness 4 mm, reconstructed spatial resolution 1.367x1.367mm^2. In both cases, acquisition was performed with assisted breath holds enacted by briefly closing the ventilator.

In pigs, attenuation correction of PET images was performed using 4 tissue compartments (soft tissue, fat, lung and air) and images reconstructed as described for rabbits.

PET/MR data analysis rabbit and pigs

All data were processed using Osirix MD v 9.5.1 (OsiriX Foundation, Geneva, Switzerland). Multiple regions of interest (ROIs) (≥ 6 per organ) were manually drawn. Anatomical images were overlaid with reconstructed PET images and SUVs of ROIs were exported with the 'Export ROIs' plugin. Cardiac function was analyzed by manually segmenting end systolic and diastolic volumes and quantifying ejection fraction with the MRHeart plugin[17].

Statistics

Results are expressed as mean ± standard error or standard deviation. GraphPad Prism 8.0c for Macintosh (GraphPad Software Inc.) was used for statistical analysis. The number of animals used is indicated as dot overlay in all bar graphs unless indicated otherwise in the figure legends. Differences between groups were evaluated by two-tailed t-tests or ANOVA tests for two-group and multi-group comparisons, respectively. Animals were randomely assigned to groups where possible (i.e. MI versus no MI). Blinding was not possible as disease group assignment was obvious from images and clinical status. Power estimation and group size was based on prior imaging studies with the nanoparticle[15]. A p value of <0.05 was used to indicate statistical significance.

Acknowledgments

We acknowledge Hye-Yeong Kim, PhD, who unfortunately was not able to contribute to the preparation of the final manuscript, for nanoparticle production and labeling, nanoparticle analysis, imaging and *in vitro* data collection and analysis, contributing to figures and drafting the manuscript. We acknowledge Kaley Joyce, PhD, for editing the manuscript. We acknowledge Servier Medical Art for figure components.

Sources of funding

This work was funded in part by federal funds from the National Institutes of Health HL131495, HL139598, HL125428, HL131478, HL144072, CA220234, CA008748; from the European Union's Horizon 2020 research and innovation

programme 667837, by the Netherlands Organization for Scientific Research (NWO; ZonMW Vici grant no. 016.176.622), the Massachusetts General Hospital Research Scholar Program, the German Research Foundation HO5279/1-2 and RO5071/1-1, German Heart Foundation, the Jung Foundation for Science and Research and by the American Heart Association 19PRE34380423.

Competing interests

M.N. has received funds or material research support from Novartis, GSK, Pfizer, GlycoMimetics, Medtronic, Biotronik, Alnylam and CSL Behring and consulting fees from Verseau Therapeutics, Sigilon, Molecular Imaging Inc., IFM Therapeutics, Gimv and Biogen.

References

1. Lavin Y, Mortha A, Rahman A, Merad M. Regulation of macrophage development and function in peripheral tissues. *Nat Rev Immunol*. 2015;15:731-744.
2. Nahrendorf M. Myeloid cell contributions to cardiovascular health and disease. *Nat Med*. 2018;24:711-720.
3. Swirski FK, Nahrendorf M. Cardioimmunology: the immune system in cardiac homeostasis and disease. *Nat Rev Immunol*. 2018;18:733-744.
4. Hoyer FF, Naxerova K, Schloss MJ, Hulsmans M, Nair AV, Dutta P, Calcagno DM, Herisson F, Anzai A, Sun Y, Wojtkiewicz G, et al. Tissue-Specific Macrophage Responses to Remote Injury Impact the Outcome of Subsequent Local Immune Challenge. *Immunity*. 2019;51:899-914.e7.
5. Panizzi P, Swirski FK, Figueiredo JL, Waterman P, Sosnovik DE, Aikawa E, Libby P, Pittet M, Weissleder R, Nahrendorf M. Impaired infarct healing in atherosclerotic mice with Ly-6C(hi) monocytosis. *J Am Coll Cardiol*. 2010;55:1629-1638.
6. Engstrom G, Melander O, Hedblad B. Leukocyte count and incidence of hospitalizations due to heart failure. *Circ Heart Fail*. 2009;2:217-222.
7. Madjid M, Awan I, Willerson JT, Casscells SW. Leukocyte count and coronary heart disease: implications for risk assessment. *J Am Coll Cardiol*. 2004;44:1945-1956.
8. Maekawa Y, Anzai T, Yoshikawa T, Asakura Y, Takahashi T, Ishikawa S, Mitamura H, Ogawa S. Prognostic significance of peripheral monocytosis after reperfused acute myocardial infarction:a possible role for left ventricular remodeling. *J Am Coll Cardiol*. 2002;39:241-246.
9. Aurora AB, Porrello ER, Tan W, Mahmoud AI, Hill JA, Bassel-Duby R, Sadek HA, Olson EN. Macrophages are required for neonatal heart regeneration. *J Clin Invest*. 2014;124:1382-1392.
10. Nahrendorf M, Sosnovik DE, French BA, Swirski FK, Bengel F, Sadeghi MM, Lindner JR, Wu JC, Kraitchman DL, Fayad ZA, et al. Multimodality cardiovascular molecular imaging, Part II. *Circ Cardiovasc Imaging*. 2009;2:56-70.
11. Rischpler C, Dirschinger RJ, Nekolla SG, Kossmann H, Nicolosi S, Hanus F, van Marwick S, Kunze KP, Meinicke A, Gotze K, et al. Prospective Evaluation of 18F-Fluorodeoxyglucose Uptake in Postischemic Myocardium by Simultaneous Positron Emission Tomography/Magnetic Resonance Imaging as a Prognostic Marker of Functional Outcome. *Circ Cardiovasc Imaging*. 2016;9:e004316.
12. Thackeray JT, Derlin T, Haghikia A, Napp LC, Wang Y, Ross TL, Schäfer A, Tillmanns J, Wester HJ, Wollert KC, et al. Molecular Imaging of the Chemokine Receptor CXCR4 After Acute Myocardial Infarction. *JACC*

Cardiovasc Imaging. 2015;8:1417-1426.

13. Heo GS, Bajpai G, Li W, Luehmann HP, Sultan DH, Dun H, Leuschner F, Brody SL, Gropler RJ, Kreisel D, et al. Targeted PET Imaging of Chemokine Receptor 2+ Monocytes and Macrophages in the Injured Heart. *J Nucl Med*. 2020;16:3016-3023.
14. Horti AG, Naik R, Foss CA, Minn I, Misheneva V, Du Y, Wang Y, Mathews WB, Wu Y, Hall A, et al. PET imaging of microglia by targeting macrophage colony-stimulating factor 1 receptor (CSF1R). *Proc Natl Acad Sci U S A*. 2019;116:1686-1691.
15. Kim H-Y, Li R, Ng TSC, Courties G, Rodell CB, Prytyskach M, Kohler RH, Pittet MJ, Nahrendorf M, Weissleder R. Quantitative Imaging of Tumor-Associated Macrophages and Their Response to Therapy Using 64Cu-Labeled Macrin. *ACS nano*. 2018;12:12015-12029.
16. Lee WW, Marinelli B, van der Laan AM, Sena BF, Gorbatov R, Leuschner F, Dutta P, Iwamoto Y, Ueno T, Begieneman MP, et al. PET/MRI of inflammation in myocardial infarction. *J Am Coll Cardiol*. 2012;59:153-163.
17. Szychta W, Werys K, Barczuk-Falecka M, Postula M, Malek LA. Validation of performance of free of charge plugin for the open-source platform to perform cardiac segmentation in magnetic resonance imaging. *Heart Beat Journal*. 2018;3:83-89.
18. Jung S, Aliberti J, Graemmel P, Sunshine MJ, Kreutzberg GW, Sher A, Littman DR. Analysis of fractalkine receptor CX(3)CR1 function by targeted deletion and green fluorescent protein reporter gene insertion. *Mol Cell Biol*. 2000;20:4106-4114.
19. Cerqueira MD, Weissman NJ, Dilsizian V, Jacobs AK, Kaul S, Laskey WK, Pennell DJ, Rumberger JA, Ryan T, Verani MS. Standardized myocardial segmentation and nomenclature for tomographic imaging of the heart. A statement for healthcare professionals from the Cardiac Imaging Committee of the Council on Clinical Cardiology of the American Heart Association. *Int J Cardiovasc Imaging*. 2002;18:539-542.
20. Lavine KJ, Epelman S, Uchida K, Weber KJ, Nichols CG, Schilling JD, Ornitz DM, Randolph GJ, Mann DL. Distinct macrophage lineages contribute to disparate patterns of cardiac recovery and remodeling in the neonatal and adult heart. *Proc Natl Acad Scie USA*. 2014;111:16029-16034.
21. Vagnozzi RJ, Maillet M, Sargent MA, Khalil H, Johansen AKZ, Schwanekamp JA, York AJ, Huang V, Nahrendorf M, Sadayappan S, et al. An acute immune response underlies the benefit of cardiac stem cell therapy. *Nature*. 2020;577:405-409.
22. Maes D, Sibila M, Kuhnert P, Segales J, Haesebrouck F, Pieters M. Update on Mycoplasma

hyopneumoniae infections in pigs: Knowledge gaps for improved disease control. *Transbound Emerg Dis*. 2018;65 Suppl 1:110-124.

23. Davis RW, Eggleston H, Johnson F, Nahrendorf M, Bock PE, Peterson T, Panizzi P. In Vivo Tracking of Streptococcal Infections of Subcutaneous Origin in a Murine Model. *Molecular Imaging and Biology*. 2015;17:793-801.
24. Ridker PM, Everett BM, Thuren T, MacFadyen JG, Chang WH, Ballantyne C, Fonseca F, Nicolau J, Koenig W, Anker SD, et al. Antiinflammatory Therapy with Canakinumab for Atherosclerotic Disease. *N Engl J Med*. 2017;377:1119-1131.
25. Hays MT, Watson EE, Thomas SR, Stabin M. MIRD dose estimate report no. 19: radiation absorbed dose estimates from (18)F-FDG. *J Nucl Med*. 2002;43:210-214.
26. Laforest R, Dehdashti F, Lewis JS, Schwarz SW. Dosimetry of 60/61/62/64Cu-ATSM: a hypoxia imaging agent for PET. *Eur J Nucl Med Mol Imaging*. 2005;32:764-770.
27. Tamura K, Kurihara H, Yonemori K, Tsuda H, Suzuki J, Kono Y, Honda N, Kodaira M, Yamamoto H, Yunokawa M, et al. 64Cu-DOTA-trastuzumab PET imaging in patients with HER2-positive breast cancer. *J Nucl Med*. 2013;54:1869-1875.
28. Benezra M, Penate-Medina O, Zanzonico PB, Schaer D, Ow H, Burns A, DeStanchina E, Longo V, Herz E, Iyer S, et al. Multimodal silica nanoparticles are effective cancer-targeted probes in a model of human melanoma. *J Clin Invest*. 2011;121:2768-2780.
29. Lavin Y, Mortha A, Rahman A, Merad M. Regulation of macrophage development and function in peripheral tissues. *Nature Reviews Immunology*. 2015;15:731.
30. Ruparelia N, Chai JT, Fisher EA, Choudhury RP. Inflammatory processes in cardiovascular disease: a route to targeted therapies. *Nat Rev Cardiol*. 2017;14:133-144.
31. Mulder WJ, Jaffer FA, Fayad ZA, Nahrendorf M. Imaging and nanomedicine in inflammatory atherosclerosis. *Sci Transl Med*. 2014;6:239sr1.
32. Cassetta L, Pollard JW. Targeting macrophages: therapeutic approaches in cancer. *Nat Rev Drug Discov*. 2018;17:887-904.
33. Harisinghani MG, Barentsz J, Hahn PF, Deserno WM, Tabatabaei S, van de Kaa CH, de la Rosette J, Weissleder R. Noninvasive detection of clinically occult lymph-node metastases in prostate cancer. *N Engl J Med*. 2003;348:2491-2499.
34. Kooi ME, Cappendijk VC, Cleutjens KB, Kessels AG, Kitslaar PJ, Borgers M, Frederik PM, Daemen MJ, van Engelshoven JM. Accumulation of ultrasmall superparamagnetic particles of iron oxide in human atherosclerotic plaques can be detected by in vivo

magnetic resonance imaging. *Circulation*. 2003;107:2453-2458.

35. Sosnovik DE, Nahrendorf M, Deliolanis N, Novikov M, Aikawa E, Josephson L, Rosenzweig A, Weissleder R, Ntziachristos V. Fluorescence tomography and magnetic resonance imaging of myocardial macrophage infiltration in infarcted myocardium in vivo. *Circulation*. 2007;115:1384-1391.
36. Alam SR, Shah AS, Richards J, Lang NN, Barnes G, Joshi N, MacGillivray T, McKillop G, Mirsadraee S, Payne J, et al. Ultrasmall superparamagnetic particles of iron oxide in patients with acute myocardial infarction: early clinical experience. *Circ Cardiovasc Imaging*. 2012;5:559-565.
37. Nahrendorf M, Zhang H, Hembrador S, Panizzi P, Sosnovik DE, Aikawa E, Libby P, Swirski FK, Weissleder R. Nanoparticle PET-CT imaging of macrophages in inflammatory atherosclerosis. *Circulation*. 2008;117:379-387.
38. Majmudar MD, Yoo J, Keliher EJ, Truelove JJ, Iwamoto Y, Sena B, Dutta P, Borodovsky A, Fitzgerald K, Di Carli MF, et al. Polymeric nanoparticle PET/MR imaging allows macrophage detection in atherosclerotic plaques. *Circ Res*. 2013;112:755-761.
39. Keliher EJ, Ye Y-X, Wojtkiewicz GR, Aguirre AD, Tricot B, Senders ML, Groenen H, Fay F, Perez-Medina C, Calcagno C, et al. Polyglucose nanoparticles with renal elimination and macrophage avidity facilitate PET imaging in ischaemic heart disease. *Nature communications*. 2017;8:14064.
40. Weissleder R, Nahrendorf M, Pittet MJ. Imaging macrophages with nanoparticles. *Nat Mater*. 2014;13:125-138.
41. Heo GS, Kopecky B, Sultan D, Ou M, Feng G, Bajpai G, Zhang X, Luehmann H, Detering L, Su Y, et al. Molecular Imaging Visualizes Recruitment of Inflammatory Monocytes and Macrophages to the Injured Heart. *Circ Res*. 2019;124:881-890.

Supplementary materials

Online Materials and Methods

Synthesis of ^{64}Cu-Macrin and ^{VT680}Macrin

Macrin is a spherically shaped dextran nanoparticle with a hydrodynamic diameter of ~20 nm15 which is composed of FDA-approved polyglucose, L-lysine cross-linkers and a radionuclide chelator. Macrin nanoparticles were synthesized from carboxymethylated polyglucose (4 kDa MW, 5% COOH, TdB consultancy) and L-lysine via amide bond formation. In brief, carboxyl groups were activated by the coupling reagents EDC and NHS, followed by cross linking through L-lysine in aqueous media. After ethanol precipitation and dialysis (MWCO 8-10 kDa), Macrin nanoparticles (NPs) were lyophilized and further functionalized. Amino groups of MacrinNPs were conjugated with radioisotope chelators (NODA-GA-NHS, Chematek) or near infrared fluorophores (VT680-NHS, Perkin Elmer) for PET or optical imaging, respectively. Remaining amine residues were succinylated to prevent interactions with plasma proteins by increasing Macrin's negative surface charge. Unreacted small molecules were removed by size exclusion methods. Pure Macrin-NODA was lyophilized and stored at -20 °C until use. ^{VT680}Macrin was stored in phosphate buffered saline (PBS). Macrin-NODA was characterized by dynamic light scattering and zeta potential (Zetasizer Nano, Malvern Panalytical Instruments Inc.): hydrodynamic diameter 16.6 ± 1.6 nm, polydispersity index 0.29 ± 0.03 and zeta -6.46 ± 0.63 mV. ^{64}Cu-Macrin was prepared under metal-free conditions. Briefly, ^{64}CuCl2 in 0.1 N HCl (University of Wisconsin) was added into Macrin-NODA buffer solution, and the mixture was incubated for 30 min at 90 °C. ^{64}Cu-Macrin (~20 MBq/μg Macrin) was obtained with ~95% radiochemical yield (decay-corrected) and >99% radiochemical purity, as determined by radioTLC using a 50 mM aqueous EDTA solution as an eluent. Before administration to animals, Macrins were reconstituted with saline and sterilized using a 0.22 μm HT Tuffryn Membrane syringe filter (Pall Life Sci).

Mice

C57BL/6J (000664), Cx3cr1$^{GFP/+}$ (B6.129P-Cx3cr^{1tm1Litt}/Jax strain #005582) and *Apoe*^{tm1Unc} (*Apoe*$^{-/-}$, 002052) mice were purchased from The Jackson Laboratory. *Apoe*$^{-/-}$ mice were fed a Western diet (TD.88137, Envigo) starting at age of 10-wk for 14 weeks to develop atherosclerosis and analyzed 24 hrs after Macrin injection. C57BL/6J breeding pairs (8-10 weeks) were used to generate newborn mice, which were imaged at postnatal day 5. Mice were housed in a temperature-controlled room with a 12 hours light and 12 hours dark cycle and acclimated at least 3 days prior to animal experiments under specific pathogen-free conditions. All experiments were approved by the Institutional Animal Care and Use Committee (IACUC) of the Massachusetts General Hospital (MGH).

Myocardial infarction in mice

Coronary ligation was conducted under sterile conditions to induce MI in female or male mice (C57BL/6J) aged 8-12 weeks. Mouse thorax fur was removed and mice were anesthetized with 2% isoflurane. For disinfection, 80% isopropyl alcohol and betadine were applied on the surgical area, and mice were intubated with a 22G catheter for ventilation. The left fourth intercostal space was located, and a 0.5 cm incision was made. The epicardial tissue was carefully cut open. The left anterior descending artery was permanently ligated with an 8.0 nylon monofilament suture (Ethicon, Somerville, NJ). The intercostal space and the skin wound were closed with 5.0 nylon monofilament sutures (Ethicon, Somerville, NJ). Mice were extubated and allowed to recover on a heating pad. All mice received buprenorphine (0.1 mg/kg i.p.) twice for three days.

Cecal ligation and puncture in mice

Bacterial peritonitis was induced via cecal ligation and puncture (CLP) under sterile conditions. Mice were anesthetized with 2% isoflurane and anesthesia was maintained through nose cones. A 1 cm abdominal incision was made parallel to the linea alba. The linea alba was carefully cut open to reveal the cecum. To induce mild-to-moderate peritonitis, ~0.6 cm of the cecal tip was

ligated using a 5.0 nylon suture filament. A 22G needle was used to puncture the cecal wall, and a small amount of feces protruded into the peritoneal cavity. The linea alba was sutured using a 5.0 nylon monofilament. Mice received 0.5 mL saline for rehydration intraperitoneally. The skin was carefully stapled with 7 mm staples (Harvard Apparatus), and mice were allowed to recover on a heating pad. Buprenorphine was used for analgesia as described above.

Pneumonia in mice

Pneumonia was induced in mice with bioluminescent streptococcus pneumoniae Xen-10 strain A66.1 serotype 3 (Caliper, LifeSciences)[1]. The bacterial colonies were cultured on TrypticaseTM Soy Agar with 5% sheep blood (Fisher, BD Diagnostics) at 37°C and 5% CO2 without aeration. Bacterial colonies were passaged daily onto new plates. To prepare for infection, bacterial colonies were transferred into Brain-Heart-Infusion broth (BHI, Sigma-Aldrich) containing 5% sheep blood (Carolina Biological Supply) and 200 µg/mL kanamycin (Sigma-Aldrich). Bacteria were allowed to grow for 3 hours. Bacterial concentration was estimated from optical density and bioluminescence. We chose a sublethal bacterial dose of ~1-2 x 10^5 colony-forming units to infect 10-week-old female C57BL/6J mice. To this end, the mice's thorax fur was shaved. Mice were anesthetized with 2% isoflurane and intubated with a 22G catheter in an upright position. The corresponding volume of BHI broth was pipetted onto the catheter. After inhalation, mice were kept in an upright position to ensure full uptake of the bacterial dose. Bacterial bioluminescence was recorded with a combined bioluminescence/X-ray scanner (AmiX, Spectral Instruments Imaging Co.) 24 and 48 hours after infection. The scanner was set at medium binning with exposure times between 20 seconds and 8 min. A corresponding X-ray was obtained after each bioluminescence scan to confirm anatomical localization of the signal. Bioluminescent images were analyzed with AMIView software (V2.8) and FIJI (NIH). Region of interests were placed over the lungs and background bioluminescence was subtracted. Signal strength was expressed as photons per second.

Rabbit model of atherosclerosis

Male New Zealand White (NZW) rabbits (2.5-3.0 months old) were purchased from Charles River Laboratories (Wilmington, MA). To induce the formation of atherosclerotic plaques, endothelial denudation of the aorta was performed. Anesthesia was induced in rabbits with an intramuscular (i.m.) administrations of ketamine (20 mg/kg) (Fort Dodge Animal Health, Overland Park, Kansas, USA) and xylazine (5 mg/kg) (Bayer AG, Leverkusen, Germany). The right femoral artery was identified and used to give access to a 4F-Fogarty embolectomy catheter (Edwards Lifesciences, Irvine, CA) which was inflated at the level of the left subclavian artery and slowly deflated while retracting until the iliac bifurcation, all performed under X-ray guidance (Philips Allura Xper FD20/10, Philips Healthcare, Amsterdam, The Netherlands). After 4 weeks, the procedure was repeated on the contralateral side. Two weeks before the first surgery mice began a cholesterol-rich diet of regular chow enriched with 0.3% cholesterol and 4.7% coconut oil (Research Diets, Inc. Brunswick, NJ), for a total of 8 weeks. Hereafter the diet was changed to a 0.15% enriched cholesterol diet that continued for the remaining months until experiments took place. Untreated healthy rabbits were fed a regular chow diet to serve as controls.

Coronary ligation surgery in rabbits

To induce myocardial infarction in rabbits, we permanently ligated the marginal artery branching from the left circumflex artery. Anesthesia was induced in rabbits with an intramuscular (i.m.) administrations of ketamine (20 mg/kg) (Fort Dodge Animal Health, Overland Park, Kansas, USA) and xylazine (5 mg/kg) (Bayer AG, Leverkusen, Germany). Rabbits were subsequently intubated for the remainder of the procedure and provided with a mixture of oxygen and isoflurane. During the surgical procedure, rabbits were additionally monitored using an ECG and pulse oximeter. After shaving the thorax, disinfection was performed using Povidone-iodine. A partial sternotomy was performed, after which the heart was visualized using a retractor. The pericardium was opened using sharp curved Metzenbaum scissors. Using a Prolene 6-0, a permanent ligation was placed at the apex of

the heart for maneuvering and to prevent any collateral artery formation. After identification of the first major branch from the left circumflex artery, a permanent ligation was placed using a Prolene 6-0. To confirm infarct development, purple coloring of the myocardium was observed while the ECG simultaneously displayed ST elevations. If there was no coloration, another marginal artery was identified and ligated. After the permanent ligation was placed, the pericardium was left open to prevent a possible tamponade. The sternum was closed using a Prolene 0-0, while muscles were approximated and the skin was closed[2]. All rabbits were monitored and kept on oxygen until anesthesia wore off and independent breathing was observed. All animal experiments were performed in accordance with protocols approved by the Institutional Animal Care and Use Committees of Mount Sinai and followed National Institutes of Health guidelines for animal welfare.

Myocardial ischemia/reperfusion injury in mini-swine

Three male and three female Yucatan mini-swine (9 months old, average weight 45.4 kg) were purchased from Exemplar Genetics (Sioux Center, IA). Animals were allowed to acclimate for one week before PET/MR imaging. A bolus of amiodarone (1–3 mg/kg) was given intravenously. Atropine (0.1 mg/kg), amiodarone (3 mg/kg) and potassium acetate (20 mEq) in saline were continuously infused at the rate of 300 mL/hour for the duration of the procedure. A 7-Fr hockey-stick catheter (Cordis, Miami, FL) was advanced to the left coronary artery. After the coronary angiogram, a 0.014-inch guide wire (Abbott, Park, IL) was advanced into the LAD and a 8-mm-long, 4.0-mm NC TREC over-the-wire balloon (Abbott) was advanced to the proximal part of the coronary artery. The balloon was then inflated to 3–4 atm for 90 minutes followed by reperfusion. After confirmation of hemodynamic stability, animals were allowed to recover. Intramuscular injections of nitroglycerine and furosemide were administered. Intravenous saline with amiodarone, atropine and potassium acetate infusion was decreased to 50 mL/hour and given overnight. The animals were housed in their cages and monitored daily.

Flow cytometry

Mice received ^{VT680}Macrin intravenously 24 hours before sacrifice. A body weight-adjusted dose was administered to mice. Adult mice received 10 nmol VT680XL in 740 µg Macrin while 5-dayold mice received 2 nmol VT680XL in 128 µg Macrin. Under anesthesia with 2% isoflurane, the right heart auricle was cut off, and mice were perfused with 3-20 mL of phosphate buffered saline (adjusted to body weight) via cardiac puncture using a 22G needle. Hearts, lungs and aortas were carefully excised, and organ weights were recorded using a fine scale. Harvested organs were thoroughly minced in a digestion cocktail containing 450 U/mL collagenase I (Sigma), 125 U/mL collagenase XI (Sigma), 60 U/mL hyaluronidase I-S (Sigma), 60 U/mL DNase I (Sigma) and 20 µL/mL HEPES buffer (Mediatech Inc.) in PBS (Lonza). Samples were incubated on a shaker at 750 rpm for 1 hour at 37 °C. PBS containing 0.5% bovine serum albumin (FACS buffer) was used to filter tissue suspensions through 40 µm cell strainers. Samples were centrifuged at 340 g and 4°C for 7 min. The supernatants were discarded, and the cell pellets were diluted in 300 µL of FACS buffer. Cells were labeled with a lineage antibody mix and a selection of antibodies against myeloid and macrophage epitopes. The following antibodies were used: PE CD45R/B220 anti-mouse/human (Clone RA3-6B2, Biolegend); PE TER-119 rat anti-mouse (Clone TER-119, BD Pharmingen); PE CD49b antimouse (Clone DX5, Biolegend); PE CD90.2 anti-mouse (Clone 53-2.1;30-H12, Biolegend) and PE NK1.1 anti-mouse (Clone PK136, Biolegend); FITC-CD11b rat anti-mouse (Clone M1/70, Biolegend); PerCP/Cy5.5 rat anti-mouse Ly6C (Clone HK1.4, Biolegend); PE/Cy7 anti-mouse F4/80 (Clone BM8, Biolegend); BV421 CD64 anti-mouse (Clone X54-5/7.1, Biolegend); PE Ly6G rat anti-mouse (Clone1A8, BD Pharmingen); FITC, PE/Cy7 CD11b anti-mouse/human (Clone M1/70, Biolegend); BV510 anti-mouse CD11c (Clone N418, Biolegend); PerCP/Cy5.5 CD31 anti-mouse (Clone 390, Biolegend); BV421 rat anti-mouse Siglec-F (Clone E50-2440 BD Biosciences); BV605 anti-mouse I-A/I-E (Clone M5/144.15.2, Biolegend); BV711 rat anti-mouse CD45 (Clone 30-F11, BD Bioscience); APC/Cy7 Ly6G anti-mouse (Clone 1A8, Biolegend); APC/ Cy7 CD3 anti-mouse (Clone 17A2, Biolegend); APC/Cy7 CD19 anti-mouse (Clone 6D5, Biolegend); PE MEFSK4 anti-mouse (Clone mEF-SK4, Miltenyi Biotech); PE MHCII anti-mouse (Clone

M5/114.15.2, Biolegend); BV605 CCR2 anti-mouse (Clone SA203G11, Biolegend). All samples were incubated in a 1:100-1:600 dilution at 4°C for 30 min. Next, samples were washed in 1 mL FACS buffer and centrifuged as described above. Data were recorded using a LSR2 flow cytometer. FlowJo X 10.0 software (Treestar) was used for analysis. A hematocytometer was used to obtain cell numbers per sample. Cardiac macrophages were identified as lineage^{low} Ly6G^{low} CD11b^{high} CD64^{high} F4/80^{high} Ly6C^{low} or CD45^{high} Ly6G^{neg} CD11b^{high} CD64^{high}. Cardiac and aortic fibroblasts were identified as CD45^{neg} CD31^{neg} MEFSK4^{pos} and endothelial cells as CD45^{neg} CD31^{high}. Alveolar macrophages were identified as CD11c^{high} SSC-A^{high} MHCII^{low} CD64^{high} Siglec-F^{high} CD11b^{low}. Lung interstitial macrophages were identified as CD11c^{intermediate} SSC-A^{low} MHCII^{high} CD64^{high} CD11b^{high} Siglec-F^{low}. Aortic lymphocytes were identified as CD45^{high} CD11b^{neg} lineage^{pos}, aortic neutrophils as CD45^{high} CD11b^{pos} lineage^{pos}, aortic macrophages as CD45h^{igh} CD11b^{pos} lineage^{neg} Ly6C^{low} F4/80^{pos}, and aortic monocytes as CD45^{high} CD11b^{pos} lineage^{neg} Ly6C^{high} F4/80^{low}.

Ex vivo biodistribution in mice

After PET/CT imaging, mice were euthanized and perfused with PBS (2-20 mL) through the left ventricle prior to organ harvesting. Excised organs were weighed, and radioactivity of organs was measured using a gamma counter (1480 Wizard 3-inch, PerkinElmer, Waltham, MA). Percent injected dose per gram tissue was calculated after corrections of radioisotope decay and residual activity at the injection site.

Biodistribution of ^{64}Cu-macrin in healthy mice for human dosimetry

The whole organ distribution of ^{64}Cu-Macrin was evaluated in healthy adult mice (C57BL/6J, 9 weeks old, 23.2 ± 3.0 g, mean ± S.D.) at 1 h, 4 h, 24 h and 48 h post-injection (4 females and 4 males per time point). Mice received tail-vein injections of ^{64}Cu-Macrin (0.040 ± 0.007 µg/g, 6.6 ± 1.1 µCi/g in 130 ± 10 µL) under anesthesia (2% isoflurane with 1 L/min O2). Mice were euthanized and perfused with PBS (20 mL) through the left ventricle prior to

organ harvesting. The following tissues and organs were collected: brain, blood, lungs, liver, spleen, right kidney, empty bladder, left rectus femoris muscle, fat, heart, brain, left femur bone, adrenals, empty stomach, empty small intestine, urine, uterus, ovaries and testes. Excised organs were weighed and subjected to radioactivity measurement using a gamma counter (1480 Wizard 3-inch, PerkinElmer, Waltham, MA). Biodistribution data were obtained after corrections for radioisotope decay and residual activity at the injection site.

Triphenyltetrazolium staining and autoradiography of mouse heart tissue

To visualize the infarct area, sliced myocardium (1 mm) was incubated with freshly prepared 1% triphenyltetrazolium chloride (TTC, Sigma Aldrich) in PBS for 30 min at 37 °C. Stained tissues were fixed in 10% formalin for 20 min and then captured with a digital flatbed scanner (HP Scanjet). Tissue uptake and distribution of ^{64}Cu-Macrin in myocardium was imaged by digital autoradiography. The tissue was placed on a film cassette and exposed on a storage phosphor screen (GE Healthcare) for 10 hours at room temperature. The phosphor screen was scanned at a pixel resolution of 25 μm with a Typhoon 9410 (Amersham Bioscience). The data were processed using ImageQuant software (Amersham Biosciences) or FIJI (NIH).

Cellular uptake of ^{64}Cu-Macrin in myocardium

Mice (C57BL/6, 8-12-wk) received ^{64}Cu-Macrin (190.6±11.9 μCi) intravenously via tail vein. Hearts were harvested 24 hours post injection. Macrin heart tissue uptake was measured by a scintillation counting. Cells were isolated using the same method that was performed for flow cytometric analysis in this manuscript, which yields a cell suspension and excludes matrix and the extracellular spaces. In brief, heart tissue was digested with enzyme cocktail for 1 hour at 37 °C after mincing the tissues into small pieces. The homogenized mixtures were passed through cell strainers (40 μm), washed and centrifuged to yield a cell pellet. The supernatant containing ECM was carefully removed without disturbing the cell pellet. After dehydration for 35

min at 95 °C, the dried cells were weighed. Radioactivity was measured using a gamma counter (1480 Wizard 3-inch, PerkinElmer, Waltham, MA). Macrin cell accumulation was calculated after corrections for radioisotope decay and residual activity at the injection site.

Ex vivo confocal microscopy

Ischemic heart injury and peritonitis were induced in Cx3cr1GFP/+ mice on a C57BL/6 background (5-day-old and 8-10-week old animals) as described in the surgery section. Mice received rhodamine-labeled lectin (Vector Labs, CA) via retro-orbital injection (20-200 µg) 30 min prior to imaging. Organs were harvested 24 hours post i.v. injection of ^{VT680}Macrin (10 nmol VT680XL in 740 µg Macrin for adult mice via tail vein injection and 2 mol VT680XL in 148 µg Macrin for 5-day-old mice via retroorbital injection) after perfusion with PBS (2-20 mL). Excised tissues were placed on glass slides with a few drops of PSB and covered with cover slips. Images were acquired using a FluoView FV1000MPE confocal imaging system (Olympus America). 473, 559 and 635 nm lasers were used with dichroic beam filters (DM473/559/635 nm), beam splitters (SDM473, SDM560, and SDM 640) and emission filters (BA490-540, BA575-620, and BA575-675) (all Olympus America). Confocal images were analyzed using FIJI (NIH). To quantify GFP expressing macrophages in Cx3cr1$^{GFP/+}$ mice, Z-projection of 3D images were created. Confocal images with the same tissue thickness and the same magnification were analyzed. After background subtraction and thresholding, fluorescent areas were quantified, and percent GFP+ area was calculated from the total area.

Histology

After *in vivo* imaging, organs were excised from mice, pigs and rabbits and fixed in 10% formalin solution. Paraffin-embedded tissue sections were deparaffinized and rehydrated prior to staining. H&E staining (Vector Laboratories) was performed to identify cell and tissue morphology. Before IHC for tissue macrophages, heat-induced epitope retrieval (HIER) methods (Retrievagen A pH 6.0, BD Biosciences) and proteolytic-induced epitope

retrieval (PIER) methods (Proteinase K, DAKO/Agilent) were performed for mouse and pig macrophage staining and rabbit macrophage staining, respectively.

Mouse aortic roots and hearts were fixed in 4% paraformaldehyde in PBS overnight. After rinsing in PBS, roots and hearts were placed in 30% sucrose in PBS overnight and embedded in OCT compound. Serial sections were prepared and stained with CD68 (clone: FA-11, BioLegend) for macrophages, CD31(clone: MEC13.3, BD Biosciences) for endothelial cells, alpha smooth muscle Actin (ab5694, Abcam) and Periostin (ab14041, Abcam) for fibroblasts, and Wheat Germ Agglutinin Oregon Green 488 Conjugate (Invitrogen) for cardiomyocytes. Goat anti-Rat IgG Alexa Fluor 488 and Goat anti-Rabbit IgG Alexa Fluore 488 (Invitorgen) were applied and DAPI was used for nuclear counterstaining. Images were acquired using BX63 (Olympus) and processed with Fiji ImageJ software.

For IHC, endogenous peroxidase activity was quenched by 1% hydrogen peroxide. To prevent nonspecific antibody binding, tissues were incubated with 4% normal horse serum or 4% normal rabbit serum. After rinsing, tissues were treated with primary antibodies for macrophages: a pig macrophage antibody (Clone: BA4D5, Bio-Rad Laboratories), a rabbit macrophage antibody (Clone: RAM11, Dako/Agilent) or a mouse Mac-3 antibody (Clone: M3/84, BD Biosciences), accordingly. After overnight incubation at 4 C° and rinsing, secondary antibodies (biotinylated horse anti-mouse IgG/biotinylate rabbit anti rat IgG, Vector Laboratories) were applied to detect macrophages using an Avidin-Biotin Complex Kit (VECTASTAIN Elite ABC HRP Kit, Vector Laboratories). AEC (3-amino-9-ethylcarbazole) substrate-chromogen (DAKO/Agilent) was used as a peroxidase substrate to form a red end-product on the target antigen in macrophages, and the sections were counterstained with Harris Hematoxylin (Sigma-Aldrich). Streptococcus pneumoniae in lung tissues were visualized using a Gram Staining Kit (MilliporeSigma). Slides were scanned by a digital slide scanner (NanoZoomer 2.0RS, Hamamatsu), and images were analyzed with NDP.view2 and FIJI (NIH).

Human dosimetry estimation

Internal human radiation dose was estimated by Organ Level INternal Dose Assessment (OLINDA/EXM, v.1.0) using biodistribution data from mice (Table S1) 3. Animal data was extrapolated to obtain human dosimetry using the direct and the mass extrapolation methods in (ref4). To account for the blood inside each organ, we have used standard values of blood volume on the main organs (i.e. brain, kidney, liver, lungs, small intestine, spleen and testes) as described[5]. For other organs without a specific blood volume, blood was assumed proportionally distributed on the organ based on the relative mass of the organ with respect to the whole-body. Blood volume (mL) per organ was converted to mass (mg) using the density of mouse blood as described[6]. Blood doses per organ were assigned proportionally to the amount of blood mass per organ and added to the calculated organ doses. The cumulative activity (Bq-h/Bq) for each source organ was determined by integrating the area under the time-activity curves using the least-squares analysis. The absorbed dose to the bladder was calculated using the OLINDA bladder model assuming voiding after 1.5 hours, and the dose to the organs was calculated assuming homogeneous distribution of the activity throughout the organ. We conservatively assumed that the pharmacokinetics of urinary clearance was identical to the bi-exponential whole-body clearance, and fractions (0.29 and 0.2 for females and 0.21 and 0.22 for males) and biological half-times (0.03 h and 3.44 h for females and 0.03 h and 2.43 h for males) were used in the voiding bladder model of OLINDA/EXM. Effective doses were calculated in accordance with ICRP-60 organ weighting factor recommendations[4].

Toxicity testing of Macrin in rodents

Sixty Sprague-Dawley rats were used to obtain data on nanoparticle toxicity (Sai Life Sciences Ltd). A single dose of Macrin-NODA solution at 0.13 and 1.3 mg/kg was injected intravenously, which is 100 and 1,000 times higher than the anticipated human dose (5-7 weeks old, female and male, n=5 per sex and group). Macrin-NODA was intravenously administered at doses of 0.13 mg/kg and 1.3 mg/kg. Control group rats received vehicle only and were

handled in a similar manner as the treatment group. Mortality and morbidity were checked at least twice a day during the study period. Clinical signs were recorded at least once a day throughout the study period. Observations included, but were not limited to, evaluation of changes at injection site; changes in skin and fur, eyes and mucous membranes; respiratory, circulatory, autonomic, and central nervous systems; somatomotor activity and behavior patterns. Body weights were recorded periodically during the study period. Rats were subjected to blood sample collection from retro-orbital plexus under light isoflurane anesthesia for clinical pathology analyses. All the animals fasted for 16-18h before blood collection. Following blood collections for clinical pathology 24 hours and 14 days after Macrin administration, rats were euthanized by carbon dioxide asphyxiation. All rats were subjected to a detailed gross pathological examination that included careful examination of the external surface of the body, all orifices and the cranial, thoracic and abdominal cavities and their contents. Major organs, including heart, spleen, thymus, lungs, kidneys and adrenals were processed using standard methods and embedded in paraffin for histopathology. Tissue sections were stained with hematoxylin-eosin and examined by a pathologist.

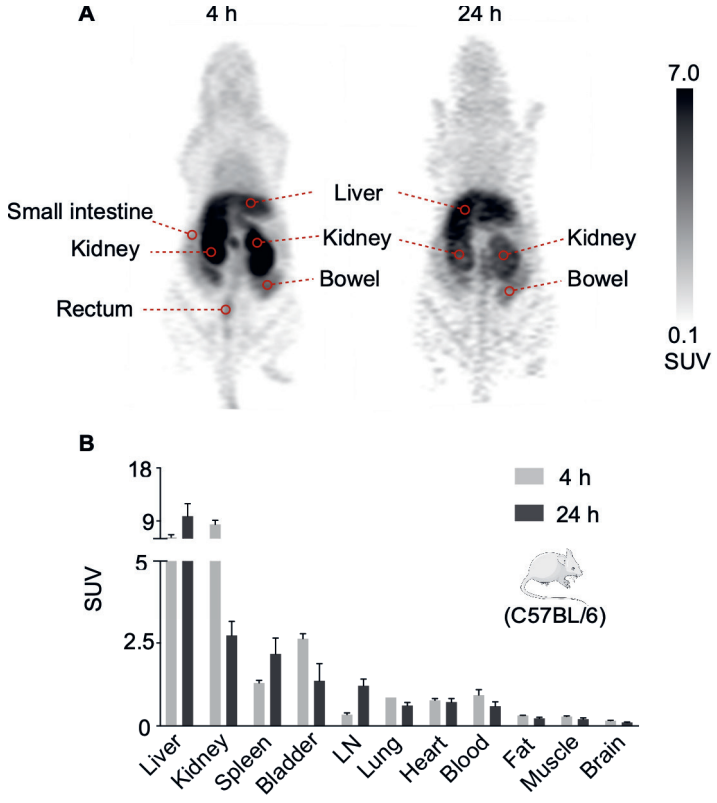
Gamma counting and autoradiography in large animals

^{64}Cu-Macrin uptake in tissues and blood was measured by gamma counting. Shortly after the scan, animals were euthanized. Rabbits and pigs were thoroughly perfused with saline before tissues of interest (liver, spleen, kidney, lung, muscle, bone marrow, bone and heart) were harvested. Rabbit aortas were carefully dissected and rinsed with saline. Samples were weighed and radioactivity was measured on a Wizard2 2480 automatic gamma counter (Perkin Elmer). Radioactivity values were corrected for decay and normalized to tissue weight to express radioactivity concentration as percentage injected dose per gram or kilogram (%ID/g or %ID/kg). Digital autoradiography was performed to determine ^{64}Cu-Macrin distribution within the heart. Hearts were sliced from the apex to the atria. Samples were placed in a film cassette against a phosphorimaging plate (BASMS-2325, Fujifilm, Valhalla, NY) for 41 hours (rabbit aortas) or 39 hours (rabbit heart slices) at -

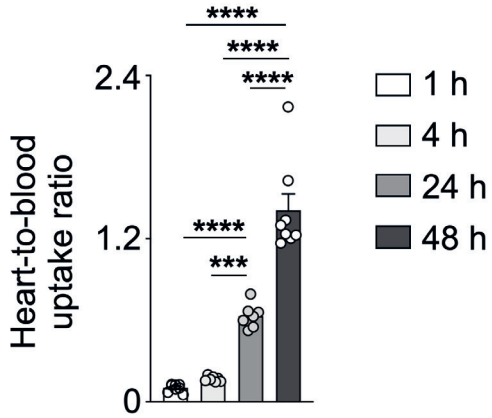
20 °C. Phosphorimaging plates were read at a pixel resolution of 25 µm with a Typhoon 7000IP plate reader (GE Healthcare, Pittsburgh, PA).

Online References

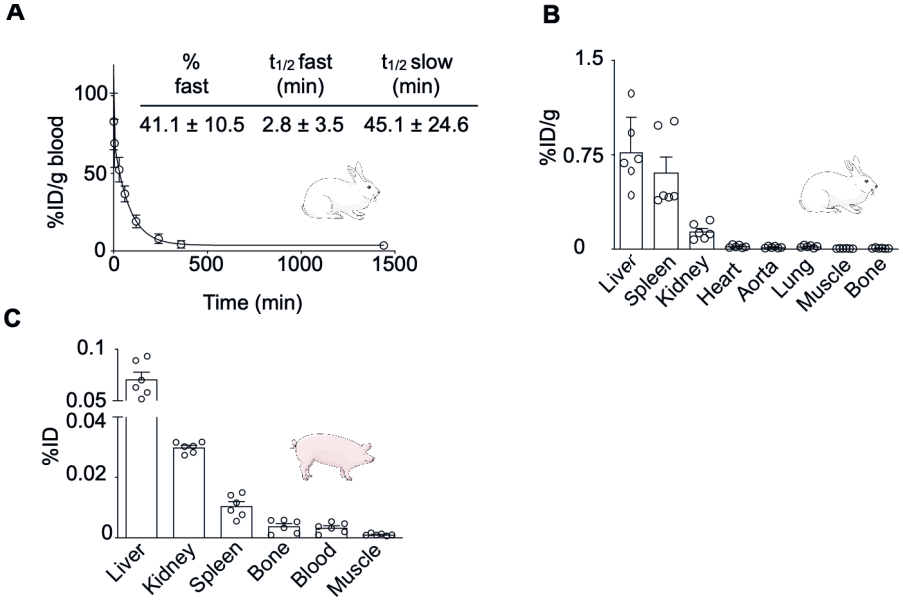
1. Davis RW, Eggleston H, Johnson F, Nahrendorf M, Bock PE, Peterson T, Panizzi P. In Vivo Tracking of Streptococcal Infections of Subcutaneous Origin in a Murine Model. Molecular Imaging and Biology. 2015;17:793-801.
2. Tan MY, Xia B, Xiao Z, Fan ZW, Zhou H, Guo X, Huang YC. Development of a new model for acute myocardial infarction in rabbits. J Vet Med Sci. 2017;79:467-473.
3. Stabin MG, Sparks RB, Crowe E. OLINDA/EXM: the second-generation personal computer software for internal dose assessment in nuclear medicine. The Journal of Nuclear Medicine. 2005;46:1023.
4. 1990 Recommendations of the International Commission on Radiological Protection. Ann ICRP. 1991;21:1-201.
5. Kaliss N, Pressman D. Plasma and blood volumes of mouse organs, as determined with radioactive iodoproteins. Proc Soc Exp Biol Med. 1950;75:16-20.
6. Riches AC, Sharp JG, Thomas DB, Smith SV. Blood volume determination in the mouse. J Physiol. 1973;228:279-284.



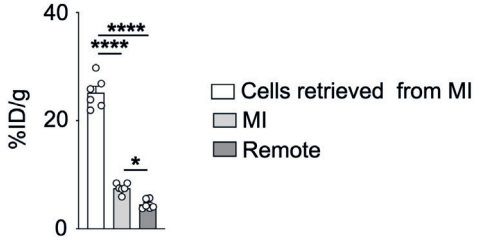
Online Fig. I. Biodistribution of ^{64}Cu-Macrin in C57BL/6 mice. A) Coronal PET images at 4 h and 24 h post injection. B) SUV reflecting ^{64}Cu-Macrin uptake at 4 h (n=2 mice) and 24 (n=5) post injection. LN, lymph node. Data are mean ± SD.



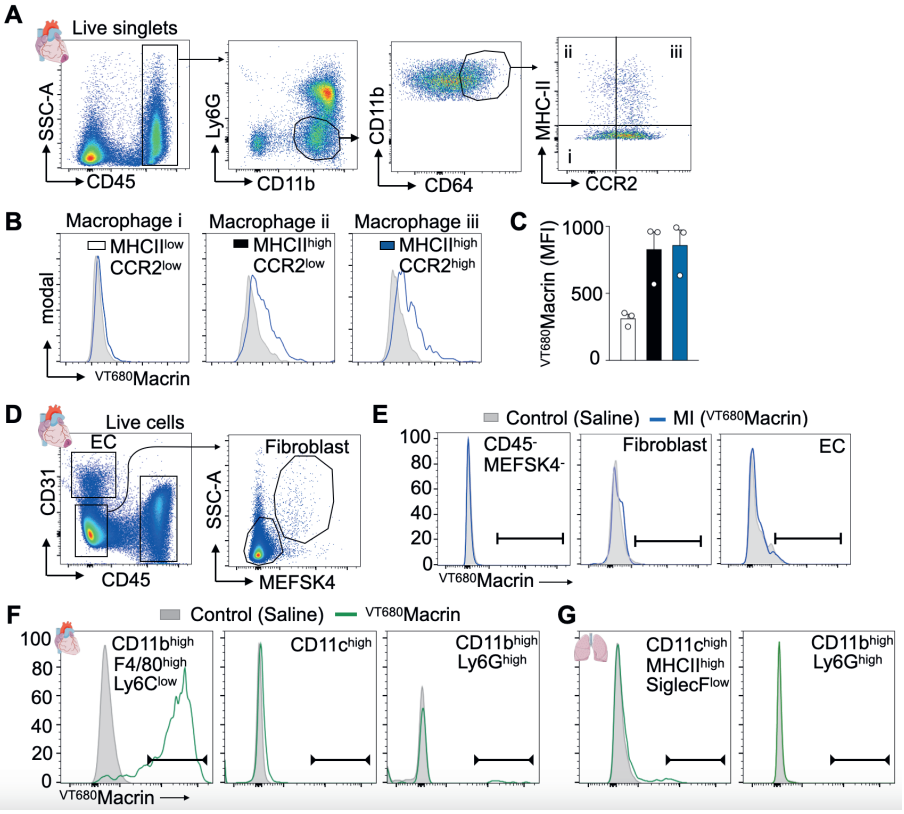
Online Fig. II. ^{64}Cu-Macrin heart-to-blood signal ratio. Heart to blood uptake ratio in healthy mice at 1, 4, 24 and 48 h post ^{64}Cu-Macrin injection (n=8, mean ± SEM).



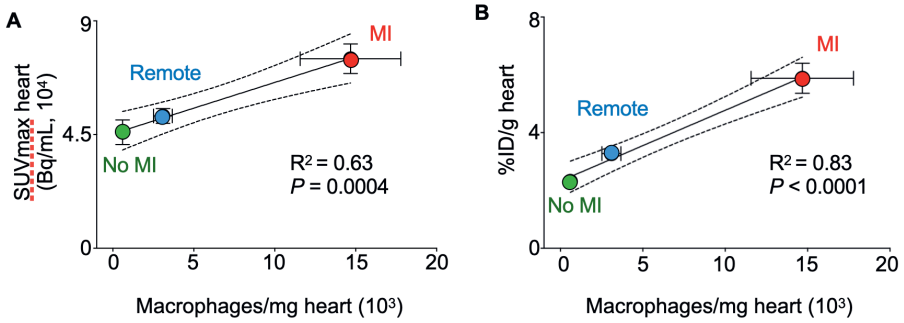
Online Fig. III. Pharmacokinetics and biodistribution of ^{64}Cu-Macrin in rabbits and pigs. A) Blood half-life of ^{64}Cu-Macrin in healthy rabbits (n=6, mean ± SEM). B) Biodistribution of ^{64}Cu-Macrin in rabbits and C) pigs 24 h post-injection (mean ± SEM).



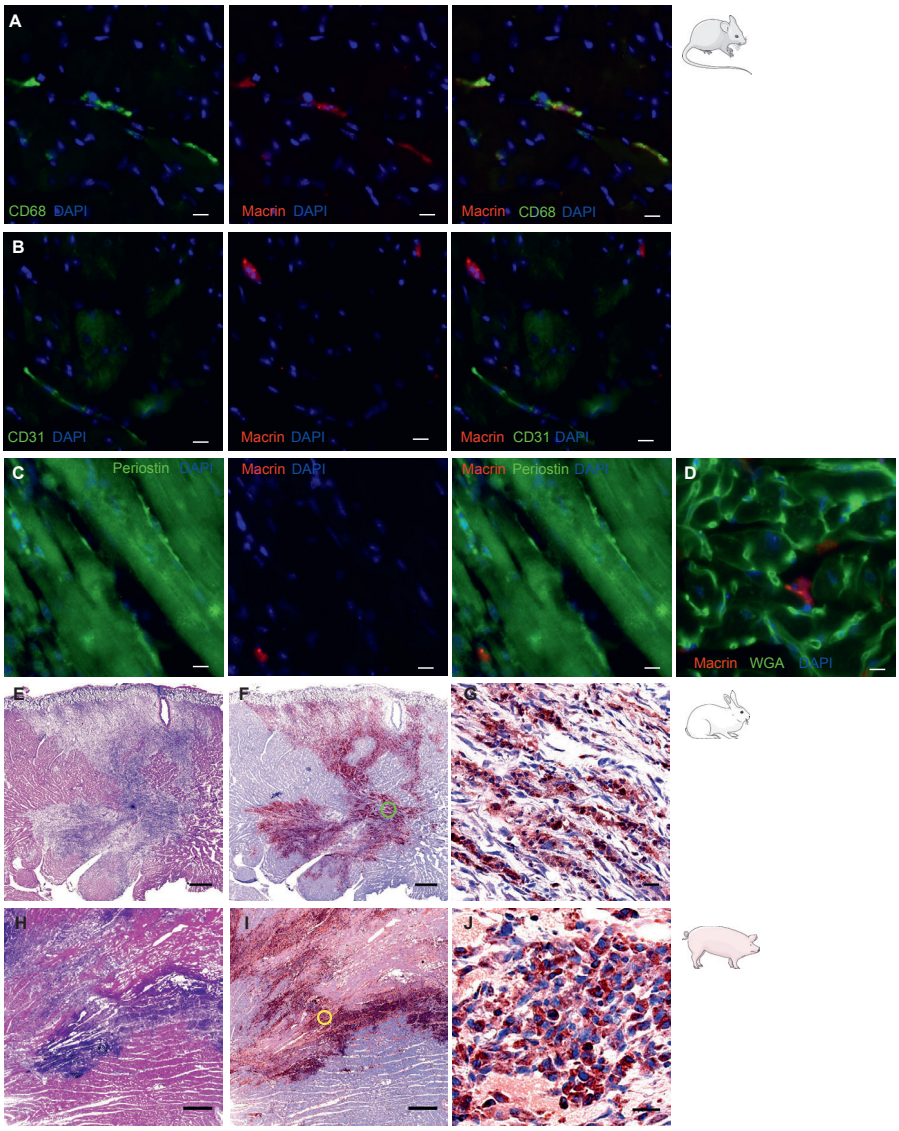
Online Fig. IV. ^{64}Cu-Macrin cellular accumulation. Cells from hearts on day 4 after MI and myocardium were subjected to scintillation counting 24 hours post injection of ^{64}Cu-Macrin (n=6 mice, mean±SEM).



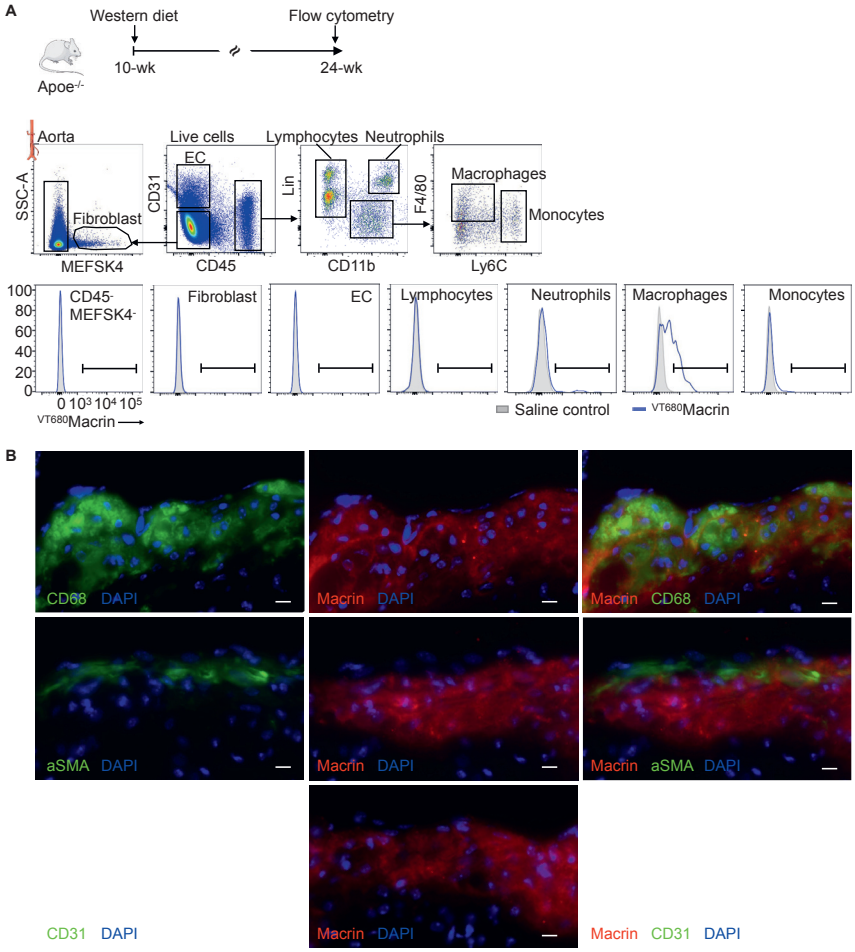
Online Fig. V. ^{VT680}Macrin accumulation in various cells assessed by FACS. A) Flow cytometry gating and B) histograms for ^{VT680}Macrin fluorescent intensity for heart macrophage subsets (grey, saline injected control; blue ^{VT680}Macrin injected mice with MI). C) Mean fluorescence intensity (MFI) for cell subset, n=3 mice, mean±SEM. D) Gating for heart fibroblasts and endothelial cells (EC). E) No uptake was observed in heart fibroblasts and EC. F) ^{VT680}Macrin uptake in cardiac macrophages (left panel), CD11c^{+} dendritic cells (middle) and neutrophils (right). G) ^{VT680}Macrin uptake in CD11c^{high}, MHCII^{high}, SiglecF^{low} cells in lung (left) and neutrophils (right).



Online Fig. VI. Correlation of ^{64}Cu-Macrin tissue concentration with cardiac macrophage density. *In vivo* PET signal intensities were quantified in SUV_{max}. *Ex vivo* Macrin uptake was obtained by scintigraphy. Macrophage numbers were calculated from flow cytometry and correlated with ^{64}Cu-Macrin tissue signal measured *in vivo* A) and *ex vivo* B).



Online Fig. VII. Histology of infarct tissue in mice, rabbits and pigs. A) Immunofluorescence histology in a mouse heart 2 days after MI showing ^{VT680}Macrin uptake into CD68^{+} macrophages but not into B) endothelial cells, C) fibroblasts or D) cardiomyocytes (scale bar, 10 μm). E) H&E staining of rabbit heart day 3 post MI (scale bar, 0.5 mm). F) Immunohistochemistry staining for macrophages in the same tissue. G) High magnification of infarcted myocardium (scale bar, 20 μm). H) H&E staining of pig heart day 3 post MI (scale bar, 0.5 mm). I) Immunohistochemistry staining for macrophages in the same tissue (scale bar, 0.5 mm). J) High magnification of infarcted myocardium (scale bar, 20 μm).



Online Fig. VIII. Macrin cellular distribution in atherosclerotic plaques. A) Aortic cells were identified by FACS gating as indicated. Fluorescence intensity corresponding to ^{VT680}Macrin uptake is shown in histograms. Blue, ^{VT680}Macrin injected mice with atherosclerosis (representative plots of n=3 mice) compared to saline injected mice with atherosclerosis (grey). B) Immunoreactive staining for CD68^{+} macrophages, aSMA^{+} fibroblasts, CD31^{+} endothelial cells and ^{VT680}Macrin fluorescence in aortic root plaques of *Apoe*$^{-/-}$ mice with atherosclerosis (scale bar, 10 μm).

Online Table I. Experimental overview, species and animal numbers. The table summarizes animal models and what they were used for in this study.

disease model	species	intervention	goal	number of animals
acute MI	mouse	coronary ligation	image increase of infarct macrophages	5 control 5 MI
acute MI	mouse	coronary ligation	define cellular uptake of Macrin in heart by FACS and histology	7 control 5 MI
acute MI	rabbit	coronary ligation	image increase of infarct macrophages in large animal	6 control 5 MI
acute MI	pig	90 min balloon occlusion	image increase of infarct macrophages in large animal	6 control 6 MI
newborn heart	mouse	none	image increase of resident macrophages	5 adult 9 newborn
newborn heart	mouse	none	FACS and histology validation in newborn	7 adult 6 newborn
heart in sepsis	mouse	induction of sepsis by cecal ligation and puncture	image increase in heart macrophages during sepsis	5 control 6 sepsis
heart in sepsis	mouse	induction of sepsis by cecal ligation and puncture	FACS and histology validation of heart in sepsis	7 control 4 sepsis
lung after MI	mouse	coronary ligation	image fluctuation of lung macrophages after MI	7 control 8 MI
lung after MI	mouse	coronary ligation	FACS and histology validation in lung after MI	4 control 5 MI
pneumonia	pig	none / accidental finding	image increase of lung macrophages in bacterial pneumonia	8
pneumonia	mouse	intratracheal bacterial instillation	image increase of lung macrophages in pneumonia	7 control 19 pneumonia
atherosclerosis	rabbit	balloon denudation atherogenic diet	image plaque macrophages	6 control 6 atherosclerosis
atherosclerosis	mouse	ApoE$^{-/-}$ mouse atherogenic diet	define cellular uptake of Macrin in plaques	5 atherosclerosis

Online Table II. *Ex vivo* biodistribution of ^{64}Cu-Macrin in healthy mice (C57BL/6, n=4 per sex/time point). Organs were excised at 1, 4, 24 and 48 hours post injection and subjected for scintigraphy. Data are shown in mean ± SD.

%ID/g	1 h			4 h			24 h			48 h		
Liver	28,090	±	2,610	35,420	±	6,660	36,040	±	11,400	32,210	±	6,910
Kidney	22,470	±	3,610	23,030	±	5,920	15,170	±	2,810	9,640	±	0,890
Blood	19,840	±	3,690	11,750	±	2,090	4,176	±	1,111	1,860	±	0,530
Spleen	8,280	±	2,230	10,600	±	2,450	16,230	±	4,950	12,170	±	4,000
Uterus	5,520	±	1,590	4,520	±	1,280	4,720	±	0,820	3,470	±	1,150
Ovaries	4,880	±	0,590	4,070	±	0,850	5,843	±	5,102	3,920	±	1,280
Small intestine	4,650	±	0,470	4,100	±	0,720	4,300	±	1,030	3,300	±	0,620
Stomach	4,400	±	0,980	4,460	±	0,540	3,860	±	1,030	2,850	±	0,370
Bladder	4,640	±	4,140	2,580	±	1,020	2,370	±	0,860	1,670	±	0,610
Lung	2,900	±	1,450	2,840	±	1,530	3,630	±	2,020	3,360	±	1,370
Adrenal	2,600	±	0,850	3,070	±	0,640	4,650	±	0,740	4,460	±	2,110
Heart	2,000	±	0,510	2,010	±	0,320	2,640	±	0,740	2,510	±	0,470
Bone	1,770	±	0,430	1,750	±	0,410	2,780	±	1,380	1,790	±	0,450
Testis	1,330	±	0,150	1,630	±	0,230	1,940	±	0,160	1,470	±	0,100
Muscle	0,500	±	0,170	0,400	±	0,080	0,510	±	0,130	0,450	±	0,090
Fat	0,390	±	0,110	0,310	±	0,090	0,530	±	0,290	0,420	±	0,110
Brain	0,160	±	0,060	0,140	±	0,040	0,270	±	0,060	0,280	±	0,060



5

Macrophage PET imaging in mouse models of cardiovascular disease and cancer with an apolipoprotein-inspired radiotracer

Published in npj Imaging, 2024.

Toner, Y.C.*, Prévot, G.*, van Leent, M.M.T., Munitz, J., Oosterwijk, R., Verschuur, A.V.D., van Elsas, Y., Peric, V., Maas, R.J.F., Ranzenigo, A., Morla- Folch, J., Wang, W., Umali, M., de Dreu, A., Fernandes, J.C., Sullivan, N.A.T., Maier, A., Mason, C., Reiner, T., Fayad, Z.A., Mulder, W.J.M., Teunissen, A.J.P., Pérez-Medina, C.

* These authors contributed equally to this work.

Toner, Y.C. planned and performed the in vivo experiments, including pharmacokinetics and PET/CT imaging, as well as ex vivo assays, such as biodistribution, sample preparation for flow cytometry, TTC staining, autoradiography and histology. In addition, she was responsible for the animal models of myocardial infarct and melanoma. She analyzed the data and wrote the manuscript.

Abstract

Macrophages are key inflammatory mediators in many pathological conditions, including cardiovascular disease (CVD) and cancer, the leading causes of morbidity and mortality worldwide. This makes macrophage burden a valuable diagnostic marker and several strategies to monitor these cells have been reported. However, such strategies are often high-priced, non-specific, invasive, and/or not quantitative. Here, we developed a positron emission tomography (PET) radiotracer based on apolipoprotein A1 (ApoA1), the main protein component of high-density lipoprotein (HDL), which has an inherent affinity for macrophages.

Methods: We radiolabeled an ApoA1-mimetic peptide (mA1) with zirconium-89 (^{89}Zr) to generate a lipoprotein-avid PET probe (^{89}Zr-mA1). We first characterized ^{89}Zr-mA1's affinity for lipoproteins *in vitro* by size exclusion chromatography. To study ^{89}Zr-mA1's *in vivo* behavior and interaction with endogenous lipoproteins, we performed extensive studies in wildtype C57BL/6 and *Apoe*$^{-/-}$ hypercholesterolemic mice. Subsequently, we used *in vivo* PET imaging to study macrophages in melanoma and myocardium infarction using mouse models. The tracer's cell specificity was assessed by histology and mass cytometry (CyTOF).

Results: Our data show that ^{89}Zr-mA1 associates with lipoproteins *in vitro*. This is in line with our *in vivo* experiments, in which we observed longer ^{89}Zr-mA1 circulation times in hypercholesterolemic mice compared to C57BL/6 controls. ^{89}Zr-mA1 displayed a tissue distribution profile similar to ApoA1 and HDL, with high kidney and liver uptake as well as substantial signal in the bone marrow and spleen. The tracer also accumulated in tumors of melanoma-bearing mice and in the ischemic myocardium of infarcted animals. In these sites, CyTOF analyses revealed that ^{nat}Zr-mA1 was predominantly taken up by macrophages.

Conclusion: Our results demonstrate that ^{89}Zr-mA1 associates with lipoproteins and hence accumulates in macrophages *in vivo*. ^{89}Zr-mA1's high uptake in these cells makes it a promising radiotracer for non-invasively and

quantitatively studying conditions characterized by marked changes in macrophage burden.

Keywords: PET imaging, macrophage burden, apolipoprotein A1-mimetic, tumor, myocardial infarct.

Introduction

Macrophages are involved in diverse physiological and pathophysiological processes [1,2]. As key mediators of inflammation, they play a central role in deleterious conditions, including cardiovascular disease (CVD) and cancer [3,4]. For example, after ischemic injury due to myocardial infarction (MI) or stroke, macrophages are recruited to repair and remodel the affected tissue. However, the release of pro-inflammatory mediators by these cells often aggravates the damage, culminating in cell death, necrosis, and in the case of atherosclerosis, dislodging of plaques [5–7]. Similarly, tumors produce growth factors and cytokines that recruit monocytes and induce their differentiation into tumor-associated macrophages (TAMs). These cells then become key regulators of the tumor microenvironment, frequently promoting tumor growth [8], immunosuppression [9], metastasis [10], angiogenesis, and chemoresistance [11]. Consequently, a high TAM burden is typically associated with a poor prognosis [4,12]. Insights into macrophage burden and dynamics, therefore, facilitate diagnosing and stratifying cancer patients. TAM's ability to modulate the immune system's response to tumor growth has led to several TAM-targeting therapies [4,13], some of which have already been trialed [14,15].

Several approaches to image macrophages have been reported in a number of pathological contexts and using various techniques, including magnetic resonance imaging (MRI), positron emission tomography (PET), and optical methods [16–19]. PET imaging often makes use of tracers targeting metabolic processes, such as ^{18}F-FDG. These probes are taken up by activated macrophages due to their high metabolic and proliferative activity, consequently targeting activated macrophages [20]. However, metabolic PET imaging lacks cell specificity and requires extensive dietary preparation to control background signals from physiological glucose metabolism [21]. Nanoparticle-based imaging strategies have been introduced to enhance cellular specificity. These formulations typically rely on macrophages' phagocytic properties and have been exploited in the context of PET,

computed tomography (CT), and MRI [16,22,23]. Macrophage-specific PET imaging has also been reported by targeting membrane proteins (over)expressed on activated macrophages using nanobody-based probes[24–26], and peptide-based radiotracers, such as DOTATATE and pentixafor [27,28]. Small molecule tracers targeting translocator protein (TSPO) have also been successfully used for macrophage PET imaging[29]. Although some of these approaches led to promising results, there is a pressing need for more inexpensive, quantitative, and non-invasive macrophage-avid imaging agents for diagnosing/prognosing inflammatory diseases and TAM-driven tumors, such as gliomas, ovarian and breast cancer.

High-density lipoprotein (HDL) is a natural nanoparticle involved in reverse cholesterol transport [30]. It predominantly consists of phospholipids, cholesterol, and apolipoprotein A1 (ApoA1), through which it binds to several membrane receptors abundantly expressed on macrophages [31]. Capitalizing on this, we have previously used radiolabeled HDL to study macrophage burden in the context of atherosclerosis, cancer, and other diseases [32]. However, the high costs associated with manufacturing and the dispersity of these formulations complicate their clinical translation as PET tracers [33]. Here, we report an ApoA1-inspired PET radiotracer and its use as a tool for studying macrophage burden *in vivo*. The radiotracer consists of an ApoA1-mimetic peptide (mA1) that is labeled with zirconium-89 (^{89}Zr) through desferrioxamine (DFO) to generate a macrophage-avid PET probe (^{89}Zr-mA1). We anticipated that, upon intravenous administration, ^{89}Zr-mA1 would associate with endogenous lipoproteins and subsequently accumulate in macrophages and other phagocytic cells. To test this hypothesis, we extensively studied tracer uptake and behavior in mouse models of normo- and hypercholesterolemia, cancer, and myocardial infarction. To achieve this, we made use of *in vivo* PET imaging and *ex vivo* assays, including CyTOF.

Results

Study outline

We have developed a PET tracer inspired by ApoA1 (^{89}Zr-mA1), the predominant protein in HDL that has a natural ability to interact with phospholipids and cholesterol esters driven by its highly hydrophobic C-terminal domain. The ApoA1-mimetic ^{89}Zr-mA1 also displays this ability, which enables it to bind lipoproteins *in vivo* and subsequently accumulate in phagocytes, as a result of lipoproteins' propensity to interact with these cells. Consequently, ^{89}Zr-mA1 enables non-invasive quantitative PET imaging of macrophage burden (Fig. 1A).

^{89}Zr-mA1 synthesis

We used an ApoA1 mimetic polypeptide (37pA) that consists of two identical class A amphipathic helices linked by a proline (Fig. 1B). We selected this sequence based on previously published literature [34,35]. A cysteine residue was incorporated on the C terminus of our peptide to enable its site-specific conjugation with deferoxamine (DFO-Mal) *via* the maleimide-thiol reaction (Fig. 1C, left). HPLC analysis confirmed the purity of our mA1-DFO conjugate (Supplementary Fig. 1A). LC-MS corroborated the identity and purity of the mA1-DFO product (Supplementary Fig. 1B). mA1-DFO was subsequently radiolabeled with ^{89}Zr (Fig. 1C, right). Chelation of ^{89}Zr afforded the radiolabeled peptide 75 ± 5 % radiochemical yield (amount of activity bound to mA1 as a percentage of starting activity corrected for radioactive decay) and >98 % radiochemical purity (n = 6), as assessed by radio-TLC (Supplementary Fig. 1C). The tracer's specific activity was approximately 170 TBq/mol (n = 6).

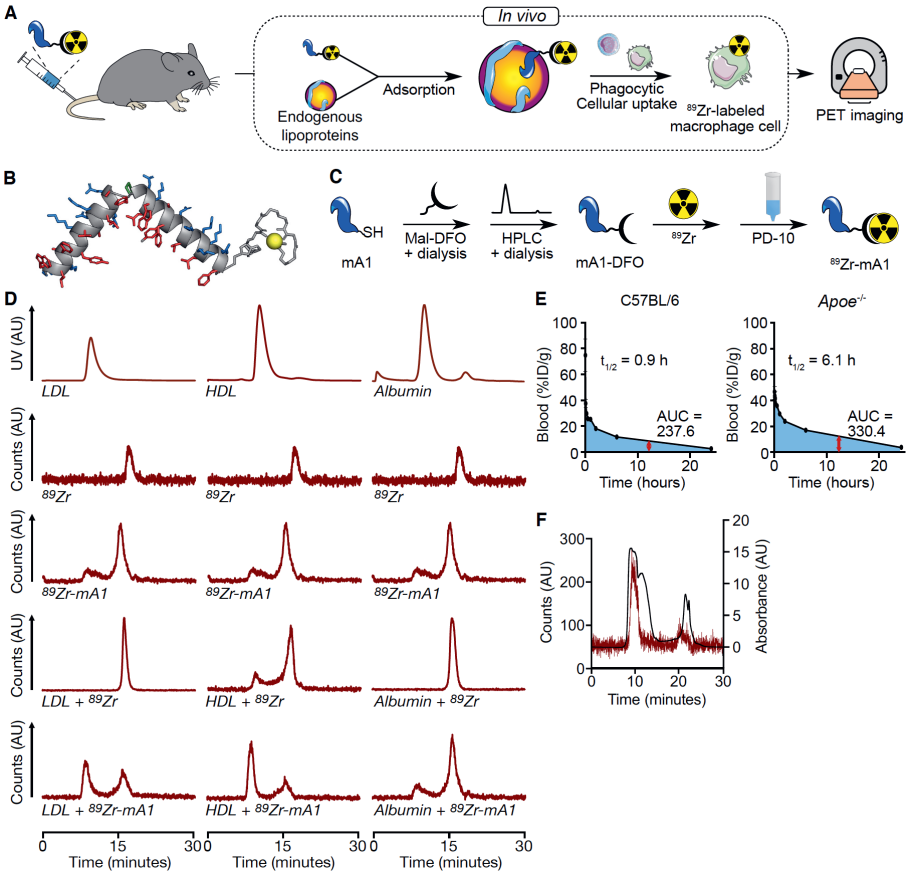


Figure 1. ^{89}Zr-mA1 as a PET probe for monitoring macrophage burden. A) ^{89}Zr-mA1 binds lipoproteins *in vivo*. These nanoparticles are subsequently taken up by macrophages, enabling PET imaging of macrophage burden. B) Optimized 3D conformation of ^{89}Zr-mA1 calculated using AlphaFold software. C) Schematic overview of ^{89}Zr-mA1 synthesis. mA1 has a C-terminus cysteine which facilitates site-specific conjugation with maleimide-functionalized deferoxamine (Mal-DFO) and subsequent radiolabeling with ^{89}Zr to form ^{89}Zr-mA1. D) *In vitro* binding of ^{89}Zr-mA1 to plasma constituents. Bare ^{89}Zr and ^{89}Zr-mA1 were incubated with either LDL, HDL or albumin before being analyzed by size-exclusion chromatography. E) Blood pharmacokinetics for intravenously infused ^{89}Zr-mA1 in C57BL/6 (n = 6) and *Apoe*$^{-/-}$ mice (n = 4) as well as the associated weighted half-lives and area under the curve values. F) Representative size exclusion chromatograms of a plasma sample taken from an *Apoe*$^{-/-}$ mouse 30 min after administration of ^{89}Zr-mA1, showing UV (black) and radioactivity (red) traces. AU, arbitrary units; AUC, area under the curve.

^{89}Zr-mA1 binds to plasma lipoproteins *in vitro*

We assessed ^{89}Zr-mA1's propensity to bind different plasma components by incubating ^{89}Zr-mA1 with HDL, LDL, or albumin and using bare ^{89}Zr as control. After incubation, ^{89}Zr-mA1 efficiently bound to HDL (70% of bound activity) and, to a lesser degree, LDL (with 45% of bound activity) (Fig. 1D). Binding to albumin was minimal, as only 13% of activity was bound to this protein under the same assay conditions. These results imply that the peptide has a high propensity for binding to lipoproteins. In an additional experiment, tracer stability was evaluated by incubating bare ^{89}Zr or ^{89}Zr-mA1 with fetal bovine serum (FBS) at 37 °C and monitoring the free ^{89}Zr fraction by radio-TLC (Supplementary Fig. 1D, left). Under these conditions, ^{89}Zr did not dissociate from tracer. More importantly, bare ^{89}Zr did not bind to serum proteins (Supplementary Fig. 1D, right).

Pharmacokinetics and *in vivo* lipoprotein binding of ^{89}Zr-mA1

To determine ^{89}Zr-mA1's blood circulation time in mice and how this depends on plasma lipoprotein concentrations, we performed pharmacokinetic studies in C57BL/6 and *Apoe*$^{-/-}$ (hypercholesterolemic) mice. The weighted tracer half-lives were 0.9 and 6.1 hours in C57BL/6 and *Apoe*$^{-/-}$ mice, respectively (Fig. 1E). At 30 minutes post-injection (p.i.), *Apoe*$^{-/-}$ blood samples were taken and separated into cellular and plasma fractions. Plasma, which contained 97 ± 2% (n = 4) of blood radioactivity, was subjected to SEC analyses. The radioactivity trace showed two peaks. The first peak had a retention time of 10 minutes, indicating compounds with a mass of >500 kDa, and was accompanied by a large peak in the UV spectrum. Based on these characteristics, we believe this signal stems from radiolabeled lipoproteins. The second peak eluted at approximately 20 minutes and matches well with the 'free' radiolabeled peptide. The larger peak represented 89±5% of the measured total radioactivity area (n = 4, Fig. 1F). These results, combined with our *in vitro* observations, strongly suggest that ^{89}Zr-mA1 rapidly binds endogenous lipoproteins *in vivo*.

^{89}Zr-mA1 PET imaging and biodistribution studies in C57BL/6 mice

We performed dynamic PET imaging in C57BL/6 mice during the first hour after i.v. ^{89}Zr-mA1 administration (Fig. 2A). Images were initially dominated by a high blood pool signal, followed by increasing kidney uptake. The liver and spleen showed a significant uptake within the first ~5 minutes p.i. which remained nearly constant at a standardized uptake value (SUV) of approximately 2 g/mL (Fig. 2B). In a different subset of animals, a static scan was performed at 24 hours p.i., showing strong signals in the liver and kidney (Fig. 2C). *Ex vivo* gamma counting of selected tissues corroborated our PET imaging results (Fig. 2D).

^{89}Zr-mA1 *in vivo* distribution in a macrophage depletion model

To evaluate tracer affinity for macrophages, we employed the clodronate liposome mouse model of macrophage depletion [38,39]. *Ex vivo* biodistribution experiments showed lower radiometric signal in the spleen 1.6 (IQR, 1.4–1.7), vs. 2.1 (IQR, 2.0-2.4) in untreated controls (p= 0.008), an organ targeted by these liposomes (Fig. 2E). This organ functions as a natural reservoir of immune cells, harboring macrophage populations responsible for cytokine production (innate immunity activators), apoptotic cell clearance, antigen presentation and pathogen scavenging [40], further evidencing ^{89}Zr-mA1's ability to target macrophage cells.

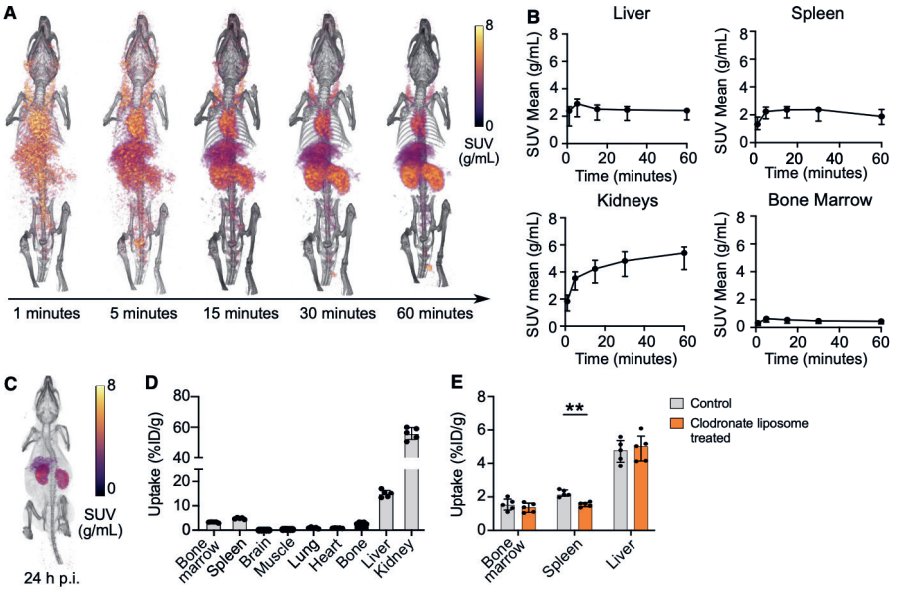


Figure 2. Biodistribution of ^{89}Zr-mA1 in mice. A) Representative 3D-rendered PET/CT images of C57BL/6 mice scanned dynamically for one hour following ^{89}Zr-mA1 injection. B) ^{89}Zr-mA1 pharmacokinetics in specific tissues (n = 4). C) Representative 3D-rendered PET/CT image of a C57BL/6 mouse 24 hours after i.v. tracer injection. D) *Ex vivo* biodistribution as assessed by gamma counting of tissues of interest 24 h p.i. (n = 5). E) *Ex vivo* biodistribution as assessed by gamma counting of tissues of interest 24 h p.i. (n = 5) in mice treated with clodronate liposomes. Matched controls that did not receive clodronate injections are represented in grey.

Employing ^{89}Zr-mA1 in a mouse model of myocardial infarction

Myocardial infarction promotes inflammation due to tissue damage and this is strongly mediated by resident and (recruited) monocyte-derived macrophages [41]. We used a mouse model of MI to evaluate ^{89}Zr-mA1's applicability toward imaging this increased macrophage burden in the infarcted area. Two days after LAD ligation, mice were injected with the radiotracer, and PET-scanned statically at 24 hours p.i. (Fig. 3A). Images revealed an overall ^{89}Zr-mA1 biodistribution similar to that observed in naive C57BL/6 mice, including a high kidney and liver uptake (Supplementary Fig. 2A and B). *Ex vivo* gamma counting of these organs at 1- and 24- hours post injection corroborated our PET observations (Supplementary Fig. 2C). Tracer

accumulation in the infarcted area was significantly higher at 24 h p.i. (Fig. 3B) as indicated by a 2-fold stronger signal compared to the remote myocardium (p=0.03) (Fig. 3C). MI-to-blood and MI-to-muscle (skeletal) ratios were 0.2 (IQR, 0.2-0.3) and 17 (IQR, 16.1-19.6) at 1 h p.i., respectively, and 2 (IQR, 1.7-2.2) and 15.1 (IQR, 10.9-15.2) at 24 h p.i., respectively (Supplementary Fig. 2D). *Ex vivo* gamma counting data confirmed the imaging results, although the contrast between inflamed and remote tissue was more pronounced due to the intrinsically higher sensitivity of gamma counting assays. Tracer uptake in the infarcted area was ~3-fold higher than in remote myocardium at both 1 and 24 hours (p=0.03 and 0.008, respectively) and 4-fold higher than in healthy myocardium of C57BL/6 mice (p=0.03 and 0.008, respectively, Fig. 3D). These data were also corroborated by autoradiography of whole hearts and 1 mm thick slices stained with TTC, showing a similarly increased radioactivity accumulation in the infarcted area compared to remote myocardium (Fig. 3E). ^{89}Zr-mA1 clearly accumulated in the infarcted area and tracer uptake correlates with regions of high macrophage accumulation, as demonstrated by H&E and Mac-3 histology staining (Fig. 3F). *Ex vivo* CyTOF analyses using mA1 labeled with non-radioactive ^{nat}Zr (^{nat}Zr-mA1, Fig. 3G, Supplementary Fig. 3A) showed a pronounced presence of viable macrophages in the infarcted myocardium (Fig. 3H), as reported in previous studies [42,43]. Both macrophages and dendritic cells showed marked uptake of ^{nat}Zr-mA1, in comparison to other immune cell subsets (Fig. 3I). More importantly, the most abundant ^{nat}Zr-positive immune cell population –when expressed as a percentage of total viable cells– were macrophages, which strongly suggests that the imaging signal is mostly due to tracer uptake by this population even in the presence of more abundant non-leukocyte cells (Fig. 3J). Further analysis showed that CD206$^+$ macrophages were preferentially targeted over their CD206$^-$ counterparts (Supplementary Fig. 3B-C).

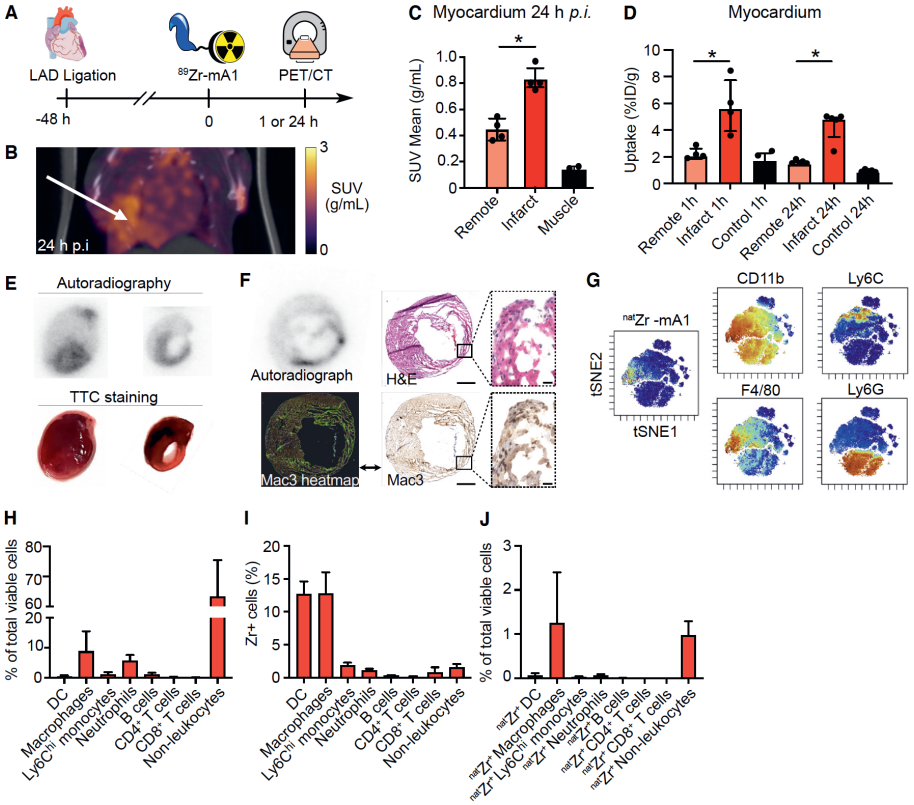


Figure 3. ^{89}Zr-mA1 as a probe for monitoring inflammation in the LAD-ligated mouse model of myocardial infarction. A) Schematic overview of the experimental design. B) Representative PET/CT images of infarcted animals scanned 24 hours after tracer injection. Arrow indicates infarcted region. C) PET-based quantification of ^{89}Zr-mA1 uptake in the myocardium 24 h post tracer injection (n = 4). D) ^{89}Zr-mA1 uptake in the myocardium measured by *ex vivo* gamma counting (n = 4-5). E) Autoradiographs showing tracer distribution in the myocardium of infarcted mice 24 h p.i. Images show whole heart followed by a representative sectioned slice of approximately 1 mm thick. Corresponding TTC-stained tissues are also shown. F) Autoradiography (left) and qualitative histology of the infarcted myocardium showing H&E staining (top right) and regions of macrophage accumulation as determined by Mac-3 staining (bottom right). Scale bars represent 1 mm in the main figure and 20 µm in the magnification. G,H) Mice were injected with ^{nat}Zr-mA1 two days after myocardial infarction. Twenty-four hours after injection, mice were euthanized and CyTOF performed on the infarct zone (n = 3). G) t-SNE plot of viable leukocytes in the infarct, color-coded for ^{nat}Zr-mA1 uptake and the expression of various myeloid cell markers. H) Quantification of leukocyte subsets in the infarct as a percentage of the total number of viable cells (left); percentage of ^{nat}Zr-positive cells within each leukocyte subset (middle); and the relative abundance of ^{nat}Zr-positive leukocyte subsets in the infarct

(right). Control: healthy myocardium of non-infarcted animals; DC, dendritic cells; remote, remote myocardium. *P < 0.05

Employing ^{89}Zr-mA1 in a melanoma mouse model

We also studied ^{89}Zr-mA1's potential in monitoring TAM burden using a B16F10 melanoma mouse model. PET scans were performed statically at 24 h p.i. (Fig. 4A). Imaging signatures were similar to those obtained in C57BL/6 mice, with strong kidney and liver signals (Supplementary Fig. 4A and B). At 24 h p.i, a clear tracer signal was observed in the tumor (Fig. 4B). Tumor uptake reached an SUV of 0.5 (IQR, 0.4-0.6, n = 10) at 24 h p.i. (Fig. 4C). These data were corroborated by *ex vivo* gamma counting of animal tissues at 1- and 24- hours post tracer injection, which showed increased uptake in the tumor over time, with 2.1 %ID/g (IQR, 1.9-2.4, n = 4) at 1 h p.i. and 4.5 %ID/g (IQR, 4.2-4.9, n = 11) at 24 h p.i. (Fig. 4D). *Ex vivo* gamma counting also indicated high radioactivity concentrations in the kidney and liver, followed by the spleen and bone marrow (Supplementary Fig. 4C). Tumor-to-blood and tumor-to-muscle ratios were 0.1 (IQR, 0.1-0.1) and 5 (IQR, 4.7-5.2) at 1 h p.i., respectively, and increased to 2.4 (IQR, 2.1-2.7) and 14.2 (IQR, 10.6-15.7) at 24 h p.i., respectively (Supplementary Fig. 4D). Our CyTOF results with ^{nat}Zr-mA1 (Fig. 4E, Supplementary Fig. 5A) show that macrophages are the main immune cell population in this tumor model (Fig. 4F), and corroborate our tracer's affinity for myeloid cells, especially macrophages and dendritic cells (Fig. 4G). Similar to our results in the MI model, the vast majority of viable ^{nat}Zr-positive leukocytes were macrophages (Fig. 4H) hence implying that macrophages make up for the majority of the signal. Macrophage subtype analysis showed that CD206^{+} macrophages were also preferentially targeted as in the MI model, albeit to a lesser degree (Supplementary Fig. 5B-C).

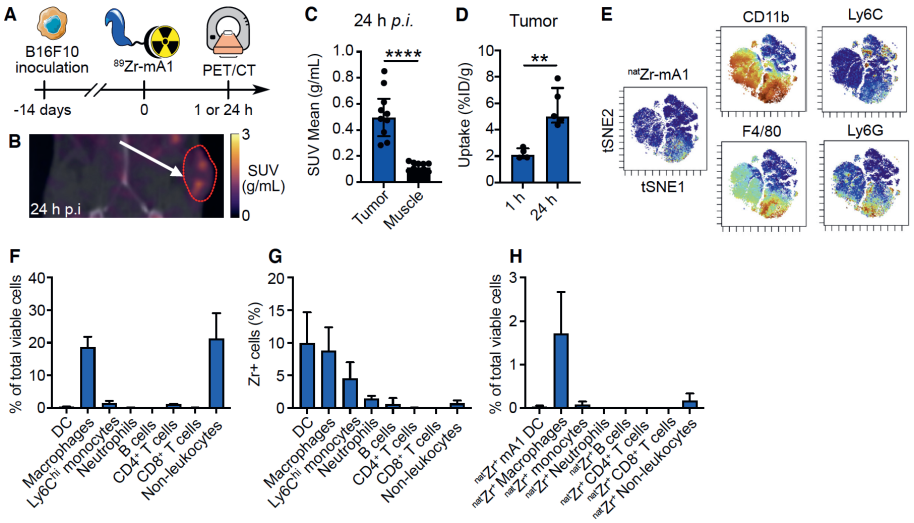


Figure 4. ^{89}Zr-mA1 as a probe for monitoring inflammation in the B16F10 melanoma mouse model. A) Schematic overview of the experimental design. B) Representative PET/CT images of tumor-bearing animals scanned 24 hours after tracer injection. Arrow indicates the tumor, delineated in red. C) PET-based quantification of ^{89}Zr-mA1 tumor uptake 24 hours post tracer injection (n = 10). D) ^{89}Zr-mA1 uptake in the tumor measured by *ex vivo* gamma counting, (n = 4-10). E,F) Mice were injected with ^{nat}Zr-mA1 14 days after tumor inoculation. Twenty-four hours after injection, mice were euthanized and CyTOF performed on the tumor (n = 3). E) t-SNE plot of viable leukocytes in the tumor, color-coded for ^{nat}Zr-mA1 uptake and the expression of various myeloid cell markers. F) Quantification of leukocyte subsets in the tumor (left); percentage of ^{nat}Zr-positive cells (middle); and relative abundance of ^{nat}Zr-positive leukocyte subsets in the tumor (right). **P < 0.01, ***P < 0.005.

Discussion

We have developed an apolipoprotein A1 mimetic-based radiotracer for monitoring macrophage burden. *In vitro* experiments show that ^{89}Zr-mA1 efficiently binds lipoproteins. In a serum incubation experiment, tracer labeling displayed great stability with no evidence of ^{89}Zr dissociation. The tracer exhibited longer circulation time in hypercholesterolemic mice (*Apoe*$^{-/-}$) than in C57BL/6 mice, further demonstrating ^{89}Zr-mA1's ability to bind endogenous lipoproteins *in vivo* as *Apoe*$^{-/-}$ mice have higher HDL and LDL plasma levels than wild type mice [44,45]. Moreover, our SEC analysis of plasma samples from *Apoe*$^{-/-}$ mice collected at 30 min post-tracer administration

suggests rapid *in vivo* lipoprotein binding, although these studies did not allow proper distinction between lipoprotein fractions. Macrophage targeting was also evaluated using clodronate liposome injected animals. We hypothesized that upon macrophage depletion, ^{89}Zr-mA1 would show diminished uptake values in macrophage-harboring organs. As expected, decreased tracer uptake was observed in the spleen, an organ with a large population of macrophages[40] and a typical site for clodronate liposome accumulation. Of note, matched controls that were injected with ^{89}Zr-mA1, but did not receive clodronate injections confirmed that the administration of clodronate liposomes did not affect the tracer's performance and biodistribution.

We used CyTOF and ^{nat}Zr-labeled mA1 as an innovative way to investigate our tracer's cellular fate in the cancer and MI models included in this study. In contrast to fluorescence-based biodistribution analyses, this approach allows using the same molecular species at a radiotracer-relevant dose. These studies showed a similar percentage of ^{nat}Zr^{+} macrophages and dendritic cells. However, the much higher abundance of macrophages means that the observed signal mainly stems from these cells. Our analyses also show that, although non-leukocytes outnumbered macrophages in both models, tracer uptake in these cells was low, resulting in limited background signal. Additionally, we explored macrophage subtype specificity by studying tracer uptake in CD206^{+} (MRC1, mannose receptor) versus CD206^{-} cells. In both models, we observed that CD206^{+} macrophages are more likely to be ^{nat}Zr-mA1-positive than CD206^{-} macrophages, which suggests that our tracer is more prone to accumulate in resident-like/alternatively activated macrophages. However, this analysis is based on a single marker and, nevertheless, both natZr^{+}CD206^{+} and natZr^{+}CD206^{-} macrophage subpopulations were sizeable suggesting that ^{89}Zr-mA1 may not have a marked subtype selectivity.

We also demonstrated ^{89}Zr-mA1's applicability toward imaging macrophage accumulation in the infarcted myocardium. In this setting, tissue damage in the MI lesion results in monocyte recruitment and their subsequent

differentiation into macrophages [41]. In our study design, we imaged these mice at 3 days post-LAD ligation, which is when infiltration of inflammatory macrophages peaks in this animal model [46]. Increased tracer uptake was observed in the infarcted area both *in vivo* and *ex vivo*. A similar assessment has been performed previously using ^{18}F-FDG imaging [47–50]. However, ^{18}F-FDG lacks cell specificity and displays high uptake in the remote myocardium [51] and other metabolically active immune and non-immune cells, creating a substantial background signal [52,53]. For these reasons, the use of ^{18}F-FDG for macrophage and inflammation quantification in the myocardium is often challenged by the need for complex dietary restrictions lasting several days prior to PET scanning [54,55]. Due to its ability to interact with endogenous lipoproteins, it is likely that ^{89}Zr-mA1 imaging would also require certain dietary adaptations, such as overnight fasting or avoiding fat-rich meals prior to the imaging session. Gratifyingly, ^{89}Zr-mA1's infarct-to-remote myocardium uptake ratios were similar or higher compared to other reported tracers, such as ^{18}F-Macroflor, ^{64}Cu-Macrin and ^{68}Ga-Pentixafor [56–58].

Macrophages also play an important role in tumor development, making TAM burden monitoring highly relevant. Furthermore, numerous immunotherapeutic interventions are being developed or already in use in the clinic. For instance, immune checkpoint blockade has afforded promising results, leading to persistent remission in 10-20% of patients with certain cancers [59]. This limited success is at least partly due to an immunosuppressive tumor environment in which macrophages are key players [9]. Indeed, a high TAM burden is associated with poor prognosis in several cancers. For these reasons, a non-invasive macrophage quantification tool like the one presented in this study could be tremendously valuable for monitoring TAM-targeting therapies. We recently showed that response to a colony-stimulating factor 1 receptor (CSF1R) inhibitor TAM-burden reducing therapy could be non-invasively assessed by PET imaging with a ^{89}Zr-HDL nanotracer [60]. However, peptide-based radiotracers are generally easier to clinically translate compared to nanomaterial-based variants. In addition, molecular radiotracers usually require microdoses in Phase 0 clinical trials (≤100 μg) [61], simplifying initial regulatory requirements and potentially reducing costs.

Noteworthy, in addition to ^{18}F-FDG and HDL-based nanotracers, other classes of PET tracers have been developed for the monitoring macrophage burden. However, low tracer specificity, patient variability and lack of translatability remain a challenge in the field, underscoring the need for the engineering of new strategies. For instance, Gaemperli *et al.* [29] investigated the use of ^{11}C-PK1195 for the imaging of carotid plaques, showing good histological colocalization of the tracer with plaque macrophages. However, the presence of genetic polymorphisms affecting TSPO expression reportedly affected tracer's aptness. Despite their complex production and high costs, radiolabeled nanobodies targeting specific immune cell epitopes have also been employed for the imaging of leukocytes [62,63] and macrophages [26,64] in different disease contexts. In comparison, ^{89}Zr-mA1 is produced through chemical synthesis, using a biocompatible mimetic peptide, offering reduced manufacturing costs.

In this study, we chose to radiolabel our tracer using ^{89}Zr as this isotope has a relatively long physical half-life ($t_{1/2}$ = 78.4 h), which simplifies extensive *in vivo* and *ex vivo* studies. While this isotope is being increasingly used in the clinic, a shorter-lived isotope, such as ^{64}Cu ($t_{1/2}$ = 12.7 h), might be desirable as this helps reduce patients' radiation exposure, including due to high kidney radioactivity retention[65]. Our future efforts will therefore focus on developing mA1-based radiotracers labeled with ^{64}Cu.

In conclusion, ^{89}Zr-mA1's high specificity for macrophages makes it an effective probe for quantitatively and non-invasively assessing macrophage-driven inflammation. ^{89}Zr-mA1 holds potential as an imaging tool for studying diseases characterized by abundant macrophage burden and infiltration.

Materials and Methods

Chemistry

The apolipoprotein A1 mimetic peptide 37pA [34,35] modified with a cysteine at the C terminus [mA1] was purchased from Peptide 2.0 (Chantilly, VA) and

had the following amino acid sequence: DWLKAFYDKVAEKLKEAFPDWLKAFYDKVAEKLKEAFC. Deferoxamine-maleimide (DFO-Mal) was purchased from Macrocyclics (Plano, TX). All other reagents were obtained from Sigma-Aldrich (St. Louis, MO) unless otherwise stated.

Radiochemistry

^{89}Zr in 1M oxalic acid was purchased from 3D imaging (Little Rock, AR). Activity measurements were performed using a Capintec CRC-15R Dose Calibrator (Capintec, Ramsey, NJ).

Modifying mA1 with DFO

The terminal cysteine on mA1 allows its site-specific conjugation with the chelator DFO *via* maleimide chemistry. mA1 was dissolved in degassed DMSO (1.9 mg in 200 µL, 1.0 eq), and a DFO-Mal solution in DMSO (0.45 mg in 200 µL, 1.5 eq.) was added. The mixture was degassed using N_2 and allowed to react at room temperature for 48 hours in the dark under a nitrogen atmosphere. Water (2 mL) was added, and the mixture was transferred to a 2,000 molecular weight cut-off (MWCO) 3 mL dialysis bag (Slide-A-Lyzer, Thermo Scientific). The solution was dialyzed against water (~1 L) in the dark and overnight to remove DMSO and any unreacted DFO-Mal. The DFO functionalized peptide (mA1-DFO) was purified using a Shimadzu HPLC system equipped with two LC-10AT pumps coupled with an SPD-M10AVP photodiode array detector. Runs were carried out on a C18 Phenomenex Gemini column (6 x 250 mm, 5 µm) using water and acetonitrile as eluents (each containing 0.1%TFA) with a gradient of 70% to 40%, 10 min, and 40% to 70% 1 min and flow rate of 1 mL/min. The obtained product was dialyzed against water (~1 L) in the dark and overnight to remove acetonitrile (2,000 MWCO, 3 mL dialysis bag from Slide-A-Lyzer, Thermo Scientific). Electrospray ionization mass spectrometry (ESI-MS) spectra were recorded with a Waters Acquity UPLC (Milford, CA) with an electrospray ionization SQ detector. The compound was lyophilized and stored at -20 °C until further use, in which case it was redissolved in PBS.

Radiolabeling of mA1-DFO

A solution of ^{89}Zr oxalate (1 M aqueous oxalic acid) was neutralized with sodium carbonate 1M to reach a pH between 6.8 and 7.4. The DFO-bearing peptide was reacted with the ^{89}Zr solution using a thermomixer (600 rpm) for 1 h at 37 °C. The solution was allowed to cool to room temperature and radiolabeled mA1 purified by gel filtration using a PD-10 column and PBS as eluent. Radiochemical yield and purity were assessed by radio-TLC using a Lablogic Scan-RAM Radio-TLC/HPLC detector. The same labeling procedure was performed with natural zirconium to obtain ^{nat}Zr-mA1 for mass cytometry experiments. Optimized 3D conformation of ^{89}Zr-mA1 was determined using AlphaFold software (Alphabet Inc., Mountain View, CA)[36] and further modified using PyMol molecular visualization system (Schrödinger Inc, New York, NY) and structural information on Zr-DFO by L. Allot *et al* [37].

In vitro ^{89}Zr-mA1 binding to lipoproteins and albumin

We used size exclusion chromatography (SEC) to assess ^{89}Zr-mA1's ability to bind common serum components, namely HDL (human, XXX), low-density lipoprotein (LDL, human, XXX), and albumin (bovine serum albumin, Sigma-Aldrich). ^{89}Zr-mA1 or free ^{89}Zr (2.22 MBq) were incubated with a solution of the corresponding component at 0.2 mg/mL (HDL and LDL) or 0.5 mg/mL (albumin) for 1 hour at 37 °C. Then, radio-SEC was performed using a LC-20AB pumps-equipped Shimadzu HPLC system with an SPD-20A detector coupled to a Superdex 75-5/150 GL column (GE Healthcare Life Sciences). 100% PBS was used as eluent at a flow rate of 0.5 mL/min. The retention profile of each aliquot was compared to bare ^{89}Zr and the UV trace of the bare serum constituent.

Animals

Female C57BL/6 mice (7 weeks old, n = 50) were purchased from the Jackson Laboratory (Bar Harbor, ME) and randomly assigned to the different experimental groups. Female *Apoe*$^{-/-}$ mice (8 weeks old, n = 8) were also purchased from Jackson Laboratory. Details on the mouse models of hypercholesterolemia, macrophage depletion, myocardial infarction, and

melanoma can be found in the Supplementary Material.

Pharmacokinetics of ^{89}Zr-mA1

C57BL/6 (n = 6) and *Apoe*$^{-/-}$ mice (n = 4) were injected with ^{89}Zr-mA1 (~1.1 and 3.5 MBq, respectively) via the lateral tail vein. Blood radioactivity half-life was determined by serial blood draws from the tail vein at 1, 5, 10, 15, 30, 60 minutes, and 2, 6, and 24 hours after injection. Blood was weighed, and gamma counted using a Wizard^2 2480 automatic gamma counter (Perkin Elmer, Waltham, MA). Results were corrected for decay, and radioactivity concentration was reported as a percentage of injected dose per gram (%ID/g). A time-activity curve was generated, and the resulting values fitted to a biphasic decay to obtain blood radioactivity half-lives for ^{89}Zr-mA1. Weighted half-life is defined as: (% fast × $t_{1/2}$ fast + % slow × $t_{1/2}$ slow)/100.

Biodistribution of ^{89}Zr-mA1

Tissue radioactivity distribution was determined at different time points after ^{89}Zr-mA1 administration to healthy (n = 5), macrophage depleted (n = 5), LAD ligated (n = 9) and melanoma (n = 14) C57Bl/6 mice. Mice were injected with approximately 3.5 MBq (or 7.4 MBq for macrophage depleted mice) of ^{89}Zr-mA1 via the lateral tail vein, and the tracer was allowed to circulate for 1 (n = 4) and/or 24 hours (n = 5-10). After euthanasia and perfusion (20 mL saline), tissues were harvested (brain, heart, lungs, bone marrow, spleen, liver, kidneys, skeletal muscle, and bone) and weighed before radioactivity counting. The values were corrected for decay and radioactivity concentration and converted to %ID/g.

In vivo ^{89}Zr-mA1 binding to blood plasma components

Female *Apoe*$^{-/-}$ mice were intravenously injected with ^{89}Zr-mA1 (~3.7 MBq, n = 4). Thirty minutes after administration, animals were euthanized, and blood (0.5-0.7 mL) was collected by cardiac puncture in a heparinized tube. The sample was rapidly centrifuged at 15,000 rpm for 2 minutes, and the two phases obtained were carefully separated. The plasma fraction was analyzed

by SEC using a Superdex 10/300 column (GE Healthcare Life Sciences) and PBS as eluent at a flow rate 1 mL/min.

In vivo PET/CT imaging

Dynamic PET imaging was performed on a cohort of C57Bl/6 animals (n = 4 per group) for 60 minutes after ^{89}Zr-mA1 administration. These mice were anesthetized with isoflurane (2% in medical air for induction, 1% for maintenance) and injected with ^{89}Zr-mA1 (3.4 MBq) via their lateral tail vein while placed on the scanner bed. Images were acquired on a nanoScan PET/CT scanner (Mediso, Budapest, Hungary). A total of 5 dynamic frames were individually reconstructed for the following timepoints: 1, 5, 15, 30 and 60 minutes. In a different cohort of C57Bl/6, LAD-ligated and B16F10 inoculated animals, ^{89}Zr-mA1 (3.5 MBq, n = 5-10 per group) was allowed to circulate for 24 hours after intravenous injection. Animals were then anesthetized with isoflurane (2% in medical air for induction, 1% for maintenance) and subsequently imaged. PET acquisition time for the static scans was 20 minutes. For both dynamic and static scans, a high-resolution CT scan was acquired at 50 kVp and 300 ms exposure per projection. CT-contrast agent (isovue-370, Bracco Diagnostics) was continuously infused through a tail vein catheter. Reconstruction was performed using the TeraTomo 3D reconstruction engine for 8 iterations and 6 subsets per iteration. The voxel size was isotropic at 0.3 mm. Immediately after the PET/CT scan, animals were euthanized for *ex vivo* analysis.

Statistical analysis

All results are presented as median and interquartile range (IQR). Unpaired data were analyzed with non-parametric Mann-Whitney tests. For all tests, $\alpha<0.05$ represents statistical significance. Levels of significance are indicated as follows: *$p<0.05$, **$p<0.01$, ***$p<0.001$, ****$p<0.0001$.

Data availability

The datasets generated during and/or analysed during the current study are available from the corresponding author on reasonable request.

Author contributions

Specific author contributions are as follows: Y.C.T, G.P., M.M.T.v.L., T.R., Z.A.F., W.J.M.M., A.J.P.T, C.P.M. engaged in the conception and design of the experiments. Y.C.T, G.P., M.M.T.v.L, J.M., R.O., A.V.V., Y.v.E., V.P., R.J.F.M, A.R., J.M-F., W.W., M.U., A.d.D., J.C.F., N.S., A.M., C.M. participated in the data acquisition process and Y.C.T, G.P., M.M.T.v.L, J.M., R.O., A.V.V., Y.v.E., V.P., R.J.F.M., A.R., J.M-F., A.d.D., J.C.F., N.S., A.M., C.M., A.J.P.T., C.P.M. performed the analysis and interpretation of the data. All authors contributed to the drafting or revision of the manuscript. The final content of the manuscript was seen and approved by all authors.

Sources of funding

This work was supported by the National Institutes of Health grant R01 CA220234, the American Heart Association (16SDG31390007), as well as a Vici grant from the Dutch Research Council (NWO), a European Research Council (ERC) Advanced Grant (TOLERANCE) (WJMM) and an I+D+i project grant from the Spanish Ministry of Science and Innovation (PID2020-114902RB-I00 | AEI/10.13039/501100011033) (CPM). The funders played no role in study design, data collection, analysis and interpretation of data, or the writing of this manuscript.

Competing interests

W.J.M.M. is a founder and CSO of Trained Therapeutix Discovery. Z.A.F. is a founder and member of the board of Trained Therapeutix Discovery. T.R. is now an employee of and shareholder in Novartis AG. No other potential financial or non-financial conflicts of interest relevant to this article exist.

References

1. Epelman, S., Lavine, K. J. & Randolph, G. J. Origin and Functions of Tissue Macrophages. *Immunity* **41**, 21–35 (2014).
2. Wynn, T. A. & Vannella, K. M. Macrophages in Tissue Repair, Regeneration, and Fibrosis. *Immunity* **44**, 450–462 (2016).
3. Moore, K. J., Sheedy, F. J. & Fisher, E. A. Macrophages in atherosclerosis: a dynamic balance. *Nat. Rev. Immunol.* **13**, 709–721 (2013).
4. Mantovani, A., Marchesi, F., Malesci, A., Laghi, L. & Allavena, P. Tumour-associated macrophages as treatment targets in oncology. *Nat. Rev. Clin. Oncol.* **14**, 399–416 (2017).
5. Frangogiannis, N. G., Smith, C. W. & Entman, M. L. The inflammatory response in myocardial infarction. *Cardiovasc. Res.* **53**, 31–47 (2002).
6. Sager, H. B., Kessler, T. & Schunkert, H. Monocytes and macrophages in cardiac injury and repair. *J. Thorac. Dis.* **9**, S30–S35 (2017).
7. Liu, J., Wang, H. & Li, J. Inflammation and inflammatory cells in myocardial infarction and reperfusion injury: A double-edged sword. *Clin. Med. Insights Cardiol.* **10**, 79–84 (2016).
8. Coffelt, S. B., Hughes, R. & Lewis, C. E. Tumor-associated macrophages: effectors of angiogenesis and tumor progression. *Biochim. Biophys. Acta* **1796**, 11–18 (2009).
9. DeNardo, D. G. & Ruffell, B. Macrophages as regulators of tumour immunity and immunotherapy. *Nat. Rev. Immunol.* 1 (2019) doi:10.1038/s41577-019-0127-6.
10. Condeelis, J. & Pollard, J. W. Macrophages: Obligate partners for tumor cell migration, invasion, and metastasis. *Cell* **124**, 263–266 (2006).
11. De Palma, M. & Lewis, C. E. Macrophage regulation of tumor responses to anticancer therapies. *Cancer Cell* **23**, 277–286 (2013).
12. Tang, X. Tumor-associated macrophages as potential diagnostic and prognostic biomarkers in breast cancer. *Cancer Lett.* **332**, 3–10 (2013).
13. Ries, C. H. *et al.* Targeting tumor-associated macrophages with anti-CSF-1R antibody reveals a strategy for cancer therapy. *Cancer Cell* **25**, 846–859 (2014).
14. Cassier, P. A. *et al.* CSF1R inhibition with emactuzumab in locally advanced diffuse-type tenosynovial giant cell tumours of the soft tissue: A dose-escalation and dose-expansion phase 1 study. *Lancet Oncol.* **16**, 949–956 (2015).
15. Noy, R. & Pollard, J. W. Tumor-Associated Macrophages: From Mechanisms to Therapy. *Immunity* **41**, 49–61 (2014).
16. Weissleder, R., Nahrendorf, M. &

Pittet, M. J. Imaging macrophages with nanoparticles. *Nature Materials* vol. 13 125–138 (2014).

17. Foss, C. A., Sanchez-Bautista, J. & Jain, S. K. Imaging Macrophage-associated Inflammation. *Seminars in Nuclear Medicine* vol. 48 242–245 (2018).
18. Li, Y. & Liu, T. M. Discovering macrophage functions using in Vivo optical imaging techniques. *Frontiers in Immunology* vol. 9 (2018).
19. Toner, Y. C. *et al.* Systematically evaluating DOTATATE and FDG as PET immuno-imaging tracers of cardiovascular inflammation. *Sci. Rep.* **12**, (2022).
20. Li, X., Rosenkrans, Z. T., Wang, J. & Cai, W. PET imaging of macrophages in cardiovascular diseases. *Am. J. Transl. Res.* **12**, 1491–1514 (2020).
21. Blomberg, B. A. & Høilund-Carlsen, P. F. [18F]-fluorodeoxyglucose PET imaging of atherosclerosis. *PET Clin.* **10**, 1–7 (2015).
22. Serkova, N. J. Nanoparticle-based magnetic resonance imaging on tumor-associated macrophages and inflammation. *Frontiers in Immunology* vol. 8 (2017).
23. Dadfar, S. M. *et al.* Iron oxide nanoparticles: Diagnostic, therapeutic and theranostic applications. *Advanced Drug Delivery Reviews* vol. 138 302–325 (2019).
24. Senders, M. L. *et al.* Nanobody-Facilitated Multiparametric PET/MRI Phenotyping of Atherosclerosis. *JACC Cardiovasc. Imaging* **12**, (2019).
25. Bao, G., Tang, M., Zhao, J. & Zhu, X. Nanobody: a promising toolkit for molecular imaging and disease therapy. *EJNMMI Res.* **11**, (2021).
26. Movahedi, K. *et al.* Nanobody-based targeting of the macrophage mannose receptor for effective in vivo imaging of tumor-associated macrophages. *Cancer Res.* **72**, 4165–4177 (2012).
27. Malmberg, C. *et al.* 64Cu-DOTATATE for noninvasive assessment of atherosclerosis in large arteries and its correlation with risk factors: Head-to-head comparison with 68Ga-DOTATOC in 60 patients. *J. Nucl. Med.* **56**, 1895–1900 (2015).
28. Li, X. *et al.* [68Ga]Pentixafor PET/MR imaging of chemokine receptor 4 expression in the human carotid artery. *Eur. J. Nucl. Med. Mol. Imaging* **46**, 1616–1625 (2019).
29. Gaemperli, O. *et al.* Imaging intraplaque inflammation in carotid atherosclerosis with 11C-PK11195 positron emission tomography/computed tomography. *Eur. Heart J.* **33**, 1902–1910 (2012).
30. Favari, E. *et al.* Cholesterol efflux and reverse cholesterol transport. *Handb. Exp. Pharmacol.* **224**,

181–206 (2015).
31. Van Eck, M., Pennings, M., Hoekstra, M., Out, R. & Van Berkel, T. J. Scavenger receptor BI and ATP-binding cassette transporter A1 in reverse cholesterol transport and atherosclerosis. *Curr. Opin. Lipidol.* **16**, 307–15 (2005).
32. Mulder, W. J. M. *et al.* High-Density Lipoprotein Nanobiologics for Precision Medicine. *Acc. Chem. Res.* **51**, 127–137 (2018).
33. Metselaar, J. M. & Lammers, T. Challenges in nanomedicine clinical translation. *Drug Deliv. Transl. Res.* 1–5 (2020) doi:10.1007/s13346-020-00740-5.
34. Owens, R. J. *et al.* Apolipoprotein A-I and its amphipathic helix peptide analogues inhibit human immunodeficiency virus-induced syncytium formation. *J. Clin. Invest.* **86**, 1142–1150 (1990).
35. Remaley, A. T. *et al.* Synthetic amphipathic helical peptides promote lipid efflux from cells by an ABCA1-dependent and an ABCA1-independent pathway. *J. Lipid Res.* **44**, 828–836 (2003).
36. Jumper, J. *et al.* Highly accurate protein structure prediction with AlphaFold. *Nature* **596**, 583–589 (2021).
37. Allott, L. *et al.* Evaluation of DFO-HOPO as an octadentate chelator for zirconium-89. *Chem. Commun.* **53**, 8529–8532 (2017).
38. Van Rooijen, N., Kors, N. & Kraal, G. Macrophage subset repopulation in the spleen: Differential kinetics after liposome-mediated elimination. *J. Leukoc. Biol.* **45**, 97–104 (1989).
39. Naito, M. *et al.* Liposome-encapsulated dichloromethylene diphosphonate induces macrophage apoptosis in vivo and in vitro. *J. Leukoc. Biol.* **60**, 337–344 (1996).
40. Den Haan, J. M. M. & Kraal, G. Innate immune functions of macrophage subpopulations in the spleen. *J. Innate Immun.* **4**, 437–445 (2012).
41. Swirski, F. K. & Nahrendorf, M. Leukocyte Behavior in Atherosclerosis, Myocardial Infarction, and Heart Failure. *Science (80-.).* **339**, 161–166 (2013).
42. Nahrendorf, M., Pittet, M. J. & Swirski, F. K. Monocytes: Protagonists of infarct inflammation and repair after myocardial infarction. *Circulation* **121**, 2437–2445 (2010).
43. Sager, H. B. *et al.* Proliferation and Recruitment Contribute to Myocardial Macrophage Expansion in Chronic Heart Failure. *Circ. Res.* **119**, 853–864 (2016).
44. Jiang, F., Gibson, A. P. & Dusting, G. J. Endothelial dysfunction induced by oxidized low-density lipoproteins in isolated mouse aorta: A comparison with apolipoprotein-E deficient mice. *Eur. J. Pharmacol.* **424**, 141–149

(2001).
45. Phenotypes of LDLR & APOE Knockout Mice | The Jackson Laboratory. https://www.jax.org/jax-mice-and-services/strain-data-sheet-pages/phenotype-information-for-002052-and-002207.
46. Thackeray, J. T. & Bengel, F. M. Molecular Imaging of Myocardial Inflammation With Positron Emission Tomography Post-Ischemia: A Determinant of Subsequent Remodeling or Recovery. *JACC Cardiovasc. Imaging* **11**, 1340–1355 (2018).
47. Andrej, Ć. *et al.* Novel Positron Emission Tomography Tracers for Imaging Vascular Inflammation. *Curr. Cardiol. Rep.* **22**, 1–11 (2020).
48. Thackeray, J. T. *et al.* Targeting post-infarct inflammation by PET imaging: comparison of 68Ga-citrate and 68Ga-DOTATATE with 18F-FDG in a mouse model. *Eur. J. Nucl. Med. Mol. Imaging* **42**, 317–327 (2015).
49. Lee, W. W. *et al.* PET/MRI of inflammation in myocardial infarction. *J. Am. Coll. Cardiol.* (2012) doi:10.1016/j.jacc.2011.08.066.
50. Vasudevan, P. *et al.* 18F-FDG PET-based imaging of myocardial inflammation following acute myocardial infarction in a mouse model. *Int. J. Mol. Sci.* **21**, (2020).
51. Tarkin, J. M. *et al.* 68Ga-DOTATATE PET Identifies Residual Myocardial Inflammation and Bone Marrow Activation After Myocardial Infarction. *J. Am. Coll. Cardiol.* **73**, 2489–2491 (2019).
52. Manabe, O. *et al.* Radiopharmaceutical tracers for cardiac imaging. *J. Nucl. Cardiol.* **25**, 1204–1236 (2018).
53. Bengel, F. M. Moving Forward Toward Clinical Application. 1–3 (2016) doi:10.1038/nm.3778.7.
54. Kumar, P., Patel, C. D., Singla, S. & Malhotra, A. Effect of duration of fasting and diet on the myocardial uptake of F-18-2-fluoro-2-deoxyglucose (F-18 FDG) at rest. *Indian J. Nucl. Med.* **29**, 140–145 (2014).
55. Surasi, D. S., Bhambhvani, P., Baldwin, J. A., Almodovar, S. E. & O'Malley, J. P. 18F-FDG PET and PET/CT patient preparation: A review of the literature. *J. Nucl. Med. Technol.* **42**, 5–13 (2014).
56. Thackeray, J. T. *et al.* Molecular Imaging of the Chemokine Receptor CXCR4 after Acute Myocardial Infarction. *JACC Cardiovasc. Imaging* **8**, 1417–1426 (2015).
57. Keliher, E. J. *et al.* Polyglucose nanoparticles with renal elimination and macrophage avidity facilitate PET imaging in ischaemic heart disease. *Nat. Commun.* **8**, (2017).
58. Nahrendorf, M. *et al.* Imaging Cardiovascular and Lung Macrophages With the Positron Emission Tomography Sensor ^{64}Cu-Macrin in Mice, Rabbits, and Pigs. *Circ. Cardiovasc.*

Imaging **13**, (2020).

59. O'Donnell, J. S., Long, G. V., Scolyer, R. A., Teng, M. W. L. & Smyth, M. J. Resistance to PD1/PDL1 checkpoint inhibition. *Cancer Treat. Rev.* **52**, 71–81 (2017).
60. Mason, C. A. *et al.* An ^{89}Zr-HDL PET Tracer Monitors Response to a CSF1R Inhibitor. *J. Nucl. Med.* **61**, (2020).
61. Burt, T. *et al.* Phase 0/microdosing approaches: time for mainstream application in drug development? *Nat. Rev. Drug Discov.* **19**, 801–818 (2020).
62. Rashidian, M. *et al.* Noninvasive imaging of immune responses. *Proc. Natl. Acad. Sci. U. S. A.* **112**, 6146–6151 (2015).
63. Maier, A. *et al.* Multiparametric Immunoimaging Maps Inflammatory Signatures in Murine Myocardial Infarction Models. *JACC Basic to Transl. Sci.* **8**, 801–816 (2023).
64. Put, S. *et al.* SPECT imaging of joint inflammation with nanobodies targeting the macrophage mannose receptor in a mouse model for rheumatoid arthritis. *J. Nucl. Med.* **54**, 807–814 (2013).
65. Pérez-Medina, C. *et al.* In Vivo PET Imaging of HDL in Multiple Atherosclerosis Models. *JACC Cardiovasc. Imaging* **9**, 950–961 (2016).

Supplementary information

Materials and Methods

Radio-TLC assessment of tracer dissociation in fetal bovine serum (FBS)

^{89}Zr-mA1 or bare ^{89}Zr were incubated in FBS at 37 °C. The retention of ^{89}Zr by mA1 was assessed by radio-TLC using a Lablogic Scan-RAM Radio-TLC/HPLC detector at 1, 15, 60, 120, 240, 360 and 1440 minutes of incubation and using bare ^{89}Zr as control.

Mouse model of hypercholesterolemia

Female *Apoe*$^{-/-}$ mice (B6.129P2-*Apoe*^{tm1Unc}/J, 8 weeks old, n = 8) were purchased from the Jackson Laboratory and fed a Western Diet (42% Kcal from fat TD88137, Envigo, Huntingdon, UK) for 12 weeks. These animals lack apolipoprotein E and develop severe hypercholesterolemia when fed a high-fat and high-cholesterol diet[1,2].

Mouse model of macrophage depletion

Female C57BL/6 mice (n=10) were purchased from Jackson Laboratory and randomly distributed over two groups. Twenty-four hours prior to the ^{89}Zr-mA1 injections, the experimental group received intravenous injections of Clodronate Liposomes (LIPOSOMA) at a dose of 100 µL of suspension / 10 grams of animal weight to deplete the macrophages. The control group received intravenous injections of 200 µL PBS.

Mouse model of melanoma

B16F10 murine melanoma cells were cultured in Dulbecco's modified Eagle's medium (DMEM) supplemented with 10% FBS, and 1% penicillin/streptomycin (P/S). The melanoma cells ($1x10^5$) were resuspended in PBS (100 µL) supplemented with 0.5% fetal bovine serum (FBS) and were injected subcutaneously in the flank of female C57BL/6 mice (n = 18). Tumors were allowed to grow for 14 days before use.

Mouse model of myocardial infarction

Myocardial infarction in mice was induced by permanent ligation of the left anterior descending (LAD) coronary artery of female C57BL/6 mice (n = 17)[3]. Animals were anesthetized with xylazine (10 mg/kg) and ketamine (100 mg/kg) and intubated using an endotracheal intubation kit from Braintree Scientific (Braintree, MA). Left-sided thoracotomy and pericardial incision were performed. A 7-0 Silk suture was used to occlude the LAD. Incisions were closed with a 5-0 Silk suture. Infarcted animals were treated with 0.1 mg/kg of buprenorphine after surgery.

Histology

Following euthanasia, heart samples were embedded in OCT containing medium and were sectioned into 30 and 7 µm subsequent sections. 30 µm slides were used for autoradiography and 10 µm slides were used for histology. Histology samples were stained with hematoxylin and eosin (H&E), and Mac3 staining (macrophages) using LAMP2 Antibody and 60 minutes of incubation (Invitrogen, Waltham, MA).

TTC staining

Hearts were incubated with 2,3,5-Triphenyltetrazolium chloride (TTC) for 10 minutes at 37 °C, washed with PBS and sectioned into approximately 1 mm thick slices.

Autoradiography

Following euthanasia, tissue samples were excised and embedded in OCT mounting medium. OCT embedded samples were cut into 30 µm and 7 µm subsequent sections for autoradiography and histology, respectively. To determine radiotracer distribution, digital autoradiography was performed by placing tissue slices and sections in a film cassette against a phosphor imaging plate (BASMS-2325, Fujifilm, Valhalla, NY) for 10 minutes (TTC stained 1 mm slices) or 90 minutes (OCT embedded 30 µm sections) at -20 °C. Phosphorimaging plates were read at a pixel resolution of 25 µm with a Typhoon 7000IP plate reader (GE Healthcare, Pittsburgh, PA).

Supplementary Table 1. PET-derived ^{89}Zr-mA1 *in vivo* uptake values in selected tissues at 24 hours post-injection [mean ± SD].

Mouse model	Tissue	%ID/cm$^3_{mean}$	SUV$_{mean}$
WT [C57BL/6]	Liver	15.5 ± 0.5	2.9 ± 0.1
	Spleen	9.5 ± 2.6	1.8 ± 0.5
	Kidney	31.3 ± 2.5	5.8 ± 0.5
	Heart	2.1 ± 0.5	0.39 ± 0.08
	Femur	3.0 ± 0.3	0.56 ± 0.05
	Muscle	0.57 ± 0.14	0.11 ± 0.02
Myocardial infarction	Infarcted myocardium	4.5 ± 0.5	0.82 ± 0.08
	Remote myocardium	2.4 ± 0.4	0.45 ± 0.07
	Muscle	0.73 ± 0.15	0.14 ± 0.03
Melanoma [B16F10]	Tumor	2.4 ± 0.8	0.52 ± 0.18
	Muscle	0.50 ± 0.14	0.11 ± 0.03

CyTOF

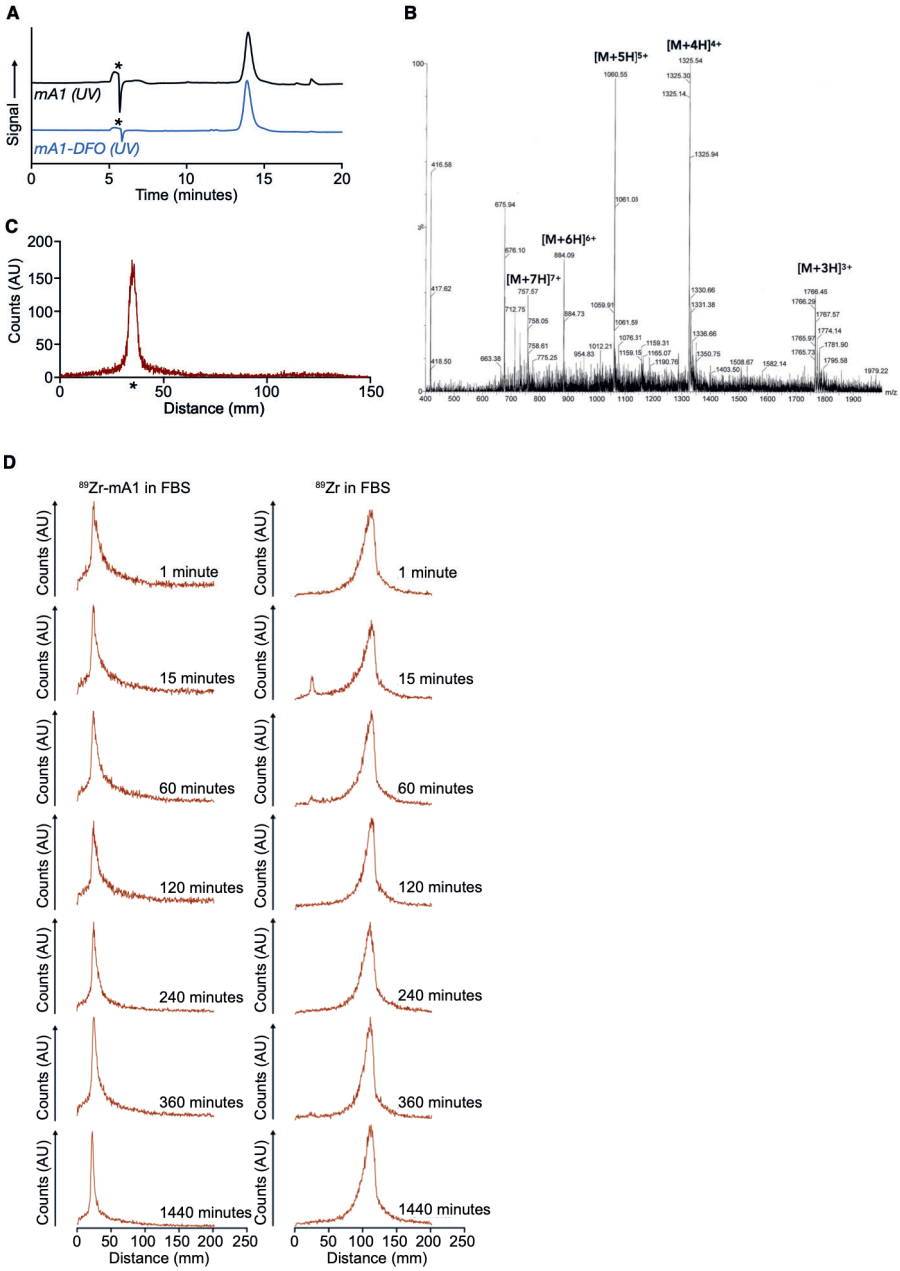
Non-radioactive ^{nat}Zr-mA1 was used for CyTOF-based investigation of the peptide's *in vivo* cellular specificity in MI and melanoma mice. The compound was administered at the same dose as in the imaging experiments (200 µg) and quantified by measuring the abundance of ^{90}Zr. ^{nat}Zr-mA1 was allowed to circulate for 24 hours before euthanasia and tissue collection. Infarcted myocardium from MI mice and tumors from melanoma-inoculated mice were minced and digested with enzymatic digestion solution containing DNAse (60 U/mL), collagenase I (450 U/mL), collagenase XI (125 U/mL) and hyaluronidase (60 U/mL) (all Sigma-Aldrich) in PBS. Samples were then washed and resuspended into C10 media (RPMI + 10% FBS). Next, samples were incubated with a 1 µM Rh103 solution (Fluidigm, San Francisco, CA) for 20 minutes at 37 °C for viability staining and blocked with FcX block solution (Biolegend, San Diego, CA). Cells were then stained for 30 minutes at room temperature with monoclonal antibodies as described in the Supplemental Table 2. Subsequently, single cell suspensions were fixed with 4%

formaldehyde in PBS and incubated with Cell-ID™ 20-Plex Pd Barcoding Kit (Fluidigm, San Francisco, CA) for 30 minutes at room temperature. Prior to data acquisition, samples were washed with Cell Staining buffer and Cell Acquisition solution and resuspended in solution containing EQ normalization beads (Fluidigm, San Francisco, CA). Data was acquired on a Helios Mass Cytometer (Fluidigm, San Francisco, CA). Repeat acquisitions of the same sample were concatenated and normalized and barcoded samples were de-multiplexed using the Fluidigm software. Barcoded samples were de-multiplexed using the Zunder single cell debarcoder. Data were analyzed using Cytobank software (Beckman Coulter, Pasadena, CA) and FlowJo v10.8.0 (BD, Ashland, OR).

Supplementary table 2. List of antibodies used for the CyTOF analysis.

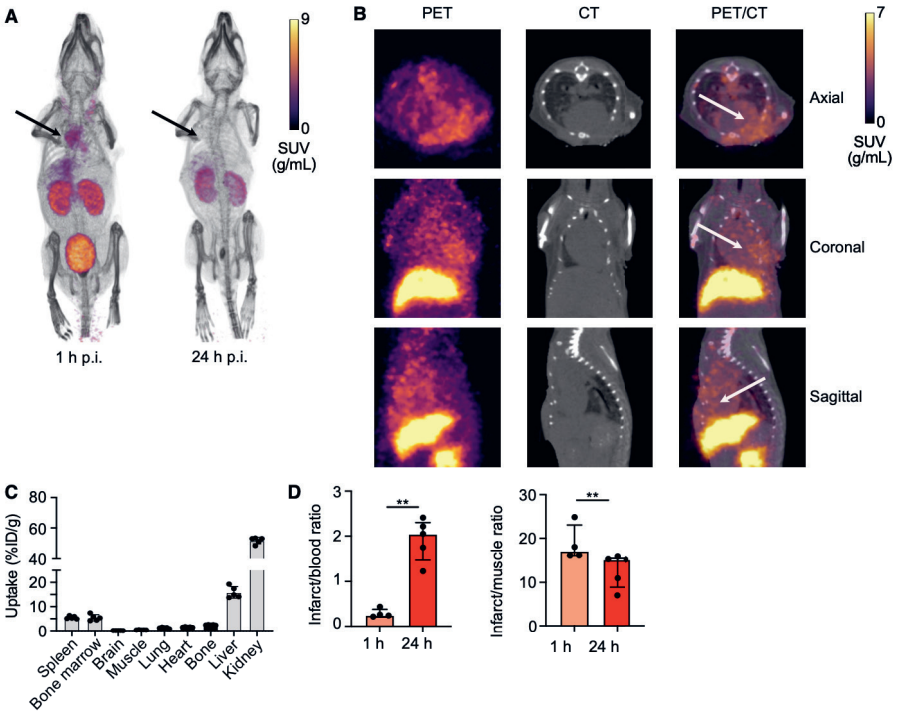
Antibody	Metal	Clone	Manufacturer
CD45	89 Y	30-F11	Fluidigm
CD90.2	113 In	30-H12	Biolegend
Ly6G	141 Pr	1A8	Fluidigm
CD11c	142 Nd	N418	Biolegend
TCRb	143 Nd	H57-597	Fluidigm
CD24	144 Nd	M1/69	Biolegend
CD69	145 Nd	H1.2F3	Fluidigm
F4/80	146 Nd	BM8	Fluidigm
CD357/GITR	147 Sm	DTA-1	Biolegend
CD11b	148 Nd	M1/70	Fluidigm
CD19	149 Sm	6D5	Fluidigm
IgD	150 Nd	11-26c.2a	Biolegend
CD25	151 Eu	3C7	Fluidigm
SiglecF	152 Sm	S17007L	Biolegend
NKp46	153 Eu	29A1.4	Fluidigm
CD73	155 Gd	TY/11.8	Biolegend
CD64	156 Gd	X54-5/7.1	Biolegend
CD117	158 Gd	2B8	Biolegend
PD-1	159 Tb	RMP1-30	Biolegend

CD62L	160 Gd	MEL-14	Fluidigm
CD103	161 Dy	2E7	Biolegend
Ly6C	162 Dy	HK1.4	Fluidigm
Sca-1	164 Dy	D7	Fluidigm
KLRG1	166 Er	2F1/KLRG1	Biolegend
CXCR3	167 Er	CXCR3-173	Biolegend
CD8a	168 Er	53-6.7	Fluidigm
CD206	169 Tm	C068C2	Fluidigm
NK1.1	170 Er	PK136	Fluidigm
CD44	171 Yb	IM7	Biolegend
CD4	172 Yb	RM4-5	Fluidigm
MHCII (I-A/I-E)	174 Yb	M5/114.15.2	Biolegend
CD127	175 Lu	A7R34	Fluidigm
B220	176 Yb	RA3-6B2	Fluidigm

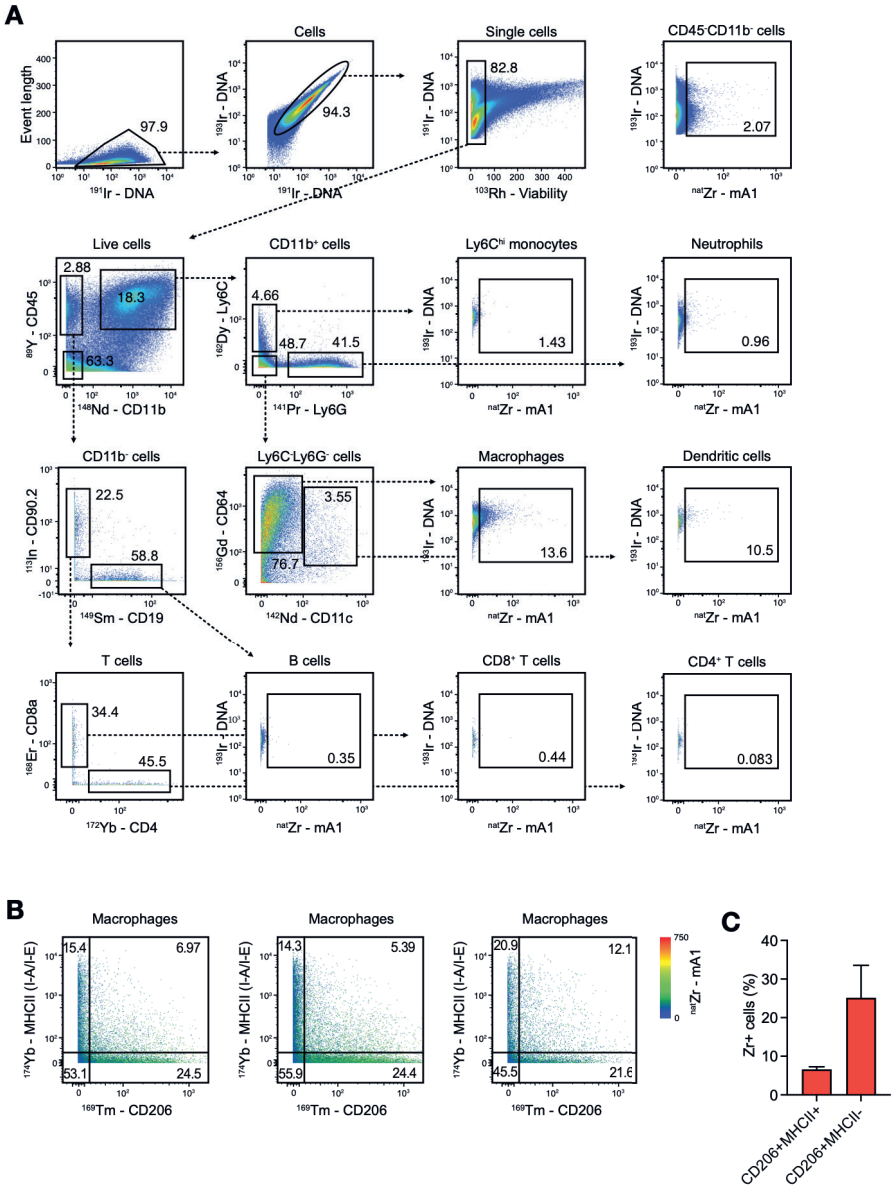


Supplementary Figure 1. A) HPLC (C_{18} column) chromatograms of mA1 (UV at 278 nm) and mA1-DFO (UV at 278 nm). * Denotes the injection peak. B) LC-MS spectrum of mA1-DFO. C) Radio-TLC analysis of ^{89}Zr-mA1 using EDTA (50 mM) as the eluent. *Denotes the baseline. Bare

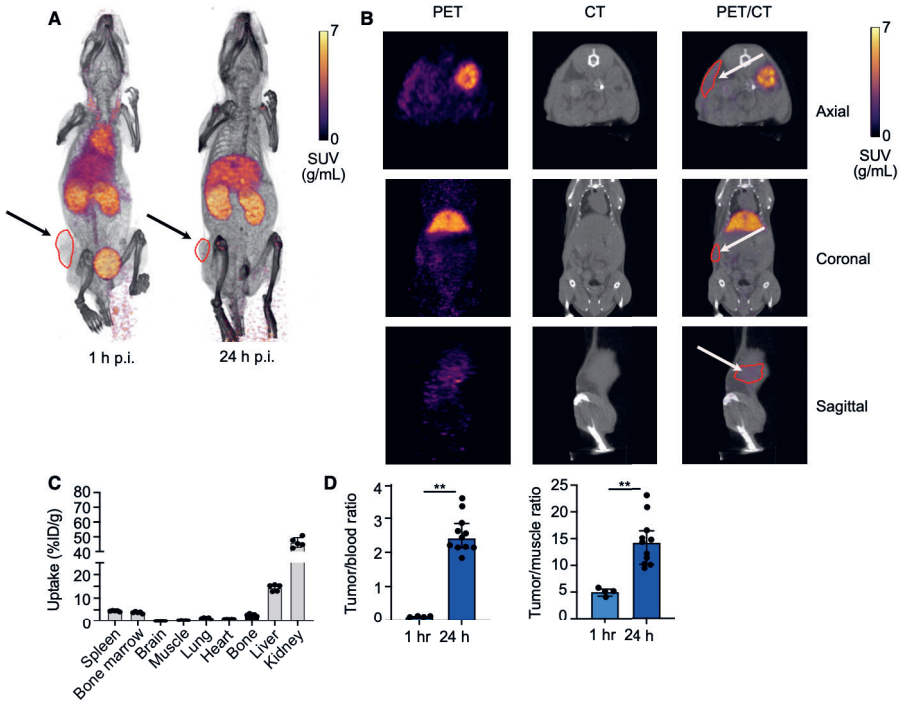
^{89}Zr would appear at the solvent front, at around 120 mm. D) Radio-TLC analysis of ^{89}Zr-mA1 or bare ^{89}Zr incubated in FBS at different timepoints.



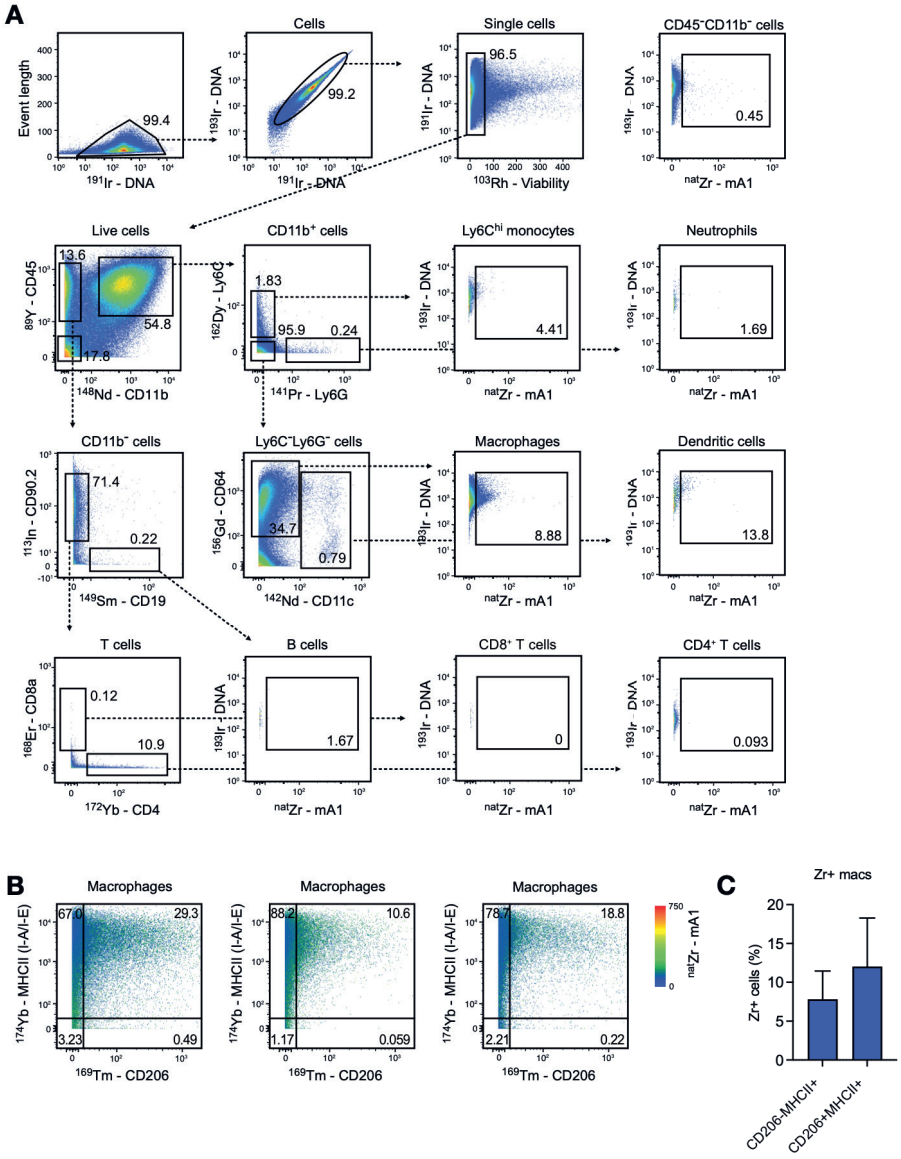
Supplementary Figure 2. A) Representative 3D-rendered PET/CT images of infarcted animals scanned at 1 (left) and 24 hours (right) after i.v. tracer injection. Arrows indicate the heart. B) Representative PET (left), CT (middle) and fused PET/CT (right) images of infarcted animals scanned 24 hours after tracer injection showing different axis: axial (upper panel), coronal (middle panel) and sagittal (lower panel). Arrows indicate the infarct area. C) B) Biodistribution of ^{89}Zr-mA1 in the mouse model of myocardial infarction, 24 hours after injection, determined by *ex vivo* gamma counting (n = 5). C) ^{89}Zr-mA1 uptake in the infarcted myocardium represented as target-to-blood (top) or target-to-muscle (bottom) ratio, as determined by *ex vivo* gamma counting (n = 5). ID/g, injected dose per gram tissue. **P < 0.01.



Supplementary Figure 3. Cell populations in the infarcted myocardium as analyzed by CyTOF. A) CyTOF gating strategy of the infarcted myocardium to identify leukocyte subsets and their ^{nat}Zr-positive fractions. See also Figure 3H-J. B) Distribution of ^{nat}Zr-mA1 in different macrophage subclusters of three independent infarcted myocardium samples. Flow plots are color coded for ^{nat}Zr signal. C) Quantification of ^{nat}Zr-mA1 uptake in the macrophage subsets as a percentage of ^{nat}Zr^{+} cells (n=3).



Supplementary Figure 4. A) Representative 3D-rendered PET/CT images of tumor-bearing animals scanned at 1 (left, n = 4) and 24 hours (right, n = 11) after tracer injection. Arrows indicate the tumor area, delineated in red. B) Representative PET (left), CT (middle) and fused PET/CT (right) images of tumor-bearing animals scanned 24 hours after tracer injection showing different axis: axial (upper panel), coronal (middle panel) and sagittal (lower panel). Arrows indicate the tumor area, delineated in red. C) Biodistribution of ^{89}Zr-mA1 in the B16F10 melanoma mouse model 24 hours after injection, determined by *ex vivo* gamma counting (n = 5). C) ^{89}Zr-mA1 uptake in the tumor represented as target-to-blood (top) or target-to-muscle (bottom) ratio, as determined by *ex vivo* gamma counting. ID/g, injected dose per gram tissue. **P < 0.01.



Supplementary Figure 5. Cell populations in the melanoma tumors as analyzed by CyTOF. A) CyTOF gating strategy of the tumor to identify leukocyte subsets and their ^{nat}Zr-positive fractions. See also Figure 4F. B) Distribution of ^{nat}Zr-mA1 in different macrophage subclusters of three independent tumor samples. Plots are color coded for ^{nat}Zr signal. C) Quantification of ^{nat}Zr-mA1 uptake in the macrophage subsets as a percentage of ^{nat}Zr^{+} cells (n=3).

References

1. Phenotypes of LDLR & APOE Knockout Mice | The Jackson Laboratory. https://www.jax.org/jax-mice-and-services/strain-data-sheet-pages/phenotype-information-for-002052-and-002207.
2. Jiang, F., Gibson, A. P. & Dusting, G. J. Endothelial dysfunction induced by oxidized low-density lipoproteins in isolated mouse aorta: A comparison with apolipoprotein-E deficient mice. *Eur. J. Pharmacol.* **424**, 141–149 (2001).
3. Tarnavski, O. *et al*. Mouse cardiac surgery: Comprehensive techniques for the generation of mouse models of human diseases and their application for genomic studies. *Physiol. Genomics* **16**, 349–360 (2004).



6

Probing myeloid cell dynamics in ischaemic heart disease by nanotracer hot-spot imaging

Published in Nature Nanotechnology, 2020.

Senders, M.L., Meerwaldt, A.E., van Leent, M.M.T., Sanchez-Gaytan, B.L., van de Voort, J.C., **Toner, Y.C.**, Maier, A., Klein, E.D., Sullivan, N.A.T., Sofias, A.M., Groenen, H., Faries, C., Oosterwijk, R.S., van Leeuwen, E.M., Fay, F., Chepurko, E., Reiner, T., Duivenvoorden, R., Zangi, L., Dijkhuizen, R.M., Hak, S., Swirski, F.K., Nahrendorf, M., Pérez-Medina, C., Teunissen, A.J.P., Fayad, Z.A., Calcagno, C., Strijkers, G.J., Mulder, W.J.M.

Toner, Y.C. was participated in the animal experiments. She helped perform the PET/CT imaging studies, with subsequent pharmacokinetics, biodistribution and autoradiography assays. She also assisted on sample preparation for flow cytometry. She was responsible for the animal models of atherosclerosis and myocardial infarct and together with Chepurko, E., she was performed the LAD ligation surgeries.

Abstract

Ischemic heart disease evokes a complex immune response. However, tools to noninvasively track leukocytes' systemic behaviour and dynamics *in vivo* are lacking. Here, we present a multimodal hot spot imaging approach using an innovative high-density lipoprotein-derived nanotracer with a perfluoro-crown ether payload (^{19}F-HDL) to allow myeloid cell tracking by ^{19}F magnetic resonance imaging (MRI). The ^{19}F-HDL nanotracer is additionally labelable with ^{89}Zr and fluorophores to respectively detect myeloid cells by *in vivo* positron emission tomography (PET) imaging and optical modalities. Using our nanotracer in atherosclerotic mice with myocardial infarction, we observed rapid myeloid cell egress from the spleen and bone marrow by *in vivo* ^{19}FHDL-MRI. Concurrently, using *ex vivo* autoradiographic techniques, we were able to show that circulating pro-inflammatory myeloid cells accumulated in atherosclerotic plaques and the myocardial infarct site. Therefore, this multimodality hotspot imaging approach can be applied to study the complex myeloid cell dynamics *in vivo*.

Introduction

Unravelling the immune system's role in pathophysiological processes has not only deepened and broadened our understanding of disease but has also yielded new therapeutic avenues[1]. In that context, research focusing on immune cell dynamics is becoming increasingly relevant[2,3]. A vast body of recent research has shown that atherosclerosis, the underlying cause of ischemic heart disease, is a lipid-driven disease that is also largely dependent on immune cell influx[4]. Moreover, cardiovascular events themselves mobilize immune cells and accelerate ongoing atherosclerosis[5]. This contemporary, more complex view of ischemic heart disease has resulted in the first clinical trial targeting inflammation with the goal of reducing the risk of recurrent cardiovascular events[6]. Although many different aspects of myeloid cell dynamics in ischemic heart disease have been deciphered[7], including their deployment from the bone marrow[8] and spleen[9], our current knowledge is exclusively based on snapshot immunological assays. Further, it is becoming more evident that these processes interact systemically[10–13]. Without suitable *in vivo* readouts, an all-encompassing view of these different processes is difficult to acquire. Therefore, this study's goal was to develop nanotechnology that can probe different aspects of myeloid cell dynamics in ischemic heart disease by multimodal imaging. We developed and applied so-called high-density lipoprotein (HDL) nanotracers with a lipophilic perfluoro-crown ether (^{19}F-HDL) payload to enable hot spot ^{19}F magnetic resonance imaging (^{19}F MRI) (Fig. 1A). These ^{19}F-HDL nanotracers can be additionally labelled with Zirconium-89 (^{89}Zr) and/or fluorophores for detection by *in vivo* positron emission tomography (PET) imaging, a variety of *ex vivo* nuclear methods and optical techniques, such as flow cytometry (Fig. 1A). Here, using this ^{19}F-HDL-facilitated multimodal *in vivo* imaging approach, we study myeloid cells in the bone marrow and spleen and monitor these cells' migration and accumulation in inflammatory tissues in mouse models of atherosclerosis and myocardial infarction (Fig. 1B).

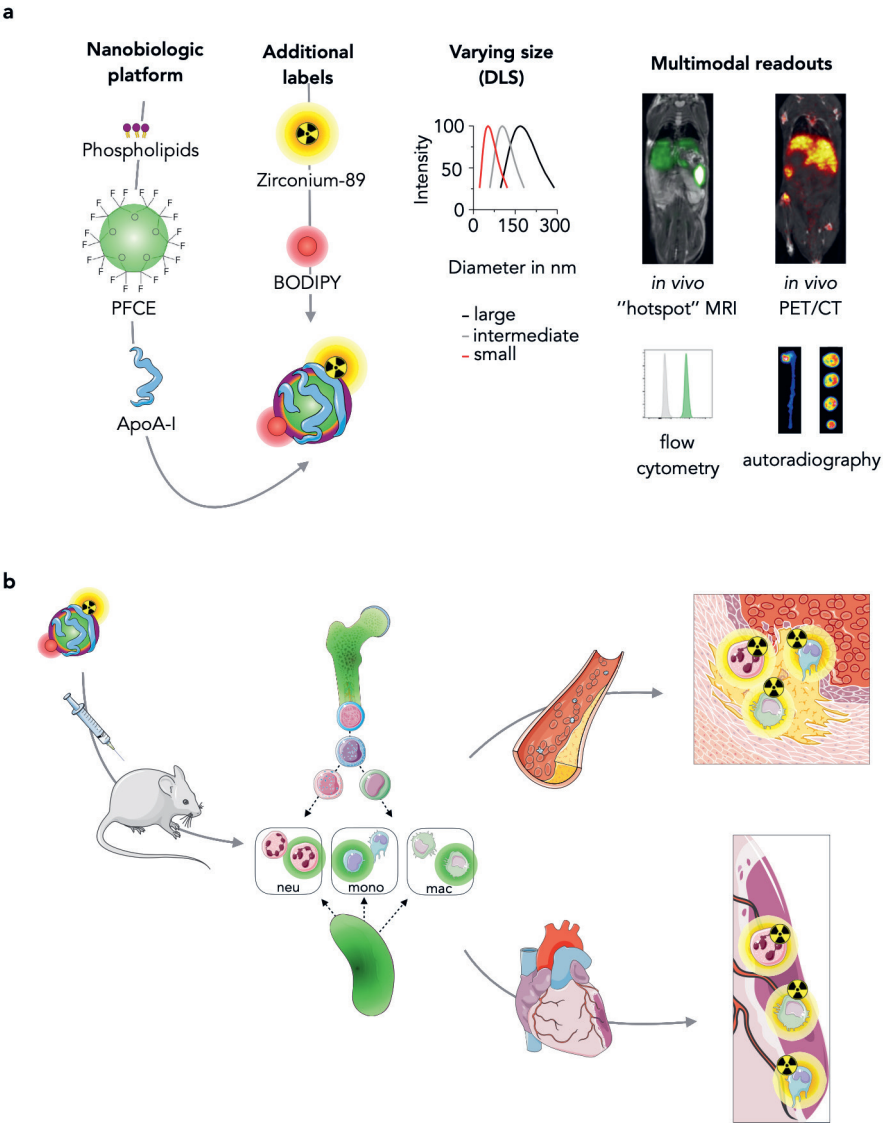


Figure 1. Nanotracer platform with multimodal evaluation in ischemic heart disease. A) The nanotracer platform consists of a perfluoro-crown ether (PFCE) core surrounded by a phospholipid layer stabilized by apoAI. Additional labeling with Zirconium-89 and BODIPY allows positron emission tomography (PET) imaging and optical assays, respectively. We developed three ^{19}F-HDL nanotracer formulations of varying size: "small (~40 nm)", "intermediate (~105 nm)" and "large (~180 nm)"; the lines represent their respective dynamic light scattering (DLS)-determined size distribution. B) Myeloid cell dynamics in the context of

ischemic heart disease. A mouse is injected with the nanotracer, which accumulates in the spleen and bone marrow as it is taken up by neutrophils (neu), monocytes (mono) and macrophages (mac). Egress from the spleen and bone marrow leads to subsequent nanotracer accumulation at the infarcted myocardium and atherosclerotic plaque.

Developing and characterizing multimodal nanotracers

We present a strategy to incorporate perfluorocarbons into high-density lipoprotein-like nanocarriers. Using this approach, we developed three formulations with varying ^{19}F payloads and sizes. These three differently sized ^{19}F-HDL nanotracers were composed of a perfluoro-crown ether core covered by a corona of phospholipids and apolipoprotein A1 (apoAI). Their hydrodynamic diameters were respectively 40 nm ('small'), 105 nm ('intermediate') and 180 nm ('large)', as measured by dynamic light scattering (DLS), and all remained stable at 37 °C in phosphate-buffered saline for 10 days (Fig. 1A, Fig. 2Ai, Supplementary Fig. 1A). Transmission electron microscopy corroborated these DLS findings and showed a narrow size distribution of mostly spherical structures (Fig. 2Aii). In an ensuing *in vivo* ^{19}F MR imaging study, the differently sized nanotracers were screened for their ability to accumulate in the spleen and bone marrow. Two days post injection, mice were anesthetized and subjected to preclinical MRI using a dedicated ^{19}F/^{1}H combination coil. Anatomical information was acquired using a standard 1H MRI protocol, while hot spot ^{19}F MRI was facilitated by a ^{19}F 3D-FLASH sequence to quantitatively visualize ^{19}F-HDL nanotracers. ^{19}F MRI revealed that the largest nanotracer displayed the most pronounced splenic uptake, while mice injected with the intermediate and small formulations showed splenic uptake levels comparable to those of the liver (Fig. 2Aiii). Quantitative analyses of the spleen indicated a significantly higher target-to-background ratio (TBR) for the large nanotracer (24.4 ± 7.3) compared to the small and intermediate formulations (10.4 ± 5.1 and 8.8 ± 2.1, respectively) $P < 0.01$ (Fig. 2B). Moreover, the largest formulation also displayed the strongest bone marrow uptake in the spine, while liver and kidney uptake did not differ among the three formulations (Fig. 2B and Supplementary Fig. 1B). Lastly, absolute muscle uptake for all ^{19}F-HDL formulations was similar, thereby justifying its use as 'background' signal for TBR calculations

(Supplementary Fig. 1C). Encouraged by the pronounced spleen uptake, we selected the large nanotracer for the ensuing extensive *in vivo* characterization. In a separate group of mice, fluorescently labelled ^{19}F-HDL was intravenously injected and allowed to distribute for 48 hours, after which the animals were sacrificed for flow cytometry experiments to study the largest nanotracer's cellular affinity in the spleen and bone marrow. In the spleen, we observed significantly stronger uptake by myeloid cells – macrophages, neutrophils and monocytes – as compared to lymphocytes, while in bone marrow, pro-inflammatory Ly6C^{high} monocytes were found to take up most of ^{19}F-HDL, $P < 0.01$ and $P = 0.005$ respectively (Fig. 2C, Supplementary Fig. 2A, B). To study its *in vivo* behaviour quantitatively, we radiolabelled the ^{19}F-HDL nanotracer with the long-lived (78.4 hours) radioisotope Zirconium-89 (^{89}Zr) to enable PET imaging. In contrast to ^{19}F MRI, this imaging method is highly sensitive, but we limited its use to 3 days due to ^{89}Zr's physical decay half-life. The nanotracer's core cannot be radiolabeled because of the perfluoro-crown ether's physicochemical properties and the ^{19}F-HDL formulation procedure. Therefore, we performed three alternative ^{89}Zr-labeling strategies involving conjugating the chelator desferrioxamine B (DFO) with the nanotracer to allow complexation of ^{89}Zr, generating ^{89}Zr-^{19}F-HDL. Free ^{89}Zr was removed by size exclusion chromatography (Supplementary Fig. 1D). The three radiolabeling strategies, involving (i) DFO-functionalized apoAI, (ii) DFO-functionalized phospholipid and (iii) using a lipophilic version of DFO called DFO-C34 showed similar PET imaging patterns, albeit the clearance dynamics (Fig. 2D, Supplementary Fig. 1E, 1F) and reproducibility varied. These differences likely result from differences in *in vivo* remodeling kinetics. For example, phospholipids are known to exchange between lipoproteins avidly, while apoAI is more tightly bound and accumulates in the kidneys, hence the differences in blood half-life and kidney uptake[14–16]. These data underscore that the apoAI labelling did not impact this protein's natural function. ^{89}Zr labelling through C34-DFO resulted in an imaging signature most similar to the ^{19}F MRI results. *Ex vivo* gamma counting two days after ^{89}Zr-19F-HDL injection validated the *in vivo* findings. For the 180 nm ^{89}Zr-19F-HDL, the spleen showed higher or similar uptake compared to the liver, irrespective of the ^{89}Zr labelling strategy, $P <$

0.005 (Fig. 2D). PET imaging showed ^{89}Zr-^{19}F-HDL in the circulation 5 minutes post injection (Fig. 2E, arrows) and mostly accumulated in the spleen, liver and kidneys one hour post injection (Fig. 2E). A PET scan 48 hours post injection corroborated Figure 2a's ^{19}F MRI findings, displaying high uptake in the spleen with substantial uptake in the liver and accumulation in the marrow-rich bone (Fig. 2E). We drew blood at multiple time points and calculated a circulation half-life of 6.2 hours (Fig. 2F, with DFO functionalized apoAI). It must be stressed that owing to the nanotracer's relative rapid accumulation in the spleen and bone marrow, the differences in remodelling kinetics had little impact on overall biodistribution. Subsequent experiments in *Apoe*$^{-/-}$ mice were performed with ^{89}Zr-^{19}FHDL using labelling strategies (ii) and (iii). The ^{19}F-HDL nanotracer's *in vivo* resilience was studied longitudinally in wild type mice (Fig. 2G). The ^{19}F MRI signal remained stable over time in the bone marrow and spleen (Fig. 2H), and flow cytometry quantification of fluorescently labelled nanotracers showed uptake by myeloid cells (CD11b+) (Supplementary Fig. 2C). Importantly, noise and muscle quantified by ^{19}F MRI did not differ over time (Supplementary Fig. 1G). Based on its ability to track myeloid cells over prolonged periods of time *in vivo*, we next set out to employ the ^{19}F-HDL nanotracer to study myeloid cell dynamics in ischemic heart disease mouse models by multimodal imaging.

Evaluation of myeloid cell dynamics in atherosclerosis development

To study myeloid cell dynamics in the context of chronic inflammation, we used the wellestablished apolipoprotein E knock-out (*Apoe*$^{-/-}$) mouse model of atherosclerosis. In these animals, the apoE ligand's absence in combination with a Western Diet (WD) results in atherosclerotic lesions that progress over

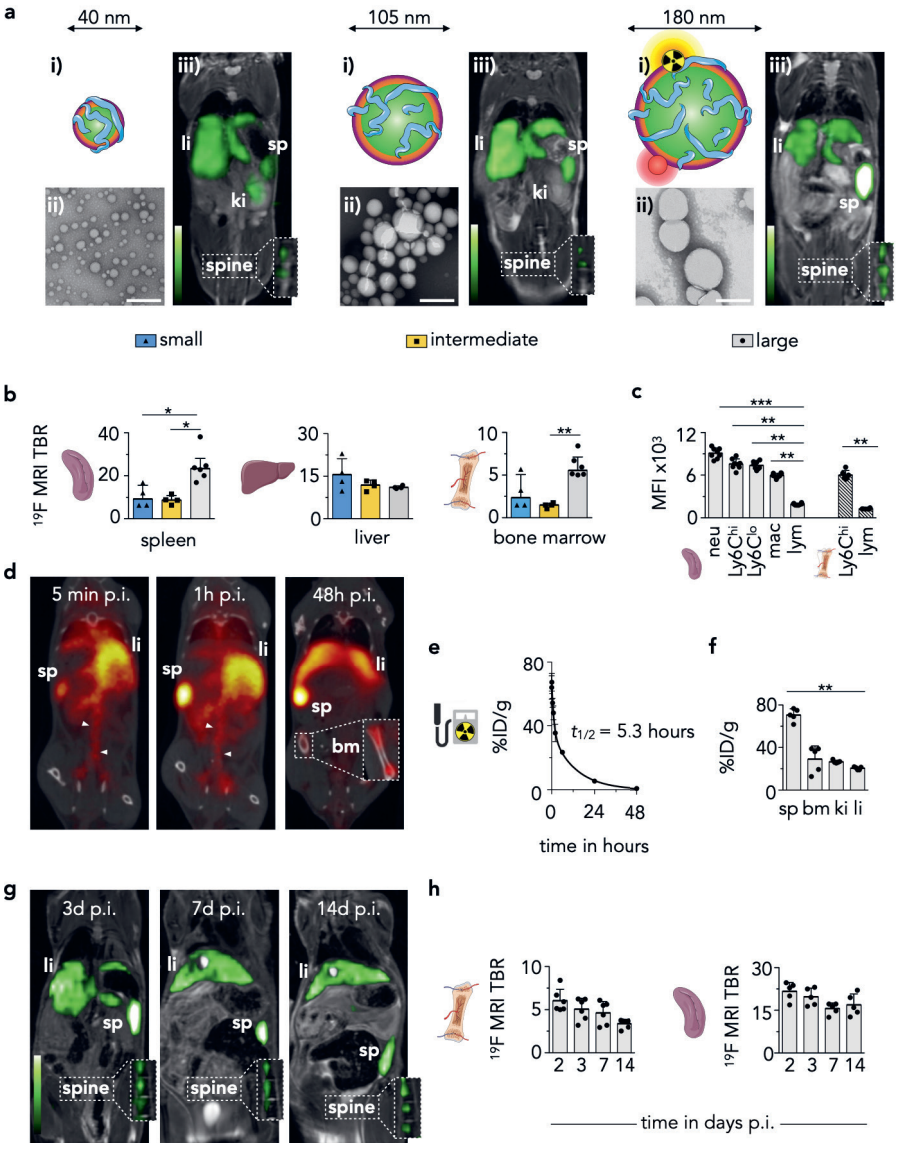


Figure 2. Developing and characterizing multimodal nanotracers. A) i) Schematic overview of ^{19}F-HDL's different sizes: small (~40 nm, *left*), intermediate (~105 nm, *middle*) and large (~180 nm, *right*) particles. ii) transmission electron microscopy (TEM) images showing different nanotracers' sizes and shapes (bar represents 200 nm). iii) representative fused ^{1}H and ^{19}F-magnetic resonance imaging (MRI) images 48 hours post injection (p.i.) of the nanotracers. MRI was repeated for n = 4 (small, intermediate) and n = 6 (large) biologically independent samples. B) Quantification of all three formulations in spleen (*left*), bone marrow (*middle*) and

liver (*right*) expressed as target-to-background (TBR) in which muscle serves as "background" signal. n = 4 mice (small, intermediate); n = 6 mice (large). *P=0.001 in spleen, **P=0.0023 for bone marrow. C) Mean fluorescence intensity (MFI) for different cells in spleen (*left*) and bone marrow (*right*). n = 8 mice (spleen); n = 6 mice (bone marrow). *P < 0.0001. D) Biodistribution 48 hours after ^{89}Zr-^{19}F-HDL injection in healthy mice with three different labeling strategies, DFO conjugated with apoAI (*top)*, DFO conjugated with liposomes (*middle*) or C_{34}-DFO incorporated in the liposome layer (*bottom*). (n = 5 mice per labelling strategy). *P=0.0042 for DFO conjugated with apoAI, *P=0.0005 for DFO conjugated with liposomes, *P=0.0018 for C_{34}-DFO E) Representative fused positron emission tomography/computed tomography (PET/CT) images at 5 minutes, 1 hour and 48 hours after ^{89}Zr-^{19}F-HDL injection (DFO conjugated with apoAI), including a magnified femur showing bone marrow (bm). Dynamic PET/CT was repeated for n = 4 biologically independent samples. F) Pharmacokinetic curve of ^{89}Zr-^{19}F-HDL in healthy mice. Data are shown as mean±s.e.m. (n = 3 independent samples for three first time points, n = 5 independent samples for the latter time points). G) Representative fused ^{1}H/^{19}F MRI images longitudinally evaluate ^{19}F-HDL 3, 7 and 14 days p.i. with magnified parts of the spine. The experiments were repeated twice independently with similar results; n = 6 biologically independent samples for each repetition. H) Quantified ^{19}F-HDL signal on different days after injection using longitudinal ^{19}F MRI in the bone marrow (*left*) and spleen (*right)* respectively. n = 5 mice, one mouse excluded based on Grubb's test for outliers. A one-way Kruskal-Wallis with Dunn's test for multiple comparisons was used unless otherwise stated. Data are shown as mean±sd in B, C, D, H. Abbreviations: neu=neutrophils, Ly6C^{hi}=Ly6C^{high} monocytes, Ly6C^{lo}=Ly6C^{low} monocytes, mac=macrophages, DC=dendritic cells, lym=lymphocytes, liver (li), spleen (sp), kidneys (ki), bone marrow (spine or bm), percentage injected dose per gram of tissue (%ID/g).

time[17]. We investigated myeloid cell dynamics in different atherosclerosis disease stages in *Apoe*$^{-/-}$ mice fed a WD for 0, 6 or 12 weeks, referred to as *Apoe*$^{-/-}$ 0WD, *Apoe*$^{-/-}$ 6WD, *Apoe*$^{-/-}$ 12WD. Upon ^{19}F-HDL administration and in line with our findings in wild type mice, we observed high accumulations in spleen and liver at three and fourteen days post injection for all atherosclerotic mice by *in vivo* ^{19}F MRI (Fig. 3A). In addition, the bone marrow signal in the spine was similar for all groups (Fig. 3A). To study the subsets of myeloid cells associated with our nanotracer at different stages of atherosclerosis development, cells were extracted from spleens that were harvested after sacrificing age and diet matched *Apoe*$^{-/-}$ mice (Fig. 3B). The nanotracer primarily labelled neutrophils, macrophages and Ly6Chigh monocytes (Fig. 3B). Subsequently, we performed quantification of the 19F MRI signal in the spleen, liver and bone marrow at different stages during atherosclerosis development (Fig. 4A). Over a time course of 28 days, 19F

MRI signal in spleen, liver, bone marrow and kidney (Fig. 4A, Supplementary Fig. 3A, B) remained stable for all groups, with one exception. The spleen and liver ^{19}F MRI signal in *Apoe*$^{-/-}$ 6WD dropped significantly at 28 days post injection, P = 0.03 (Fig. 4A). This decrease in signal was accompanied by increased Ly6C^{high} monocytes in aortas of *Apoe*$^{-/-}$ 6WD as compared to *Apoe*$^{-/-}$ 0WD, P = 0.002, while no difference was found with *Apoe*$^{-/-}$ 12WD, P = 0.06 (Fig. 4B, Supplementary Fig. 3C). The ^{19}F MRI visualized decrease in ^{19}F MRI signal in *Apoe*$^{-/-}$ 6WD can be the result of increased Ly6Chigh monocyte recruitment from bone marrow and spleen to the plaque (Fig. 4B) that occurs in the intermediate stages of atherosclerosis development[18]. In the advanced plaques of *Apoe*$^{-/-}$ 12WD, local proliferation dominates macrophage accumulation in the vessel wall[19], which explains the increased myeloid cell numbers in the vessel wall in the absence of myeloid cell egress from the spleen.

In addition to identifying increased myeloid cell departure from the spleen in *Apoe*$^{-/-}$ 6WD, this extensive longitudinal evaluation in atherosclerotic mice also showed the ^{19}F-HDL nanotracer to be stable over time.

Imaging of myeloid cell dynamics in myocardial infarction

To study the effects of myocardial infarction (MI) on myeloid cell dynamics in atherosclerosis, we fed *Apoe*$^{-/-}$ a WD for 6 weeks and then subjected them to either permanent (MI+) or transient ligation of the left anterior descending (LAD) artery, causing ischemia reperfusion injury (I/R)[20,21]. The latter is a relevant model of MI patients in whom the blockage of the coronary artery is treated, e.g., by stenting[22]. Two days prior to inducing ischemia, ^{19}F-HDL was injected and allowed to accumulate in the spleen and bone marrow (see outline Fig. 5A). We observed a rapid decline in ^{19}F MRI TBR in bone marrow and spleen one day after MI, for both permanent ligation and I/R, compared to non-MI controls, all P < 0.005 except for bone marrow in I/R P < 0.02 (Fig. 5B, C). A similar decrease was observed for the liver but not the kidneys at 3 days, P < 0.005 (Fig. 5C, Supplementary Fig. 4A). Mice injected with ^{89}Zr-19F-HDL and subjected to PET imaging one day after MI had less pronounced hematopoietic organ signal decrease, while liver signal did not differ among

the groups, all based on gamma counting (Supplementary Fig. 4B, C). When ^{19}F MR imaging was repeated 14 days post injection, the differences between mice with MI (permanent ligation or I/R) and without MI persisted, $P < 0.005$ (Fig. 5D, E, Supplementary Fig. 4A). Other than tissues and organs directly involved in myeloid cell dynamics, the ^{89}Zr-19F-HDL distribution did not significantly differ between MI and non-MI *Apoe*$^{-/-}$ mice (Supplementary Fig. 4D). The spleen acts as a reservoir that, in the event of MI or stroke, rapidly deploys large amounts of immune cells[9]. In addition, the liver and bone marrow serve as harbours for neutrophils that are released during acute injury[23,24], phenomena that have thus far only been studied using *ex vivo* readouts.

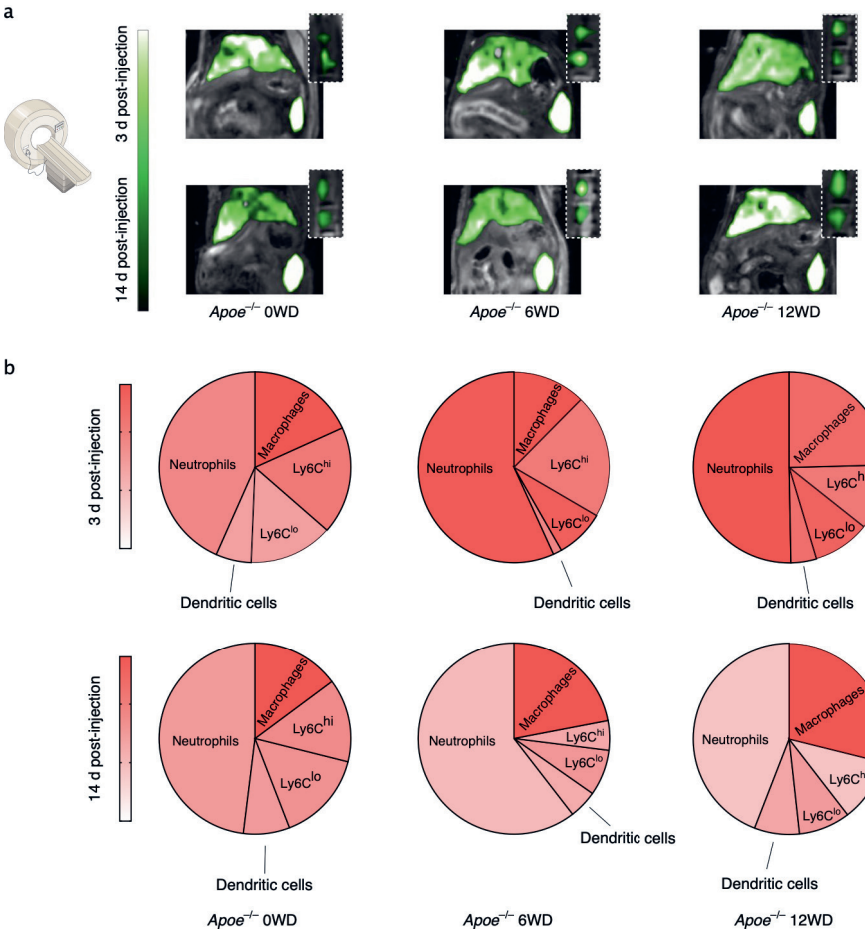


Figure 3. Characterization in atherosclerosis. A) Representative images of $^{1}H/^{19}F$ magnetic resonance imaging of upper abdominal area at 3 and 14 days post ^{19}F-HDL injection with magnifications of the spine containing bone marrow. Similar results were obtained in six (*Apoe*$^{-/-}$$_{0WD}$, *Apoe*$^{-/-}$$_{6WD}$) and five (*Apoe*$^{-/-}$$_{12WD}$) independent experiments. B)**.** Mean fluorescence intensity (MFI) for different myeloid cell subsets in spleen at 3, and 14 days post BODIPY-^{19}F-HDL injection. The size of each wedge represents the relative contribution of each cell type to the total number of myeloid cells in the spleen. n = 5 for all groups *Apoe*$^{-/-}$$_{0WD}$ and for *Apoe*$^{-/-}$$_{12WD}$ 3 days; n = 6 for all groups *Apoe*$^{-/-}$$_{6WD}$ and for *Apoe*$^{-/-}$$_{12WD}$ 14 days. Atherosclerotic *Apoe*$^{-/-}$ mice had been fed Western diet for 0 (*Apoe*$^{-/-}$$_{0WD}$), 6 (*Apoe*$^{-/-}$$_{6WD}$) or 12 (*Apoe*$^{-/-}$$_{12WD}$) weeks at the time of injection.

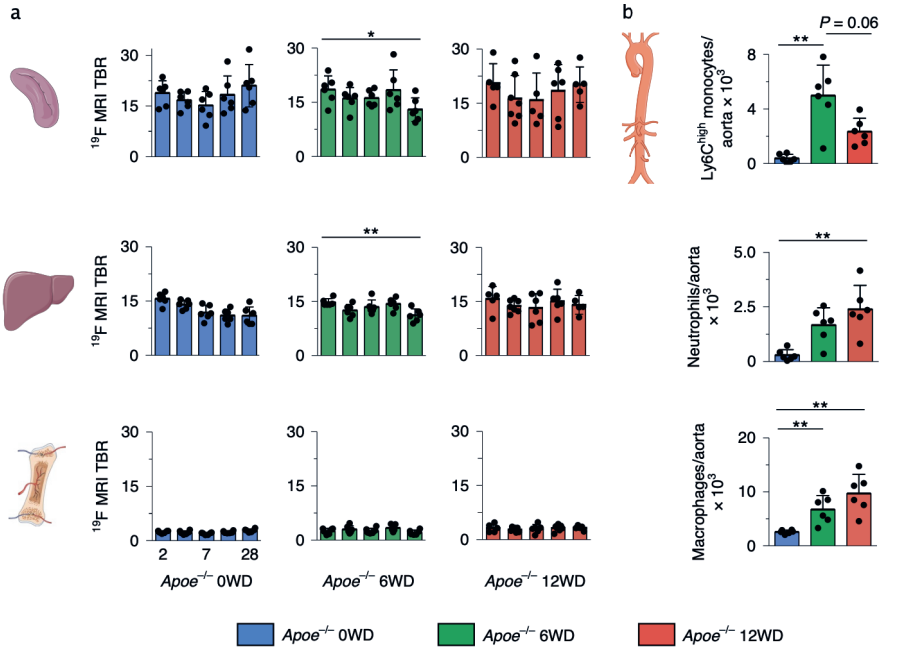


Figure 4. Longitudinal evaluation of myeloid cell dynamics during atherosclerosis development. A) Quantification of ^{19}F MRI signal expressed as target-to-background ratio (TBR) at 2, 3, 7, 14 and 28 days for spleen, liver and bone marrow. n = 6 mice for *Apoe*$^{-/-}$$_{0WD}$; n = 6 mice for *Apoe*$^{-/-}$$_{6WD}$; for *Apoe*$^{-/-}$$_{12WD}$ n = 5 mice at 2 d, 28 d, n = 7 at 3d, n = 6 at 14 d and n = 5 for spleen (one sample is excluded based on Grubb's test for outlier) and n = 6 for bone marrow and liver at 7 d. One sample is excluded completely in *Apoe*$^{-/-}$$_{12WD}$ at 7 days due to non-usable MRI data. A two-tailed Mann-Whitney U test was used for spleen and liver in *Apoe*$^{-/-}$$_{6WD}$ between 2 and 28 days, *P=0.0152 and *P=0.0022, respectively. B) Flow cytometry quantification of cells in the aorta. n = 6. All data are shown as mean±sd. A one-tailed Kruskal-Wallis test with Dunn's test for multiple comparisons was used unless otherwise stated. *P=0.0015 for Ly6C^{hi}, *P=0.0039 for neutrophils and *P=0.0023 for macrophages in the aorta. Abbreviations: Ly6C^{hi}=Ly6C^{high} monocytes, neu=neutrophils, mac=macrophages. Atherosclerotic mice had been fed Western diet for 0 (blue), 6 (green) or 12 (red) weeks at the time of injection.

Pro-inflammatory cells deploying from the hematopoietic organs into the circulation can aggravate peripheral inflammation, for example in atherosclerotic plaques[5]. In the current study, we observed decreased neutrophil levels in the bone marrow one day after permanent ligation, while in the circulation elevated levels of pro-inflammatory myeloid cells – neutrophils and Ly6C^{high} monocytes – made up more than 50% of all circulating leukocytes (neutrophils: 49.6% ± 12.9%; Ly6C^{high} monocytes: 8.5% ± 2.0%, P = 0.008 and P = 0.03, respectively (Supplementary Fig. 5A, B). Upon ^{89}Zr-^{19}F-HDL administration, increased myeloid cell uptake in the infarct and remote myocardium was observed in mice after permanent ligation (MI+) by autoradiography and confirmed by gamma counting of the whole heart, as compared to non-infarcted hearts, P = 0.02 (Fig. 5F, G). In I/R mice, myeloid cell recruitment to the infarct area was not significantly elevated, P = 0.15 (Fig. 5F, G). Additionally, the atherosclerotic aortic roots of Apoe$^{-/-}$ mice subjected to permanent MI showed an increased trend compared to non-MI mice, although no significant differences were found by gamma counting (Fig. 5G). In age-matched mice, flow cytometry identified an upsurge of neutrophils and Ly6C^{high} monocytes in the ischemic myocardium one day after permanent ligation, accompanied by death of resident macrophages, P < 0.005 for neutrophils and monocytes, P < 0.01 for macrophages, respectively (Supplementary Fig. 5C, D). Similarly, we observed massive neutrophil and Ly6C^{high} monocyte influx in whole aortas (P = 0.008 and P < 0.02 respectively), while macrophage numbers were unaffected (Supplementary Fig. 5C, D). In summary, our nanotracer multimodal imaging approach revealed pro-inflammatory cell egress from hematopoietic organs in two different models of MI, *in vivo* and noninvasively. This process could be monitored for up to at least 12 days after MI using ^{19}F MR imaging. As a consequence of myeloid cell deployment, we concurrently observed enhanced accumulation of these pro-inflammatory cells at peripheral inflammation sites by autoradiography and gamma counting.

Pro-inflammatory cells deploying from the hematopoietic organs into the circulation can aggravate peripheral inflammation, for example in

atherosclerotic plaques[5]. In the current study, we observed decreased neutrophil levels in the bone marrow one day after permanent ligation, while in the circulation elevated levels of pro-inflammatory myeloid cells – neutrophils and Ly6C^{high} monocytes – made up more than 50% of all circulating leukocytes (neutrophils: 49.6% ± 12.9%; Ly6C^{high} monocytes: 8.5% ± 2.0%, P = 0.008 and P = 0.03, respectively (Supplementary Fig. 5A, B). Upon ^{89}Zr-^{19}F-HDL administration, increased myeloid cell uptake in the infarct and remote myocardium was observed in mice after permanent ligation (MI+) by autoradiography and confirmed by gamma counting of the whole heart, as compared to non-infarcted hearts, P = 0.02 (Fig. 5F, G). In I/R mice, myeloid cell recruitment to the infarct area was not significantly elevated, P = 0.15 (Fig. 5F, G). Additionally, the atherosclerotic aortic roots of Apoe$^{-/-}$ mice subjected to permanent MI showed an increased trend compared to non-MI mice, although no significant differences were found by gamma counting (Fig. 5G). In age-matched mice, flow cytometry identified an upsurge of neutrophils and Ly6C^{high} monocytes in the ischemic myocardium one day after permanent ligation, accompanied by death of resident macrophages, P < 0.005 for neutrophils and monocytes, P < 0.01 for macrophages, respectively (Supplementary Fig. 5C, D). Similarly, we observed massive neutrophil and Ly6C^{high} monocyte influx in whole aortas (P = 0.008 and P < 0.02 respectively), while macrophage numbers were unaffected (Supplementary Fig. 5C, D). In summary, our nanotracer multimodal imaging approach revealed pro-inflammatory cell egress from hematopoietic organs in two different models of MI, *in vivo* and noninvasively. This process could be monitored for up to at least 12 days after MI using ^{19}F MR imaging. As a consequence of myeloid cell deployment, we concurrently observed enhanced accumulation of these pro-inflammatory cells at peripheral inflammation sites by autoradiography and gamma counting.

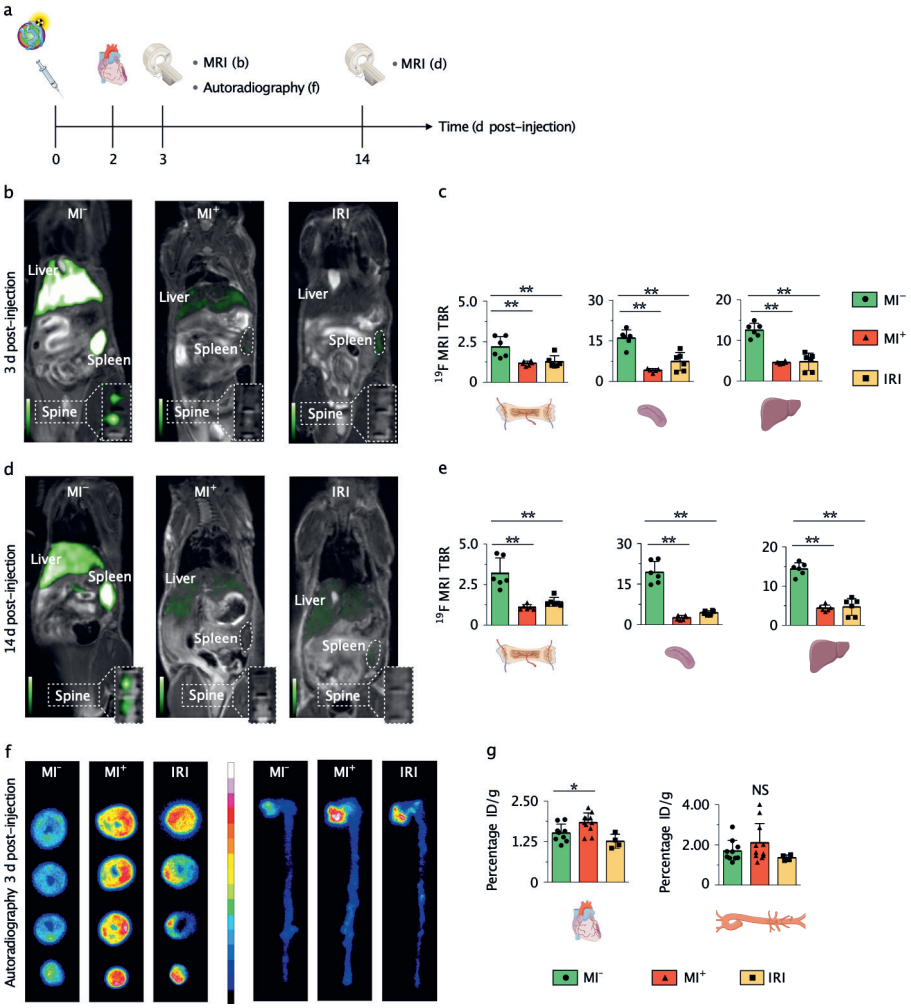


Figure 5. Multimodal imaging myeloid cell egress from hematopoietic organs and recruitment to inflammatory sites in myocardial infarction. A) Schematic overview of performed experiments. B) Representative ^{1}H/^{19}F magnetic resonance images of *Apoe*$^{-/-}$ mice without (*left*) and with permanent (*MI+, center*) or transient (*I/R, right*) myocardial infarction and C) quantification of ^{19}F-HDL in bone marrow, spleen and liver 3 days post ^{19}F-HDL injection (p.i.). expressed as target-to-background (TBR) in which muscle serves as "background" signal. n = 6 for MI, I/R and control groups except for MI+ spleen where n = 5, one sample is excluded based on Grubb's test for outliers. Two-sided Mann-Whitney *U*- test was used for bone marrow (*P=0.0022), spleen (*P=0.0043) and liver (*P=0.0022) D) Representative ^{1}H/^{19}F MR images of *Apoe*$^{-/-}$ mice without (*left*) and with permanent (*center*) or transient (*right)* myocardial infarction and E) quantification of ^{19}F -HDL in bone marrow, spleen and liver 14 days p.i. n = 6

for all groups. Two-sided Mann-Whitney *U*- test was used for bone marrow (*P=0.0043), spleen (*P=0.0022), and liver (*P=0.0022). F) Representative autoradiography of sliced heart sections and whole aortas from *Apoe*$^{-/-}$ mice without (*left*) or 1 day after permanent (*center)* or transient (*right)* myocardial infarction 3 days after ^{89}Zr-^{19}F-HDL injection. n = 7 (MI-); n = 8 (MI+); n = 4 (I/R). G) Gamma counting quantification of whole hearts and aortas from *Apoe*$^{-/-}$ mice without (*green*) or 1 day after permanent (*red)* or transient (*yellow)* myocardial infarction and 3 days p.i. ^{89}Zr-^{19}F-HDL. n = 9 for MI-, n = 11 for MI+ and n = 4 for I/R groups. Two-sided Mann-Whitney *U*-test was used. *P=0.0276 MI+ heart %ID/g compared to MI-, P=0.3418 for MI+ aorta %ID/g compared to MI-. In **b,d** experiments were repeated in n = 6 mice per group with similar results. All data are shown as mean±sd.

Abbreviations: I/R = ischemia/reperfusion, bm or spine indicates bone marrow, percentage injected dose per gram of tissue (%ID/g). *Apoe*$^{-/-}$ without MI are indicated in green, with MI are indicated in red (permanent ligation) and yellow (transient ligation).

Conclusions

Here we describe a systems imaging approach based on myeloid cell-specific and multimodal nanotracers. The nanotracer can label myeloid cells *in vivo* to map their dynamics in ischemic heart disease using a combination of *in vivo* hot spot ^{19}F MRI and PET imaging, *ex vivo* autoradiography and gamma counting, as well as optical techniques, including flow cytometry. Using this approach, we exploit the integrative strengths of PET/CT, optical and MR imaging. Labelling of the nanotracer with ^{89}Zr allows short-term studying of dynamics and biodistribution at high levels of sensitivity, while at a cellular level optical imaging can be used to study the associated cell subsets. Due to the physical decay, PET imaging is not appropriate to study systemic inflammatory changes over prolonged periods of time, and therefore we limited it to three days. By incorporating a fluorine core, our nanotracer allows quantification of immune cell dynamics up to 28 days after injection, however at less sensitivity compared to PET imaging First, we screened different sized nanotracers for favourable uptake in the spleen and bone marrow, hematopoietic organs that produce and deploy myeloid cells upon specific inflammatory triggers. The largest nanotracer displayed unusually high spleen uptake, as deduced from a TBR of ~24 as compared to ~10 for the smaller nanotracer. In the context of atherosclerosis progression, we

identified egress from the spleen by ^{19}F MRI, while flow cytometry showed accumulated pro-inflammatory monocytes in the aortas. When atherosclerotic mice were subjected to permanent or transient myocardial infarction, we observed significantly decreased fluorine signal in the spleen, bone marrow and liver by ^{19}F MRI, which was corroborated by PET imaging. At the same time, flow cytometry identified larger myeloid cell populations in the blood, the infarcted myocardium and the aorta, increases that coincided with enhanced myeloid cell accumulation as observed by *ex vivo* nuclear techniques. The apparent signal decline by ^{19}F MRI from the liver as a consequence of myocardial infarction was an unexpected finding and warrants further research. Author Manuscript Author Manuscript Author Manuscript We developed a nanotracer-based multimodal imaging approach to study immune cell dynamics longitudinally on a systemic level. In the current study, we used this imaging approach alongside cell sorting techniques to unravel regulatory pathways and pathophysiological processes in cardiovascular disease. Future research should include scaling up the nanotracer production and amending of imaging protocols to clinical systems to confirm our findings in translational studies. Ultimately, we anticipate its use in other inflammatory diseases and to aid in the development and evaluation of immunotherapies.

Methods

Formulating perfluoro-15-crown-5-ether (PFCE) loaded 19F-HDL nanotracers

1,2-dimyristoyl-sn-glycero-3-phosphocholine (DMPC, 59 mg) and 1-myristoyl-2-hydroxysn-glycero-3-phosphocholine (MHPC, 41 mg) (both Avanti Lipids) were dissolved in 2 mL of chloroform. The chloroform solution was slowly dripped in hot PBS (10 mL, 80 °C). The obtained solution was stirred for another 5 minutes at this temperature and then allowed to cool to room temperature. If necessary, additional PBS was added to obtain a total volume of 10 mL. The lipid solution (0.5 mL), PBS (4.5 mL) and perfluoro-15-crown-5-ether (PFCE, Oakwood Chemicals), 20 µL for ~36 nm particles, 80 µL for 105 nm particles, 160 µL for 180 nm particles were sonicated for 30

minutes at 0 °C using a 150 V/T ultrasonic homogenizer working at 30% power output for tip sonication. Apolipoprotein A1 (apoAI, purified in house from human HDL) (0.5 mg) was added and the mixture was incubated at room temperature for at least 12 hours after which the mixture was shaken and left to stand for 30 seconds. Any precipitate formed was discarded and the remaining solution was transferred to a Vivaspin tube (Sartorius Biotech) (100 kDa MWCO for ~36 and ~105 nm sized particles, 1 MDa MWCO for ~180 nm particles). The tube was spun at 4000 g at 4°C until the solution was concentrated to ~0.5 mL, and then the particles were resuspended by repeatedly moving them up and down a pipette. To determine particle size, an aliquot (10 mL) of the final particle solution was diluted in PBS (1 mL) and analysed by dynamic light scattering (DLS) to determine the mean of the number average size distribution. DLS measurements were performed on a Brookhaven Instrument Corporation ZetaPals analyser. The mean of the number distribution was taken as the particles size. All chemicals were obtained from Sigma Aldrich unless stated otherwise.

Determining PFCE concentration by 19F NMR

To determine the PFCE concentration in the prepared nanotracers, a solution containing nanotracers (90 vol %), D2O (10 vol %) and a known amount of sodium trifluoroacetate (NaTFA) was prepared. The solution was analysed by ^{19}F NMR and the PFCE concentration determined using NaTFA as an internal standard. ^{19}F NMR samples were analysed using a Bruker 600 ultrashield magnet connected to a Bruker advance 600 console. Data were processed using Topspin version 3.5 pl 7.

Modifying 19F-HDL nanotracers with BODIPY-cholesteryl

Cholesteryl 4,4-difluoro-5,7-dimethyl-4-bora-3a,4a-diaza-s-indacene-3-dodecanoate (BODIPY-cholesteryl) was obtained from ThermoFisher Scientific (catalog #C3927MP). To prepare nanotracers containing the BODIPY-cholesteryl dye the exact same protocol as for the unlabelled particles was used, except that BODIPY-cholesteryl was added to the lipid mixture at 1.0 wt % of the lipid amount used.

Functionalizing nanotracers with desferrioxamine B (DFO) for radiolabeling
Three strategies were pursued, either involved the DFO labelling of apoAI (strategy 1) or incorporation of a DSPE-DFO or aliphatic C34-DFO conjugate (strategies 2 and 3, respectively). While all labelling strategies resulted in stable 89Zr-labeled nanotracers, it was found that C34-DFO-based labelling strategy 3 is most reproducible. Strategy 1: DFO labelling apoA1 in preformulated nanotracers. DFO was conjugated to apoAI by basifying premade nanotracers in approximately 1–3 mL of PBS using a carbonate buffer (1 M, pH 9) until a pH of ~8.5 was reached. The apoAI concentration was kept between 1–10 mg/mL (assuming all apoAI used in formulating the nanotracers was recovered). p-NCS-Bz-DFO (Macrocyclics) was dissolved in DMSO to obtain 5 mg/mL solution and added to the nanotracers until a 2-fold molar excess of p-NCS-Bz-DFO (753 g/ mol) over apoAI (28,000 g/mol) was achieved. To minimize the influence of DMSO on the nanotracers, the p-NCS-Bz-DFO solution was added in aliquots of 5 µL and the total DMSO concentration kept below 5 vol. %. The solution containing nanotracers and p-NCS-Bz-DFO was incubated at 37 °C in a water bath for 2 hours and subsequently transferred to a Vivaspin centrifugal filtration tube (100 kDa MWCO). The Vivaspin tube was spun at 4000 g and 4°C until a volume of 1–2 mL was obtained, PBS (2 mL) was added and the solution was again concentrated to a volume of 1–2 mL. This washing step was repeated twice, after which the particles were resuspended by repeatedly moving them up and down a pipette. Strategies 2 and 3: Incorporating DSPE-DFO or C34-DFO in the nanotracers. To prepare nanotracers containing DSPE-DFO or C34-DFO, the exact same protocol as for formulating the unlabelled nanotracers was used, except that either DSPE-DFO or C34-DFO (synthesized using procedures previously reported by us)[1,2] was added to the lipid mixture at 0.5 wt. % of the amount of lipids used.

Radiolabelling DFO-bearing nanotracers with ^{89}Zr

Zirconium-89 (^{89}Zr) oxalate was made at Memorial Sloan Kettering Cancer Center using an EBCO TR19/9 variable beam energy cyclotron via the ^{89}Y(p,n)^{89}Zr reaction and purified using a previously published method[28], resulting in a ^{89}Zr solution in 1M aqueous oxalic acid. The ^{89}Zr solution was

diluted with PBS and aqueous sodium sulphate solution (1 M) added until a pH of 6.8–7.4 was reached. This solution was added to a solution of DFOfunctionalized nanotracers (either containing DSPE-DFO, C34-DFO or apoAI-DFO) and the obtained solution (1–2 mL total) incubated for 1 hour in a thermoshaker at 37 °C. The Zrlabelled nanotracers were purified using a PD-10 column (General Electric, Sephadex G-25 M) using PBS as the eluent. In the case of DSPE-DFO or C34-DFO labelled nanotracers (strategy 2 or 3), the nanoparticles were additionally washed 3 times with PBS by centrifugal filtration using a 10 kDA MWCO Vivaspin tube. Radiochemical purity was assessed using SEC radio-HPLC, typically a purity above 95 % was achieved. Author Manuscript Author Manuscript Author Manuscript Radiochemical yields were typically between 50–90 % for strategy 1, and reproducibly above 80 % for strategies 2 and 3. Size-exclusion chromatography (SEC) radio-high performance liquid chromatography (radio-HPLC) analyses were performed on a Shimadzu system equipped with a Superdex 10/300 SEC column using a flow rate of 1 ml/min and demi water as the eluent. A Lablogic Scan-RAM radiodetector was used.

Animals

All animal experiments were performed in accordance with protocols approved by the Institutional Animal Care and Use Committees of the Icahn School of Medicine at Mount Sinai and followed National Institutes of Health guidelines for animal welfare. Mouse models—Female *Apoe*$^{-/-}$ (B6.129P2-*Apoe*^{tm1Unc}/J, 8 weeks old) were purchased from the Jackson Laboratory and fed a cholesterol-enriched, Western diet (WD, Harlan Teklad TD.88137, 42 % calories from fat) for either 0, 6 or 12 weeks before injection and remained on this diet for the remainder of the experiment. Due to the elevated circulating LDL concentrations resulting from their lack of apolipoprotein E, these animals develop atherosclerotic plaques, especially at locations with disturbed flow, i.e. the aortic root, and the aortic arch with its branches[26,27]. Age matched female C57BL/6J received regular chow and served as controls. Myocardial infarction—Age-matched 8-weeks-old female *Apoe*$^{-/-}$ mice received a WD for 6 weeks before undergoing permanent or temporary ligation of the left descending artery (LAD) to induce a myocardial infarction,

as described in full detail here3. Anaesthesia was induced using Ketamine (100 mg/kg) with Xylazine (10 mg/kg) intraperitoneally and maintained using isoflurane. Analgesia was provided using Buprenorphine (0.1 mg/kg) before and 12 hours after surgery. The left side of thorax was shaved and disinfected, a thoracotomy was performed using the 5th or 4th intercostal space and a retractor was used to keep the surgical field exposed. Attention was paid not to puncture the left lung. Temporary ligation was maintained for 40 minutes by a small tube between the ligation suture and LAD. All infarctions were created 2 days after injection with either ^{19}F-HDL or ^{89}Zr-^{19}FHDL. For more details, see outline (Fig. 5A).

MRI imaging

C57BL/6 or *Apoe*$^{-/-}$ mice were injected with 1.3 µL of ^{19}F-HDL solution per gram of body weight via the lateral tail vein. Mice were anesthetized with isoflurane (Baxter Healthcare)/oxygen gas mixture (2% for induction, 1 % for maintenance), and images were acquired on a 7T Bruker BioSpec 70/30 scanner (Bruker) using a ^{19}F/^{1}H birdcage coil for mice (MR Coils B.V.). After acquiring localizer scans, a hydrogen (^{1}H) 3-dimensional (3D) fast low angle shot (FLASH) sequence was performed to identify the liver and spleen (orientation, coronal; repetition time [TR], 20 ms; echo time [TE], 3.7 ms; field-of-view [FOV], 60 × 60 × 30 mm3; matrix, 256 × 128 × 128; reconstructed voxel size, 0.23 × 0.23 × 0.23 mm3; flip angle 20°; signal averages, 2; acquisition time, 6min8s). An additional ^{1}H TURBO rapid Author Manuscript Author Manuscript Author Manuscript imaging with refocused echoes (RARE), T2-weighted sequence, was also acquired for this purpose (orientation, coronal; repetition time [TR], 3000 ms; echo time [TE], 33 ms; number of slices, 27; slice thickness, 1 mm; slice gap, 0.1 mm; field-of-view [FOV], 60 × 30 mm2; matrix size, 256 × 128, RARE factor 8, pixel size 0.23 × 0.23 mm2; signal averages, 12; acquisition time, 9m36s). Next, the coil was switched to 19F mode. After centring the frequency on the perfluoro-crown ether (PFCE) peak, a 3D FLASH sequence was performed to quantify 19F signal in the liver and spleen (orientation, coronal; repetition time [TR], 20 ms; echo time [TE], 2.9 ms; field-of-view [FOV], 60 × 60 × 30 mm3; matrix, 64 ×

32 × 32; voxel size, 0.94 × 0.94 × 0.94 mm3; flip angle 25°; signal averages, 200; acquisition time, 1h8min16s).

PET/CT imaging

C57BL/6 or *Apoe*$^{-/-}$ mice were injected with the 89Zr-19F-HDL (0.07 – 0.30 mCi) in 100 µL PBS solution via the lateral tail vein. Animals were anesthetized with isoflurane (Baxter Healthcare, Deerfield, IL)/oxygen gas mixture (2% for induction, 1 % for maintenance), and a scan was performed using a Mediso nanoScan PET/CT (Mediso, Budapest, Hungary). Wild type mice were imaged immediately after injection followed by a second imaging 48 hours later. *Apoe*$^{-/-}$ mice were imaged 72 hours post injection. A whole body CT scan was performed (energy 50 kVp, current 180 µAs, isotropic voxel size at 0.25 × 0.25 mm) followed by a 20 or 60 minutes PET scan. Reconstruction for the PET data utilized the CT acquisition for attenuation correction. Reconstruction was performed using the TeraTomo 3D reconstruction algorithm using the Mediso Nucline software. The coincidences were filtered with an energy window between 400 – 600 keV. The voxel size was isotropic with 0.6 mm width and the reconstruction was applied for two full iterations, 6 subsets per iteration.

Image analysis

All obtained imaging data were analysed using Osirix (5.6) software (OsiriX Foundation, Geneva, Switzerland). Regions of interest (ROI) were measured by manually drawing a contour on different tissues. In the case of 19F MRI, a target-to-background ratio was calculated by dividing the mean of multiple (>10) maximum ROI values (ROI_{max}) from tissue of interest by the mean of multiple ROI_{max} from muscle tissue.

Pharmacokinetics and biodistribution in mice

Blood radioactivity half-life was determined by serial blood draws from the tail vein at 1, 5, 30, 60 and 120 minutes and 6, 24 and 48 hours after ^{89}Zr-^{19}F-HDL injection. Blood was weighed and counted using a Wizard2 2480 automatic gamma counter (Perkin Elmer). After scans were completed,

animals were sacrificed and perfused, and tissues (brain, heart, lungs, aorta, spleen, liver, kidneys, skeletal muscle and bone marrow) were collected, blotted and weighed in pre-weighed tubes. Radioactivity content was measured by gamma counting, and tissue radioactivity concentration was calculated and expressed as % injected dose per gram (%ID/g) or normalized by activity found in muscle tissue.

Autoradiography

Digital autoradiography was performed to determine Zirconium-89 distribution within the whole aorta and infarct. Samples were placed in a film cassette against a phosphorimaging plate (BASMS-2325, Fujifilm) for 1.5 h (whole aortas) or, 2h (hearts) and stored at −20 °C. Phosphorimaging plates were read at a pixel resolution of 25 µm with a Typhoon 7000IP plate reader (GE Healthcare). Quantification was carried out using ImageJ software.

Flow cytometry

For flow cytometry analysis, blood was obtained by cardiac puncture and collected in an EDTA-coated tube. Mice were subsequently perfused through the left ventricle with 10 mL cold PBS. Femur and spleen were harvested. The aorta, from aortic root to the iliac bifurcation, was collected. The infarcted heart tissue was collected and weighed. The aorta was minced and digested using an enzymatic digestion solution containing liberase TH (4 U/mL) (Roche), deoxyribonuclease (DNase) I (40 U/mL) (Sigma-Aldrich) and hyaluronidase (60 U/mL) (Sigma-Aldrich) in PBS. Heart tissue was minced and digested using an enzymatic digestion solution containing DNAse (60 U/mL), collagenase I (450 U/ mL), collagenase XI (125 U/mL) and hyaluronidase (60 U/mL) (all Sigma-Aldrich) in PBS. Aortas and heart tissues were incubated for 1 hour at 37°C under agitation. Cells were filtered through a 70 µm cell strainer and washed with FACS buffer (DPBS with 1% FBS, 0.5% BSA, 0.1%NaN3 and 1mM EDTA). Blood was incubated with lysis buffer for 4 minutes and washed with FACS buffer and repeated 2 more times. Spleens were weighed. A piece of 25 mg was mashed, filtered through a 70 µm cell strainer, incubated with lysis buffer for 4 minutes and washed with FACS

buffer. Bone marrow was flushed out of the femur with PBS, filtered through a 70 µm cell strainer, incubated with lysis buffer for 30 seconds and washed with FACS buffer. Single cell suspensions were stained with the following monoclonal antibodies: anti-CD11b (clone M1/70), anti-F4/80 (clone BM8), antiCD11c (clone N418), anti-CD45 (clone 30-F11), anti-Ly6C (clone AL-21) and a lineage cocktail (Lin) containing anti-CD90.2 (clone 53–2.1), anti-Ter119 (clone TER119), antiNK1.1 (clone PK136), anti-CD49b (clone DX5), anti-CD45R (clone RA3–6B2), antiCD103 (clone 2E7) and anti-Ly6G (clone 1A8). Antibodies were purchased from eBioscience, Biolegend or BD Biosciences. Macrophages were identified as $CD45^{+}$, $CD11b^{high}$, $Lin^{-/low}$, $CD11c^{low}$ and $F4/80^{hi}$. Monocytes were identified as $CD45^{+}$, $CD11b^{high}$, $Lin^{-/low}$, $CD11c^{low}$ and $Ly6C^{high/low}$. Neutrophils were identified as $CD45^{+}$, $CD11b^{high}$ and Lin^{+}. Lymphocytes were identified as $CD45^{+}$ and Lin^{+}. $CD11b^{+}$ cells were identified as $CD45^{+}$ and $CD11b^{+}$. To measure ^{19}F-HDL's cellular specificity, BODIPY-^{19}FHDL was intravenously injected 48 hours before euthanasia. BODIPY uptake was measured in the FITC channel. Mean fluorescence intensity was corrected to fluorescent bead signal (Sphero AccuCount Fluorescent Particles, Spherotech). Data were acquired on a Fortessa flow cytometer (BD Biosciences), and data were analysed using FlowJo v10.4.0 (Tree Star).

Statistics

Data are presented as mean ± standard deviation. Differences were evaluated using twosided Mann-Whitney test (between 2 groups) or a student's t-test for repeated measures (between 2 groups). For differences among more than 2 groups, a Kruskal-Wallis was followed by Dunn's test for multiple comparisons unless otherwise stated. For all tests, $\alpha < 0.05$ represents statistical significance. Statistical analyses were performed with GraphPad Prism®, Version 6.0c.

Data availability

All data generated or analysed during this study are included in this published article (and its supplementary information files).

Source of funding

This work was supported by the "De Drie Lichten" Foundation in The Netherlands (M.L.S.); American Heart Association 17PRE33660729 (M.L.S.) and 16SDG3139000, (C.P.M.), German Research Foundation grant MA 7059/1 (A.M.), HO 5953/1-1, National Heart, Lung, and Blood Institute grants (HL096576, HL117829, HL139598 and HL128264) and the MGH Research Scholar Award (M.N. and F.K.S.); Dutch Applied and Engineering Sciences (TTW) grant #14716 (G.J.S); National Institutes of Health grants R01 HL118440, R01 HL125703, R01 HL144072 and ZonMW Vidi 91713324 and Vici 91818622 (W.J.M.M.) and NIH grants R01EB009638 and P01HL131478 (Z.A.F.).

References

1. Moore KJ & Tabas I Macrophages in the pathogenesis of atherosclerosis. Cell 145, 341–355 (2011).

2. Yona S et al. Fate mapping reveals origins and dynamics of monocytes and tissue macrophages under homeostasis. Immunity 38, 79–91 (2013).

3. Geissmann F et al. Development of Monocytes, Macrophages, and Dendritic Cells. Science (80-.). 327, 656–661 (2010).

4. Swirski FK & Nahrendorf M Leukocyte behavior in atherosclerosis, myocardial infarction, and heart failure. Science 339, 161–6 (2013).

5. Dutta P et al. Myocardial infarction accelerates atherosclerosis. Nature 487, 325–329 (2012).

6. Ridker PM et al. Antiinflammatory Therapy with Canakinumab for Atherosclerotic Disease. N. Engl. J. Med NEJMoa1707914 (2017). doi:10.1056/NEJMoa1707914

7. Nahrendorf M Myeloid cell contributions to cardiovascular health and disease. Nat. Med 24, 711720 (2018).

8. Herisson F et al. Direct vascular channels connect skull bone marrow and the brain surface enabling myeloid cell migration. Nat. Neurosci (2018). doi:10.1038/s41593-018-0213-2

9. Swirski FK et al. Identification of Splenic Reservoir Monocytes and Their Deployment to Inflammatory Sites. Science (80-.). 235, 612–616 (2009).

10. Tawakol A et al. Relation between resting amygdalar activity and cardiovascular events: a longitudinal and cohort study. Lancet 6736, (2017).

11. Thackeray JT et al. Myocardial Inflammation Predicts Remodeling and Neuroinflammation After Myocardial Infarction. J. Am. Coll. Cardiol 71, 263–275 (2018).

12. Heidt T et al. Chronic variable stress activates hematopoietic stem cells. Nat. Med 20, 754–8 (2014).

13. Roth S et al. Brain-released alarmins and stress response synergize in accelerating atherosclerosis progression after stroke. Sci. Transl. Med 10, (2018).

14. Pérez-Medina C et al. A Modular Labeling Strategy for In Vivo PET and Near-Infrared Fluorescence Imaging of Nanoparticle Tumor Targeting. J. Nucl. Med 55, 1706–1712 (2014).

15. Tang J et al. Immune cell screening of a nanoparticle library improves atherosclerosis therapy. Proc. Natl. Acad. Sci 201609629 (2016). doi:10.1073/pnas.1609629113

16. Pérez-Medina C et al. In Vivo PET Imaging of HDL in Multiple Atherosclerosis Models. JACC Cardiovasc. Imaging (2016). doi:10.1016/j.jcmg.2016.01.020

17. Nakashima Y, Plump AS, Raines EW, Breslow JL & Ross R ApoE-deficient mice develop lesions of all phases of atherosclerosis throughout the arterial tree. Arterioscler. Thromb 14, 133–40 (1994).

18. Swirski FK et al. Ly-6Chi monocytes dominate hypercholesterolemia-associated monocytosis and give rise to macrophages in atheromata. J. Clin. Invest 117, 195–205 (2007).

19. Robbins CS et al. Local proliferation dominates lesional macrophage

accumulation in atherosclerosis. Nat Med 19, 1166–1172 (2013).

20. Panizzi P et al. Impaired Infarct Healing in Atherosclerotic Mice With Ly-6ChiMonocytosis. J. Am. Coll. Cardiol 55, 1629–1638 (2010).

21. Von Elverfeldt D et al. Dual-contrast molecular imaging allows noninvasive characterization of myocardial ischemia/reperfusion injury after coronary vessel occlusion in mice by magnetic resonance imaging. Circulation 130, 676–687 (2014).

22. Heusch G et al. Cardiovascular remodelling in coronary artery disease and heart failure. Lancet 383, 1933–1943 (2014).

23. Kolaczkowska E & Kubes P Neutrophil recruitment and function in health and inflammation. Nat. Rev. Immunol 13, 159–175 (2013).

24. Soehnlein O Multiple roles for neutrophils in atherosclerosis. Circ. Res 110, 875–888 (2012).

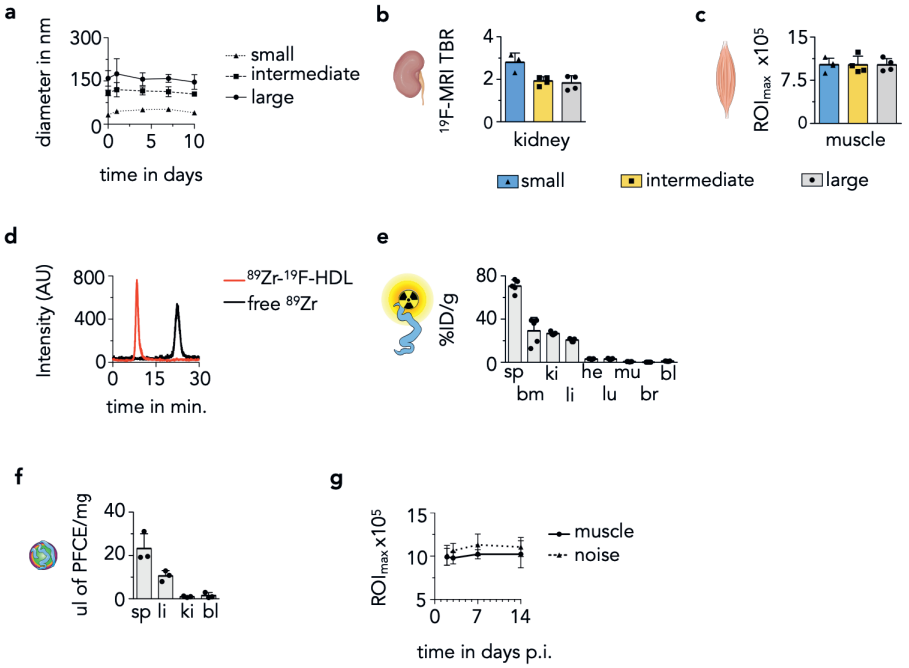
25. Holland JP, Sheh Y & Lewis JS Standardized methods for the production of high specific-activity zirconium-89. Nucl. Med. Biol 36, 729–739 (2009).

26. Nakashima Y, Plump AS, Raines EW, Breslow JL & Ross R ApoE-deficient mice develop lesions of all phases of atherosclerosis throughout the arterial tree. Arterioscler. Thromb 14, 133–40 (1994).

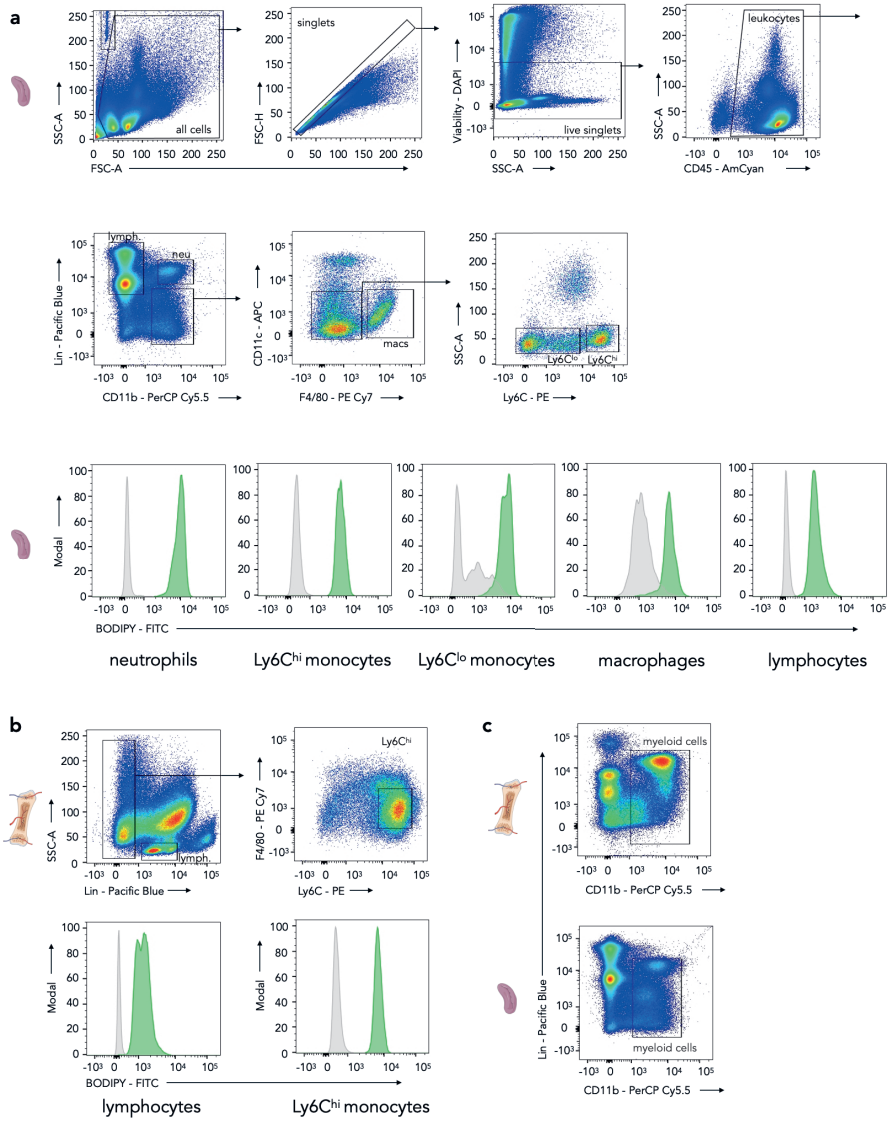
27. Plump AS et al. Severe hypercholesterolemia and atherosclerosis in apolipoprotein E-deficient mice created by homologous recombination in ES cells. Cell 71, 343–53 (1992).

28. Tarnavski O et al. Mouse Cardiac Surgery: Comprehensive Techniques for the Generation of Mouse Models of Human Diseases and Their Application for Genomic Studies. Physiol. Genomics 349360 (2003). doi:10.1152/physiolgenomics.00041.2003

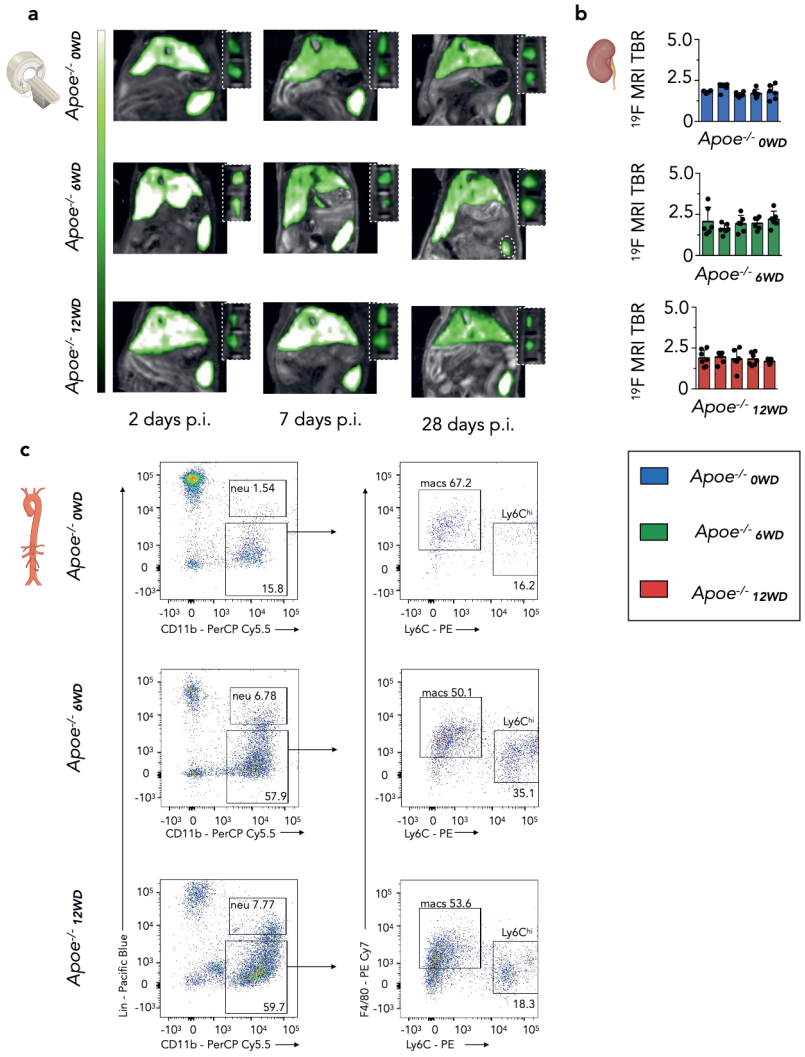
Supplemental information



Supplementary Figure 1. A) Stability of the three different nanotracer formulations in phosphate buffered saline at 37 °C. n = 5 B) Quantification of 19F MRI in kidney expressed as target-tobackground ratio (TBR) for all three nanotracer formulations. Muscle serves as "background". n = 3 for small formulation (one sample excluded based on Grubb's test for outliers), n = 4 intermediate and large formulations. One way Kruskall-Wallis was not significant after Dunn's multiple comparison test, P = 0.0498. C) Quantification of muscle values by ^{19}F MRI for all three formulations. n = 4 for all formulations, One way Kruskall-Wallis was not significant, P = 0.9260. D) Size exclusion chromatography of ^{89}Zr-^{19}F-HDL and free 89Zr. The same sample was measured repeatedly over time. E) Complete ^{89}Zr-^{19}F-HDL nanotracer biodistribution in wild type mice 48 hours post injection (conjugation of deferoxamine (DFO) to apoAI). n = 5. F) Quantification of perfluoro-crown ether by ^{19}F NMR expressed as PFCE per µL of ^{19}F-HDL nanotracer suspension. n = 3. G) Mean of 10 ≥ ROImax muscle and noise values at 2, 3, 7, and 14 days post injection of ^{19}F-HDL by ^{19}F MRI. Two-way ANOVA with Bonferroni correction for multiple comparisons did not reveal differences over time in either muscle or noise (P = 0.2167). n = 6. Abbreviations: spleen (sp), liver (li), kidneys (ki), bone marrow (bm), heart (he), lung (lu), muscle (mu), brain (br), blood (bl). Percentage injected dose per gram of tissue (%ID/g). All data are shown as mean±sd.

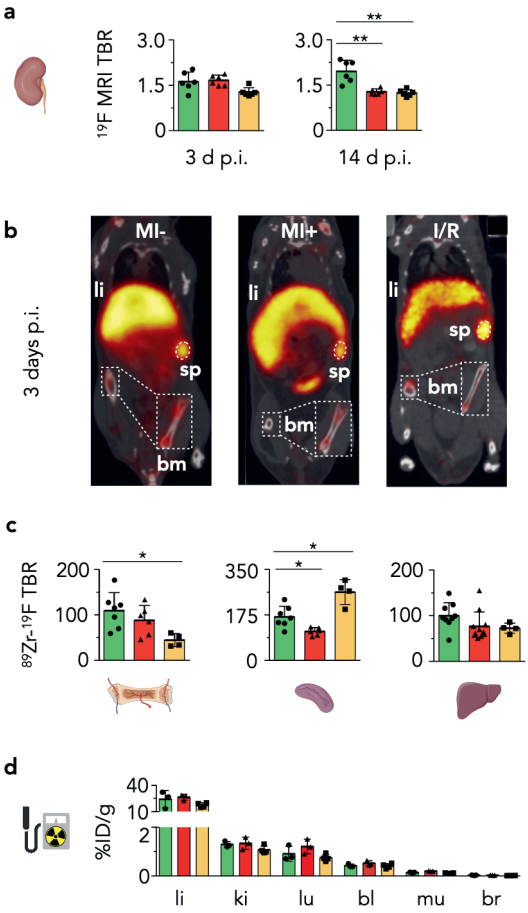


Supplementary Figure 2. A) Gating strategy of myeloid subpopulations in the spleen and representative histograms for different cell types 48 hours after intravenous injection of BODIPY-^{19}F-HDL (green) as compared to control (grey). Experiments were repeated in n = 4 biologically independent samples for similar results. B) Gating strategy and representative histograms for lymphocytes and Ly6C^{high} monocytes in bone marrow 48 hours after intravenous injection of BODIPY-^{19}F-HDL. Experiments were repeated in n = 4 biologically independent samples for similar results. C) Identification of CD11b^{+} cells in bone marrow (top, left) and in the spleen (bottom, left). Flow cytometry quantification of BODIPY-^{19}F-HDL in the bone marrow (top, right) and spleen (bottom, right) on different days after injection. n = 4 mice per time point. Data are shown as mean±sd.



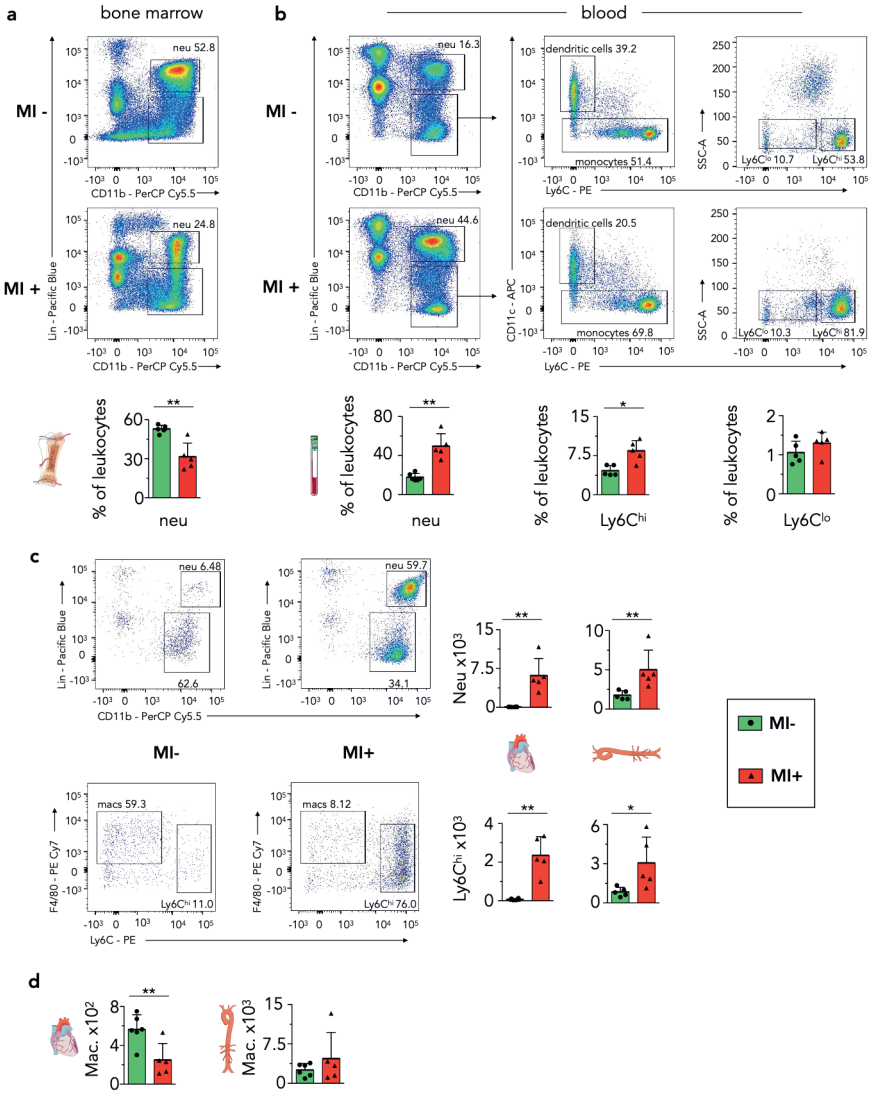
Supplementary Figure 3. A) Representative images of $^{1}H/^{19}F$ magnetic resonance imaging of upper abdominal area at 2, 7, and 28 days post ^{19}F-HDL injection with magnifications of the spine containing bone marrow. Similar results were obtained in six (*Apoe*$^{-/-}$0WD, *Apoe*$^{-/-}$6WD) and five (*Apoe*$^{-/-}$12WD) biologically independent samples per group. B) Quantification of ^{19}F MRI expressed as target-to-background ratio (TBR) at 2, 3, 7, 14, and 28 days post ^{19}F-HDL injection in kidneys. n ≥ 5 per group. n = 6 for *Apoe*$^{-/-}$12WD and *Apoe*$^{-/-}$6WD for all time points, n = 7 for *Apoe*$^{-/-}$12WD for 2, 3 and 14 days, n = 6 for 7 days and n = 5 for 28 days post ^{19}F-HDL injection. Data are shown as mean±sd C) Representative flow cytometry plots of aortas from *Apoe*$^{-/-}$ mice. Atherosclerotic *Apoe*$^{-/-}$ mice had been fed Western diet for 0 (blue), 6 (green) or 12 (red) weeks at the time of injection. Similar results were obtained in n = 5 (*Apoe*$^{-/-}$0WD, *Apoe*$^{-/-}$12WD) and n = 6 (*Apoe*$^{-/-}$6WD) biologically independent samples 3 days after ^{19}F-HDL-BODIPY

injection and in n = 5 (*Apoe*$^{-/-}$0WD) and n = 6 (*Apoe*$^{-/-}$6WD, *Apoe*$^{-/-}$12WD) biologically independent samples 14 days after ^{19}F-HDL-BODIPY injection.



Supplementary Figure 4. A) Quantification of ^{19}F-HDL in kidneys 3 (left) and 14 (right) days post ^{19}F-HDL injection in *Apoe*$^{-/-}$ mice 6 weeks on a Western diet without (green) or with myocardial injury (red = permanent ligation, yellow = ischemia/reperfusion). n = 6 for all groups. A two-tailed Mann-Whitney U test was used, **P = 0.0022 between MI- and MI+ and between MI- and I/R at 14 days after 19F-HDL injection. B) Representative fused positron emission tomography/computed tomography (PET/CT) images of *Apoe*$^{-/-}$ mice without (left) and with permanent (center) or transient (right) myocardial infarction and C) gamma counting of bone marrow, spleen and liver 3 days p.i. ^{89}Zr-^{19}F-HDL. Representative results and gamma counting quantification were obtained in n = 7 (MI-), n = 6 (MI+) and n = 4 (I/R) biologically independent samples for b, c. A two-tailed Mann-Whitney U test was used, *P = 0.012 between MI- and I/R for bone marrow, *P = 0.014 between MI- and MI+ and *P = 0.024 between MI- and I/R for spleen. D) Biodistribution 3 days post ^{89}Zr-^{19}F-HDL injection in *Apoe*$^{-/-}$ mice with (red, yellow) and without myocardial infarction (green). n = 3 for MI- and MI+ groups, n = 4 for I/R group.

Abbreviations: spleen (sp), bone marrow (bm), liver (li), kidneys (ki), lung (lu), blood (bl), muscle (mu), brain (br). Percentage injected dose per gram of tissue (%ID/g). All data are shown as mean±sd.



Supplementary Figure 5. A) Identification of neutrophils in bone marrow in mice without (top) and 1 day after (middle) permanent myocardial infarction and quantification of these cells as percentage of total leukocytes in bone marrow (bottom). n = 6 for MI-, n = 5 for MI+. *P = 0.0087. B) Representative flow cytometry plots identifying circulating neutrophils, Ly6C^{high} and Ly6C^{low} monocytes in mice without (top) and 1 day after (middle) permanent myocardial infarction and quantification of these cell subsets as percentage of circulating leukocytes (bottom). n = 5 for all MI+, n = 6 for MI- except for Ly6C^{hi} and Ly6C^{lo} n = 5 as one sample was

excluded based on Grubb's test for outliers. **P = 0.008 for neutrophils and *P = 0.0317 for Ly6C^{hi}. C) Representative flow plots of neutrophils, macrophages and Ly6C^{high} monocytes in healthy (left) and infarcted (right) myocardium and quantification of neutrophils and Ly6C^{high} monocytes in the infarcted or healthy myocardium or whole aorta from *Apoe*$^{-/-}$ mice without (green) or 1 day after permanent MI (red), quantified as number of cells per mg and in the case of aortas, number of cells per whole aorta. n = 6 for MI- in heart, n = 5 for MI+ in heart, aorta and MI- in aorta. One sample in MI- in aorta was excluded based on Grubb's test for outliers. ** P = 0.0043 and ** P = 0.0078 for neutrophils in heart and aorta, respectively, and ** P = 0.0043 and * P = 0.0159 for Ly6C^{hi} in heart and aorta, respectively. D) Quantification of macrophages in the infarcted (1 day after permanent ligation) or healthy myocardium or whole aorta from *Apoe*$^{-/-}$ mice. n = 6 for MI-; n = 5 for MI+ in heart and aorta. ** P = 0.0087 for macrophages in heart. Abbreviations: Percentage injected dose per gram of tissue (%ID/g). neu=neutrophils, Ly6C^{hi}=Ly6C^{high} monocytes, Ly6C^{lo}=Ly6C^{low} monocytes, mac=macrophages. All data are shown as mean±sd. A two-tailed Mann-Whitney U test was used in a-d.

Part 3

In vivo imaging to evaluate anti-inflammatory nanotherapy



7

Targeting myelopoiesis prevents organ inflammation

Published in iScience, 2020.

Toner, Y.C., Munitz, J., Prevot, G., Morla-Folch, J., Wang, W., van Elsas, Y., Priem, B., Deckers, J., Anbergen, T., Beldman, T.J., Brechbühl, E.E.S., Aksu, M.D., Ziogas, A., Sarlea, S.A., Ozturk, M., Zhang, Z., Li, W., Li, Y., Maier, A., Fernandes, J.C., Cremers, G.A.O., van Genabeek, B., Kreijtz, J.H.C.M., Lutgens, E., Riksen, N.P., Janssen, H.M., Söntjens, S.H.M., Hoeben, F.J.M., Kluza, E., Singh, G., Giamarellos-Bourboulis, E.J., Schotsaert, M.,

Duivenvoorden, R., van der Meel, R., Joosten, L.A.B., Cai, L., Temel, R.E. Fayad, Z.A., Mhlanga, M.M., van Leent, M.M.T., Teunissen, A.J.P., Netea, M.G., Mulder, W.J.M. Toner, Y.C. planned and performed the in vitro experiments in human cells (including cell isolation and trained immunity assays), as well as the animal experiments, including PET/CT imaging, biodistribution and flow cytometry. She was also responsible for the animal models of hyperinflammation and ARDS. She analyzed the data and wrote the manuscript.

Abstract

Infections, cancer, and trauma can cause life-threatening hyperinflammation. In the present study, using single-cell RNA sequencing of circulating immune cells, we found that the mammalian target of rapamycin (mTOR) pathway plays a critical role in myeloid cell regulation in COVID-19 patients. Previously, we developed an mTOR-inhibiting nanobiologic (mTORi-nanobiologic) that efficiently targets myeloid cells and their progenitors in the bone marrow. *In vitro*, we demonstrated that mTORi-nanobiologics potently inhibit infection-associated inflammation in human primary immune cells. Next, we investigated the *in vivo* effect of mTORi-nanobiologics in mouse models of hyperinflammation and acute respiratory distress syndrome. Using ^{18}F-FDG uptake and flow cytometry readouts, we found mTORi-nanobiologic therapy to efficiently reduce hematopoietic organ metabolic activity and inflammation to levels comparable to those of healthy control animals. Together, we show that regulating myelopoiesis with mTORi-nanobiologics is a compelling therapeutic strategy to prevent deleterious organ inflammation in infection-related complications.

Introduction

Exacerbated host immune response, also known as hyperinflammation, is a life-threatening condition for which limited treatment options exist[1]. It can be triggered by diverse circumstances, including autoimmune and autoinflammatory diseases, trauma, or severe infections such as sepsis, but is also observed as an adverse effect of cancer immunotherapy. It is estimated that 13.7 million patients die annually as a result of infection-related complications among which many are linked to dysregulated inflammatory responses[2]. In these patients, immune activation becomes dysregulated resulting in exaggerated release of proinflammatory mediators such as cytokines, which subsequently spearheads endothelial cell activation, disseminated intravascular coagulation, hypotension, organ failure, and sometimes death[1,3]. Such a hyperinflammatory response can manifest either systemically, culminating in septic shock, or locally in certain organs, such as the lungs leading to the development of acute respiratory distress syndrome (ARDS). ARDS is a prototype clinical syndrome characterized by tissue disruption, compromised gas exchange in the lungs[4] and excessive cytokine release. It contributes to a systemic process referred to as cytokine storm, which conversely exacerbates ARDS, highlighting their interconnected nature[5–7]. Currently, there are few therapeutic options available for the treatment of ARDS. In fact, poor management of ARDS is linked to mortality rates of 40% or higher in moderate-to-severe cases of hospitalized patients[8–10].

Although sepsis and pneumonia drive the majority of all ARDS cases[8], the COVID-19 pandemic intensified research on the subject. Studies consistently report that COVID-19-triggered hyperinflammation and ARDS increase mortality[11–14]. Current disease management strategies include alleviating symptoms and some pathophysiological approaches, such as epithelial/endothelial repair, anticoagulants and anti-inflammatory medication[15]. Besides the direct effects, individuals surviving ARDS often

experience long-term physical and cognitive decline[16–18], further underscoring the need for innovative immunotherapeutic strategies.

While most immunotherapies for sepsis focus on the inhibition of proinflammatory cytokines[19], emerging research highlights the role of metabolic dysregulation in hyperinflammation. In particular, the mammalian target of rapamycin (mTOR) signaling is crucial for the activation of immune cells and is central to systemic inflammation[20–22]. Sensitive to stress and inflammatory signals, mTOR controls cellular metabolism and can increase glycolytic activity by stimulating the production and activation of hexokinase, phosphofructokinase, and pyruvate kinase[23]. Moreover, mTOR prompts hypoxia-inducible factor 1-alpha (HIF-1**α**) expression, which in turn promotes the release of IL-1ß[24,25] and upregulates the expression of glycolytic enzymes and glucose transporters, increasing glucose influx and usage by immune cells[26]. This switch to glycolysis provides energy for cellular proliferation, migration, phagocytosis and production of inflammatory cytokines and mediators.[20,27,28] Targeting mTOR in innate immune cells therefore represents an attractive approach to manage infection-associated hyperinflammation.

In this study, we used single-cell RNA sequencing (scRNA-seq) to profile peripheral blood mononuclear cells (PBMCs) from SARS-CoV-2-infected patients. In line with non-COVID-19 sepsis, we found differential expression of mTOR-related genes, especially in innate immune cells. Inspired by these findings, we evaluated our mTORi-nanobiologic[29] in inflammation and trained immunity[30] assays using primary human monocytes. Using the quantification of [^{18}F]fluorodeoxyglucose (^{18}F-FDG) uptake and flow cytometric analyses as readouts for metabolic activity and inflammation, respectively, we evaluated mTORi-nanobiologics' *in vivo* therapeutic potential in murine models of hyperinflammation and ARDS.

Results

SARS-CoV-2 infection leads to differential expression of mTOR pathway genes in circulating immune cells

We first studied mTOR signaling in scRNA-seq datasets of whole blood and PBMC samples of COVID-19 cohorts (Supplementary Table S1). More precisely, we evaluated the expression profiles of 156 genes from the mTOR pathway in the circulating immune cell populations from patients with mild, severe, and convalescent COVID-19[31–33] (Fig. 1A, Supplementary Table S2). Towards this aim, we identified cell type-specific differentially expressed genes (DEGs) from the mTOR pathway between these four independent COVID-19 patient cohorts, for which scRNA-seq data of immune cells were available. From the cohorts reported by Schulte-Schrepping *et al*[31] (Bonn and Berlin cohorts, C1 and C2, respectively), we compared healthy volunteers (control), mild and severe COVID-19 patients for each immune cell cluster. Additionally, we compared hospitalized and convalescent participants in a different cohort (MHH50 cohort, C3) from Zhang *et al*[32], as well as convalescent COVID-19 patients and healthy volunteers (control) in the Convalescent COVID-19 (C4) cohort[33].

We identified 79 mTOR pathway-related DEGs in at least one of the analyses (Supplementary Fig. S1A-D). Compared to healthy volunteers, we found that mainly in classical monocytes from the COVID-19 patients, the mTOR pathway-related genes were differentially expressed (Fig. 1B and Supplementary Fig. S2A). We observed Growth Factor Receptor Bound Protein 2 (GRB2), Serum/Glucocorticoid Regulated Kinase 1 (SGK1), ras homolog family member A (RHOA) and CAP-Gly domain containing linker protein 1 (CLIP1), which are associated with PI-3 kinase-mediated signal transduction, cytoskeletal modulation and cell migration [34–36], to be upregulated in classical monocytes of different cohorts. Of note, the levels of an essential downstream effector of mTOR signaling, ribosomal subunit protein S6 (Rps6), were downregulated in most of the clusters in hospitalized or severe COVID-19 samples pointing towards decreased ribosomal biogenesis (Supplementary Fig. S1A-C). Interestingly, cells from mild and

control patients differed most, while cells from mild versus severe patients showed the fewest dissimilarities. We observed the same trend in the convalescent COVID-19 cohort when focusing on upregulated DEGs, while for downregulated genes, in addition to monocytes, differences were also pronounced in natural killer cells (Fig. 1C and Supplementary Fig. S2B). Out of all cell types, classical and non-classical monocytes displayed the most DEGs occurring exclusively in one cell population. Our analysis of the previously published COVID-19 dataset showed that mTOR pathway-associated genes are dysregulated across various immune cell populations, albeit to a greater extent on monocyte subsets in hyperinflammatory conditions.

Nanobiologics targeting mTOR in myeloid cells

The nanobiologics platform is composed of phospholipids, cholesterol, propane-1,2,3-triyl trioctanoate and apolipoprotein A1 (apo-A1), as we previously described[29]. Owing to their size (of approximately 50 nm in diameter) and the apo-A1 coating, nanobiologics efficiently target myeloid cells and their hematopoietic progenitors (Fig. 2A). By loading nanobiologics with an mTOR-inhibitory prodrug, the mTOR pathways can be effectively inhibited *in vivo*. We characterized the mTORi-nanobiologics' size by dynamic light scattering (DLS, Fig. 2B), while cryogenic electron microscopy reviewed spherical morphology (cryoEM, Fig. 2C).

mTOR-inhibiting nanobiologics reduce inflammation in primary human cells *in vitro*

We investigated the potential of mTORi-nanobiologics for the modulation of infection-associated inflammation by conducting *in vitro* experiments profiling the function of human monocytes after stimulation, in the presence or absence of nanobiologics. We previously developed a trained immunity assay[37] that allows for the study and treatment of monocytes' hyperresponsiveness *in vitro* (Fig. 3A). Monocytes were stimulated for 24 hours with **β**-1,3-(D)-glucan (**β**-glucan) or heat-inactivated SARS-CoV-2 Wuhan-Hu-1 variant[38] or remained unstimulated in the presence or absence

of 1 or 10 µM mTORi-nanobiologics. After washing the cells with warm PBS at 24 hours, we washed them again at 72 hours. On day 6, the cells were restimulated with 10 ng/mL *E. coli* lipopolysaccharide (LPS), and supernatant

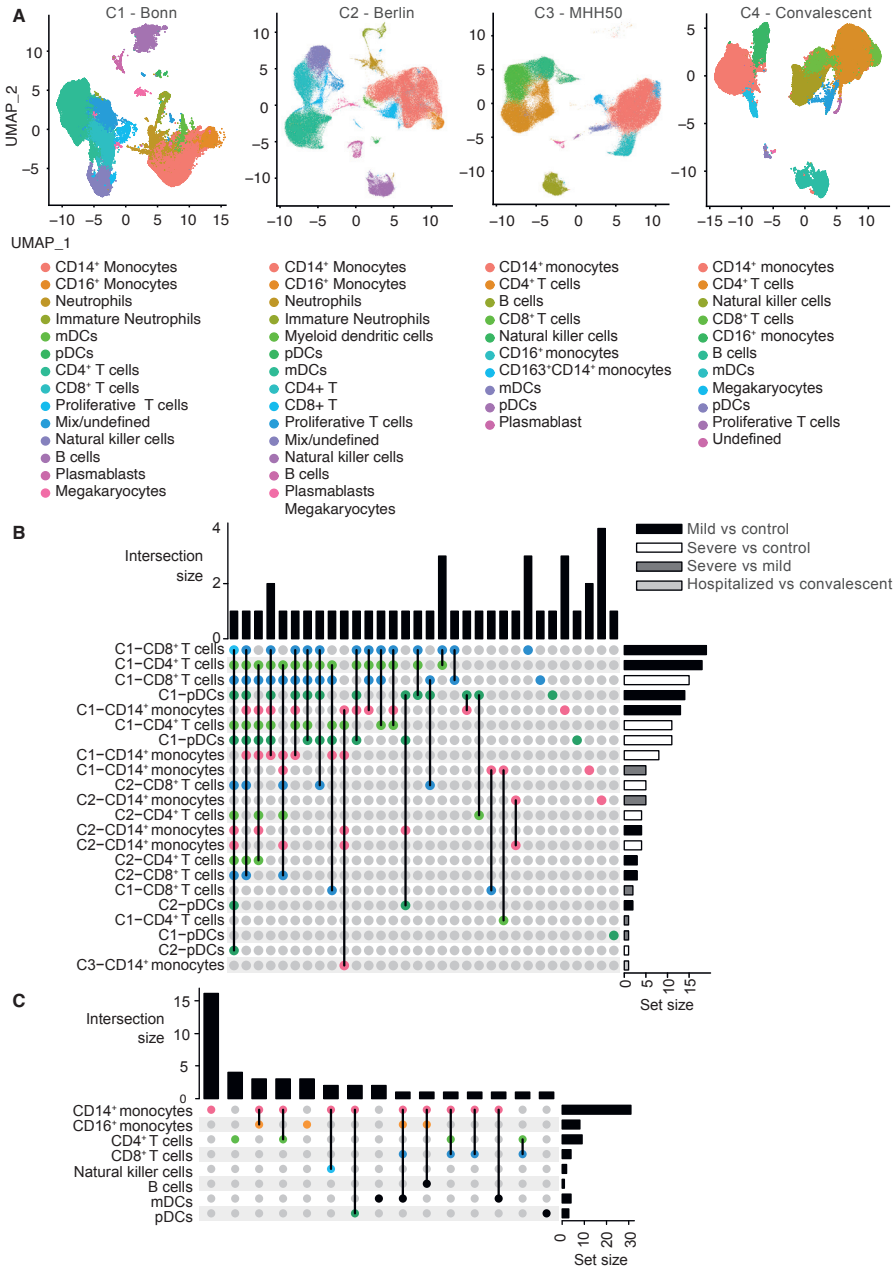


Figure 1. mTOR signaling pathway gene expression profiles support the use of mTORi-nanobiologics for the treatment of inflammation in COVID-19 patients. A) UMAP of scRNA-seq from the Berlin (C1), Bonn[31] (C2) and MHH50[32] (C3) cohorts datasets, respectively, and UMAP of scRNA-seq from convalescent COVID-19 patients[33] (C4). B) Upregulated differentially expressed genes across the Berlin (C1), Bonn[31] (C2), and MHH50[32] (C3) datasets. Intersection size represents the number of genes that were differentially expressed across the different comparisons, connected by dots, in the y-axis. Set size represents the number of genes that were differentially expressed within each comparison on the y-axis. C) The number of upregulated mTOR genes in specific cell types in convalescent COVID-19 patients (C4 cohort)[33]. Intersection size represents the number of genes that were differentially expressed across different cell types, connected by dots, in the y-axis. Set size represents the number of genes that were differentially expressed within each cell type on the y-axis. Differentially expressed genes between every two disease conditions were identified using FindMarkers() function by Wilcoxon rank sum test. Control = healthy volunteers, pDCs = plasmacytoid dendritic cells, mDCs = myeloid dendritic cells. See also Supplementary Figures S1 and S2 and Supplementary Tables S1 and S2.

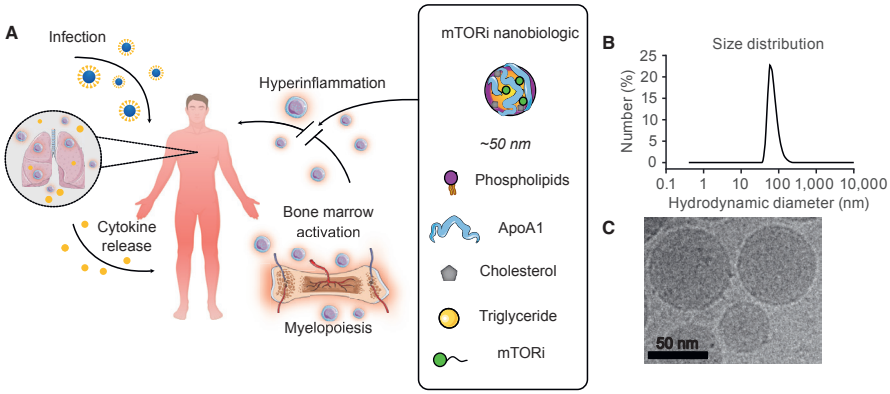


Figure 2. Bone marrow-avid mTORi-nanobiologics characterization. A) Study concept overview. Nanobiologics are lipoprotein-based nanoparticles with high avidity for myeloid cells and their progenitors in the bone marrow. We have loaded nanobiologics with a lipophilic prodrug of rapamycin, which is a potent mTOR inhibitor. These mTOR-inhibiting nanobiologics (mTORi-nanobiologics) dampen bone marrow activation and reduce systemic hyperinflammation upon infection. B) mTORi-nanobiologic's characterization by dynamic light scattering and C) cryo-EM. Scale bar = 50 nm.

was collected 24 hours later to determine TNF-α (Fig. 3B) and IL-6 production (Fig. 3C) by ELISA. TNF-α and IL-6 are gold standard markers of trained immunity, as they reflect the functional state of innate immune cells[39,40]. We

found that cells incubated with β-glucan or SARS-CoV-2 enhanced cytokine secretion upon LPS restimulation, a hyperresponsiveness indicative of innate immune memory[30]. In contrast, cells that were treated with mTORi-nanobiologics during the initial 24-hour training phase did not become hyperresponsive. A trend towards a dose-dependent effect was observed in the β-glucan group for cells treated with mTORi-nanobiologics. Similar results were also attained for trained immunity-associated pro-inflammatory chemokines (Supplementary Fig. S3A-C), where mTOR-nanobiologics treated cells showed lower CXCL-9, CXCL-10 and IL-8 production upon LPS restimulation.

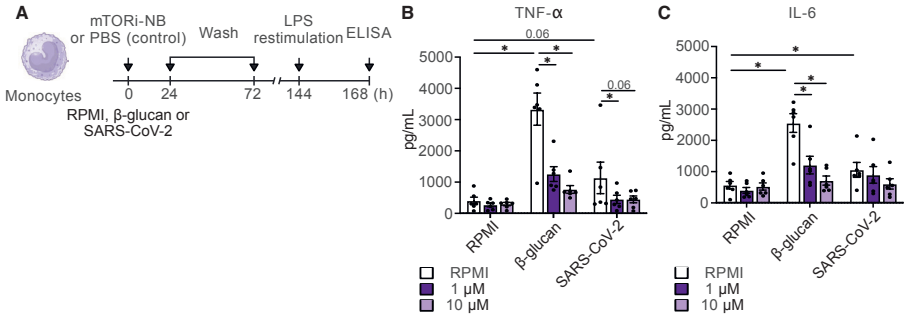


Figure 3. mTORi-nanobiologics reduces inflammatory response in human monocytes *in vitro*. A) Schematic representation of trained immunity assays, employed on primary monocytes derived from healthy donors. B) *In vitro* trained immunity assay showing TNF-α production upon LPS restimulation. C) *In vitro* trained immunity assay showing IL-6 production upon LPS restimulation. Statistical analysis was performed using the Wilcoxon signed-rank test. *p<0.05. See also Supplementary Figure S3 and Supplementary Table S3.

mTORi-nanobiologic therapy prevents systemic inflammation in mice

Critical aspects of the exaggerated systemic inflammation caused by bacterial sepsis can be mimicked in mice by administering the Gram-negative bacterial component LPS[41,42]. To investigate the effects of our mTORi-nanobiologics in regulating myelopoiesis during hyperinflammation processes, we intraperitoneally (i.p.) injected 0.1 mg/kg of LPS in naive mice and, one hour later, intravenously (i.v.) administered one 5 mg/kg dose of

mTORi-nanobiologics (Fig. 4A). Naive mice were used as negative controls, while LPS-injected PBS-treated animals served as placebo controls. We then applied a combination of *in vivo* ^{18}F-FDG positron emission tomography (^{18}F-FDG PET) imaging[43–45] (Fig. 4B), *ex vivo* gamma counting, and flow cytometric analyses. Compared to naive mice, we observed a 4-fold increase *ex vivo* in ^{18}F-FDG bone marrow uptake following i.p. LPS injection, indicative of systemic hyperinflammation (Fig. 4C, $p<0.0001$). In the same analysis, LPS-injected mice that received the mTORi-nanobiologic treatment displayed significantly less bone marrow activity after 24 hours (Fig. 4C, $p=0.0007$). Interestingly, no statistical significance between negative control and mTORi-nanobiologic treated groups was attained ($p=0.3967$), suggestive of inflammation reduction to baseline levels. A similar trend was observed by *in vivo* SUV analysis, although statistical significance was not attained (Supplementary Fig. S4A), most likely attributed to the lower sensitivity of PET scanners due to partial volume effects, background noise and limitations in spatial resolution[46,47].

We set out to investigate these changes at the cellular level by flow cytometry analysis of bone marrow cells. We observed a reduction of Ly6C^{hi} monocytes after mTORi-nanobiologics administration, when compared to placebo-treated animals (Fig. 4D, $p=0.0011$). Similarly, neutrophil populations also underwent a 5-fold reduction after mTORi-nanobiologics treatment, when compared to the placebo group. However, those differences did not reach statistical significance (Fig. 4E, $p=0.4133$). Interestingly, a different trend was observed in the blood with decreased Ly6C^{hi} monocyte and neutrophil populations in animals of the placebo group (Supplementary Fig. S4B), despite the lack of statistical significance ($p=0.3624$ and $p=0.5288$). This phenomenon is most likely due to enhanced margination and cell migration to inflamed organs after LPS injection[48,49]. However, mTORi-nanobiologics treatment restored Ly6C^{hi} monocyte and neutrophil levels to baseline ($p=0.2060$ and $p=0.9707$, respectively).

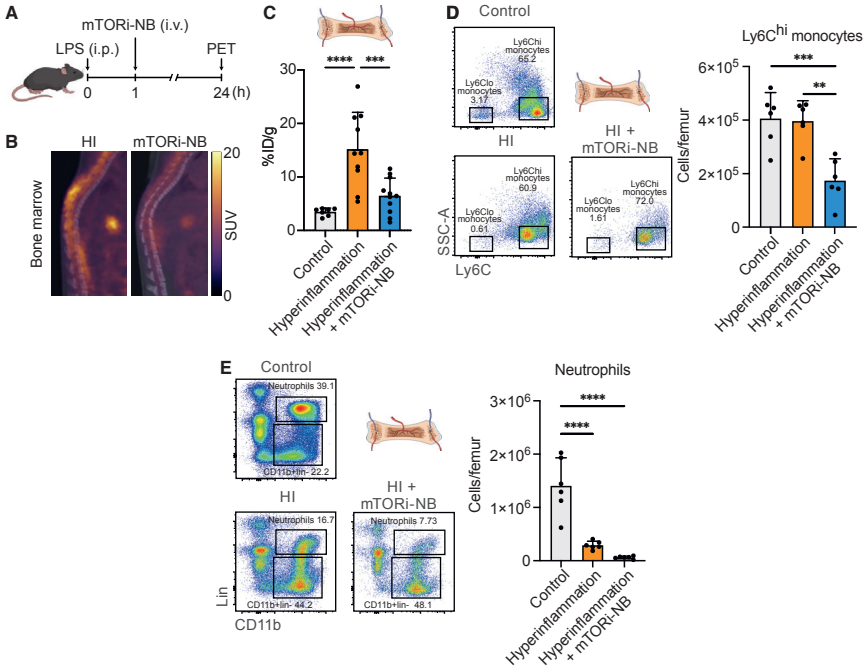


Figure 4. mTORi-nanobiologics reduce systemic inflammation. A) Schematic overview of the LPS-induced hyperinflammation mouse model. B) Representative fused ^{18}F-FDG PET/CT images of the spine of placebo (left panel) and mTORi-nanobiologics-treated (right panel) animals. C) *Ex vivo* quantification of bone marrow ^{18}F-FDG uptake (n=7-11). D) Representative flow cytometry plots showing Ly6C^{hi} monocytes in the bone marrow of control naive mice (negative control), mice with hyperinflammation (placebo control), and hyperinflammation mice treated with mTORi-nanobiologics, gated on live CD45$^+$CD11b$^+$lin$^-$CD11c$^-$ cells (left panel) and the associated quantification of bone marrow Ly-6C^{hi} monocytes (right panel, n=6). E) Representative flow cytometry plots showing neutrophils in the bone marrow of control naive mice (negative control), untreated hyperinflammation mice (placebo control), and hyperinflammation mice treated with mTORi-nanobiologics, gated on live CD45$^+$ cells (left panel). The associated quantification of bone marrow neutrophils is also shown (right panel, n=6). HI = hyperinflammation, hyperinflammation = placebo control, SUV = standardized uptake value. Data in panels **C**-**E** are plotted as mean ± SD. Statistical analyses were performed using the Shapiro-Wilk test, followed by one-way ANOVA (with Tukey's multiple comparisons test) or Kruskal-Wallis (followed by Dunn's multiple comparison test) according to Gaussian distribution. **p<0.01, ***p<0.001, ****p<0.0001. See also Supplementary Figure S4.

mTORi-nanobiologics modulate ARDS-driven inflammation in mice

Encouraged by the anti-inflammatory effects of mTORi-nanobiologic therapy in systemic inflammation, we set out to test its efficacy in a mouse model of ARDS. This model involves intratracheally administering LPS (i.t., 0.1 mg/kg, Fig. 5A). mTORi-nanobiologics treatment (or PBS for the placebo group) was intravenously injected 1 hour and 48 hours after LPS exposure, while the negative control group did not receive LPS. Animals were then ^{18}F-FDG-PET imaged (Fig. 5B) and euthanized for *ex vivo* radiometric assays. *Ex vivo* readouts of bone marrow ^{18}F-FDG uptake showed 2-fold increase in LPS-injected animals (Fig. 5C, p=0.0271), while LPS-injected mTORi-nanobiologics-treated mice had significantly reduced ^{18}F-FDG uptake, when compared to placebo group (Fig. 5C, p=0.0207). However, similar to the hyperinflammation model, these differences did not reach statistical significance during *in vivo* SUV analysis (Supplementary Fig. S5A).

Ex vivo ^{18}F-FDG uptake in the lungs at the same timepoint showed a 3-fold increase after ARDS induction (Fig. 5D, p<0.0001), when compared to naive control. Similar to the treatment response in the systemic hyperinflammation mouse model, we found that two i.v. doses of mTORi-nanobiologics (5 mg/kg) significantly reduced ^{18}F-FDG uptake in the lungs (Fig. 5D, p=0.0001) to baseline (negative control) levels (p=0.1940). These data were corroborated by *in vivo* SUV analysis (Supplementary Fig. S5B, p=0.0024, 0.0379 and >0.9999, respectively).

On a cellular level, mTORi-nanobiologics-treated animals also showed a significant reduction in both bone marrow Ly6C^{hi} monocytes and neutrophils, when compared to the placebo group (Figs. 5E and F, p=0.0006 and 0.0011, respectively). Similar trends were observed in the lungs (Figs. 5G and H, p=0.1168 and 0.1168, respectively) and in the neutrophils in the blood (Supplementary Fig. S5C, p=0.0401).

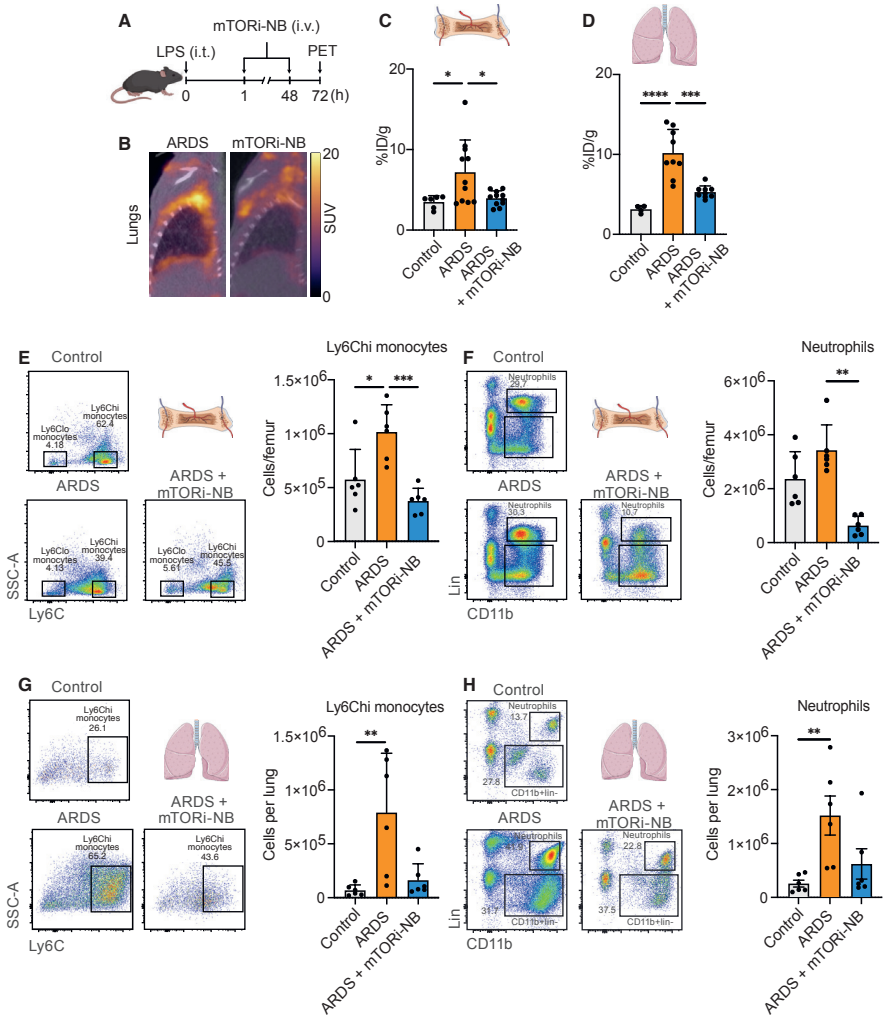


Figure 5. mTORi-nanobiologics reduce inflammation in ARDS mouse model. A) Schematic overview of the LPS-induced ARDS mouse model. B) Representative fused ^{18}F-FDG PET/CT images of the lungs of untreated (placebo control, left panel) and mTORi-nanobiologics-treated (right panel) animals. C) *Ex vivo* quantification of bone marrow ^{18}F-FDG uptake (n=6-11). D) *Ex vivo* quantification of ^{18}F-FDG lung uptake (n=4-9). E) Representative flow cytometry plots showing Ly6C^{hi} monocytes in the bone marrow of control naive mice (negative control), untreated ARDS mice (placebo control), and ARDS mice treated with mTORi-nanobiologics, gated on live CD45^{+}CD11b^{+}lin^{-}CD11c^{-} cells (left panel) and the associated quantification of bone marrow Ly-6C^{hi} monocytes (right panel, n=6). F) Representative flow cytometry plots showing neutrophils in the bone marrow of control naive mice (negative control), untreated ARDS mice (placebo control), and ARDS mice treated with mTORi-nanobiologics, gated on live CD45^{+} cells

(left panel). The associated quantification of bone marrow neutrophils is also shown (right panel, n=6). (**G**) Representative flow cytometry plots showing Ly6C^{hi} monocytes in the lungs of naive mice (negative control), untreated ARDS mice (placebo control), and ARDS mice treated with mTORi-nanobiologics, gated on live CD45^{+}CD11b^{+}lin^{-}CD11c^{-} cells (left panel) and the associated quantification of lung Ly-6C^{hi} monocytes are also shown (right panel, n=6). (**H**) Representative flow cytometry plots showing neutrophils in the lungs of control naive mice (negative control), untreated ARDS mice (placebo control), and ARDS mice treated with mTORi-nanobiologics, gated on live CD45^{+} cells (left panel). The associated quantification of lung neutrophils is also shown (right panel, n=6). ARDS = placebo control, SUV = standardized uptake value. Data in panels **C**-**H** are plotted as mean ± SD. Statistical analyses were performed using the Shapiro-Wilk test, followed by one-way ANOVA (with Tukey's multiple comparisons test) or Kruskal-Wallis (followed by Dunn's multiple comparison test) according to Gaussian distribution. *p<0.05, **p<0.01, ***p<0.001, ****p<0.0001. See also Supplementary Figure 5.

Discussion

Over the course of the past century, infection-related death rates have declined dramatically due to advancements in hygiene, the improved quality of life and modern medicine[50]. Nevertheless, sepsis induced by infection remains one of the most notorious killers worldwide[2,51,52]. While sepsis is an immune-mediated condition, immunotherapy trials demonstrating clinical benefits are scarce, which has stagnated their development[53,54]. However, the COVID-19 pandemic forced the medical community and pharma to refocus their attention on treating sepsis and hyperinflammation. Numerous trials were performed with existing drugs[55], such as anakinra[56,57] and T cell targeting therapies[58]. Although success rates varied considerably, it has become evident that with proper patient stratification immunotherapy has significant potential for treating infection-related complications, including sepsis.

In the current study, we found differential expression of genes related to the mTOR pathway in myeloid cells from COVID-19 patients. The link between mTOR and COVID-19-driven hyperinflammation has been investigated in previous studies[59,60]. Basile *et al* outlined that SARS-CoV-2 infection disrupts mTOR signaling and suggested that its inhibition could be a powerful tool for immune response regulation in COVID-19, a conclusion supported by

Abu-Eid *et al*[61,62]. Moreover, the correlation between COVID-19 immune dysregulation and mTOR effectors is further aggravated in subjects with underlying comorbidities such as diabetes[63] and obesity[64].

Indeed, our scRNA-Seq results indicate that SARS-CoV-2 infection upregulates mTOR-related genes involved in actin polymerization and cytoskeletal rearrangements, mechanisms that enhance immune cell trafficking and motility[34–36]. These processes are key drivers of tissue infiltration and damage, often culminating in hyperinflammation[65–67]. Furthermore, these genes also modulate PI-3 kinase signaling and, consequently, the production of pro-inflammatory cytokines and chemokines[68,69]. In contrast, other mTOR downstream targets, such as Rps6, a component of the small (40S) ribosomal unit, were downregulated. This is also aligned with typical physiological responses to infection and could be part of a well-established feedback loop mechanism to counteract inflammation[70,71]. In fact, evidence suggests that the activation of mTOR signaling concomitantly triggers compensatory processes to help restore metabolic and inflammatory homeostasis by downregulating downstream genes via insulin/IGF receptor and other tyrosine kinase receptors[72,73]. However, these modulatory effects are often insufficient to counteract an exacerbated immune response, especially in hyperinflammation and can paradoxically further compromise patient health under certain conditions[74–76]. Interestingly, certain changes in mTOR-related gene expression persisted in monocytes, even after disease recovery. Thus, we foresee that mTOR pathway regulation may be applied not only to mitigate direct consequences of SARS-CoV-2 infection, but also to reduce its chronic adverse effects[77] and the aggravation of comorbidities, such as cardiovascular disease[78,79]. Together, these findings highlight the complexity and dynamic nature of mTOR signaling, which combines pro-inflammatory and homeostasis restoration properties, and underscore its potential as a therapeutic target for addressing short and long-lasting effects of infection.

Drugs that inhibit mTOR, such as rapamycin, are Food and Drug Administration (FDA) approved for organ transplant rejection prevention,

treatment of certain tumors[80], pulmonary lymphangioleiomyomatosis[81], and are applied in drug-eluding stents to prevent restenosis of coronary arteries[82]. In addition, rapamycin has been studied for the treatment of lung injuries due to infection, including in SARS-CoV-2[83,84]. However, the use of this medication for inhibition of hyperinflammation and its clinical manifestations (such as ARDS) has limitations, due to its immunosuppressive effects. It is well-documented that rapamycin negatively impacts T cell function[28] and consequently hampers immune responses to infectious agents. mTOR inhibition also leads to suppression of B cell development and proliferation, hampering the production of antigen-specific memory B cells[85]. Moreover, despite its immunosuppressive function, impaired immune responses due to mTOR inhibition may also lead to unexpected pro-inflammatory effects. This paradoxical outcome is caused by decreased anti-inflammatory IL-10 production with parallel increase in expression and release of pro-inflammatory cytokine IL-12[86,87]. A recent study also points out to the deleterious effects that rapamycin may have in non-immune tissues, such as the skeletal muscle, especially in older patients[88]. Therefore, alternative strategies for more precise and cell-specific mTOR inhibition, which do not mute essential immune responses, must be engineered.

We previously introduced a nanobiologic platform for myeloid cell-specific immunoregulation. Nanobiologics are nanomedicines based on natural lipoprotein nanoparticles that integrate small molecule drugs[89]. Owing to their lipoprotein features, nanobiologics are highly biocompatible, safe in large animals[90,91], and specifically target myeloid cells and their bone marrow progenitors. In a series of separate studies, we applied nanobiologics that are functionalized with rapamycin-based drugs for myeloid cell-specific mTOR regulation. We showed compelling therapeutic benefits of mTORi-nanobiologic treatment in mouse models of atherosclerosis[92] and organ transplantation[93], without causing widespread immunosuppression. In the latter, mTORi-nanobiologics' cellular specificity towards myeloid cells was characterized by flow cytometry. Important to clinical translation, mTORi-nanobiologics' intravenous application is safe in non-human primates[29]. Thus,

we sought out to investigate the use of this mTORi-nanobiologics formulation in the context of infection-driven dysregulated immune response.

Our in *vitro* experiments on primary cells and mouse models uncovered mTORi-nanobiologic therapy's compelling potential. In primary human immune cells, treatment prevented inflammation and trained immunity induction. Furthermore, our *in vivo* data provided new insights into the poorly understood temporal-spatial dynamics of mTOR inhibition across distinct models of inflammation. Hyperinflammation induced by intraperitoneal injection with LPS is a well-established model for acute systemic inflammation[94,95]. In the 24-hours post administration, LPS induced production of Ly6C^{hi} monocytes and neutrophils by the bone marrow, which migrated to inflamed organs, as evidenced by rapid depletion of circulating cells. This is in line with the bone marrow's high metabolic activity measured by ^{18}F-FDG. Conversely, intravenous mTORi-nanobiologic treatment evoked rapamycin-type effects on the bone marrow, hampering the development of Ly6C^{hi} monocytes and neutrophils[96,97], and impairing immune cells' migratory capacity[98]. Therefore, we observed elevated myeloid cell blood levels, despite their numbers being reduced in the bone marrow. Similarly, in the ARDS experiment LPS led to increased production of immune cells. However, the inflammation kinetics in ARDS are vastly different. Indeed, 72-hours post LPS injection we observed persistent recruitment of immune cells to the lungs, which likely reflects replenishment of bone marrow cells after emergency myelopoiesis, as well as sustained influx to the bloodstream and affected organ. This difference was also observed in the treatment groups, where cell numbers for mTORi-nanobiologics-treated animals are stabilized to naïve levels.

While our study provides clear proof-of-concept for myeloid cell-specific mTOR inhibition in infection-associated inflammation, it is limited to studying myeloid cells from COVID-19 patients only. However, mTOR dysregulation in myeloid cells is found in diverse infections, ranging from HIV[99–101] to Dengue[102,103]. Besides viral infections, mTOR pathway involvement is also

implicated in conditions such as bacterial pneumonia[104] and tuberculosis[105], providing much broader opportunities for our therapeutic approach.

The experimental models used in this study accurately reflect critical features of sepsis but have their limitations. We evaluated mTORi-nanobiologics in an *in vitro* model that involves primary cells from healthy subjects, which are exposed to inactivated SARS-CoV-2. We did not treat myeloid cells from COVID-19 patients with mTORi-nanobiologics. For the therapeutic studies in mouse models, we induced inflammation by administering LPS, rather than through actual infection. LPS is found in the outer membrane of gram-negative bacteria[106]. It is a potent immune cell activator and is often used in well-established models of post-infection immune dysregulation[107–109]. When administered intraperitoneally, LPS can trigger systemic hyperinflammation, whereas intratracheal instillation leads to ARDS-like symptoms. Both phenomena (hyperinflammation and ARDS) are common COVID-19 complications[110,111], hence overarching our *in vitro* data. We chose this approach because despite WT mice not being susceptible to SARS-CoV-2 infections due to differences in their ACE2 receptor structure[112], LPS still has high relevance in the context of infection-driven inflammation. With this strategy, our human data is integrated with our mouse data in a complementary fashion. However, future studies with diverse infection mouse models are required to optimize the treatment regimen and evaluate mTORi-nanobiologic therapy's full potential in sepsis-associated inflammation.

In summary, our data demonstrate that mTOR dysregulation in the myeloid compartment is a compelling therapeutic target. While monocytes and neutrophils are essential for host defense, exacerbated release, activation, and accumulation of myeloid cells at the site of infection – and systemically – can be harmful and lead to sepsis and death. Our mTORi-nanobiologic treatment downregulates bone marrow activity in LPS-induced systemic inflammation and ARDS, thereby limiting the deleterious accumulation of these myeloid cells in vital organs, without widespread immunosuppression.

Limitations of the study

Our study investigates the potential of mTORi-nanobiologic treatment for regulating post-infection hyperinflammation. However, we evaluated the efficacy of this therapy *in vivo* only in animal models. In humans, we relied on data from scRNA-Seq and *in vitro* approaches. Further studies are needed to understand the systemic effects of mTORi-nanobiologics in patients. Moreover, our analyses focused on COVID-19 patients, ARDS and hyperinflammation models. We believe nanobiologics could be applied to other diseases with similar mechanisms of inflammation dysregulation. Future research should explore the efficacy of our therapy in a broader range of diseases.

Methods

Experimental model and study participant details

Mouse models of hyperinflammation and ARDS

All animal procedures were reviewed and approved by the Institutional Animal Care and Use Committees at the Icahn School of Medicine at Mount Sinai (LA12-00111), in accordance with federal regulations and the guidelines contained in the National Research Council Guide for the Care and Use of Laboratory Animals. Female C57BL/6 mice were purchased from the Jackson Laboratory at 7 to 10 weeks of age and randomly assigned to the different experimental groups. Animals were housed in a specific pathogen-free facility, maintained at constant room temperature of 25 ± 2°C. In the hyperinflammation model, mice received an intraperitoneal injection with LPS (0.1 mg/kg; E. coli O55:B5) 1 hour prior to intravenous injection with placebo (PBS, n=10) or mTORi-nanobiologics (5 mg/kg, n=11). Control animals (n=7) did not receive LPS injection. Similarly, for the ARDS model, animals were subjected to one intratracheal injection of LPS at 0.1 mg/kg, followed by two doses of PBS (n=10) or mTORi-nanobiologics (5 mg/kg, n=11) at 1 and 48 hours post LPS injection. Control group (n=6) did not receive LPS injection. Animals underwent ^{18}F-FDG PET and *ex vivo* radiometric assays. In addition, 6 animals in each model group underwent flow cytometric analyses. A total of 2 lung samples per group were excluded from the ARDS *ex vivo*

radiometric analyses due to PBS infiltration during perfusion, which interferes with the weight of the tissue, compromising the %ID/g calculation. In addition, 1 mouse was excluded from the *in vivo* ARDS analysis due to image reconstruction issues. In the placebo group of the cytokine storm analysis, 1 animal had to be euthanized before data collection due to LPS-induced complications.

Human monocyte isolation

Blood was collected from 12 healthy adult donors (n = 6 per batch) after written informed consent, according to the approval of the Ethical Committee Arnhem-Nijmegen (NL-nummer: NL32357.091.10) in compliance with the Medical Research Involving Human Subjects Act (WMO) and in accordance with the Declaration of Helsinki. Batch one included the analysis of IL-6 and TNF-**α** production. Later, a second batch of donors was recruited to perform additional analyses (CXCL-9, CXCL-10 and IL-8). However, in both batches, samples from each subject were subjected to all experimental conditions. Specifically, the same blood sample was exposed to different mTORi-nanobiologics concentrations, stimuli and control conditions. This within-subject set up minimizes individual variability. Information on age and sex of such donors are available on **Supplementary Table 3**. PBMCs isolation was performed by differential density centrifugation[113]. First, buffy coat was diluted in 200 mL of RPMI medium and overlayed in Ficoll (2:1). Samples were then centrifuged at 950 g for 15 minutes. PBMCs were collected from the interface between Ficoll and plasma-medium layers, washed with RPMI medium and centrifuged to 350g for 7 minutes. Supernatant was allowed to decant, and cells were resuspended in RPMI medium for one more round of washing and centrifugation. PBMCs suspension was brought to a 150-200 x 10^6 cells/3 mL concentration and were added to 10 mL of hyperosmotic Percoll solution (4.85 mL of Percoll, 4.15 mL of sterile water and 1 mL of 1.6 M NaCl). Samples were then centrifuged at 580 g for 15 minutes at room temperature. Interface layer was collected, and cold PBS was added to a final volume of 50 mL. Samples were centrifuged at 350 g for 7 minutes at 4°C. Supernatant was removed, percoll-isolated monocytes (1 x 10^5 cells) were re-

suspended in RPMI culture medium and *in vitro* trained immunity experiments were performed.

Method details

scRNA-Seq of COVID patients

To understand the role of mTOR in COVID-19 patients, genes involved in mTOR signaling pathways were downloaded from KEGG (entry hsa04150) and analyzed in three independent scRNA-seq datasets including COVID-19 patients and healthy controls[31–33], with a total n = 157. Mild and severe patients were classified in accordance with the WHO clinical ordinal scale. The Seurat objects were imported and analyzed by Seurat package (version 4. 2.0) in R (version 4.2.0). In this study, we focus exclusively on genes related to the mTOR signaling pathway for the subsequent analysis.

Trained immunity assay

Monocytes were incubated with RPMI culture medium (RPMI medium Dutch modified), supplemented with 50 µg/mL gentamicin, 2 mM Glutamax, and 1 mM 2-oxopropanoate and stimulated with 1 µg/mL **β**-glucan (**β**-1,3-(D)-glucan, kindly provided by Professor David Williams) or heat-inactivated SARS-CoV-2 Wuhan-Hu-1 variant[38] (8.9 x 10^4 TCID50/mLl; NRW-42 isolate, kindly provided by Heiner Schaal, University Hospital Duesseldorf, Germany) or remained unstimulated for 24 h in the presence or absence of 1 or 10 µM mTORi-nanobiologics. Cells were washed with warm PBS and incubated for 5 days in culture medium supplemented with 10% human pool serum and medium was refreshed once. Cells were restimulated with 10 ng/mL *E. coli* LPS. After 24 h, supernatants were collected and stored at -20°C until analysis. Cytokine production from human cells was determined in supernatants using commercial ELISA kits for IL-6, TNF-**α**, CXCL-9, CXCL-10 and IL-8, following manufacturer's instructions.

Preparation and characterization of mTOR inhibitor-loaded nanobiologics

Trained Therapeutix Discovery (Oss, the Netherlands) provided one of their proprietary rapamycin lipophilic mTOR inhibitor prodrugs. Stock solutions (10 mg/mL) in trichloromethane of POPC (250 µL), PHPC (65 µL), cholesterol (35 µL), propane-1,2,3-triyl trioctanoate (1000 µL) and rapamycin prodrug (200 µL) were combined in a 20 mL vial and dried under vacuum to yield a lipid film. The film was then dissolved in 3 mL ethanenitrile /methanol mixture (95:5 vol. %) and sonicated using an ultrasonic bath for 5 minutes. Separately, 24 mL PBS solution at 1 mg/mL ApoA-1 protein was prepared. Microfluidic setup with herringbone mixer was employed, loading both solutions simultaneously with a flow rate of 0.75 mL/min and 6 mL/min, for lipid solution and Apo-A1 solution, respectively. The nanoparticle suspension was concentrated to approximately 5 mL by centrifugal filtration (100k MWCO Vivaspin tube at 4000 rpm), followed by the addition of 10 mL of PBS. This step was repeated twice ensuring the removal of free components from the solution. The washed solution, concentrated to approximately 3 mL, was filtered using 0.22 µm PES syringe filter, resulting in the final mTORi-nanobiologics.

Nanoparticle quality control and characterization

Dynamic light scattering measurements of the nanotherapeutics were performed on a Malvern Zetasizer Ultra, indicating a mean size of 50 nm (based on number distribution) and a dispersity of 0.1 – 0.2, in line with our previous results[29]. The rapamycin prodrug concentration was determined in triplicate by HPLC using a photodiode array detector (**λ** = 278 nm), diluting the nanobiologics in acetonitrile (1:50). Typical drug concentration were 1.5 mg/mL and drug incorporation efficiencies > 70%. For the cryogenic electron microscopy assay, the surface of 200-mesh lacey carbon supported copper grids was plasma charged for 40 seconds using a carbon coater (Cressington 208). Subsequently, 3 µl of nanobiologics sample (~ 1 mg protein/mLl) was pipetted on a grid and vitrified into a thin film by plunge vitrification in liquid ethane. This step was performed by using an automated robot (FEI Vitrobot

Mark IV). Cryo-EM imaging was acquired on the cryo-transmission electron microscope TITAN (Thermo Fisher), equipped with a field emission gun (FEG), a post-column Gatan imaging filter (model 2002) and a post-GIF 2k × 2k Gatan CCD camera (model 794). The imaging was performed at 300 kV acceleration voltage in bright-field TEM mode with zero-loss energy filtering at 24,000× magnification (dose rate of 11.8 e-/Å2⍰s), and 1s acquisition time.

In vivo PET/CT imaging and *ex vivo* measurements of radioactivity in mice

Static PET imaging was performed on mice at 24 (cytokine storm model) or 72 hours (ARDS model) after LPS administration. Animals were first fasted for 16 hours and then injected with ^{18}F-FDG (~12.84 ± 2.52 MBq) via their lateral tail vein and kept under 1% isoflurane anesthesia for 60 minutes to allow for tracer circulation. Anesthesia was maintained while animals were placed in the PET scanner (Mediso nanoScan PET/CT). First, a whole-body CT scan was performed (energy, 50 kVp; current, 180 μAs; isotropic voxel size, 0.25 mm) followed by a PET acquisition time of 20 minutes. Reconstruction was performed with attenuation correction using the TeraTomo 3D reconstruction algorithm from the Mediso Nucline software. The coincidences were filtered with an energy window between 400 and 600 keV. The voxel size was isotropic with 0.4-mm width, and the reconstruction was applied for four full iterations, six subsets per iteration. Immediately after the PET/CT scan, animals were euthanized for *ex vivo* radioactivity concentration measurements using a Wizard^2 2480 automatic gamma counter by PerkinElmer, which reported as a decay corrected percentage of injected dose per gram (%ID/g).

Image analysis

Upon reconstruction, image analysis was performed using Osirix MD, version 11.0. Whole-body CT images were fused with PET images and analyzed in a coronal plane. Regions of interest (ROIs) were drawn on organs of interest,

using the femur for assessment of bone marrow uptake. Mean standardized uptake values (SUVs) were calculated for each ROI.

Flow cytometry of mouse samples

For the flow cytometry analysis, animals were euthanized and perfused with cold PBS. Tissues of interest were harvested and processed. Bone marrow was extracted from the femur and strained though a 70 µm filter. Samples were subsequently incubated with RBC lysis buffer for 30 seconds and washed with PBS. Blood samples were lysed using RBC lysis buffer for 4 minutes, followed by two additional rounds of lysis and washing with PBS. Lung samples were treated with enzymatic solution containing 1 mg/mL of DNAse I and 5 mg/mL of Collagenase A in PBS supplemented with 0.5% FBS for 50 minutes at 37 °C before being passed through a 70 µm filter and washed with PBS. Samples were stained with antibodies against CD45, Ly6C, CD11b, CD11c and F4/80 and a lineage cocktail containing antibodies against CD90.2, TER-119, NK1.1, CD49b, CD45R and Ly6G, for 30 minutes on ice. DAPI was used as a viability stain. Counting beads were used for absolute quantification of leukocyte subsets. Data were acquired on LSR Fortessa (BD Biosciences) and analyzed using FlowJo v10.0.7 (Tree Star).

Quantification and statistical analysis

Statistics

All results are presented as mean with standard deviation (SD), unless otherwise stated. Details on n-numbers are disclosed in the figure legend. Statistical tests were performed using GraphPad Prism 10.2. *In vitro* data was analyzed using Wilcoxon signed-rank test. $\alpha < 0.05$ represents statistical significance. For multiple comparisons in the mouse study, data was tested for normality using Shapiro-Wilk test. Subsequent Ordinary one-way ANOVA test was employed for normally distributed data, followed by Tukey's multiple comparison test, while non-parametric Kruskal-Wallis test was applied to non-Gaussian distributed data, followed by Dunn's multiple comparison test. *$p < 0.05$, **$p < 0.01$, ***$p < 0.001$, ****$p < 0.0001$. For the analysis of the scRNA-Seq data, in each cell type from each dataset, the differentially

expressed genes between every two disease conditions were identified using FindMarkers() function by Wilcoxon rank sum test. In the Bonn and Berlin cohorts, Bonferroni correction was used to control false discovery rate for multiple test results. Specifically, in the MHH50 cohort, we used the raw $p < 0.05$ to define significant differentially expressed genes in the convalescent COVID-19 dataset regarding the subtle differences between convalescent patients and healthy control.

Additional Resources

Patient cells analyses used here were obtained from data collected in previous studies[31–33].

In addition to the deposition of the raw sequencing data on EGA, we provide an interactive platform for data inspection and analysis via FASTGenomics. The FASTGenomics platform (fastgenomics.org) provides processed count tables of the datasets generated in this study as well as key analytical results, such as UMAP coordinates and cluster identities, and the code written to analyze the respective data.

Resource availability

Lead contact

Further information and requests for resources and reagents should be directed to and will be fulfilled by the lead contact, Prof. Dr. Willem Mulder (Willem.Mulder@radboudumc.nl).

Materials availability

Unique/stable reagents will be made available on request, but we may require a payment and/or a completed Materials Transfer Agreement if there is potential for commercial application.

Data and code availability

- scRNA-seq data presented in this study have been deposited at the European Genome-phenome Archive (EGA). Accession numbers are listed in the key resources table.
- This paper does not report original code.

- Any additional information required to reanalyze the data reported in this work paper is available from the lead contact upon request.

Sources of funding

We thank Heiner Schaal for providing us with the heat-inactivated SARS-CoV-2 Wuhan-Hu-1 variant and Professor David Williams for providing us with (**β**-1,3-(D)-glucan. This work was funded by NIHNHLBI (R01 HL144072 and P01 HL131478), NIHNIAID (P01 AI168258), NWO Vici (91818622), ERC Advanced Grant TOLERANCE, Leducq Foundation CHECKPOINT ATHERO and Trained Therapeutix Discovery. E.J.G.B. was supported by the Horizon 2020 European Grants ImmunoSep and RISCinCOVID and the Horizon Health grant EPIC-CROWN-2 (granted to the Hellenic Institute for the Study of Sepsis). SARS-CoV-2 research in the M.S. lab is further supported by NIH NIAID R01 AI160706 and R01 DK130425.

Competing interests

W.J.M.M., L.A.B.J, M.N. and Z.A.F. are founders of Trained Therapeutix Discovery (TTxD). W.J.M.M is also a shareholder and CSO at the company. W.J.M.M. is founder, CTO and shareholder of BioTrip. Z.A.F. and W.J.M.M. are members of the board of TTxD. J.H.C.M.K., B.G., G.A.O.C. and T.J.B. are employees at TTxD. H.M.J. is a director at SyMO-Chem. S.H.M.S. and F.J.M.H. are employees at SyMO-Chem. M.S. has received unrelated research support from ArgenX N.V., Moderna, 7Hills and Phio Pharmaceuticals. E.J.G.B. has received honoraria from Abbott Products Operations, bioMérieux, GSK, UCB, Sobi AB and ThermoFisher Brahms GmbH, independent educational grants from Abbott Products Operations, AbbVie, bioMérieux Inc, Johnson & Johnson, InCyte, MSD, Novartis, UCB, Sanofi and Sobi. M.M.M. is the scientific founder of Lemba Therapeutics. No other potential conflicts of interest relevant to this article exist.

Author contributions

Specific author contributions are as follows: W.J.M.M. conceived and supervised the study. W.J.M.M. and Y.C.T. designed and managed experiments. T.J.B., A.Z., Y.L., B.G., J.H.C.M.K, E.L., N.P.R., H.M.J., S.H.M.S., F.J.M.H., E.J.G.B., M.M.M., M.S., R.M., R.D., L.A.B.J., R.E.T., Z.A.F., M.M.T.v.L., A.J.P.T., and M.N. were involved in the design of specific experiments. Y.C.T., J.M., J.M.F., W.W., G.P., Y.E., B.P., J.D., T.A., T.J.B., E.E.S.B., M.D.A., A.Z., S.A.S., Z.Z., W.L., Y.L., A.M., J.C.F., G.A.O.C., E.K., G.S., L.C. and B.J.P.T. performed experiments and data acquisition. Y.C.T., J.M., J.M.F., T.J.B., E.E.S.B., A.Z., Z.Z., W.L., Y.L., E.K., M.O., G.S., Z.A.F., M.M.T.v.L., A.J.P.T., and W.J.M.M. performed analyses and interpretation of the data. Y.C.T. and W.J.M.M. wrote the manuscript. All authors provided input and approved the manuscript's final content.

References

1. Fajgenbaum, D.C., and June, C.H. (2020). Cytokine Storm. New England Journal of Medicine *383*, 2255–2273. https://doi.org/10.1056/NEJMra2026131.
2. Ikuta, K.S., Swetschinski, L.R., Robles Aguilar, G., Sharara, F., Mestrovic, T., Gray, A.P., Davis Weaver, N., Wool, E.E., Han, C., Gershberg Hayoon, A., et al. (2022). Global mortality associated with 33 bacterial pathogens in 2019: a systematic analysis for the Global Burden of Disease Study 2019. The Lancet *400*, 2221–2248. https://doi.org/10.1016/S0140-6736(22)02185-7.
3. Behrens, E.M., and Koretzky, G.A. (2017). Review: Cytokine Storm Syndrome: Looking Toward the Precision Medicine Era. Arthritis & Rheumatology *69*, 1135–1143. https://doi.org/10.1002/art.40071.
4. Bos, L.D.J., and Ware, L.B. (2022). Acute respiratory distress syndrome: causes, pathophysiology, and phenotypes. The Lancet *400*, 1145–1156. https://doi.org/10.1016/S0140-6736(22)01485-4.
5. Han, S., and Mallampalli, R.K. (2015). The acute respiratory distress syndrome: from mechanism to translation. J Immunol *194*, 855–860. https://doi.org/10.4049/jimmunol.1402513.
6. Zheng, J., Miao, J., Guo, R., Guo, J., Fan, Z., Kong, X., Gao, R., and Yang, L. (2022). Mechanism of COVID-19 Causing ARDS: Exploring the Possibility of Preventing and Treating SARS-CoV-2. Front Cell Infect Microbiol *12*, 931061. https://doi.org/10.3389/fcimb.2022.931061.
7. Montazersaheb, S., Hosseiniyan Khatibi, S.M., Hejazi, M.S., Tarhriz, V., Farjami, A., Ghasemian Sorbeni, F., Farahzadi, R., and Ghasemnejad, T. (2022). COVID-19 infection: an overview on cytokine storm and related interventions. Virol J *19*, 92. https://doi.org/10.1186/s12985-022-01814-1.
8. Bellani, G., Laffey, J.G., Pham, T., Fan, E., Brochard, L., Esteban, A., Gattinoni, L., van Haren, F., Larsson, A., McAuley, D.F., et al. (2016). Epidemiology, Patterns of Care, and Mortality for Patients With Acute Respiratory Distress Syndrome in Intensive Care Units in 50 Countries. JAMA *315*, 788. https://doi.org/10.1001/jama.2016.0291.
9. Tzotzos, S.J., Fischer, B., Fischer, H., and Zeitlinger, M. (2020). Incidence of ARDS and outcomes in hospitalized patients with COVID-19: a global literature survey. Crit Care *24*, 516. https://doi.org/10.1186/s13054-020-03240-7.
10. Villar, J., Blanco, J., Añón, J.M., Santos-Bouza, A., Blanch, L., Ambrós, A., Gandía, F., Carriedo, D., Mosteiro, F., Basaldúa, S., et al. (2011). The ALIEN study: incidence and outcome of acute respiratory distress syndrome in the era of lung protective ventilation. Intensive Care Med *37*, 1932–1941. https://doi.org/10.1007/s00134-011-2380-4.
11. Hojyo, S., Uchida, M., Tanaka, K., Hasebe, R., Tanaka, Y., Murakami, M., and Hirano, T. (2020). How COVID-19 induces cytokine storm with high mortality. Inflamm Regen *40*, 37. https://doi.org/10.1186/s41232-020-00146-3.
12. Basheer, M., Saad, E., and Assy, N. (2022). The Cytokine Storm in COVID-19: The Strongest Link to Morbidity and Mortality in the Current Epidemic. COVID *2*, 540–

552. https://doi.org/10.3390/covid2050040.

13. Ruan, Q., Yang, K., Wang, W., Jiang, L., and Song, J. (2020). Clinical predictors of mortality due to COVID-19 based on an analysis of data of 150 patients from Wuhan, China. Intensive Care Med *46*, 846–848. https://doi.org/10.1007/s00134-020-05991-x.
14. Xu, Z., Shi, L., Wang, Y., Zhang, J., Huang, L., Zhang, C., Liu, S., Zhao, P., Liu, H., Zhu, L., et al. (2020). Pathological findings of COVID-19 associated with acute respiratory distress syndrome. Lancet Respir Med *8*, 420–422. https://doi.org/10.1016/S2213-2600(20)30076-X.
15. Horie, S., McNicholas, B., Rezoagli, E., Pham, T., Curley, G., McAuley, D., O'Kane, C., Nichol, A., dos Santos, C., Rocco, P.R.M., et al. (2020). Emerging pharmacological therapies for ARDS: COVID-19 and beyond. Intensive Care Med *46*, 2265–2283. https://doi.org/10.1007/s00134-020-06141-z.
16. Palakshappa, J.A., Krall, J.T.W., Belfield, L.T., and Files, D.C. (2021). Long-Term Outcomes in Acute Respiratory Distress Syndrome: Epidemiology, Mechanisms, and Patient Evaluation. Crit Care Clin *37*, 895–911. https://doi.org/10.1016/j.ccc.2021.05.010.
17. Mart, M.F., and Ware, L.B. (2020). The long-lasting effects of the acute respiratory distress syndrome. Expert Rev Respir Med *14*, 577–586. https://doi.org/10.1080/17476348.2020.1743182.
18. Fazzini, B., Battaglini, D., Carenzo, L., Pelosi, P., Cecconi, M., and Puthucheary, Z. (2022). Physical and psychological impairment in survivors of acute respiratory distress syndrome: a systematic review and meta-analysis. Br J Anaesth *129*, 801–814. https://doi.org/10.1016/j.bja.2022.08.013.
19. Giamarellos-Bourboulis, E.J., Aschenbrenner, A.C., Bauer, M., Bock, C., Calandra, T., Gat-Viks, I., Kyriazopoulou, E., Lupse, M., Monneret, G., Pickkers, P., et al. (2024). The pathophysiology of sepsis and precision-medicine-based immunotherapy. Nat Immunol *25*, 19–28. https://doi.org/10.1038/s41590-023-01660-5.
20. Jones, R.G., and Pearce, E.J. (2017). MenTORing Immunity: mTOR Signaling in the Development and Function of Tissue-Resident Immune Cells. Immunity *46*, 730–742. https://doi.org/10.1016/j.immuni.2017.04.028.
21. Li, W., Li, D., Chen, Y., Abudou, H., Wang, H., Cai, J., Wang, Y., Liu, Z., Liu, Y., and Fan, H. (2022). Classic Signaling Pathways in Alveolar Injury and Repair Involved in Sepsis-Induced ALI/ARDS: New Research Progress and Prospect. Dis Markers *2022*, 1–9. https://doi.org/10.1155/2022/6362344.
22. Ning, L., Shishi, Z., Bo, W., and Huiqing, L. (2023). Targeting immunometabolism against acute lung injury. Clinical Immunology *249*, 109289. https://doi.org/10.1016/j.clim.2023.109289.
23. Szwed, A., Kim, E., and Jacinto, E. (2021). Regulation and metabolic functions of mTORC1 and mTORC2. Physiol Rev *101*, 1371–1426. https://doi.org/10.1152/physrev.00026.2020.

24. Palsson-McDermott, E.M., Curtis, A.M., Goel, G., Lauterbach, M.A.R., Sheedy, F.J., Gleeson, L.E., van den Bosch, M.W.M., Quinn, S.R., Domingo-Fernandez, R., Johnston, D.G.W., et al. (2015). Pyruvate kinase M2 regulates Hif-1α activity and IL-1β induction and is a critical determinant of the warburg effect in LPS-activated macrophages. Cell Metab *21*, 65–80. https://doi.org/10.1016/j.cmet.2014.12.005.

25. Tannahill, G.M., Curtis, A.M., Adamik, J., Palsson-McDermott, E.M., McGettrick, A.F., Goel, G., Frezza, C., Bernard, N.J., Kelly, B., Foley, N.H., et al. (2013). Succinate is an inflammatory signal that induces IL-1β through HIF-1α. Nature *496*, 238–242. https://doi.org/10.1038/nature11986.

26. Zhong, W.-J., Liu, T., Yang, H.-H., Duan, J.-X., Yang, J.-T., Guan, X.-X., Xiong, J.-B., Zhang, Y.-F., Zhang, C.-Y., Zhou, Y., et al. (2023). TREM-1 governs NLRP3 inflammasome activation of macrophages by firing up glycolysis in acute lung injury. Int J Biol Sci *19*, 242–257. https://doi.org/10.7150/ijbs.77304.

27. Powell, J.D., Pollizzi, K.N., Heikamp, E.B., and Horton, M.R. (2012). Regulation of immune responses by mTOR. Annu Rev Immunol *30*, 39–68. https://doi.org/10.1146/annurev-immunol-020711-075024.

28. Chi, H. (2012). Regulation and function of mTOR signalling in T cell fate decisions. Nat Rev Immunol *12*, 325–338. https://doi.org/10.1038/nri3198.

29. van Leent, M.M.T., Meerwaldt, A.E., Berchouchi, A., Toner, Y.C., Burnett, M.E., Klein, E.D., Verschuur, A.V.D., Nauta, S.A., Munitz, J., Prévot, G., et al. (2021). A modular approach toward producing nanotherapeutics targeting the innate immune system. Sci Adv *7*, 1–12. https://doi.org/10.1126/sciadv.abe7853.

30. Netea, M.G., Domínguez-Andrés, J., Barreiro, L.B., Chavakis, T., Divangahi, M., Fuchs, E., Joosten, L.A.B., van der Meer, J.W.M., Mhlanga, M.M., Mulder, W.J.M., et al. (2020). Defining trained immunity and its role in health and disease. Nat Rev Immunol *20*, 375–388. https://doi.org/10.1038/s41577-020-0285-6.

31. Schulte-Schrepping, J., Reusch, N., Paclik, D., Baßler, K., Schlickeiser, S., Zhang, B., Krämer, B., Krammer, T., Brumhard, S., Bonaguro, L., et al. (2020). Severe COVID-19 Is Marked by a Dysregulated Myeloid Cell Compartment. Cell *182*, 1419-1440.e23. https://doi.org/10.1016/j.cell.2020.08.001.

32. Zhang, B., Zhang, Z., Koeken, V.A.C.M., Kumar, S., Aillaud, M., Tsay, H.-C., Liu, Z., Kraft, A.R.M., Soon, C.F., Odak, I., et al. (2022). Altered and allele-specific open chromatin landscape reveals epigenetic and genetic regulators of innate immunity in COVID-19. Cell genomics, 100232. https://doi.org/10.1016/j.xgen.2022.100232.

33. Liu, Z., Kilic, G., Li, W., Bulut, O., Gupta, M.K., Zhang, B., Qi, C., Peng, H., Tsay, H.C., Soon, C.F., et al. (2022). Multi-Omics Integration Reveals Only Minor Long-Term Molecular and Functional Sequelae in Immune Cells of Individuals Recovered From COVID-19. Front Immunol *13*, 1–15. https://doi.org/10.3389/fimmu.2022.838132.

34. Papakonstanti, E.A., Ridley, A.J., and Vanhaesebroeck, B. (2007). The p110delta isoform of PI 3-kinase negatively controls

RhoA and PTEN. EMBO J *26*, 3050–3061. https://doi.org/10.1038/sj.emboj.7601763 .

35. Di Cristofano, A. (2017). SGK1: The Dark Side of PI3K Signaling. Curr Top Dev Biol *123*, 49–71. https://doi.org/10.1016/bs.ctdb.2016.11.006.
36. Bardelli, A., Basile, M.L., Audero, E., Giordano, S., Wennström, S., Ménard, S., Comoglio, P.M., and Ponzetto, C. (1999). Concomitant activation of pathways downstream of Grb2 and PI 3-kinase is required for MET-mediated metastasis. Oncogene *18*, 1139–1146. https://doi.org/10.1038/sj.onc.1202607.
37. Domínguez-Andrés, J., Arts, R.J.W., Bekkering, S., Bahrar, H., Blok, B.A., de Bree, L.C.J., Bruno, M., Bulut, Ö., Debisarun, P.A., Dijkstra, H., et al. (2021). In vitro induction of trained immunity in adherent human monocytes. STAR Protoc *2*. https://doi.org/10.1016/j.xpro.2021.100365.
38. Ramani, A., Müller, L., Ostermann, P.N., Gabriel, E., Abida-Islam, P., Müller-Schiffmann, A., Mariappan, A., Goureau, O., Gruell, H., Walker, A., et al. (2020). SARS -CoV-2 targets neurons of 3D human brain organoids . EMBO J *39*, 1–14. https://doi.org/10.15252/embj.2020106230.
39. Mishra, S., Arsh, A.M., and Rathore, J.S. (2022). Trained innate immunity and diseases: Bane with the boon. Clinical Immunology Communications *2*, 118–129. https://doi.org/10.1016/j.clicom.2022.08.004.
40. Quintin, J., Saeed, S., Martens, J.H.A., Giamarellos-Bourboulis, E.J., Ifrim, D.C., Logie, C., Jacobs, L., Jansen, T., Kullberg, B.-J., Wijmenga, C., et al. (2012). Candida albicans Infection Affords Protection against Reinfection via Functional Reprogramming of Monocytes. Cell Host Microbe *12*, 223–232. https://doi.org/10.1016/j.chom.2012.06.006.
41. Guo, Y., Luan, L., Patil, N.K., Wang, J., Bohannon, J.K., Rabacal, W., Fensterheim, B.A., Hernandez, A., and Sherwood, E.R. (2017). Interleukin-15 Enables Septic Shock by Maintaining Natural Killer Cell Integrity and Function 1 HHS Public Access. J Immunol *198*, 1320–1333. https://doi.org/10.4049/jimmunol.1601486.Interleukin-15.
42. Juskewitch, J.E., Knudsen, B.E., Platt, J.L., Nath, K.A., Knutson, K.L., Brunn, G.J., and Grande, J.P. (2012). LPS-induced murine systemic inflammation is driven by parenchymal cell activation and exclusively predicted by early MCP-1 plasma levels. American Journal of Pathology *180*, 32–40. https://doi.org/10.1016/j.ajpath.2011.10.001.
43. Pijl, J.P., Kwee, T.C., Slart, R.H.J.A., Yakar, D., Wouthuyzen-Bakker, M., and Glaudemans, A.W.J.M. (2021). Clinical implications of increased uptake in bone marrow and spleen on FDG-PET in patients with bacteremia. Eur J Nucl Med Mol Imaging *48*, 1467–1477. https://doi.org/10.1007/s00259-020-05071-8.
44. Ye, Y., Calcagno, C., Binderup, T., Courties, G., Keliher, E.J., Wojtkiewicz, G.R., Iwamoto, Y., Tang, J., Pérez-medina, C., Ishino, S., et al. (2016). Imaging Macrophage and Hematopoietic Progenitor Proliferation in Atherosclerosis.

117, 835–845. https://doi.org/10.1161/CIRCRESAHA.115.307024.Imaging.

45. Emami, H., Singh, P., Macnabb, M., Vucic, E., Lavender, Z., Rudd, J.H.F., Fayad, Z.A., Lehrer-Graiwer, J., Korsgren, M., Figueroa, A.L., et al. (2015). Splenic metabolic activity predicts risk of future cardiovascular events: Demonstration of a cardiosplenic axis in humans. JACC Cardiovasc Imaging *8*, 121–130. https://doi.org/10.1016/j.jcmg.2014.10.009.

46. Chomet, M., Schreurs, M., Vos, R., Verlaan, M., Kooijman, E.J., Poot, A.J., Boellaard, R., Windhorst, A.D., van Dongen, G.A., Vugts, D.J., et al. (2021). Performance of nanoScan PET/CT and PET/MR for quantitative imaging of 18F and 89Zr as compared with ex vivo biodistribution in tumor-bearing mice. EJNMMI Res *11*, 57. https://doi.org/10.1186/s13550-021-00799-2.

47. Löffler, J., Hamp, C., Scheidhauer, E., Di Carlo, D., Solbach, C., Abaei, A., Hao, L., Glatting, G., Beer, A.J., Rasche, V., et al. (2021). Comparison of Quantification of Target-Specific Accumulation of [18F]F-siPSMA-14 in the HET-CAM Model and in Mice Using PET/MRI. Cancers (Basel) *13*, 4007. https://doi.org/10.3390/cancers13164007.

48. Hamon, P., Loyher, P.-L., Baudesson de Chanville, C., Licata, F., Combadière, C., and Boissonnas, A. (2017). CX3CR1-dependent endothelial margination modulates Ly6Chigh monocyte systemic deployment upon inflammation in mice. Blood *129*, 1296–1307. https://doi.org/10.1182/blood-2016-08-732164.

49. O'Dea, K.P., Wilson, M.R., Dokpesi, J.O., Wakabayashi, K., Tatton, L., van Rooijen, N., and Takata, M. (2009). Mobilization and Margination of Bone Marrow Gr-1high Monocytes during Subclinical Endotoxemia Predisposes the Lungs toward Acute Injury. The Journal of Immunology *182*, 1155–1166. https://doi.org/10.4049/jimmunol.182.2.1155.

50. Aiello, A.E., Larson, E.L., and Sedlak, R. (2008). Hidden heroes of the health revolution Sanitation and personal hygiene. Am J Infect Control *36*, S128–S151. https://doi.org/10.1016/j.ajic.2008.09.008.

51. Rudd, K.E., Johnson, S.C., Agesa, K.M., Shackelford, K.A., Tsoi, D., Kievlan, D.R., Colombara, D. V., Ikuta, K.S., Kissoon, N., Finfer, S., et al. (2020). Global, regional, and national sepsis incidence and mortality, 1990–2017: analysis for the Global Burden of Disease Study. The Lancet *395*, 200–211. https://doi.org/10.1016/S0140-6736(19)32989-7.

52. Fleischmann, C., Scherag, A., Adhikari, N.K.J., Hartog, C.S., Tsaganos, T., Schlattmann, P., Angus, D.C., and Reinhart, K. (2016). Assessment of Global Incidence and Mortality of Hospital-treated Sepsis. Current Estimates and Limitations. Am J Respir Crit Care Med *193*, 259–272. https://doi.org/10.1164/rccm.201504-0781OC.

53. Bernard, G.R., Vincent, J.-L., Laterre, P.-F., LaRosa, S.P., Dhainaut, J.-F., Lopez-Rodriguez, A., Steingrub, J.S., Garber, G.E., Helterbrand, J.D., Ely, E.W., et al. (2001). Efficacy and Safety of

Recombinant Human Activated Protein C for Severe Sepsis. New England Journal of Medicine *344*, 699–709. https://doi.org/10.1056/NEJM200103083441001.

54. Ranieri, V.M., Thompson, B.T., Barie, P.S., Dhainaut, J.-F., Douglas, I.S., Finfer, S., Gårdlund, B., Marshall, J.C., Rhodes, A., Artigas, A., et al. (2012). Drotrecogin Alfa (Activated) in Adults with Septic Shock. New England Journal of Medicine *366*, 2055–2064. https://doi.org/10.1056/NEJMoa1202290.

55. Arevalo-Romero, J.A., Chingaté-López, S.M., Camacho, B.A., Alméciga-Díaz, C.J., and Ramirez-Segura, C.A. (2024). Next-generation treatments: Immunotherapy and advanced therapies for COVID-19. Heliyon *10*, e26423. https://doi.org/10.1016/j.heliyon.2024.e26423.

56. Kyriazopoulou, E., Panagopoulos, P., Metallidis, S., Dalekos, G.N., Poulakou, G., Gatselis, N., Karakike, E., Saridaki, M., Loli, G., Stefos, A., et al. (2021). An open label trial of anakinra to prevent respiratory failure in COVID-19. Elife *10*. https://doi.org/10.7554/eLife.66125.

57. Kyriazopoulou, E., Poulakou, G., Milionis, H., Metallidis, S., Adamis, G., Tsiakos, K., Fragkou, A., Rapti, A., Damoulari, C., Fantoni, M., et al. (2021). Early treatment of COVID-19 with anakinra guided by soluble urokinase plasminogen receptor plasma levels: a double-blind, randomized controlled phase 3 trial. Nat Med *27*, 1752–1760. https://doi.org/10.1038/s41591-021-01499-z.

58. Papadopoulou, A., Karavalakis, G., Papadopoulou, E., Xochelli, A., Bousiou, Z., Vogiatzoglou, A., Papayanni, P.-G., Georgakopoulou, A., Giannaki, M., Stavridou, F., et al. (2023). SARS-CoV-2-specific T cell therapy for severe COVID-19: a randomized phase 1/2 trial. Nat Med *29*, 2019–2029. https://doi.org/10.1038/s41591-023-02480-8.

59. Husain, A., and Byrareddy, S.N. (2020). Rapamycin as a potential repurpose drug candidate for the treatment of COVID-19. Chem Biol Interact *331*, 109282. https://doi.org/10.1016/j.cbi.2020.109282.

60. Karam, B.S., Morris, R.S., Bramante, C.T., Puskarich, M., Zolfaghari, E.J., Lotfi-Emran, S., Ingraham, N.E., Charles, A., Odde, D.J., and Tignanelli, C.J. (2021). mTOR inhibition in COVID-19: A commentary and review of efficacy in RNA viruses. J Med Virol *93*, 1843–1846. https://doi.org/10.1002/jmv.26728.

61. Abu-Eid, R., and Ward, F.J. (2021). Targeting the PI3K/Akt/mTOR pathway: A therapeutic strategy in COVID-19 patients. Immunol Lett *240*, 1–8. https://doi.org/10.1016/j.imlet.2021.09.005.

62. Basile, M.S., Cavalli, E., McCubrey, J., Hernández-Bello, J., Muñoz-Valle, J.F., Fagone, P., and Nicoletti, F. (2022). The PI3K/Akt/mTOR pathway: A potential pharmacological target in COVID-19. Drug Discov Today *27*, 848–856. https://doi.org/10.1016/j.drudis.2021.11.002.

63. Pinchera, B., Scotto, R., Buonomo, A.R., Zappulo, E., Stagnaro, F., Gallicchio, A., Viceconte, G., Sardanelli, A., Mercinelli, S., Villari, R., et al. (2022). Diabetes and COVID-19: The potential role of mTOR. Diabetes Res Clin Pract *186*, 109813.

https://doi.org/10.1016/j.diabres.2022.109813.

64. Gnoni, M., Beas, R., and Vásquez-Garagatti, R. (2021). Is there any role of intermittent fasting in the prevention and improving clinical outcomes of COVID-19?: intersection between inflammation, mTOR pathway, autophagy and calorie restriction. Virusdisease *32*, 625–634. https://doi.org/10.1007/s13337-021-00703-5.

65. Lu, R., Zhang, Y., Zhao, H., Guo, R., Jiang, Z., and Guo, R. (2022). SGK1, a Critical Regulator of Immune Modulation and Fibrosis and a Potential Therapeutic Target in Chronic Graft-Versus-Host Disease. Front Immunol *13*. https://doi.org/10.3389/fimmu.2022.822303.

66. Li, M., Wang, M., Wen, Y., Zhang, H., Zhao, G., and Gao, Q. (2023). Signaling pathways in macrophages: molecular mechanisms and therapeutic targets. MedComm (Beijing) *4*. https://doi.org/10.1002/mco2.349.

67. Bros, M., Haas, K., Moll, L., and Grabbe, S. (2019). RhoA as a Key Regulator of Innate and Adaptive Immunity. Cells *8*, 733. https://doi.org/10.3390/cells8070733.

68. Vergadi, E., Ieronymaki, E., Lyroni, K., Vaporidi, K., and Tsatsanis, C. (2017). Akt Signaling Pathway in Macrophage Activation and M1/M2 Polarization. The Journal of Immunology *198*, 1006–1014. https://doi.org/10.4049/jimmunol.1601515.

69. Acosta-Martinez, M., and Cabail, M.Z. (2022). The PI3K/Akt Pathway in Meta-Inflammation. Int J Mol Sci *23*, 15330. https://doi.org/10.3390/ijms232315330.

70. Wang, W.Y., Hyang Lim, J., and Li, J.-D. (2012). Synergistic and feedback signaling mechanisms in the regulation of inflammation in respiratory infections. Cell Mol Immunol *9*, 131–135. https://doi.org/10.1038/cmi.2011.65.

71. Murray, P.J., and Smale, S.T. (2012). Restraint of inflammatory signaling by interdependent strata of negative regulatory pathways. Nat Immunol *13*, 916–924. https://doi.org/10.1038/ni.2391.

72. Koundouros, N., and Blenis, J. (2022). Targeting mTOR in the Context of Diet and Whole-body Metabolism. Endocrinology *163*. https://doi.org/10.1210/endocr/bqac041.

73. Yoon, M.-S. (2017). The Role of Mammalian Target of Rapamycin (mTOR) in Insulin Signaling. Nutrients *9*, 1176. https://doi.org/10.3390/nu9111176.

74. Marafie, S.K., Al-Mulla, F., and Abubaker, J. (2024). mTOR: Its Critical Role in Metabolic Diseases, Cancer, and the Aging Process. Int J Mol Sci *25*, 6141. https://doi.org/10.3390/ijms25116141.

75. Kaldirim, M., Lang, A., Pfeiler, S., Fiegenbaum, P., Kelm, M., Bönner, F., and Gerdes, N. (2022). Modulation of mTOR Signaling in Cardiovascular Disease to Target Acute and Chronic Inflammation. Front Cardiovasc Med *9*. https://doi.org/10.3389/fcvm.2022.907348.

76. Nathan, C., and Ding, A. (2010). Nonresolving Inflammation. Cell *140*, 871–882. https://doi.org/10.1016/j.cell.2010.02.029.

77. Davis, H.E., McCorkell, L., Vogel, J.M., and Topol, E.J. (2023). Long COVID: major findings, mechanisms and recommendations. Nat Rev Microbiol *21*,

133–146. https://doi.org/10.1038/s41579-022-00846-2.

78. Xie, Y., Xu, E., Bowe, B., and Al-Aly, Z. (2022). Long-term cardiovascular outcomes of COVID-19. Nat Med *28*, 583–590. https://doi.org/10.1038/s41591-022-01689-3.

79. Satterfield, B.A., Bhatt, D.L., and Gersh, B.J. (2022). Cardiac involvement in the long-term implications of COVID-19. Nat Rev Cardiol *19*, 332–341. https://doi.org/10.1038/s41569-021-00631-3.

80. Mohamed, M.A., Elkhateeb, W.A., and Daba, G.M. (2022). Rapamycin golden jubilee and still the miraculous drug: a potent immunosuppressant, antitumor, rejuvenative agent, and potential contributor in COVID-19 treatment. Bioresour Bioprocess *9*, 65. https://doi.org/10.1186/s40643-022-00554-y.

81. Koul, P.A., and Mehfooz, N. (2019). Sirolimus in lymphangioleiomyomatosis: A case in point for research in "orphan" diseases. Lung India *36*, 353–355. https://doi.org/10.4103/lungindia.lungindia_280_19.

82. Serruys, P.W., Regar, E., and Carter, A.J. (2002). Rapamycin eluting stent: the onset of a new era in interventional cardiology. Heart *87*, 305–307. https://doi.org/10.1136/heart.87.4.305.

83. Mullen, P.J., Garcia, G., Purkayastha, A., Matulionis, N., Schmid, E.W., Momcilovic, M., Sen, C., Langerman, J., Ramaiah, A., Shackelford, D.B., et al. (2021). SARS-CoV-2 infection rewires host cell metabolism and is potentially susceptible to mTORC1 inhibition. Nat Commun *12*, 1876. https://doi.org/10.1038/s41467-021-22166-4.

84. Singla, A., Harun, N., Dilling, D.F., Merchant, K., McMahan, S., Ingledue, R., French, A., Corral, J.A., Korbee, L., Kopras, E.J., et al. (2024). Safety and efficacy of sirolimus in hospitalised patients with COVID-19 pneumonia. Respir Investig *62*, 216–222. https://doi.org/10.1016/j.resinv.2023.12.009.

85. Ghasemnejad-Berenji, M. (2021). mTOR inhibition: a double-edged sword in patients with COVID-19? Hum Cell *34*, 698–699. https://doi.org/10.1007/s13577-021-00495-2.

86. Weichhart, T., Hengstschläger, M., and Linke, M. (2015). Regulation of innate immune cell function by mTOR. Nat Rev Immunol *15*, 599–614. https://doi.org/10.1038/nri3901.

87. Yang, P., Zhao, Y., Zhao, L., Yuan, J., Chen, Y., Varghese, Z., Moorhead, J.F., Chen, Y., and Ruan, X.Z. (2015). Paradoxical effect of rapamycin on inflammatory stress-induced insulin resistance in vitro and in vivo. Sci Rep *5*, 14959. https://doi.org/10.1038/srep14959.

88. Lees, M.J., Hodson, N., Tinline-Goodfellow, C.T., Fung, H.J.W., Elia, A., and Moore, D.R. (2022). Challenges of rapamycin repurposing as a potential therapeutic candidate for COVID-19: implications for skeletal muscle metabolic health in older persons. Am J Physiol Endocrinol Metab *322*, E551–E555. https://doi.org/10.1152/ajpendo.00064.2022.

89. Mulder, W.J.M., van Leent, M.M.T., Lameijer, M., Fisher, E.A., Fayad, Z.A., and Pérez-Medina, C. (2018). High-Density Lipoprotein Nanobiologics for Precision Medicine. Acc Chem Res *51*, 127–137.

https://doi.org/10.1021/acs.accounts.7b00339.

90. Binderup, T., Duivenvoorden, R., Fay, F., Van Leent, M.M.T., Malkus, J., Baxter, S., Ishino, S., Zhao, Y., Sanchez-Gaytan, B., Teunissen, A.J.P., et al. (2019). Imaging-assisted nanoimmunotherapy for atherosclerosis in multiple species. Sci Transl Med *11*. https://doi.org/10.1126/scitranslmed.aaw7736.

91. Lameijer, M., Binderup, T., van Leent, M.M.T., Senders, M.L., Fay, F., Malkus, J., Sanchez-Gaytan, B.L., Teunissen, A.J.P., Karakatsanis, N., Robson, P., et al. (2018). Efficacy and safety assessment of a TRAF6-targeted nanoimmunotherapy in atherosclerotic mice and non-human primates. Nat Biomed Eng *2*, 279–292. https://doi.org/10.1038/s41551-018-0221-2.

92. van Leent, M.M.T., Beldman, T.J., Toner, Y.C., Lameijer, M.A., Rother, N., Bekkering, S., Teunissen, A.J.P., Zhou, X., van der Meel, R., Malkus, J., et al. (2021). Prosaposin mediates inflammation in atherosclerosis. Sci Transl Med *13*. https://doi.org/10.1126/scitranslmed.abe1433.

93. Braza, M.S., van Leent, M.M.T., Lameijer, M., Sanchez-Gaytan, B.L., Arts, R.J.W., Pérez-Medina, C., Conde, P., Garcia, M.R., Gonzalez-Perez, M., Brahmachary, M., et al. (2018). Inhibiting Inflammation with Myeloid Cell-Specific Nanobiologics Promotes Organ Transplant Acceptance. Immunity *49*, 819-828.e6. https://doi.org/10.1016/j.immuni.2018.09.008.

94. Seemann, S., Zohles, F., and Lupp, A. (2017). Comprehensive comparison of three different animal models for systemic inflammation. J Biomed Sci *24*, 60. https://doi.org/10.1186/s12929-017-0370-8.

95. Fuijkschot, W.W., Morrison, M.C., Zethof, I.P.A., Krijnen, P.A.J., Kleemann, R., Niessen, H.W.M., and Smulders, Y.M. (2018). LPS-Induced Systemic Inflammation Does Not Alter Atherosclerotic Plaque Area or Inflammation in APOE3∗LEIDEN Mice in the Early Phase Up to 15 Days. Shock *50*, 360–365. https://doi.org/10.1097/SHK.0000000000001026.

96. Zhao, Y., Shen, X., Na, N., Chu, Z., Su, H., Chao, S., Shi, L., Xu, Y., Zhang, L., Shi, B., et al. (2018). mTOR masters monocyte development in bone marrow by decreasing the inhibition of STAT5 on IRF8. Blood *131*, 1587–1599. https://doi.org/10.1182/blood-2017-04-777128.

97. Geest, C.R., Zwartkruis, F.J., Vellenga, E., Coffer, P.J., and Buitenhuis, M. (2009). Mammalian target of rapamycin activity is required for expansion of CD34+ hematopoietic progenitor cells. Haematologica *94*, 901–910. https://doi.org/10.3324/haematol.13766.

98. Lin, H.Y.-H., Chang, K.-T., Hung, C.-C., Kuo, C.-H., Hwang, S.-J., Chen, H.-C., Hung, C.-H., and Lin, S.-F. (2014). Effects of the mTOR inhibitor Rapamycin on Monocyte-Secreted Chemokines. BMC Immunol *15*, 37. https://doi.org/10.1186/s12865-014-0037-0.

99. Cotto, B., Natarajanseenivasan, K., and Langford, D. (2019). HIV-1 infection alters energy metabolism in the brain: Contributions to HIV-associated neurocognitive disorders. Prog Neurobiol

181, 101616. https://doi.org/10.1016/j.pneurobio.2019.101616.

100. Palmer, C.S., Cherry, C.L., Sada-Ovalle, I., Singh, A., and Crowe, S.M. (2016). Glucose Metabolism in T Cells and Monocytes: New Perspectives in HIV Pathogenesis. EBioMedicine *6*, 31–41. https://doi.org/10.1016/j.ebiom.2016.02.012.

101. Vekariya, U., Saxena, R., Singh, P., Rawat, K., Kumar, B., Kumari, S., Agnihotri, S.K., Kaur, S., Sachan, R., Nazir, A., et al. (2018). HIV-1 Nef-POTEE; A novel interaction modulates macrophage dissemination via mTORC2 signaling pathway. Life Sci *214*, 158–166. https://doi.org/10.1016/j.lfs.2018.10.068.

102. Carter, C.C., Mast, F.D., Olivier, J.P., Bourgeois, N.M., Kaushansky, A., and Aitchison, J.D. (2022). Dengue activates mTORC2 signaling to counteract apoptosis and maximize viral replication. Front Cell Infect Microbiol *12*. https://doi.org/10.3389/fcimb.2022.979996.

103. Lahon, A., Arya, R.P., and Banerjea, A.C. (2021). Dengue Virus Dysregulates Master Transcription Factors and PI3K/AKT/mTOR Signaling Pathway in Megakaryocytes. Front Cell Infect Microbiol *11*, 715208. https://doi.org/10.3389/fcimb.2021.715208.

104. Yu, F.-Y., Zheng, K., Wu, Y.-F., Gao, S.-W., Weng, Q.-Y., Zhu, C., Wu, Y.-P., Li, M., Qin, Z.-N., Lou, J.-F., et al. (2023). Rapamycin Exacerbates Staphylococcus aureus Pneumonia by Inhibiting mTOR-RPS6 in Macrophages. J Inflamm Res *16*, 5715–5728. https://doi.org/10.2147/JIR.S434483.

105. Biswas, V.K., Sen, K., Ahad, A., Ghosh, A., Verma, S., Pati, R., Prusty, S., Nayak, S.P., Podder, S., Kumar, D., et al. (2023). NCoR1 controls Mycobacterium tuberculosis growth in myeloid cells by regulating the AMPK-mTOR-TFEB axis. PLoS Biol *21*, e3002231. https://doi.org/10.1371/journal.pbio.3002231.

106. Wang, X., and Quinn, P.J. (2010). Endotoxins: Lipopolysaccharides of Gram-Negative Bacteria. In, pp. 3–25. https://doi.org/10.1007/978-90-481-9078-2_1.

107. Wang, M., Feng, J., Zhou, D., and Wang, J. (2023). Bacterial lipopolysaccharide-induced endothelial activation and dysfunction: a new predictive and therapeutic paradigm for sepsis. Eur J Med Res *28*, 339. https://doi.org/10.1186/s40001-023-01301-5.

108. Lewis, A.J., Seymour, C.W., and Rosengart, M.R. (2016). Current Murine Models of Sepsis. Surg Infect (Larchmt) *17*, 385–393. https://doi.org/10.1089/sur.2016.021.

109. Cai, L., Rodgers, E., Schoenmann, N., and Raju, R.P. (2023). Advances in Rodent Experimental Models of Sepsis. Int J Mol Sci *24*, 9578. https://doi.org/10.3390/ijms24119578.

110. Chen, R., Lan, Z., Ye, J., Pang, L., Liu, Y., Wu, W., Qin, X., Guo, Y., and Zhang, P. (2021). Cytokine Storm: The Primary Determinant for the Pathophysiological Evolution of COVID-19 Deterioration. Front Immunol *12*. https://doi.org/10.3389/fimmu.2021.589095.

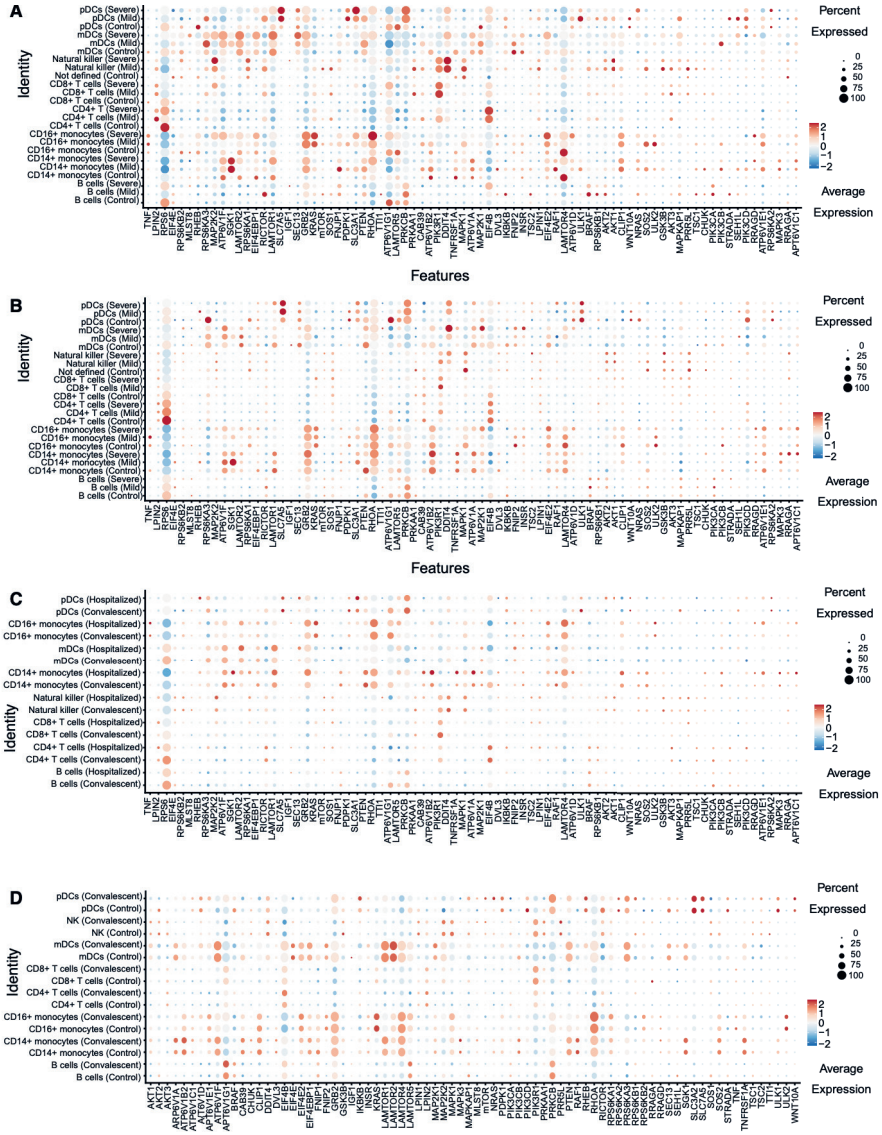
111. Tang, Y., Liu, J., Zhang, D., Xu, Z., Ji, J., and Wen, C. (2020). Cytokine Storm in

COVID-19: The Current Evidence and Treatment Strategies. Front Immunol *11*. https://doi.org/10.3389/fimmu.2020.01708.

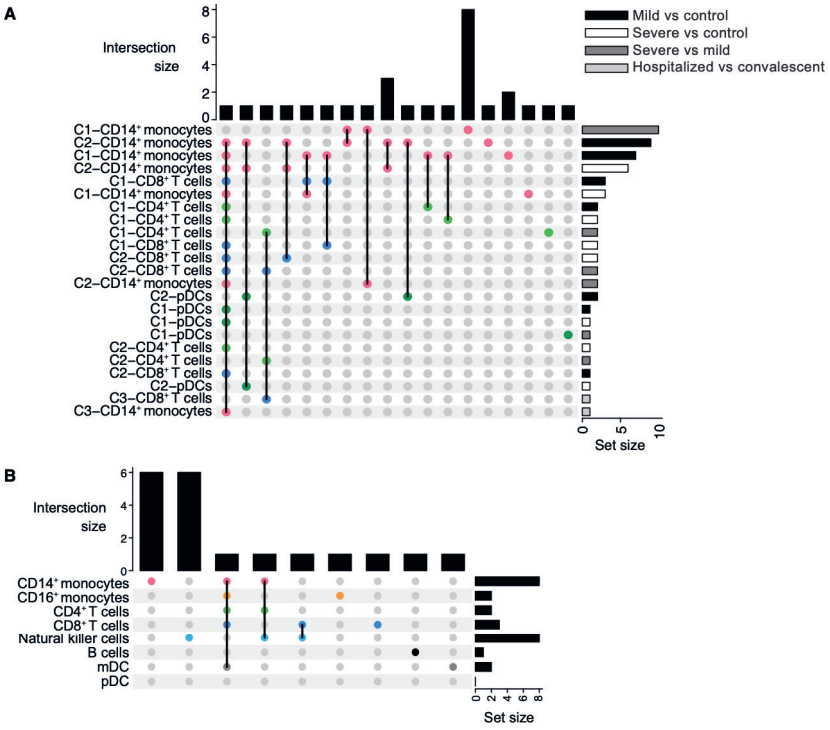
112. Muñoz-Fontela, C., Dowling, W.E., Funnell, S.G.P., Gsell, P.-S., Riveros-Balta, A.X., Albrecht, R.A., Andersen, H., Baric, R.S., Carroll, M.W., Cavaleri, M., et al. (2020). Animal models for COVID-19. Nature *586*, 509–515. https://doi.org/10.1038/s41586-020-2787-6.

113 Repnik, U., Knezevic, M., and Jeras, M. (2003). Simple and cost-effective isolation of monocytes from buffy coats. J Immunol Methods *278*, 283–292. https://doi.org/10.1016/S0022-1759(03)00231-X.

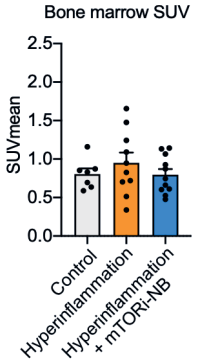
Supplemental material



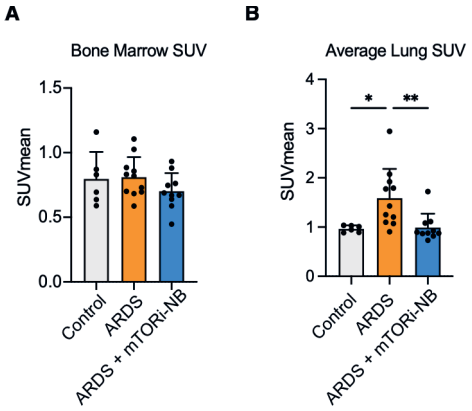
Supplementary Figure 1. mTOR signaling pathway genes expression profiles in different COVID-19 datasets. Expression profile of mTOR signaling pathway genes that are differentially expressed in at least one comparison in the Berlin A), Bonn B)[1], MHH50 C)[2] or Convalescent COVID-19 D)[3] cohorts.



Supplementary Figure 2. mTOR signaling pathway downregulated gene expression profiles A) Downregulated differentially expressed genes across the Berlin (C1), Bonn (C2)[1], and MHH50 (C3)[2] datasets. B) The number of downregulated mTOR genes in specific cell types in convalescent COVID-19 patients[3] C4).



Supplementary Figure 3. *In vivo* assessment of organ inflammation in the hyperinflammation mouse model. PET-based quantification of ^{18}F-FDG in the bone marrow 24 h post LPS injection (n = 7-11). SUV = standardized uptake value. Statistical analyses were performed using the Shapiro-Wilk test, followed by one-way ANOVA (with Tukey's multiple comparisons test).



Supplementary Figure 4. *In vivo* assessment of organ inflammation in the ARDS mouse model. A) PET-based quantification of ^{18}F-FDG in the bone marrow 72 h post LPS injection (n = 6-11). B) PET-based quantification of ^{18}F-FDG in the lungs 72 h post LPS injection (n = 6-10). SUV = standardized uptake value. Statistical analyses were performed using the Shapiro-Wilk test, followed by one-way ANOVA (with Tukey's multiple comparisons test) or Kruskal-Wallis (followed by Dunn's multiple comparison test) according to Gaussian distribution. *p<0.05, **p<0.01.

Supplementary Table 1. Genes involved in mTOR signaling pathway downloaded from KEGG (hsa04150)

KEGG Gene entry	Gene symbol	Description
8140	SLC7A5	solute carrier family 7 member 5 [KO:K13780]
6520	SLC3A2	solute carrier family 3 member 2 [KO:K06519]
153129	SLC38A9	solute carrier family 38 member 9 [KO:K14995]
523	ATP6V1A	ATPase H+ transporting V1 subunit A [KO:K02145] [EC:7.1.2.2]
525	ATP6V1B1	ATPase H+ transporting V1 subunit B1 [KO:K02147]
526	ATP6V1B2	ATPase H+ transporting V1 subunit B2 [KO:K02147]
245973	ATP6V1C2	ATPase H+ transporting V1 subunit C2 [KO:K02148]
528	ATP6V1C1	ATPase H+ transporting V1 subunit C1 [KO:K02148]
51382	ATP6V1D	ATPase H+ transporting V1 subunit D [KO:K02149]
90423	ATP6V1E2	ATPase H+ transporting V1 subunit E2 [KO:K02150]
529	ATP6V1E1	ATPase H+ transporting V1 subunit E1 [KO:K02150]
9296	ATP6V1F	ATPase H+ transporting V1 subunit F [KO:K02151]
9550	ATP6V1G1	ATPase H+ transporting V1 subunit G1 [KO:K02152]
127124	ATP6V1G3	ATPase H+ transporting V1 subunit G3 [KO:K02152]
534	ATP6V1G2	ATPase H+ transporting V1 subunit G2 [KO:K02152]
51606	ATP6V1H	ATPase H+ transporting V1 subunit H [KO:K02144]

55004	LAMTOR1	late endosomal/lysosomal adaptor, MAPK and MTOR activator 1 [KO:K20397]
28956	LAMTOR2	late endosomal/lysosomal adaptor, MAPK and MTOR activator 2 [KO:K20398]
8649	LAMTOR3	late endosomal/lysosomal adaptor, MAPK and MTOR activator 3 [KO:K04370]
389541	LAMTOR4	late endosomal/lysosomal adaptor, MAPK and MTOR activator 4 [KO:K20399]
10542	LAMTOR5	late endosomal/lysosomal adaptor, MAPK and MTOR activator 5 [KO:K16344]
201163	FLCN	folliculin [KO:K09594]
96459	FNIP1	folliculin interacting protein 1 [KO:K20400]
57600	FNIP2	folliculin interacting protein 2 [KO:K20401]
10670	RRAGA	Ras related GTP binding A [KO:K16185]
10325	RRAGB	Ras related GTP binding B [KO:K16185]
64121	RRAGC	Ras related GTP binding C [KO:K16186]
58528	RRAGD	Ras related GTP binding D [KO:K16186]
83667	SESN2	sestrin 2 [KO:K20394]
652968	CASTOR1	cytosolic arginine sensor for mTORC1 subunit 1 [KO:K23080]
729438	CASTOR2	cytosolic arginine sensor for mTORC1 subunit 2 [KO:K23081]
54468	MIOS	meiosis regulator for oocyte development [KO:K20407]
81929	SEH1L	SEH1 like nucleoporin [KO:K14299]
84219	WDR24	WD repeat domain 24 [KO:K20408]
79726	WDR59	WD repeat domain 59 [KO:K20409]
6396	SEC13	SEC13 homolog, nuclear pore and COPII coat complex component [KO:K14004]
9681	DEPDC5	DEP domain containing 5, GATOR1 subcomplex subunit [KO:K20404]
10641	NPRL2	NPR2 like, GATOR1 complex subunit [KO:K20405]
8131	NPRL3	NPR3 like, GATOR1 complex subunit [KO:K20406]
6502	SKP2	S-phase kinase associated protein 2 [KO:K03875]
220441	RNF152	ring finger protein 152 [KO:K15705] [EC:2.3.2.27]
57521	RPTOR	regulatory associated protein of MTOR complex 1 [KO:K07204]
84335	AKT1S1	AKT1 substrate 1 [KO:K16184]
2475	MTOR	mechanistic target of rapamycin kinase [KO:K07203] [EC:2.7.11.1]
64798	DEPTOR	DEP domain containing MTOR interacting protein [KO:K20402]

64223	MLST8	MTOR associated protein, LST8 homolog [KO:K08266]
9894	TELO2	telomere maintenance 2 [KO:K11137]
9675	TTI1	TELO2 interacting protein 1 [KO:K20403]
6249	CLIP1	CAP-Gly domain containing linker protein 1 [KO:K10421]
2887	GRB10	growth factor receptor bound protein 10 [KO:K20064]
23175	LPIN1	lipin 1 [KO:K15728] [EC:3.1.3.4]
64900	LPIN3	lipin 3 [KO:K15728] [EC:3.1.3.4]
9663	LPIN2	lipin 2 [KO:K15728] [EC:3.1.3.4]
8408	ULK1	unc-51 like autophagy activating kinase 1 [KO:K21357] [EC:2.7.11.1]
9706	ULK2	unc-51 like autophagy activating kinase 2 [KO:K08269] [EC:2.7.11.1]
1978	EIF4EBP1	eukaryotic translation initiation factor 4E binding protein 1 [KO:K07205]
1977	EIF4E	eukaryotic translation initiation factor 4E [KO:K03259]
9470	EIF4E2	eukaryotic translation initiation factor 4E family member 2 [KO:K03259]
253314	EIF4E1B	eukaryotic translation initiation factor 4E family member 1B [KO:K03259]
6198	RPS6KB1	ribosomal protein S6 kinase B1 [KO:K04688] [EC:2.7.11.1]
6199	RPS6KB2	ribosomal protein S6 kinase B2 [KO:K04688] [EC:2.7.11.1]
1975	EIF4B	eukaryotic translation initiation factor 4B [KO:K03258]
6194	RPS6	ribosomal protein S6 [KO:K02991]
92335	STRADA	STE20 related adaptor alpha [KO:K08271]
55437	STRADB	STE20 related adaptor beta [KO:K17532]
6794	STK11	serine/threonine kinase 11 [KO:K07298] [EC:2.7.11.1]
51719	CAB39	calcium binding protein 39 [KO:K08272]
81617	CAB39L	calcium binding protein 39 like [KO:K08272]
5562	PRKAA1	protein kinase AMP-activated catalytic subunit alpha 1 [KO:K07198] [EC:2.7.11.11]
5563	PRKAA2	protein kinase AMP-activated catalytic subunit alpha 2 [KO:K07198] [EC:2.7.11.11]
7248	TSC1	TSC complex subunit 1 [KO:K07206]
7249	TSC2	TSC complex subunit 2 [KO:K07207]
51256	TBC1D7	TBC1 domain family member 7 [KO:K20396]
107080638	TBC1D7-LOC100130357	readthrough [KO:K20396]
6009	RHEB	Ras homolog, mTORC1 binding [KO:K07208]
54541	DDIT4	DNA damage inducible transcript 4 [KO:K08270]
7471	WNT1	Wnt family member 1 [KO:K03209]
7472	WNT2	Wnt family member 2 [KO:K00182]

7482	WNT2B	Wnt family member 2B [KO:K00182]
7473	WNT3	Wnt family member 3 [KO:K00312]
89780	WNT3A	Wnt family member 3A [KO:K00312]
54361	WNT4	Wnt family member 4 [KO:K00408]
7474	WNT5A	Wnt family member 5A [KO:K00444]
81029	WNT5B	Wnt family member 5B [KO:K00444]
7475	WNT6	Wnt family member 6 [KO:K00445]
7476	WNT7A	Wnt family member 7A [KO:K00572]
7477	WNT7B	Wnt family member 7B [KO:K00572]
7478	WNT8A	Wnt family member 8A [KO:K00714]
7479	WNT8B	Wnt family member 8B [KO:K00714]
7483	WNT9A	Wnt family member 9A [KO:K01064]
7484	WNT9B	Wnt family member 9B [KO:K01064]
7480	WNT10B	Wnt family member 10B [KO:K01357]
80326	WNT10A	Wnt family member 10A [KO:K01357]
7481	WNT11	Wnt family member 11 [KO:K01384]
51384	WNT16	Wnt family member 16 [KO:K01558]
8321	FZD1	frizzled class receptor 1 [KO:K02432]
8324	FZD7	frizzled class receptor 7 [KO:K02432]
2535	FZD2	frizzled class receptor 2 [KO:K02235]
7976	FZD3	frizzled class receptor 3 [KO:K02329]
8322	FZD4	frizzled class receptor 4 [KO:K02354]
7855	FZD5	frizzled class receptor 5 [KO:K02375]
8325	FZD8	frizzled class receptor 8 [KO:K02375]
8323	FZD6	frizzled class receptor 6 [KO:K02376]
11211	FZD10	frizzled class receptor 10 [KO:K02842]
8326	FZD9	frizzled class receptor 9 [KO:K02842]
4041	LRP5	LDL receptor related protein 5 [KO:K03068]
4040	LRP6	LDL receptor related protein 6 [KO:K03068]
1857	DVL3	dishevelled segment polarity protein 3 [KO:K02353]
1856	DVL2	dishevelled segment polarity protein 2 [KO:K02353]
1855	DVL1	dishevelled segment polarity protein 1 [KO:K02353]
2932	GSK3B	glycogen synthase kinase 3 beta [KO:K03083] [EC:2.7.11.26]
7124	TNF	tumor necrosis factor [KO:K03156]
7132	TNFRSF1A	TNF receptor superfamily member 1A [KO:K03158]
3551	IKBKB	inhibitor of nuclear factor kappa B kinase subunit beta [KO:K07209] [EC:2.7.11.10]
3630	INS	insulin [KO:K04526]
3479	IGF1	insulin like growth factor 1 [KO:K05459]
3643	INSR	insulin receptor [KO:K04527] [EC:2.7.10.1]

3480	IGF1R	insulin like growth factor 1 receptor [KO:K05087] [EC:2.7.10.1]
2885	GRB2	growth factor receptor bound protein 2 [KO:K04364]
6654	SOS1	SOS Ras/Rac guanine nucleotide exchange factor 1 [KO:K03099]
6655	SOS2	SOS Ras/Rho guanine nucleotide exchange factor 2 [KO:K03099]
3265	HRAS	HRas proto-oncogene, GTPase [KO:K02833]
3845	KRAS	KRAS proto-oncogene, GTPase [KO:K07827]
4893	NRAS	NRAS proto-oncogene, GTPase [KO:K07828]
673	BRAF	B-Raf proto-oncogene, serine/threonine kinase [KO:K04365] [EC:2.7.11.1]
5894	RAF1	Raf-1 proto-oncogene, serine/threonine kinase [KO:K04366] [EC:2.7.11.1]
5604	MAP2K1	mitogen-activated protein kinase kinase 1 [KO:K04368] [EC:2.7.12.2]
5605	MAP2K2	mitogen-activated protein kinase kinase 2 [KO:K04369] [EC:2.7.12.2]
5594	MAPK1	mitogen-activated protein kinase 1 [KO:K04371] [EC:2.7.11.24]
5595	MAPK3	mitogen-activated protein kinase 3 [KO:K04371] [EC:2.7.11.24]
6197	RPS6KA3	ribosomal protein S6 kinase A3 [KO:K04373] [EC:2.7.11.1]
6195	RPS6KA1	ribosomal protein S6 kinase A1 [KO:K04373] [EC:2.7.11.1]
6196	RPS6KA2	ribosomal protein S6 kinase A2 [KO:K04373] [EC:2.7.11.1]
27330	RPS6KA6	ribosomal protein S6 kinase A6 [KO:K04373] [EC:2.7.11.1]
3667	IRS1	insulin receptor substrate 1 [KO:K16172]
5295	PIK3R1	phosphoinositide-3-kinase regulatory subunit 1 [KO:K02649]
5296	PIK3R2	phosphoinositide-3-kinase regulatory subunit 2 [KO:K02649]
8503	PIK3R3	phosphoinositide-3-kinase regulatory subunit 3 [KO:K02649]
5290	PIK3CA	phosphatidylinositol-4,5-bisphosphate 3-kinase catalytic subunit alpha [KO:K00922] [EC:2.7.1.153]
5293	PIK3CD	phosphatidylinositol-4,5-bisphosphate 3-kinase catalytic subunit delta [KO:K00922] [EC:2.7.1.153]
5291	PIK3CB	phosphatidylinositol-4,5-bisphosphate 3-kinase catalytic subunit beta [KO:K00922] [EC:2.7.1.153]
5728	PTEN	phosphatase and tensin homolog [KO:K01110] [EC:3.1.3.16 3.1.3.48 3.1.3.67]

5170	PDPK1	3-phosphoinositide dependent protein kinase 1 [KO:K06276] [EC:2.7.11.1]
207	AKT1	AKT serine/threonine kinase 1 [KO:K04456] [EC:2.7.11.1]
208	AKT2	AKT serine/threonine kinase 2 [KO:K04456] [EC:2.7.11.1]
10000	AKT3	AKT serine/threonine kinase 3 [KO:K04456] [EC:2.7.11.1]
1147	CHUK	component of inhibitor of nuclear factor kappa B kinase complex [KO:K04467] [EC:2.7.11.10]
79109	MAPKAP1	MAPK associated protein 1 [KO:K20410]
253260	RICTOR	RPTOR independent companion of MTOR complex 2 [KO:K08267]
55615	PRR5	proline rich 5 [KO:K20411]
79899	PRR5L	proline rich 5 like [KO:K20411]
387	RHOA	ras homolog family member A [KO:K04513]
5578	PRKCA	protein kinase C alpha [KO:K02677] [EC:2.7.11.13]
5579	PRKCB	protein kinase C beta [KO:K19662] [EC:2.7.11.13]
5582	PRKCG	protein kinase C gamma [KO:K19663] [EC:2.7.11.13]
6446	SGK1	serum/glucocorticoid regulated kinase 1 [KO:K13302] [EC:2.7.11.1]

Supplementary Table 2. Cohort details

Cohort	Seks (M/F)	Age	Status
Bonn (C1)	10/6; 4/4; 4/6	57,6; 72,8; 70,4	16 control; 8 mild; 10 severe
Berlin (C2)	N/A; 6/2; 6;4	N/A; 56,5; 63,1	12 control; 8 mild; 10 severe
MHH50 (C3)	17/10; 25; 12	N/A	27 convalescent; 37 hospitalized
Convalescent (C4)	7/7; 7/8	60; 50	14 convalescent; 15 control

References

1. Schulte-Schrepping, J., Reusch, N., Paclik, D., Baßler, K., Schlickeiser, S., Zhang, B., Krämer, B., Krammer, T., Brumhard, S., Bonaguro, L., et al. (2020). Severe COVID-19 Is Marked by a Dysregulated Myeloid Cell Compartment. Cell *182*, 1419-1440.e23. 10.1016/j.cell.2020.08.001.

2. Zhang, B., Zhang, Z., Koeken, V.A.C.M., Kumar, S., Aillaud, M., Tsay, H.-C., Liu, Z., Kraft, A.R.M., Soon, C.F., Odak, I., et al. (2022). Altered and allele-specific open chromatin landscape reveals epigenetic and genetic regulators of innate immunity in COVID-19. Cell genomics, 100232. 10.1016/j.xgen.2022.100232.

3. 3. Liu, Z., Kilic, G., Li, W., Bulut, O., Gupta, M.K., Zhang, B., Qi, C., Peng, H., Tsay, H.C., Soon, C.F., et al. (2022). Multi-Omics Integration Reveals Only Minor Long-Term Molecular and Functional Sequelae in Immune Cells of Individuals Recovered From COVID-19. Front Immunol *13*, 1–15. 10.3389/fimmu.2022.838132.



8

Imaging-assisted nanoimmunotherapy for atherosclerosis

Published in Science Translational Medicine, 2019.

Binderup, T.*, Duivenvoorden, R.*, Fay, F.*, van Leent, M.M.T., Malkus, J., Baxter, S., Ishino, S., Zhao, Y., Sánchez-Gaytán, B., Teunissen, A.J.P., **Frederico, Y.C.A.**, Tang, J., Carlucci, G., Lyashchenko, S., Calcagno, C., Karakatsanis, N., Soultanidis, G., Senders, M.L., Robson, P.M., Mani, V., Ramachandran, S., Lobatto, M.E., Hutten, B.A., Granada, J.F., Reiner, T., Swirski, F.K., Nahrendorf, M., Kjær, A., Fisher, E.A., Fayad, Z.A., Pérez- Medina, C., Mulder, W.J.M.

* These authors contributed equally to this work.

Toner, Y.C. (née Frederico, Y.C.A.) helped perform the *in vitro* and *ex vivo* analysis. She was also responsible for the histology data and analysis.

Abstract

While the nanomedicine research field produces hundreds of studies every year, very few formulations have been approved for clinical use, due in part to nanomedicine's reliance on mouse studies. In this study, we report the escalation of a nanoimmunotherapy from mouse to large rabbit and porcine atherosclerosis models, with an emphasis on the solutions we implemented to overcome production and evaluation challenges. Specifically, we integrated translational imaging readouts within the workflow to both analyze the nanoimmunotherapeutic's *in vivo* behavior and assess treatment response in larger animals. We observed our nanoimmunotherapeutic's anti-inflammatory efficacy in mice as well as rabbits and pigs. Importantly, in the larger animal models, nanoimmunotherapeutically reduced inflammation halted plaque progression, underlining the approach's translatability and potential to acutely treat atherosclerosis.

Introduction

The nanomedicine research field continues to grow, with hundreds of new nanoformulations reported every year. However, comparatively few formulations are clinically translated to benefit patients. Indeed, the overwhelming majority of preclinical work is limited to proof-of-concept mouse studies, and serious concerns have been raised about these studies' relevance, particularly in relation to efficient nanomedicine drug delivery in patients[1]. At the same time, a paradigm shift in the nanomedicine field has gained momentum as new nanotherapies are being designed to deliberately engage the immune system[2,3] rather than evading it, which has been nanomedicine's primary focus for decades. The ability to selectively modulate the immune response via nanomedicines[4,5], *i.e.* nanoimmunotherapy, is reinvigorating the field. This approach can treat conditions, such as cancer, atherosclerosis or autoimmune diseases, in which a dysregulated immune response is either an underlying or contributing factor. In the last decade, we have pioneered nanoimmunotherapeutic approaches to treat atherosclerosis, a chronic inflammatory disorder of medium and large arteries that is the major underlying cause of cardiovascular disease. We developed a myeloid cell-specific nanoimmunotherapy that rapidly and efficiently silences vessel wall inflammation[6] by inhibiting macrophage proliferation[7].

Such nanoimmunotherapies can be translationally significant if two key challenges are addressed. First, orders of magnitude more nanomaterial must be produced for larger animals and humans than for mice. Producing multigram amounts in a controlled and reproducible manner requires developing alternatives to traditional benchtop formulation methods. Second, the significantly lower number of large animals that can be reasonably included in a translational study necessitates different therapeutic readouts than those typically used in mouse studies. Concurrently, successful translation crucially requires developing both techniques to quantitatively determine the nanoimmunotherapeutic's distribution in the body after administration and related non-invasive imaging methods to probe this over time[8].

Here, we report a strategy that surmounts the aforementioned translation hurdles to close the daunting gap between benchtop and bedside nanomedicine research. Our approach involves scaling up a nanoimmunotherapeutic production strategy using a microfluidizer-based high-pressure homogenization process and its imaging-guided evaluation in three different atherosclerosis animal models. After establishing the high-pressure homogenization-produced nanoimmunotherapy's efficacy in atherosclerotic mice, we perform non-invasive assessments of its *in vivo* behavior and treatment response in atherosclerotic rabbits and pigs by integrated positron emission tomography (PET) magnetic resonance imaging (MRI). We thus demonstrate the translatability of our nanoimmunotherapeutic approach and its ability to acutely treat vessel wall inflammation in atherosclerosis.

Results

Development and production scale-up of S-HDL nanoimmunotherapy

In two recent publications, we reported the development of a simvastatin-loaded high-density lipoprotein (S-HDL) nanotherapeutic that we successfully applied in atherosclerosis mouse models to treat vessel wall inflammation[6,7]. However, due to its low production rate (120 mg/hour), our original benchtop sonication-based S-HDL production method was not suitable for producing the necessary amounts for studies in large animal models. Therefore, we designed and implemented a high-pressure homogenization process, including innovative purification methods, to scale up S-HDL production, and generate the required amounts (Fig. 1A).

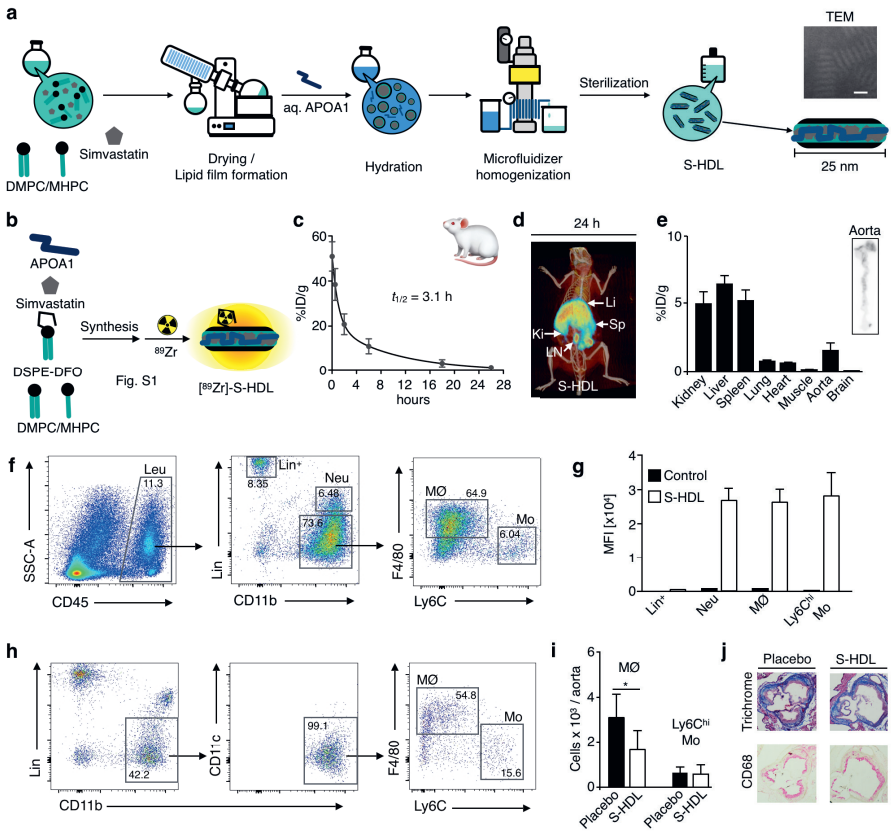


Figure 1. Nanoimmunotherapy production scale-up and evaluation in *Apoe*$^{-/-}$ mice. A) Schematic of simvastatin-loaded HDL (S-HDL) production by high-pressure microfluidic homogenization. Scale bar on transmission electron microscopy (TEM) image = 25 nm. B) Radiolabeling of S-HDL with ^{89}Zr by incorporating the phospholipid chelator DSPE-DFO in the formulation. C) Blood time-activity curve for [^{89}Zr]-S-HDL in *Apoe*$^{-/-}$ mice (n=4, 12 weeks on Western diet). D) Representative 3D-rendered PET/CT fusion image of an *Apoe*$^{-/-}$ mouse 26 p.i. of ^{89}Zr-S-HDL. E) Tissue radioactivity distribution at 26 hours post injection of [^{89}Zr]-S-HDL in *Apoe*$^{-/-}$ mice (n=4, 12 weeks on Western diet). On the right, representative autoradigraph showing radioactivity distribution on the aorta of an *Apoe*$^{-/-}$ mouse 26 p.i. of ^{89}Zr-S-HDL. F) Gating procedure employed in the flow cytometric analysis to evaluate S-HDL treatment efficacy in *Apoe*$^{-/-}$ mice. G) Aortic macrophage (MØ) and monocyte (Ly6Chi Mo) numbers after treatment with PBS (Placebo) or S-HDL in *Apoe*$^{-/-}$ mice (n=10 per group, 12 weeks on Western diet). H) Representative aortic sections from *Apoe*$^{-/-}$ mice (n=2 per group, 12 weeks on Western diet) treated with PBS (Placebo) or S-HDL. Li = liver; Sp = spleen; Ki = kidney; LN = lymph node. * $P < 0.05$.

We first implemented a large-scale apolipoprotein A1 (APOA1) extraction method. Using the optimized workflow described in the methods section, we isolated 10 g of APOA1 from purified human HDL, which is one order of magnitude more than we typically generate. Our previously reported benchtop S-HDL formulation method involves hydrating a film composed of phospholipids and simvastatin with a buffered APOA1 solution, followed by 1 hour of sonication and multiple purification steps[6,7]. The new production method also uses the formation of a dry film, albeit one containing at least 40 times more phospholipid/simvastatin. After the film's complete hydration with 0.5 L of an APOA1-containing saline buffer in the appropriate ratio, the suspension was homogenized using a microfluidizer 110-S Processor (Microfluidics, Newton, MA). This high-pressure homogenization method processes batches containing 5 g of total bulk ingredients in 30 minutes, leading to an 80-fold higher production rate compared to our original method. Due to the large amount of S-HDL produced, we scaled the purification steps using tangential flow filtration and funnel vacuum filtration methods. This process enabled the production of up to 18 g (total bulk ingredients) of S-HDL per production run, with a simvastatin recovery of 67 ± 6% (n=8, Supplementary Table S1), yielding discoidal S-HDL particles (see TEM images in Fig. 1A and Supplementary Fig. S1A) with a mean diameter of 23.6 ± 3.7 nm (dispersity index: 0.24 ± 0.04, n=8). These morphological features are comparable to S-HDL prepared using our original benchtop method[6,7]. We produced a total of approximately 90 g of S-HDL nanoimmunotherapeutic with suitable physicochemical properties for *in vivo* application. (An overview of all individual batches' physicochemical properties is provided in Supplementary Table S1).

To assess our nanoimmunotherapeutic's biodistribution and pharmacokinetics, we developed a ^{89}Zr-labeled S-HDL analog ([^{89}Zr]-S-HDL) following a strategy previously reported by us[9]. In short, we included the phospholipid chelator DSPE-DFO in the formulation to allow radiolabeling with ^{89}Zr. Radiolabeling was performed by reacting with [^{89}Zr]zirconium (IV) oxalate, and radiochemically pure [^{89}Zr]-S-HDL (Supplementary Fig. S1B) was

obtained in high yield (>85%). The radiolabeling allowed localization of our nanobiologic by *in vivo* PET imaging.

S-HDL's biodistribution, targeting and therapeutic efficacy in *Apoe*$^{-/-}$ mice

In two previously reported studies, we extensively evaluated benchtop-produced S-HDL's therapeutic efficacy in atherosclerotic apolipoprotein E deficient (*Apoe*$^{-/-}$) mice[6,7]. To ensure the S-HDL produced in large batches by high-pressure homogenization exerts similar therapeutic effects, we first conducted mouse experiments. We studied [^{89}Zr]-S-HDL biodistribution and pharmacokinetics in *Apoe*$^{-/-}$ mice that had been fed a Western diet for 12 weeks to induce advanced atherosclerosis. The blood radioactivity half-life was 3.1 hours (Fig. 1C; two-phase decay, weighted $t_{1/2}$), which is comparable to the blood half-life of other HDL nanobiologics[2]. PET imaging at 24 hours post injection showed [^{89}Zr]-S-HDL's accumulation in the spleen, kidneys, liver and periaortic lymph nodes (Fig. 1D). PET imaging data were complemented by *ex vivo* gamma counting results (Fig. 1E). Importantly, digital autoradiography of excised aortas revealed high radioactivity deposition in the aortic arch and roots, indicating high accumulation of our nanoimmunotherapy in atherosclerotic lesions (Fig. 1E).

Subsequently, we investigated the anti-atherosclerotic efficacy of the S-HDL formulation produced by high pressure homogenization in *Apoe*$^{-/-}$ mice with advanced atherosclerosis. As readouts, we combined whole aorta flow cytometry (Fig. 1F) and histological analysis of cross sections of the aortic arch, which is where plaque development is most reproducible in this mouse model. We found that four infusions of S-HDL (Simvastatin dose 60 mg/kg) within 1 week decreased aortic macrophage numbers by 45% (P<0.05, Fig. 1G). Representative images from aortic arch histological sections are shown in Fig. 1H. Collectively, these results demonstrate that microfluidizer-produced S-HDL's biodistribution, targeting and therapeutic efficacy mirror those of traditional S-HDL[7]. This marks an important advancement, since

production scale-up is a prerequisite for translation to large animal models and, ultimately, the ability to conduct human studies.

S-HDL nanoimmunotherapy translation to large animal models of atherosclerosis

The results of our mouse model experiments incentivized us to proceed with testing S-HDL in large animal models of atherosclerosis, namely rabbit and porcine models. Both are well-established atherosclerosis models in which plaque development is induced by a combination of Western diet and surgical denudation of the endothelium, resulting in accelerated plaque development (Fig. 2A). In the rabbit model, aortic angioplasty was performed, whereas in the swine model lesions were induced in the femoral arteries. The therapeutic dose was calculated from human equivalent dose FDA tabulated values[10] based on body weight and surface area. Drawing on our previous studies in mice, we used 60 mg simvastatin/kg body weight (180 mg/m^2) as a starting point and applied a ratio between correction factors (Km) of the different species. The calculated rabbit and pig doses were 15 (Km ratio = ¼) and 7.5 (Km ratio = 1/8) mg/kg, respectively.

Our translational evaluation encompassed PET imaging of biodistribution and plaque targeting (Fig. 2B–F) and a non-invasive imaging-based assessment of treatment response (Figs. 3 and 4). These protocols were developed and evaluated in a separate cohort of six pigs not included in the ensuing biodistribution and therapeutic experiments. Protocol development included optimizing imaging parameters for a) non-contrast-enhanced time-of-flight (TOF) MR angiography to identify the aorta and femoral arteries; b) 3-dimensional (3D), isotropic, high-resolution black blood vessel wall MRI for plaque quantification in the whole femoral arterial tree; c) 3D black blood dynamic contrast-enhanced (DCE) MRI with high spatial resolution and coverage to quantify plaque endothelial permeability. Specifically, flip angle and number of imaging slabs were varied for TOF angiography until adequate coverage and blood pool contrast were obtained. For 3D black blood vessel wall and DCE MRI, the acquisition plane, number of acquired

slices, spatial resolution and number of signal averages were optimized to obtain high signal-to-noise ratios and minimize blood pool signal for adequate vessel wall delineation.

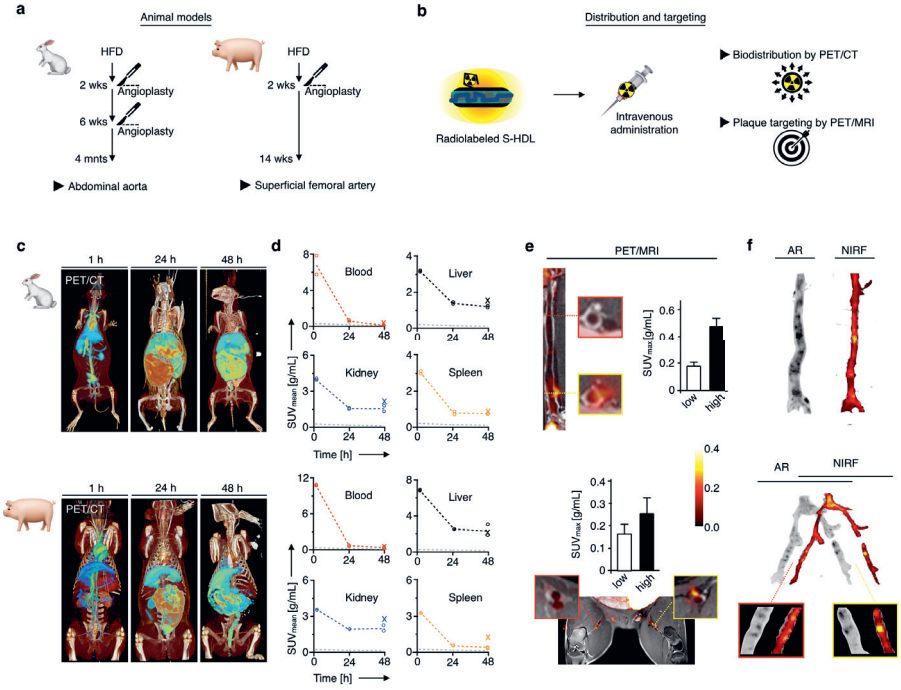


Figure 2. S-HDL nanoimmunotherapy *in vivo* evaluation by non-invasive imaging in rabbits and pigs. A) Schematic description of the rabbit and porcine atherosclerosis models used in this study. B) [^{89}Zr]-S-HDL was used to non-invasively probe biodistribution and plaque targeting by PET/CT and PET/MRI, respectively. C) Representative 3D-rendered PET/CT fusion images of atherosclerotic rabbits (top) and pigs (bottom) at 1, 24 and 48 hours post administration of [^{89}Zr]-S-HDL. D) PET imaging-derived time-activity curves in selected tissues in rabbits (n=2, top) and pigs (n=2, bottom) injected with [^{89}Zr]-S-HDL. The x represents the value obtained *ex vivo* by gamma counting. The grey line is the muscle time-activity curve, included for reference. E) PET/MR imaging assessment of plaque targeting in rabbits (top) and pigs (bottom), 48 hours p.i. of [^{89}Zr]-S-HDL. F) Regional distribution of S-HDL in atherosclerotic samples from rabbits (top) and pigs (bottom), as determined by autoradiography (AR, [^{89}Zr]-S-HDL) and near-infrared fluorescence (NIRF, DiD-S-HDL) at 48 hours p.i.

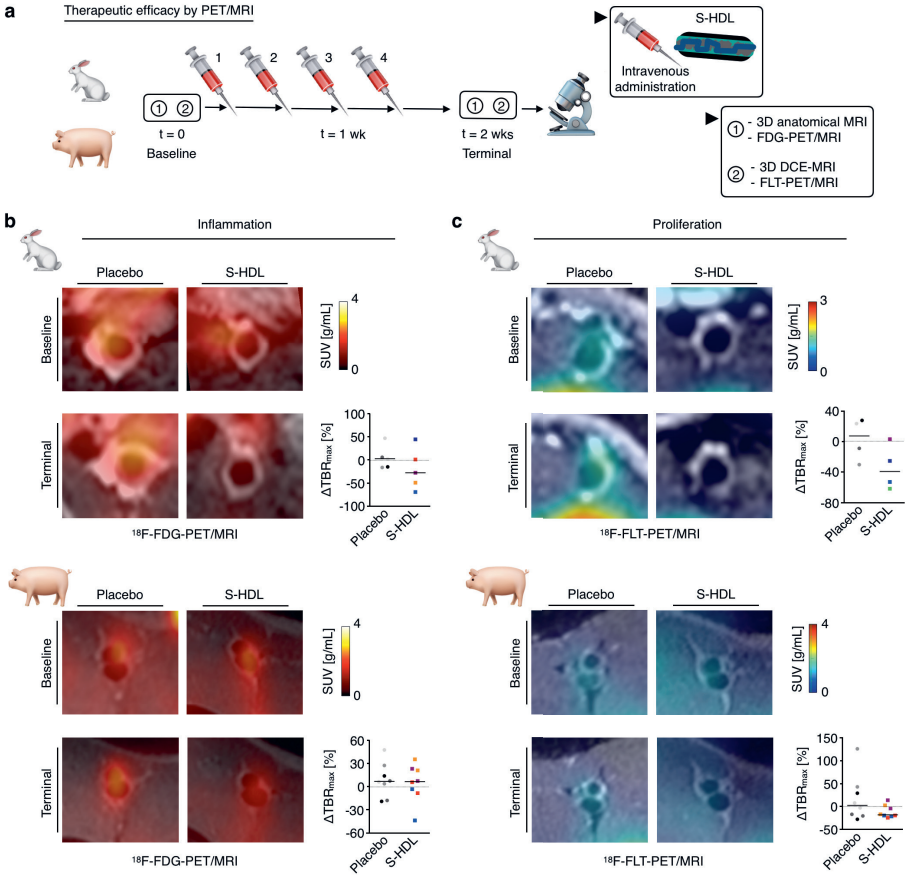


Figure 3. Imaging-guided S-HDL nanoimmunotherapy in rabbits and pigs. PET-based readouts. A) Schematic representation of S-HDL imaging-guided treatment. Treatment response was evaluated longitudinally by performing a baseline scan before the first S-HDL administration, and a terminal scan 48 hours after the last one. B) ^{18}F-FDG-PET imaging-based assessment of vessel wall inflammation in rabbits (top) and pigs (bottom) treated with PBS (Placebo) or S-HDL. C) ^{18}F-FLT-PET imaging-based assessment of cellular proliferation in the vessel wall in rabbits (top) and pigs (bottom) treated with PBS (Placebo) or S-HDL. In panels b and c, dots are color-coded for individual animals, and two data points are represented per pig, corresponding to values obtained from analysis on each of the femoral arteries. Line is situated at median.

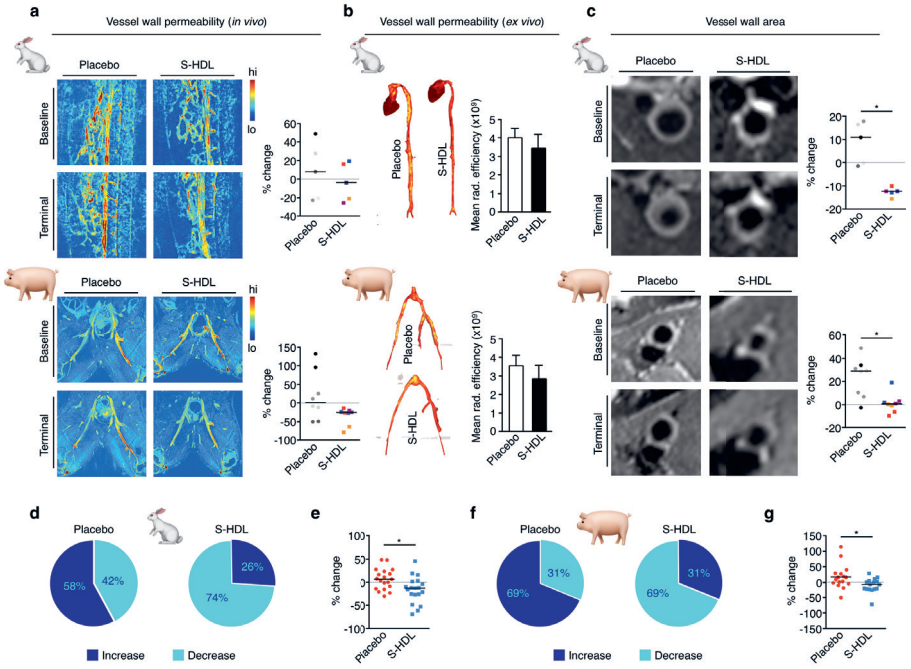


Figure 4. Imaging-guided S-HDL nanoimmunotherapy in rabbits and pigs. MRI-based readouts. A) 3D dynamic contrast-enhanced MRI-based vessel wall permeability measurements in rabbits (top) and pigs (bottom) treated with PBS (Placebo) or S-HDL. B) *Ex vivo* vessel wall permeability assessed by Evans blue near-infrared fluorescence imaging in rabbit aortas and porcine femoral arteries. C) T2-weighted MRI-based vessel wall area measurements in rabbits (top) and pigs (bottom) treated with PBS (Placebo) or S-HDL. In panels A and C, dots are color-coded for individual animals, and two data points are represented per pig, corresponding to values obtained from analysis on each of the femoral arteries. Line is situated at median. D) Proportion of scans that afforded increased or decreased imaging marker values in rabbits treated with PBS (Placebo) or S-HDL. E) Pooled representation of the variation in the four independent imaging parameters in rabbits treated with PBS (Placebo) or S-HDL (line is situated at median). F) Proportion of scans that afforded increased or decreased imaging marker values in pigs treated with PBS (Placebo) or S-HDL. G) Pooled representation of the variation in the four independent imaging parameters in pigs treated with PBS (Placebo) or S-HDL (line is situated at median). * $P < 0.05$, ** $P < 0.01$.

PET imaging of S-HDL's *in vivo* behavior in atherosclerotic rabbits and pigs

First, we performed *in vivo* PET/CT imaging to assess biodistribution and pharmacokinetics in atherosclerotic rabbits and pigs. Rabbits (n=2) and pigs

(n=2) were infused with [^{89}Zr]-S-HDL. One rabbit and one pig were co-injected with DiD-S-HDL to validate targeting *ex vivo*. Whole-body static scans were acquired 1, 24 and 48 hours post injection. Images were initially dominated by a high blood-pool signal (1 hour), followed by liver and intestinal accumulation (24 and 48 hours), consistent with hepatobiliary excretion (Fig. 2C). The clearance kinetics (Supplementary Fig. S2A) and radioactivity distribution pattern were similar in both species, with liver and kidneys as the main accumulation sites (Fig. 2D).

After the last PET/CT scan (48 hours post injection), PET/MRI was performed in [^{89}Zr]-S-HDL-injected rabbits and pigs to assess plaque targeting *in vivo*. Clear focal vessel wall accumulation in rabbits' abdominal aortas and pigs' femoral arteries was visualized (Fig. 2E). In these regions, radioactivity concentration was more than two-fold higher than in uninjured arterial fragments (Fig. 2E). We performed near-infrared fluorescence (NIRF) imaging with DiD-S-HDL (1 rabbit and 1 pig) and Evans Blue (1 rabbit and 1 pig) to evaluate plaque targeting and vessel wall permeability, respectively. The corresponding arterial samples were compared against [^{89}Zr]-S-HDL autoradiography. DiD-S-HDL and [^{89}Zr]-S-HDL were co-localized in plaque (Fig. 2F), whereas [^{89}Zr]-S-HDL and Evans Blue (Supplementary Fig. S2B) had a different distribution pattern in both rabbit and pig samples, revealing that HDL nanobiologics' accumulation in the vessel wall is not merely governed by microvessel permeability. The discrepancy between Evans blue and HDL nanobiologics' accumulation patterns corroborates our previous observations[11] that HDL nanobiologics' plaque accumulation is due to their inherent avidity for macrophages[6,7,9,11].

PET/MR imaging of S-HDL's anti-atherosclerotic activity

Next, we investigated the efficacy of S-HDL therapy in large animal atherosclerosis models. Rabbits and pigs received four intravenous S-HDL infusions using simvastatin doses of 15 and 7.5 mg/kg, respectively. The infusions were given over the course of 2 weeks. We evaluated therapeutic response non-invasively and longitudinally using a multiparametric PET/MR imaging protocol (Fig. 3A; details are presented in the Methods section).

Four different atherosclerosis-related parameters were measured, namely (**i**) vessel wall inflammation by ^{18}F-FDG-PET, (**ii**) cellular proliferation by ^{18}F-FLT-PET, (**iii**) vessel wall permeability by *in vivo* DCE MRI (and *ex vivo* by Evans Blue NIRF imaging), and (**iv**) vessel wall thickness by T2-weighted MRI. Imaging sessions were performed at baseline and 2 weeks after the onset of therapy. Imaging was performed on the aorta in rabbits and the femoral arteries in pigs.

We used a linear mixed model (LMM) to statistically analyze differences in imaging-derived parameters between treatment groups. The imaging parameter at the end of the study (terminal scan) was used as the dependent variable. Type of treatment and imaging parameter at the start of the study (baseline) were defined as fixed effects, and the side (left or right femoral artery in pigs) as a random effect. Based on this analysis, vessel wall inflammation, as measured by ^{18}F-FDG-PET (Fig. 3B), was not different between the S-HDL and placebo groups (LMM P=0.292 for rabbits, P=0.372 for pigs, Supplementary Fig. S3). A trend towards reduced cellular proliferative activity in the vessel wall as assessed by PET imaging of ^{18}F-FLT uptake (Fig. 3C) was observed in rabbits and pigs treated with S-HDL (LMM P=0.146 for rabbits, P=0.086 for pigs, Supplementary Fig. S3). S-HDL did not affect vessel wall permeability in rabbits and pigs, as measured both *in vivo* by DCE-MRI (Fig. 4A; LMM P=0.219 for rabbits, P=0.292 for pigs, Supplementary Fig. S3) and *ex vivo* by Evans Blue NIRF imaging (Fig. 4B). Importantly, the most significant results were related to vessel wall thickness as assessed by T2-weighted-MRI. In rabbits, we observed significantly reduced vessel wall area in the abdominal aortas of S-HDL treated animals compared to controls (Fig. 4C, top; LMM P=0.001, Supplementary Fig. S3), whereas in pigs, S-HDL treatment significantly halted vessel wall enlargement as compared to untreated animals (Fig. 4C, bottom; LMM P=0.036, Supplementary Fig. S3). Representative histological sections from rabbit and porcine specimens are shown in Supplementary Fig. S4.

Overall, in rabbits we observed decreased imaging marker values in 74% of terminal scans with respect to baseline in the S-HDL group, while in the placebo group we noted increased values in 58% of the scans (Fig. 4D). The median change between scans for the measured imaging parameters in the S-HDL group was −12.8% [interquartile range (IQR): −27.1 – 1.8 %], which was significantly different from that in the placebo group (Median: 6.6% [IQR: −14.3 – 23.4 %], *P*=0.005) (Fig. 4E). Similarly, in pigs we observed elevated imaging marker values in 69% of terminal scans compared to baseline in the placebo group, with exactly the same proportion of scans showing decreased values in the S-HDL group (Fig. 4F). The variation in the monitored imaging markers was significantly different between groups (Median placebo: 12.1 % [IQR: −3.9 – 28.0 %] versus median S-HDL: −7.7% [IQR: −22.5 – 0.9 %], *P*=0.01) (Fig. 4G). A combined representation of the variation in all imaging markers as a result of treatment in individual rabbits and pigs can be found in Supplementary Fig. S5.

S-HDL toxicity evaluation in pigs

Blood samples from pigs in both treatment groups were collected at the end of the study and analyzed for general biochemistry (Table 1) and complete blood count (Table 2) analysis. Liver enzymes (ALP, ALT, AST and GGT) and bilirubin concentrations were unaffected by S-HDL treatment. Interestingly, S-HDL treatment did not affect blood cholesterol concentration (*P*=0.80), confirming that S-HDL's effects are independent of simvastatin's cholesterol-lowering properties. The other analyzed parameters had no significant differences between the two groups except for decreased blood glucose concentration in the S-HDL-treated animals (*P*=0.03). Complete blood count results showed no difference in red blood cell, white blood cell, neutrophil, lymphocyte or monocyte numbers. However, the neutrophil compartment was reduced (*P*=0.03) while the lymphocyte compartment expanded (*P*=0.03) in S-HDL-treated animals compared to controls.

Table 1. Blood biochemistry results from pigs with atherosclerosis treated with PBS (Placebo) or S-HDL. Data are presented as median [interquartile range].

	Placebo	S-HDL	*P*
Alkaline phosphatase (ALP)(U/L)	127 [87-175]	85 [70-132]	0.15
SGPT (ALT)(U/L)	45 [39-67]	51 [38-65]	0.94
SGOT (AST)(U/L)	69 [43-222]	67 [53-160]	0.80
Gamma-glutamyl transferase (GGT)(U/L)	40 [34-78]	41 [39-56]	0.67
Creatine phosphokinase (CPK)(U/L)	740 [406-1817]	796 [431-1024]	0.94
Total bilirubin (mg/dL)	0.2 [0.1-0.2]	0.2 [0.2-0.3]	0.28
- Direct bilirubin (mg/dL)	0.0 [0.0-0.1]	0.0 [0.0-0.1]	>0.99
- Indirect bilirubin (mg/dL)	0.1 [0.1-0.2]	0.2 [0.1-0.3]	0.37
Total protein (g/dL)	6.6 [5.9-6.7]	6.8 [6.5-7.1]	0.21
- Albumin (g/dL)	3.5 [3.4-4.0]	4.0 [3.7-4.5]	0.29
- Globulin (g/dL)	2.6 [2.5-3.1]	2.8 [2.5-2.9]	0.81
- Albumin/Globulin ratio	1.4 [1.2-1.6]	1.4 [1.3-1.8]	0.75
Blood urea nitrogen (BUN)(mg/dL)	12 [10-14]	10 [8.5-17]	0.79
Creatinine (mg/dL)	0.9 [0.8-1.2]	1.0 [0.9-1.2]	0.69
BUN/Creatinine ratio	13 [9.1-17]	11 [9.0-15]	0.94
Glucose (mg/dL)	76 [71-80]	67 [34-69]	0.03
Cholesterol (mg/dL)	573 [450-628]	507 [426-747]	0.80
Triglycerides (mg/dL)	62 [26-72]	72 [48-186]	0.31
Sodium (mmol/L)	140 [140-141]	139 [136-141]	0.20
Potassium (mmol/L)	4.4 [4.3-5.1]	4.6 [4.1-7.5]	0.44
Na/K ratio	32 [28-33]	30 [21-35]	0.44
Magnesium (mg/dL)	2.0 [1.9-2.4]	2.1 [1.9-2.8]	0.81
Calcium (mg/dL)	10 [9.4-11]	10 [9.9-10.2]	0.88
Phosphorus (mg/dL)	7.4 [7.2-7.9]	6.9 [6.4-8.6]	0.53
Bicarbonate (mmol/L)	22 [19-24]	19 [17-24]	0.49
Chloride (mmol/L)	99 [98-101]	102 [97-105]	0.49

SGPT = serum glutamic pyruvic transaminase; ALT = alanine aminotransferase; SGOT = serum glutamic-oxaloacetic transaminase; AST = Aspartate aminotransferase.

Table 2. Complete blood count results from pigs with atherosclerosis treated with PBS (Placebo) or S-HDL. Data are presented as median [interquartile range].

	Placebo	S-HDL	*P*
Red blood cell # (M/μL)	8.1 [6.3-9.7]	5.0 [3.8-6.5]	0.06
Hemoglobin (g/dL)	13 [10-16]	8.9 [7.3-11]	0.19
Hematocrit (%)	43 [32-54]	31 [25-45]	0.29
Mean corpuscular volume (MCV)(fL)	53 [51-56]	66 [62-69]	**0.02**
Mean corpuscular hemoglobin (MCH)(pg)	16 [16-17]	18 [17-19]	**0.03**
MCH concentration (g/dL)	30 [29-31]	28 [26-30]	0.11
Reticulocyte # (K/μL)	27 [20-42]	65 [38-161]	0.06
Reticulocyte (%)	0.28 [0.25-0.60]	1.5 [0.7-3.2]	0.06
Platelet # (K/μL)	175 [142-193]	226 [166-393]	0.19
White blood cell # (K/μL)	6.9 [5.5-9.6]	5.5 [5.2-5.9]	0.25
Neutrophil # (K/μL)	3.3 [2.4-5.2]	1.6 [1.1-2.1]	0.06
Lymphocyte # (K/μL)	3.4 [2.8-3.8]	3.8 [3.1-4.1]	0.68
Monocyte # (K/μL)	0.35 [0.24-0.49]	0.24 [0.17-0.36]	0.26
Eosinophil # (K/μL)	0.08 [0.05-0.16]	0.03 [0.02-0.12]	0.44
Basophil # (K/μL)	0.0 [0.0-0.01]	0.01 [0.0-0.01]	0.52
Neutrophil (%)	51 [41-56]	33 [20-37]	**0.03**
Lymphocyte (%)	41 [39-52]	63 [59-72]	**0.03**
Monocyte (%)	4.4 [3.8-5.9]	4.3 [3.1-6.3]	0.71
Eosinophil (%)	1.0 [0.6-2.1]	0.5 [0.3-2.0]	0.44
Basophil (%)	0.0 [0.0-0.1]	0.2 [0.0-0.2]	0.29

Taken together, these data demonstrate that just 2 weeks of S-HDL nanoimmunotherapy had rapid effects on different atherosclerosis-related parameters with no measurable toxicity.

Discussion

A record 1,500+ nanomedicine-related studies were published in 2018, according to the Web of Science. However, until late 2017, only 50

nanodrugs were available for clinical use in the United States[12]. When nanoformulations reach late clinical trial phases, the vast majority of them fail to show their purported advantages over the free drug and hence any additional benefit to patients. This abysmal gap between preclinical nanomedicine and clinical application reflects the numerous translational challenges facing the field. While many factors likely contribute to this gap, oftentimes translation fails because of a lack of appropriate evaluation before moving to humans. In this study, we show the translational workflow we developed to escalate a nanoimmunotherapy's evaluation from mouse to large rabbit and porcine atherosclerosis models.

In our quest to translate our S-HDL nanoimmunotherapy, we first faced the need to produce bulk amounts of nanoimmunotherapeutic to treat large animals. We handled this issue by developing and implementing a new scaled-up microfluidizer-based method that affords an 80-fold higher production rate. Notably, the resulting material had similar physicochemical properties to the traditionally produced nanoimmunotherapy. Most importantly, the scaled-up nanoimmunotherapeutic's *in vivo* behavior, including its biodistribution, pharmacokinetic profile, ability to reach the plaque and therapeutic efficacy, were comparable to our previous observations with benchtop-produced S-HDL.

Non-invasive imaging can probe molecular processes *in vivo* and is therefore a very powerful tool for evaluating new therapies. In fact, imaging is increasingly integrated in clinical trials to provide surrogate endpoints of treatment response without the need for long follow-up periods or large patient cohorts[13]. In this study, we used imaging at two different stages in the translational workflow. First, we conducted a quantitative *in vivo* performance evaluation using a radiolabeled analog of the nanoimmunotherapy, which allowed us to verify plaque accumulation and visualize overall biodistribution. Second, we developed a multiparametric imaging protocol to quantify the effect of nanoimmunotherapy on several disease markers. The complexity of the atherosclerotic process mandates the use of a multimodal approach, allowing assessment of plaque morphology

and activity to better characterize lesions. PET/MRI is very well suited to this task, as it combines MRI's excellent soft tissue contrast and spatial resolution with PET's high sensitivity and the specificity of the radiotracers. Despite the treatment's short duration, our results show a clear trend towards reduction in all evaluated atherosclerosis burden parameters, including vessel wall thickness and permeability, inflammation and proliferation. This latter outcome seems to mirror our observations from previous studies, since S-HDL nanoimmunotherapy exerts its effects through macrophage proliferation inhibition[7], which is a dominant process in plaque inflammation in advanced atherosclerosis.

The use of HDL nanobiologics as myeloid cell-specific therapies is a promising treatment avenue for many immune-related diseases. One of the biggest hurdles for clinically translating these nanoimmunotherapies will be implementing large-scale APOA1 extraction/production methods. In this study, we optimized a high throughput method to isolate APOA1 through purification and delipidation of human HDL. While this is a convenient way to extract the protein, safety concerns regarding sterility and risk of contamination would need to be addressed. Alternatively, APOA1 can be produced recombinantly in bacteria or mammalian cells, but production and purification processes in this case can be troublesome and result in low yields. Another pivotal issue in developing and translating these nanoimmunotherapies is assessing their safety. Simvastatin can have deleterious effects on muscle and liver, especially with higher doses. Yet our nanoimmunotherapy's uptake in muscle was low. Blood biochemistry analysis revealed no difference in creatine phosphokinase, indicating our treatment had no harmful effect on myocytes. In contrast to muscle tissue, our nanoimmunotherapy is taken up by the liver in high quantities, as shown by the biodistribution data. Therefore, it is vital to evaluate signs of liver toxicity. In previous mouse studies, we observed neither metabolic changes nor signs of liver toxicity[14]. Our current study confirms this point as transaminases (ALT and AST), alkaline phosphatase and bilirubin levels were unaffected. Effects on the immune system must also be investigated. We observed no changes

in white blood cell count, or in lymphocyte, neutrophil and monocyte numbers.

The promising results we obtained in large animals are encouraging and may represent a new therapeutic option for acutely treating atherosclerosis-related inflammation. This option has clinically relevant value after an acute cardiovascular event, *i.e.* myocardial infarction or stroke. These events are known to exacerbate inflammation and thus aggravate ongoing atherosclerosis, leading to a high recurrence rate of acute events in these patients. Thus, it is conceivable that an intervention with our nanoimmunotherapy after a cardiovascular event may be beneficial by rapidly suppressing the exaggerated inflammatory activity in atherosclerotic lesions during that critical period[15].

Our study has limitations. First, owing to logistical considerations, the number of large animals was limited. A total of six pigs were used to develop the imaging protocols, plus another 12 for the biodistribution and efficacy studies. For symmetry, we used the same number of rabbits. However, implementing a longitudinal multiparametric imaging-based therapy monitoring approach allowed us to measure treatment response in individual animals from different angles, *i.e.* assessing different markers of disease progression. Second, using FDG as an imaging marker of inflammation may also have certain limitations in large plaques, since hypoxia-induced uptake may be predominant[16]. This could have masked the anti-inflammatory effects of S-HDL to a certain degree.

In conclusion, we presented the production scaling and imaging-facilitated development workflow for evaluating a nanoimmunotherapeutic. In the context of cardiovascular disease, we showed that our nanoimmunotherapeutic's anti-atherosclerotic effects in mice were maintained in large animals. Not only do we anticipate increased potential for nanomedicines as immunotherapeutics, we also demonstrate the value of – and need for – non-invasive imaging readouts when evaluating such nanoimmunotherapies in large animal disease models.

Materials and Methods

Materials

Phospholipids (DMPC, MHPC and DSPE) and simvastatin were purchased from Avanti Polar Lipids (Alabaster, AL) and AK Scientific (Union City, CA), respectively. All other chemicals were acquired from Sigma-Aldrich (St. Louis, MO). APOA1 was isolated from human HDL concentrates (Bioresource Technology, Weston, FL) following a previously described procedure[17]. ^{89}Zr was produced at Memorial Sloan-Kettering Cancer Center on an EBCO TR19/9 variable-beam energy cyclotron (Ebco Industries Inc., Vancouver, BC, Canada) via the ^{89}Y(p,n)^{89}Zr reaction and purified in accordance with previously reported methods[18]. ^{18}F was produced via the ^{18}O(p,n)^{18}F reaction using a GEMS PETtrace-800 cyclotron (GE Healthcare, Chicago, IL).

Radiotracers

^{18}F-labeled 2-deoxy-2-fluoro-D-glucose (^{18}F-FDG) was purchased from NCM USA (Bronx, NY), while ^{18}F-labeled 3'-fluoro-3'-deoxythymidine (^{18}F-FLT) was synthesized in-house by adapting already published procedures[19,20]. Briefly, a QMA cartridge containing cyclotron-produced [^{18}F]fluoride was eluted with a solution containing 9 mg 4,7,13,16,21,24-hexaoxa-1,10 diazabicyclo[8.8.8]hexacosane (Kryptofix [2.2.2]), 0.08 mL 0.15 M K_2CO_3 and 1.92 mL acetonitrile into a 5 mL reaction vial. Solvents were removed azeotropically at 120 °C under a slight flow of nitrogen. Then, 5 mg of precursor 3-*N*-Boc-5'-*O*-dimethoxytrityl-3'-*O*-nosyl-thymidine (ABX, Dresden, Germany) (6.02 µmol) in 500 µL dry acetonitrile was added and the reaction mixture was heated to 150 °C for 10 min. After cooling to room temperature, 1 N hydrochloric acid (400 µL) was added and the mixture was heated to 90 °C for 10 min. The reaction mixture was finally quenched by adding 2 M sodium acetate solution (1.3 mL) and purified by HPLC to yield pure ^{18}F-FLT using a C-18 semi-preparative column (Luna C-18, 250 × 10 mm, 5µm; Phenomenex, Torrance, CA) and isocratic elution with 8% EtOH/92% water at 5.5 mL*min^{-1} flow (RT ~ 16 min). Purity was assessed via Radio-HPLC using a C-18 analytical column (Atlantis T3, 100Å, 250 × 4.6 mm, 5µm;

Waters, Milford, MA) and isocratic elution with 10% EtOH/90% water at 1mL* min^{-1} flow (RT = 7.4 min).

HPLC and Radio-HPLC

HPLC was performed on a Prominence HPLC system (Shimadzu, Kyoto, Japan) equipped with two LC-10AT pumps and an SPD-M10AVP photodiode array detector. Radio-HPLC was performed using a Lablogic Scan-RAM Radio-TLC/HPLC detector. Size exclusion chromatography was performed on a Superdex 10/300 column (GE Healthcare Life Sciences, Pittsburgh, PA) using PBS as eluent at a flow rate of 1 mL/min.

Animals

Female *Apoe*$^{-/-}$ mice were purchased from Jackson Laboratories (Sacramento, CA). Male CRL SPF White New Zealand rabbits (n=12) and male familial hypercholesterolemia pigs (n=11; 4 males and 7 females) were acquired from Charles River Laboratories (Wilmington, MA) and University of Wisconsin, respectively. All animal experiments were performed in accordance with protocols approved by the Institutional Animal Care and Use Committees of Mount Sinai, Memorial Sloan Kettering Cancer Center and/or Skirball Center for Cardiovascular Research and followed National Institutes of Health guidelines for animal welfare.

Mouse model of atherosclerosis

Female *Apoe*$^{-/-}$ mice (B6.129P2-Apoe$^{tm1Unc/J}$, 4–6 weeks old) were fed a high-fat diet (Harlan Teklad TD.88137, 42% calories from fat; Envigo, Somerset, NJ) for 12 weeks. Under these conditions, this animal model develops atherosclerotic lesions due to high LDL cholesterol concentrations in blood resulting from their lack of apolipoprotein E[21,22].

Rabbit model of atherosclerosis[23,24]

Male CRL SPF White New Zealand rabbits (2.5–3 months old) underwent double balloon injury of the thoracic and abdominal aorta to induce atherosclerosis. Denudation was performed by introducing a 4F-Fogarty

embolectomy catheter (Edwards Lifesciences, Irvine, CA) through the femoral artery and inflating the balloon to 2 atm under fluoroscopic guidance. The procedure was repeated on the contralateral extremity 4 weeks later. Surgery was performed under anesthesia with intramuscular ketamine (35 mg/kg) and xylazine (5 mg/kg). To further accelerate plaque progression, animals were fed a high-cholesterol diet (Research Diets, New Brunswick, NJ) enriched initially with 0.3% cholesterol for 8 weeks and subsequently 0.15% for at least 8 weeks.

Porcine model of atherosclerosis[25]

We used the familial hypercholesterolemia swine (FHS) model of atherosclerosis. Due to a mutation in Lpb5 at the apolipoprotein B locus, these animals carry a liver low-density lipoprotein receptor deficiency that results in hypercholesterolemia and atherosclerosis. To accelerate plaque development, animals were fed a high-fat diet (enriched with 2% cholesterol) for 12 weeks and balloon injuries were performed in the deep and superficial femoral arteries on both legs with access through the carotid artery with a 4F-Fogarty embolectomy catheter (Edwards Lifesciences, Irvine, CA).

Synthesis of S-HDL by high-pressure microfluidic homogenization

Simvastatin and phospholipids 1-myristoyl-2-hydroxy-*sn*-glycero-phosphocholine (MHPC) and 1,2-dimyristoyl-*sn*-glycero-3-phosphatidylcholine (DMPC) were mixed in chloroform/methanol 4:1 in a 2-liter round bottom flask. A lipid film was formed by reduced-pressure rotary evaporation removal of solvents. The resulting film was further dried under a nitrogen flow for 1 hour. A solution of APOA1 was added, followed by PBS to reach a volume of approximately 0.5 L. The film was left to hydrate at 37 °C using a rotary evaporator to facilitate mixing. In batches of 0.25 L, the crude suspension underwent high-pressure microfluidics homogenization using a microfluidizer 110-S (Microfluidics, Newton, MA). The solution was pressurized at 120 psi to pass through the microfluidics chamber, which was refrigerated with an ice/water bath, 8 to 12 times. The resulting solution was

left overnight at room temperature and then centrifuged at 4,000 rpm for 1 hour at 4 °C. The supernatant was then passed through a 0.2 µm Stericup Vacuum Filter Unit (MilliporeSigma, Burlington, MA), and subsequently concentrated and washed twice with PBS using a 100 kDa Vivaflow device (Sartorius, Göttingen, Germany). After the final concentration round, the final volume was ~0.1 L. Samples were left overnight at 4 °C and then centrifuged at 4,000 rpm for 1 hour at 4 °C. Finally, the supernatant was passed through a 0.2 µm Stericup Vacuum Filter Unit (MilliporeSigma, Burlington, MA) under clean, sterile conditions and kept at 4 °C until use. Due to simvastatin's sensitivity to light, samples were protected from light during the whole formulation process.

S-HDL quality control

Size, dispersity and simvastatin concentration were measured for every S-HDL batch to assess the production quality. Size and dispersity were determined just after homogenization and at the end of the purification/sterilization process by dynamic light scattering, using a Zeta PALS analyzer (Brookhaven Instruments Corporation, Holtsville, MY). Simvastatin concentration was measured by HPLC using a previously described method[26]. Briefly, an aliquot of S-HDL (100 µL) formulation was dried for 18 hours in a desiccator then solubilized in acetonitrile (1 mL) and sonicated for 30 min on ice. After centrifugation (14,000 *g* for 10 min), supernatants were analyzed by reverse phase HPLC using an Ascentis C18 column (100 mm x 4.6 mm, 3 µm particles) using acetonitrile/water 80:20 as eluent. Simvastatin absorption was quantified at 238 nm.

Evaluation of S-HDL treatment efficacy in mice

Female *Apoe*$^{-/-}$ (n=24, 12 weeks on Western diet; weight: 29.6 ± 4.1 g) were randomized into two groups of 12 animals: 1) PBS and 2) S-HDL, at a simvastatin dose of 60 mg/kg body weight. Nanobiologic doses as well as PBS were administered via a lateral tail vein. Treatment consisted of four administrations, one every 48 hours. Twenty-four hours after the last dose, animals were euthanized and extensively perfused with saline, and the aortas

were carefully excised for *ex vivo* evaluation by flow cytometry (n=10) and histological analysis (n=2).

Flow cytometry

The aorta, from aortic root to the iliac bifurcation, was gently cleaned of fat, collected and then digested using an enzymatic digestion solution containing liberase TH (4 U/mL) (Roche, Basel, Switzerland), deoxyribonuclease (DNase) I (40 U/mL) (Sigma-Aldrich), and hyaluronidase (60 U/mL) (Sigma-Aldrich, St. Louis, MO) in PBS at 37 °C for 60 minutes. Cells were filtered through a 70 µm cell strainer and washed with serum containing media. Single cell suspensions were stained with the following monoclonal antibodies: anti-CD11b (clone M1/70), anti-F4/80 (clone BM8), anti-CD11c (clone N418), anti-CD45 (clone 30-F11), anti-Ly6C (clone AL-21) and a lineage cocktail (Lin) containing anti-CD90.2 (clone 53–2.1), anti-Ter119 (clone TER119), anti-NK1.1 (clone PK136), anti-CD49b (clone DX5), anti-CD45R (clone RA3–6B2) and anti-Ly6G (clone 1A8). Macrophages were identified as $CD45^{+}$, $CD11b^{hi}$, $Lin^{-/lo}$, $CD11c^{lo}$ and $F4/80^{hi}$. $Ly6C^{hi}$ monocytes were identified as $CD45^{+}$, $CD11b^{hi}$, $Lin^{-/lo}$, $CD11c^{lo}$ and $Ly6C^{hi}$. Data were acquired on an LSRII flow cytometer (BD Biosciences, Woburn, MA), and the data were analyzed using FlowJo v10.0.7 (Tree Star, Ashland, OR).

Antibody	Vendor
Anti-mouse CD11b (clone M1/70)	BioLegend
Anti-mouse F4/80 (clone BM8)	BioLegend
Anti-mouse CD11c (clone N418)	BioLegend
Anti-mouse CD45 (clone 30-F11)	BioLegend
Anti-mouse Ly6C (clone AL-21)	BD Biosciences
Anti-mouse CD90.2 (clone 53–2.1)	eBioScience
Anti-mouse Ter119 (clone TER119)	eBioScience
Anti-mouse NK1.1 (clone PK136)	eBioScience
Anti-mouse CD49b (clone DX5)	eBioScience

Antibody	Vendor
Anti-mouse CD45R/B220 (clone RA3–6B2)	eBioScience
Anti-mouse Ly6G (clone 1A8)	BioLegend

Radiolabeling of S-HDL

Ready-to-label S-HDL was prepared following a previously described procedure[9] by adding 0.7 weight % of the phospholipid chelator DSPE-DFO[27] to the lipid mix at the expense of DMPC. The resulting nanoparticles were radiolabeled following a previously reported method[9]. Briefly, DFO-bearing S-HDL was reacted with ^{89}Zr-oxalate at a ratio of ~37 MBq/mg APOA1 in phosphate buffered saline (PBS, pH = 6.8–7.1) at 37 °C for 2 hours. [^{89}Zr]-S-HDL was purified by centrifugal filtration using 10 kDa molecular weight cut-off Visvaspin tubes. Radiochemically pure [^{89}Zr]-S-HDL was mixed with unlabeled S-HDL to achieve the desired simvastatin dose, and the mixture was allowed to equilibrate for at least 4 hours.

Fluorescent labeling of S-HDL

For NIRF imaging, DiD-S-HDL was prepared, as previously reported[6,7], by adding DiD to the phopholipid/simvastatin mix at a 1.5% w/w during the lipid film formation process. Finally, DiD-S-HDL was mixed with unlabeled S-HDL to achieve the desired simvastatin dose.

PET/CT imaging, biodistribution and pharmacokinetics in mice

Apoe$^{-/-}$ mice (n=4; 12 weeks on high-fat diet) were injected with [^{89}Zr]-S-HDL (7.0 ± 1.1 MBq, 60 mg simvastatin/kg) in 150–200 µL PBS solution via the lateral tail vein. At 2 and 30 min and 2, 6 and 18 hours, blood (5–10 µL) was sampled from the tail vein and weighed. Radioactivity content was measured using a Wizard^2 2480 automatic gamma counter (Perkin Elmer, Waltham, MA). At 24 hours post administration, animals were anesthetized with isoflurane (Baxter Healthcare, Deerfield, IL)/oxygen gas mixture (2% for induction, 1 % for maintenance), and a scan was then performed using an

Inveon PET/CT scanner (Siemens Healthcare Global, Erlangen, Germany). Whole body PET static scans recording a minimum of 30 million coincident events were performed, with duration of approximately 20 min. The energy and coincidence timing windows were 350–700 keV and 6 ns, respectively. The image data were normalized to correct for non-uniform PET response, dead-time count losses, positron branching ratio and physical decay to the time of injection, but no attenuation, scatter or partial-volume averaging correction was applied. Whole body standard low magnification CT scans were performed with the following acquisition parameters: voltage of 80 kV, current of 500 μA, exposure time of 145 ms per frame and 120 rotational steps for a total of 220 degrees.

After the scan, at 26 h p.i., animals were euthanized and perfused with PBS. Tissues of interest (blood, kidneys, liver, spleen, lungs, heart, brain, aorta and muscle) were collected, blotted and weighed before radioactivity counting on a Wizard^2 2480 automatic gamma counter. Radioactivity values were corrected for decay and normalized to tissue weight to express radioactivity concentration as percentage injected dose per gram (%ID/g).

[^{89}Zr]-S-HDL PET imaging, biodistribution and plaque targeting in rabbits and pigs

[^{89}Zr]-S-HDL was administered via the ear vein to atherosclerotic rabbits (n=2, 20.4 ± 3.1 MBq, 15 mg simvastatin/kg) and pigs (n=2, 142.4 ± 18.3 MBq, 7.5 mg simvastatin/kg) while anesthetized on the bed of a Siemens Biograph mCT PET/CT time-of-flight (TOF) scanner. For the CT scan, iodine contrast (Iopamidol injection 76%, Bracco Diagnostics, Monroe Township, NJ) was injected in rabbits (10 mL, 1 mL/s, no delay) and pigs (70 mL, 1 mL/s, 6 s delay). Whole-body static scans were acquired 0.5, 24 and 48 hours post injection. Before PET acquisition, a CT scan was recorded with the following parameters: voltage, 140 kVp; tube current, 34 mA; exposure time, 1000 ms; slice thickness, 1 mm. The CT scan was used for attenuation correction of the PET data.

In addition to biodistribution imaging by PET/CT, the ability of the nanoimmunotherapeutic to reach and accumulate in atherosclerotic plaques was imaged *in vivo* using PET/MRI. After the 48-hour PET/CT scan, animals were transferred to a Siemens Biograph mMR 3T PET/MRI scanner and imaged using a body matrix coil. After scout scans, a bright-blood, 3D time-of-flight (TOF) non-contrast enhanced angiography sequence was acquired to better localize arterial anatomical landmarks (rabbits: renal arteries and iliac bifurcation, pigs: superficial femoral arteries). Imaging parameters for the rabbit protocol were: TR, 23 ms; TE, 2.83 ms; flip angle 20 degrees; spatial resolution, 0.7×0.7×1 mm^3; acquisition plane, axial; number of slices, 200; number of signal averages, 1, and the parameters for the pig protocol were: TR, 23 ms; TE, 3.69 ms; flip angle 20 degrees; spatial resolution, 1.4×1.4×1.5 mm^3; acquisition plane, axial; number of slices, 228; number of signal averages, 1. Subsequently, the PET scan was initiated simultaneously with a black-blood, 3D T2-weighted SPACE (Sampling Perfection with Application optimized Contrasts using different flip angle Evolution) sequence acquired for vessel wall delineation, with the following imaging parameters for rabbits: TR, 1600 ms; TE, 115 ms; spatial resolution, 0.63×0.63×0.63 mm^3; acquisition plane, sagittal; number of slices, 30; number of signal averages, 4, and the parameters for pigs were: TR, 1200 ms; TE, 112 ms; spatial resolution, 0.63×0.63×0.63 mm^3; acquisition plane, coronal; number of slices, 144; number of signal averages, 4. Attenuation correction of PET images was performed using the built-in MR-based attenuation correction (MR-AC) map, obtained from a two-point Dixon sequence allowing for fat/water separation. Rabbit attenuation maps were segmented into 2 compartments (soft tissue and air), while pigs attenuation maps were segmented into 4 compartments (soft tissue, fat, air and lungs). Shortly after the last scan, animals were euthanized, rabbits were thoroughly perfused with isotonic saline and tissues of interest (liver, spleen, kidney, lung, muscle and artery of interest) were collected for *ex vivo* radioactivity quantification, as described above, near-infrared fluorescence imaging and autoradiography. In both cases, PET images were reconstructed using the ordinary Poisson Ordered subset expectation–maximization (OP-OSEM) algorithm with point-spread function correction. Image analysis was conducted using OsiriX Imaging Software by

drawing regions of interest (ROIs) on the selected tissues (liver, kidneys, spleen for both rabbit and pigs, as well as abdominal aorta – from renal artery to iliac bifurcation – and superficial femoral arteries for rabbit and pigs, respectively). Blood activity was quantified in the left ventricle. Standardized uptake values (SUVs, defined as [Pixel value (Bq/mL) * Weight of the subject (kg) / Dose (Bq)] * 1000 g/kg) were obtained by averaging SUV_{mean} or SUV_{max} values in each ROI drawn on at least five slices of the organ of interest and on all slices of the abdominal aorta (rabbits) and superficial femoral arteries (pigs). Maximal target-to-background (TBR_{max}) values were calculated by dividing average SUV_{max} from the abdominal aorta (rabbits) and superficial femoral arteries (pigs) by average SUV_{max} from muscle in the same animal.

Evaluation of S-HDL treatment efficacy in rabbits and pigs

Rabbits (n=10, weight 3.5 ± 0.3 kg) and pigs (n=8, weight 31.2 ± 5.7 kg) with atherosclerosis were randomized into two groups of five animals, receiving either PBS or S-HDL. The simvastatin dose was 15 and 7.5 mg/kg for rabbits and pigs, respectively. Treatment consisted of four intravenous injections, one every 4 days. Response was evaluated non-invasively and longitudinally using a multiparametric PET/MR imaging protocol (see below). Shortly after the last scan and 30 min prior to euthanasia, Evans blue was injected i.v. for *ex vivo* assessment of vessel wall permeability. Immediately following euthanasia animals were perfused with isotonic saline and tissues of interest (aorta for rabbits, femoral tree for pigs) were collected for *ex vivo* evaluation by near-infrared fluorescence imaging and histological analysis. The femoral tree was thoroughly rinsed in isotonic saline once harvested.

Non-invasive PET/MR imaging evaluation of S-HDL treatment response in rabbits and pigs

A multiparametric PET/MR imaging protocol was implemented to monitor treatment. Twenty-four hours before the first injection, animals underwent a PET/MR imaging session consisting of ^{18}F-FDG-based assessment of plaque inflammation and 3D anatomical MRI using the 3D T2-weighted SPACE sequence described above. The next day, animals had a second PET/MR

imaging session to determine plaque macrophage proliferation with ^{18}F-FLT and vessel wall permeability by 3D dynamic contrast-enhanced (DCE) MRI. DCE-MRI was performed using a 3D motion-sensitized driven equilibrium prepared rapid gradient echo (MERGE) sequence to simultaneously achieve blood pool signal suppression, and signal enhancement in atherosclerotic plaques. 3D DCE-MRI parameters in rabbits were: TR, 491.08 ms; TE, 5.32 ms; flip angle 20 degrees; spatial resolution, 0.63×0.63×0.63 mm^3; acquisition plane, sagittal; number of slices, 20; number of dynamics, 20; number of signal averages, 1; temporal resolution, 31 s, and the parameters for pigs were: TR, 1106.1 ms; TE, 4.3 ms; flip angle 20 degrees; spatial resolution, 0.63×0.63×0.63 mm^3; acquisition plane, coronal; number of slices, 40; number of dynamics, 12; number of signal averages, 1; temporal resolution, 101 s. Dynamic images were acquired before, during and after the injection of 0.2 mmol/Kg of Gd-DTPA (Magnevist, Bayer). The same imaging sessions were performed at the end of treatment, on days 14 and 15 after the first injection. Radiotracers ^{18}F-FDG ($rabbits_{baseline}$: 118.4 ± 17.4 MBq, n=10; $rabbits_{terminal}$: 121.4 ± 16.4 MBq, n=10), ($pigs_{baseline}$: 260.3 ± 14.7 MBq, n=10; $pigs_{terminal}$: 269.5 ± 32.8 MBq, n=10) and ^{18}F-FLT ($rabbits_{baseline}$: 108.8 ± 24.5 MBq, n=10; $rabbits_{terminal}$: 119.4 ± 12.2 MBq, n=10) and ($pigs_{baseline}$: 230.2 ± 34.0 MBq, n=10; $pigs_{terminal}$: 201.7 ± 54.1 MBq, n=10) were administered via the ear vein. For ^{18}F-FDG imaging, animals were fasted for at least 6 hours before the scan, which was performed 2.5 hours (rabbits) and 1 hour (pigs) after administration. ^{18}F-FLT PET scans were performed 2 hours (rabbits) and 1 hour (pigs) post injection with acquisition times of 30 min for each tracer. Both PET imaging sessions were performed on a Siemens mMR 3T PET/MRI scanner using a body matrix coil.

Near-infrared fluorescence imaging

Shortly after euthanasia, perfused tissue samples were placed on thick black paper and imaged on a Xenogen IVIS Spectrum Preclinical Imaging System (Perkin Elmer, Waltham, MA). Fluorescence images were acquired with selected excitation and emission band-pass filters: DiD ($\boldsymbol{\lambda}_{Exc}$ = 640 nm, $\boldsymbol{\lambda}_{Em}$ = 680 nm) and Evans Blue ($\boldsymbol{\lambda}_{Exc}$ = 605, $\boldsymbol{\lambda}_{Em}$ = 680 nm). Exposure time for each image was 4 s. Data were processed and analyzed using Living Image

software (Perkin Elmer) by drawing a region of interest around the arteries of interest and quantified as radiant efficiency.

Autoradiography

Following euthanasia, animals were perfused and their aortas (mice and rabbits) or femoral arteries (pigs) were excised and blotted. To determine radiotracer distribution, digital autoradiography was performed by placing tissue samples in a film cassette against a phosphorimaging plate (BASMS-2325, Fujifilm, Valhalla, NY) for 2 hours (mouse aortas) or 48 hours (rabbit aortas, pig femoral arteries) at −20 °C. Phosphorimaging plates were read at a pixel resolution of 25 μm with a Typhoon 7000IP plate reader (GE Healthcare, Pittsburgh, PA). Quantification was carried out using ImageJ software.

Histology and immunohistochemistry

Tissue samples from mice, rabbits and pigs were placed in paraformaldehyde overnight and subsequently embedded in paraffin. Sections were taken from the aortic arch in mice, from the abdominal aorta of rabbits, and from the abdominal aorta just proximal to the iliac bifurcation and from the largest palpable plaque in the right femoral artery in pigs. Samples were cut in 5-μm sections, mounted on slides and stained with Hematoxylin & Eosin (rabbits), Masson trichrome (mice, rabbits and pigs), CD68 (mice) and RAM-11(rabbits) according to standard protocols.

Blood tests in pigs

Blood was collected by vena puncture from all pigs at the end of the study. Serum was sent to IDEXX Laboratories (Totowa, NJ) and analyzed using an Olympus AU400 Chemistry Analyzer. Whole blood was collected in EDTA-containing tubes and analyzed using an IDEXX procyte DX Hematology Analyzer for complete blood count analysis.

Statistics

Data are presented as mean ± SD, unless otherwise stated. Mann-Whitney tests were used to assess group differences. In the therapeutic study in rabbits and pigs, a linear mixed model (LMM) was used to statistically analyze differences in imaging-derived parameters between treatment groups. The imaging parameter at the end of the study (terminal scan) was used as the dependent variable. Type of treatment and imaging parameter at the start of the study (baseline) were defined as fixed effects, and the side (left or right femoral artery in pigs) as a random effect. For all tests, $\alpha < 0.05$ represents statistical significance. Statistical analyses were performed with GraphPad Prism®, Version 6.0c (La Jolla, CA).

Acknowledgments

Funding: This work was supported by the National Institutes of Health grants R01 EB009638, P01 HL131478 (Z.A.F.); R01 HL125703, R01 HL118440 (W.J.M.M.); P30 CA008748; the American Heart Association 16SDG31390007 (C.P.M.); the Netherlands Organization for Scientific Research NWO Vidi (W.J.M.M) and ZonMW Veni 016156059 (R.D.); the Danish Council for Independent Research DFF-1333-00235A (T.B.); the Danish Cancer Society R71-A4285 (T.B.); and the Rigshospitalets Research Foundation (T.B.). The authors also thank the Center for Molecular Imaging and Nanotechnology (CMINT) for financial support (T.R.).

References

1.Wilhelm S, Tavares AJ, Dai Q, Ohta S, Audet J, Dvorak HF, Chan WCW, Analysis of nanoparticle delivery to tumours, Nat. Rev. Mater 1, 16014 (2016).

2.Lameijer M, Binderup T, van Leent MMT, Senders ML, Fay F, Malkus J, Sanchez-Gaytan BL, Teunissen AJP, Karakatsanis N, Robson P, Zhou X, Ye Y, Wojtkiewicz G, Tang J, Seijkens TTP, Kroon J, Stroes ESG, Kjaer A, Ochando J, Reiner T, Pérez-Medina C, Calcagno C, Fischer EA, Zhang B, Temel RE, Swirski FK, Nahrendorf M, Fayad ZA, Lutgens E, Mulder WJM, Duivenvoorden R, Efficacy and safety assessment of a TRAF6-targeted nanoimmunotherapy in atherosclerotic mice and non-human primates, Nat. Biomed. Eng 2, 279–292 (2018).

3.Duivenvoorden R, Senders ML, van Leent MMT, Pérez-Medina C, Nahrendorf M, Fayad ZA, Mulder WJM, Nanoimmunotherapy to treat ischaemic heart disease, Nat. Rev. Cardiol 16, 21–32 (2019).

4.Braza MS, van Leent MMT, Lameijer M, Sanchez-Gaytan BL, Arts RJW, Pérez-Medina C, Conde P, Garcia MR, Gonzalez-Perez M, Brahmachary M, Fay F, Kluza E, Kossatz S, Dress RJ, Salem F, Rialdi A, Reiner T, Boros P, Strijkers GJ, Calcagno CC, Ginhoux F, Marazzi I, Lutgens E, Nicolaes GAF, Weber C, Swirski FK, Nahrendorf M, Fisher EA, Duivenvoorden R, Fayad ZA, Netea MG, Mulder WJM, Ochando J, Inhibiting Inflammation with Myeloid Cell-Specific Nanobiologics Promotes Organ Transplant Acceptance, Immunity 49, 819–828.e6 (2018).

5.Bird L, Targeting trained immunity, Nat. Rev. Immunol 19, 2–3 (2018).

6.Duivenvoorden R, Tang J, Cormode DP, Mieszawska AJ, Izquierdo-Garcia D, Ozcan C, Otten MJ, Zaidi N, Lobatto ME, van Rijs SM, Priem B, Kuan EL, Martel C, Hewing B, Sager H, Nahrendorf M, Randolph GJ, Stroes ESG, Fuster V, a Fisher E, a Fayad Z, Mulder WJM, A statin-loaded reconstituted high-density lipoprotein nanoparticle inhibits atherosclerotic plaque inflammation., Nat. Commun 5, 3065 (2014).

7.Tang J, Lobatto ME, Hassing L, van der Staay S, van Rijs SM, Calcagno C, Braza MS, Baxter S, Fay F, Sanchez-Gaytan BL, Duivenvoorden R, Sager HB, Astudillo YM, Leong W, Ramachandran S, Storm G, Pérez-Medina C, Reiner T, Cormode DP, Strijkers GJ, Stroes ESG, Swirski FK, Nahrendorf M, Fisher EA, Fayad ZA, Mulder WJM, Inhibiting macrophage proliferation suppresses atherosclerotic plaque inflammation, Sci. Adv 1 (2015).

8.Sanhai WR, Sakamoto JH, Canady R, Ferrari M, Seven challenges for nanomedicine, Nat. Nanotechnol 3, 242–244 (2008).

9.Pérez-Medina C, Tang J, Abdel-Atti D, Hogstad B, Merad M, Fisher EA, Fayad

ZA, Lewis JS, Mulder WJM, Reiner T, PET imaging of tumor-associated macrophages with 89Zr-labeled high-density lipoprotein nanoparticles, J. Nucl. Med 56, 1272–1277 (2015).

10. https://www.fda.gov/downloads/Drugs/Guidances/UCM078932.pdf.

11.Pérez-Medina C, Binderup T, Lobatto ME, Tang J, Calcagno C, Giesen L, Wessel CH, Witjes J, Ishino S, Baxter S, Zhao Y, Ramachandran S, Eldib M, Sánchez-Gaytán BL, Robson PM, Bini J, Granada JF, Fish KM, Stroes ESG, Duivenvoorden R, Tsimikas S, Lewis JS, Reiner T, Fuster V, Kjær A, Fisher EA, Fayad ZA, Mulder WJM, In Vivo PET Imaging of HDL in Multiple Atherosclerosis Models, JACC Cardiovasc. Imaging 9, 950–961 (2016).

12.Ventola CL, Progress in Nanomedicine: Approved and Investigational Nanodrugs., P T 42, 742–755 (2017).

13.Fayad ZA, Mani V, Woodward M, Kallend D, Abt M, Burgess T, Fuster V, Ballantyne CM, Stein EA, Tardif J-C, Rudd JHF, Farkouh ME, Tawakol A, dal-PLAQUE Investigators, Safety and efficacy of dalcetrapib on atherosclerotic disease using novel non-invasive multimodality imaging (dal-PLAQUE): a randomised clinical trial, Lancet 378, 1547–1559 (2011).

14.Alaarg A, Senders ML, Varela-Moreira A, Pérez-Medina C, Zhao Y, Tang J, Fay F, Reiner T, Fayad ZA, Hennink WE, Metselaar JM, Mulder WJM, Storm G, A systematic comparison of clinically viable nanomedicines targeting HMG-CoA reductase in inflammatory atherosclerosis, J. Control. Release 262, 47–57 (2017).

15.Ridker PM, Everett BM, Thuren T, MacFadyen JG, Chang WH, Ballantyne C, Fonseca F, Nicolau J, Koenig W, Anker SD, Kastelein JJP, Cornel JH, Pais P, Pella D, Genest J, Cifkova R, Lorenzatti A, Forster T, Kobalava Z, Vida-Simiti L, Flather M, Shimokawa H, Ogawa H, Dellborg M, Rossi PRF, Troquay RPT, Libby P, Glynn RJ, Antiinflammatory Therapy with Canakinumab for Atherosclerotic Disease, N. Engl. J. Med 377, 1119–1131 (2017).

16.Folco EJ, Sheikine Y, Rocha VZ, Christen T, Shvartz E, Sukhova GK, Di Carli MF, Libby P, Hypoxia But Not Inflammation Augments Glucose Uptake in Human Macrophages, J. Am. Coll. Cardiol 58, 603–614 (2011).

17.Zamanian-Daryoush M, Lindner D, Tallant TC, Wang Z, Buffa J, Klipfell E, Parker Y, Hatala D, Parsons-Wingerter P, Rayman P, Yusufishaq MSS, Fisher EA, Smith JD, Finke J, DiDonato JA, Hazen SL, The cardioprotective protein apolipoprotein A1 promotes potent anti-tumorigenic effects, J. Biol. Chem 288, 21237–52 (2013).

18.Holland JP, Sheh Y, Lewis JS, Standardized methods for the production of high specific-activity zirconium-89., Nucl. Med. Biol 36, 729–39 (2009).

19.Kolb HC, Padgett HC, Zigler S, Patanella J, Mu F, Gangadharmath UB, Mocharla VP, Scott PJH, Walsh JC, in Radiochemical Syntheses, (John Wiley & Sons, Inc., Hoboken, NJ, USA, 2012), pp. 21–30.

20.Shao X, Hoareau R, Hockley B, Modification of fluorine-18 synthesis modules to enable cGMP synthesis of radiopharmaceuticals using multiple radiochemical strategies, J. Nucl. Med 51, s2, 1453 (2010).

21.Plump AS, Smith JD, Hayek T, Aalto-Setälä K, Walsh A, Verstuyft JG, Rubin EM, Breslow JL, Severe hypercholesterolemia and atherosclerosis in apolipoprotein E-deficient mice created by homologous recombination in ES cells., Cell 71, 343–53 (1992).

22.Nakashima Y, Plump AS, Raines EW, Breslow JL, Ross R, ApoE-deficient mice develop lesions of all phases of atherosclerosis throughout the arterial tree., Arterioscler. Thromb 14, 133–40 (1994).

23.Lobatto ME, Calcagno C, Metselaar JM, Storm G, Stroes ESG, Fayad ZA, Mulder WJM, in Methods in enzymology, (2012), vol. 508, pp. 211–228.

24.Senders ML, Lobatto ME, Soler R, Lairez O, Pérez-Medina C, Calcagno C, Fayad ZA, Mulder WJM, Fay F, in Methods in molecular biology (Clifton, N.J.), (2018), vol. 1816, pp. 385–400. =

25.Granada JF, Milewski K, Zhao H, Stankus JJ, Tellez A, Aboodi MS, Kaluza GL, Krueger CG, Virmani R, Schwartz LB, Nikanorov A, Vascular response to zotarolimus-coated balloons in injured superficial femoral arteries of the familial hypercholesterolemic Swine., Circ. Cardiovasc. Interv 4, 447–55 (2011).

26.Kim Y, Fay F, Cormode DP, Sanchez-Gaytan BL, Tang J, Hennessy EJ, Ma M, Moore K, Farokhzad OC, Fisher EA, Mulder WJM, Langer R, Fayad ZA, Single Step Reconstitution of Multifunctional High-Density Lipoprotein-Derived Nanomaterials Using Microfluidics, ACS Nano 7, 9975–9983 (2013).

27.Pérez-Medina C, Abdel-Atti D, Zhang Y, Longo VA, Irwin CP, Binderup T, Ruiz-Cabello J, Fayad ZA, Lewis JS, Mulder WJM, Reiner T, A modular labeling strategy for in vivo PET and near-infrared fluorescence imaging of nanoparticle tumor targeting, J. Nucl. Med 55, 1706–1711 (2014).

Supplemental materials

Table S1. Composition and size of different S-HDL batches prepared for this study. *Based on simvastatin

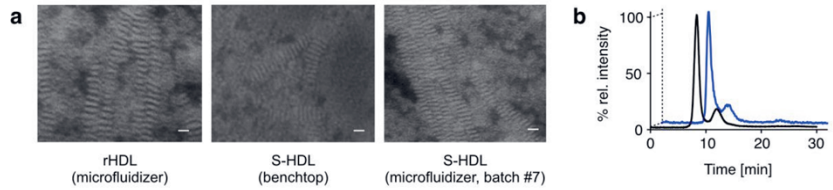


Figure S1. A) Representative transmission electron microscopy (TEM) images of reconstituted high-density lipoprotein (rHDL, left), benchtop-produced simvastatin-HDL (S-HDL, middle) and microfluidizer-produced S-HDL (right). Scale bar = 10 nm. B) HPLC size exclusion chromatograms demonstrating co-elution of [^{89}Zr]-S-HDL (blue trace, radioactivity signal) and unlabeled S-HDL (black trace, UV absorption at 220 nm).

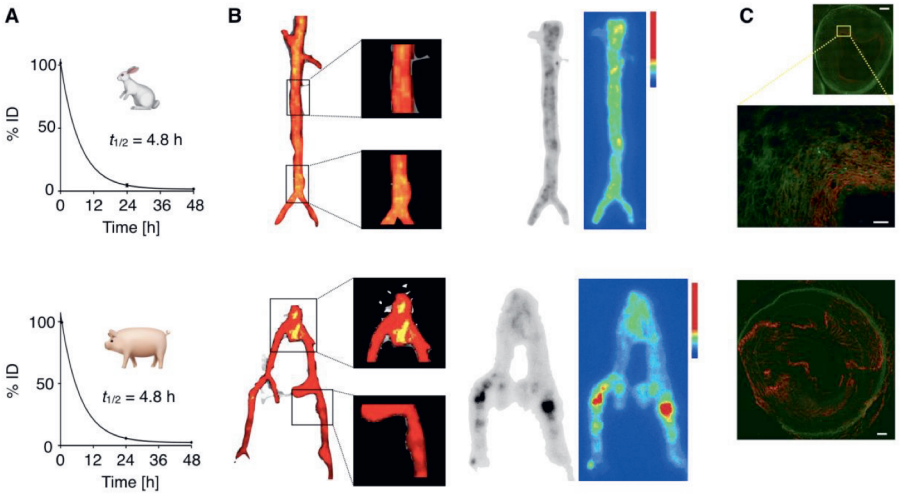


Figure S2. A) Blood time–activity curve for [^{89}Zr]-S-HDL in rabbits (top, n=2) and pigs (bottom, n=2) with atherosclerosis. B) Representative Evans Blue near-infrared fluorescence imaging (left) and [^{89}Zr]-S-HDL autoradiography (right) performed on arterial samples from one rabbit (abdominal aorta, top) and one pig (femoral artery tree, bottom). C) Representative fluorescence microscopy images of arterial sections from one rabbit (top) and one pig (bottom) injected with DiD-S-HDL.

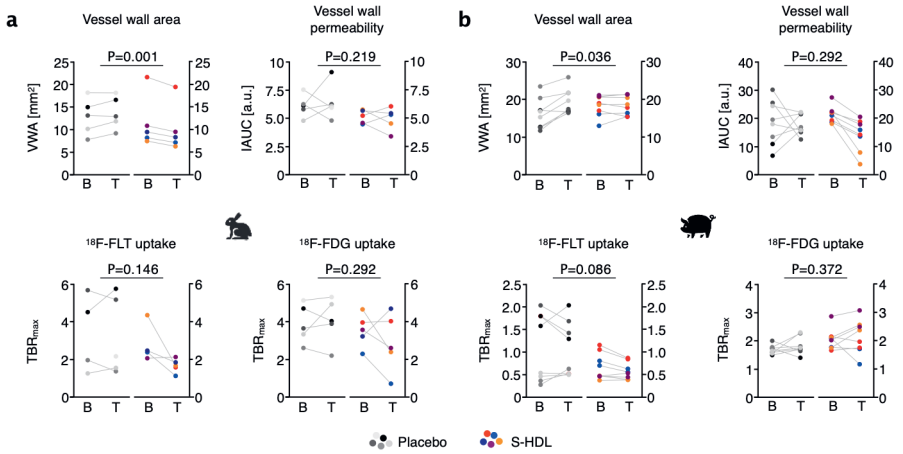


Figure S3. A) Variation in the monitored parameters in rabbits treated with PBS (Placebo, red dots) or S-HDL (blue dots) between baseline (B) and terminal (T) scans. B) Variation in the monitored parameters in pigs treated with PBS (Placebo) or S-HDL between baseline (B) and terminal (T) scans. Dots are color-coded for individual animals. Two data points are represented per pig, corresponding to each of the femoral arteries. P values were calculated using the linear mixed model described in the manuscript. VWA = vessel wall area; IAUC = intensity area under the curve; TBR = target-to-background ratio.

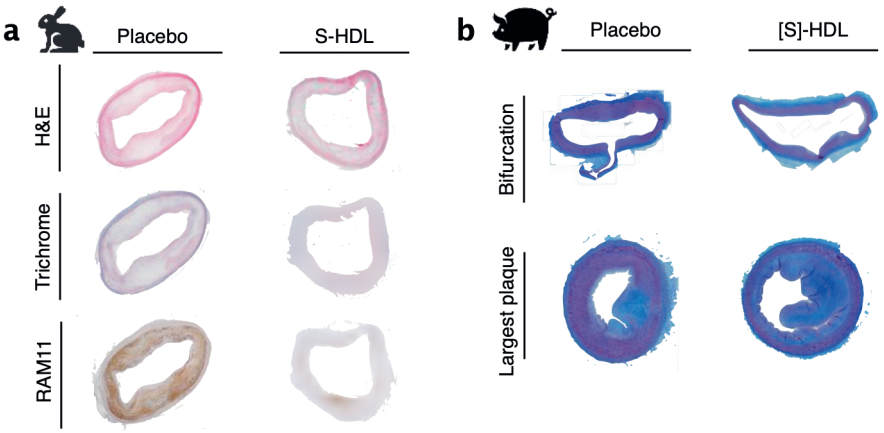


Figure S4. A) Rabbit aortic sections stained with hematoxylin & eosin (H&E, top), Masson trichrome (middle) and RAM11 (macrophages, bottom) from animals treated with PBS (Placebo) or S-HDL. B) Porcine femoral artery sections (right) stained with Masson trichrome from animals treated with PBS (Placebo) or S-HDL. Sections were taken from the iliac bifurcation (top) and largest plaque in the femoral artery (bottom) of the same pig.

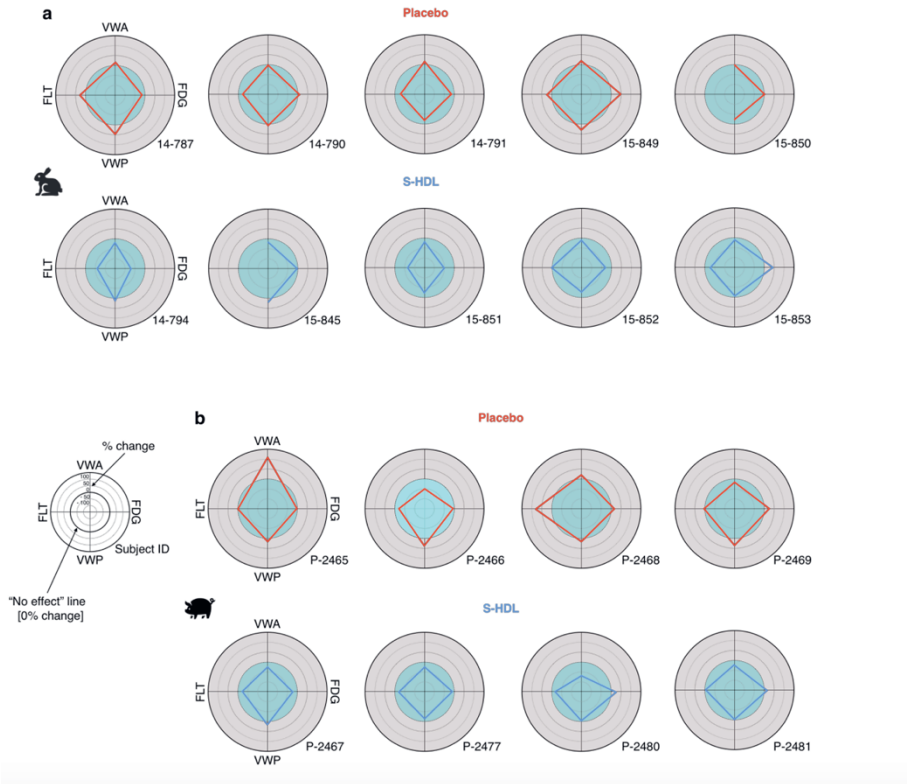


Fig. S5. A) Combined representation of the variation in the monitored parameters in individual rabbits treated with PBS (Placebo, top) or S-HDL (bottom), expressed as % change between baseline and terminal scans. B) Combined representation of the variation in the monitored parameters in individual pigs treated with PBS (Placebo, top) or S-HDL (bottom), expressed as % change between baseline and terminal scans. For FDG and FLT, data represent variation in TBR_{max}; VWA = vessel wall area; VWP = vessel wall permeability.



9

Epilogue

Epilogue

Targeting immune cells for disease and inflammation imaging

In drug development, particularly within immunotherapy, molecular imaging enables the non-invasive monitoring of immunological processes at a whole-systems level[1,2]. Conventional static and *ex vivo* readouts, such as plasma drug concentrations, histological and immunological methods, as well as tissue biopsies, capture only isolated snapshots of complex biological events[3–5]. Consequently, they miss the dynamic, spatial, and systemic dimensions of inflammation that are essential for determining disease trajectories and therapeutic responses.

Molecular imaging is an *in vivo* method that overcomes these limitations. It can detect the earliest pathogenic events, often before irreversible structural or anatomical changes occur[6], by interrogating the mechanistic processes that drive disease. Simultaneously, it provides a longitudinal window into both local and systemic effects[2,7]. This potential is exemplified by the first whole-body ^{89}Zr-atezolizumab PET imaging of PD-L1 conducted by Bensch et al[8]. In that study, pre-treatment whole-body PET imaging revealed that tracer uptake in lymphoid tissues, tumor lesions, and inflamed sites correlated more strongly with clinical responses than conventional biopsy-based PD-L1 immunohistochemistry or RNA-sequencing biomarkers. Similarly, another group demonstrated the use of ^{18}F-DCFPyL PET to track the accumulation of CD19 CAR-T cells in the bone marrow and tumor sites[9]. The tissue distribution observed via PET diverged significantly from CAR-T cell counts in peripheral blood, confirming that standard blood monitoring yields an incomplete picture of therapeutic engagement.

While these examples clearly illustrate advances in the field of immune checkpoint inhibitors and CAR-T cell-directed therapies, substantial opportunities are upstream of the adaptive immune system. Myeloid cell activation is a shared pathogenic component across a diverse range of diseases[10], rendering it a compelling target for both therapeutic intervention and molecular imaging. Nanomedicine is uniquely positioned to engage this

upstream biology; it can target hematopoietic stem and progenitor cells (HSPCs) and mature myeloid cells within primary and secondary lymphoid organs, such as the bone marrow and spleen[11]. However, realizing this potential necessitates concurrent, quantitative imaging readouts.

Current and emerging tools for inflammation imaging

Tracers that report on innate immune cells and their progenitors are of particular clinical interest. Myeloid cells act as first responders, amplifiers, and resolution mediators across various disease stages[12]. Their high phagocytic activity and residence in hematopoietic organs render them readily accessible to imaging probes[13]. Furthermore, as they are key drivers of multi-tissue systemic inflammation[10], they constitute high-value imaging targets.

Despite this promise, the availability of such molecular imaging tools remains limited. Although initially developed for and mostly applied for cancer diagnosis and staging, ^{18}F-FDG PET currently can be considered the clinical gold standard for inflammation imaging[14]. Its strengths lie in its high sensitivity, and the presence of standardized protocols[15], all of which have established it as the *de facto* benchmark throughout this thesis. Yet, despite its affinity for neutrophils and activated macrophages, ^{18}F-FDG is fundamentally non-specific; it accumulates in the brain, skeletal muscle, myocardium, and other metabolically active cells[16,17]. This off-target uptake generates a high physiological background and necessitates logistically demanding patient preparation protocols. Alternatively, TSPO ligands that target a translocator protein upregulated in activated macrophages, suffer from multi-cellular expression and genotype-dependent binding affinities. These factors confound quantification and preclude clean, cell-resolved inflammation imaging[18–20].

To address these limitations, this thesis evaluates radiotracers designed to surmount current constraints. In **Chapter II**, a side-by-side comparison with ^{18}F-FDG demonstrated that the radiolabeled somatostatin-receptor 2 (SST2) ligand DOTATATE is a robust candidate for imaging inflammation in cardiovascular disease. Because SST2 is preferentially expressed on M1-like

macrophages[21], DOTATATE yielded a macrophage-selective signal with significantly cleaner background and markedly lower physiological myocardial uptake than ^{18}F-FDG. Together, these two tracers capture complementary aspects of inflammation: ^{18}F-FDG reports on global metabolic activation across multiple leukocyte populations, whereas DOTATATE specifically measures macrophage-associated inflammatory burden.

Beyond small-molecule tracers, nanoparticle-based probes capitalize on the intrinsic phagocytic activity of myeloid cells[13]. As demonstrated in this work, ^{64}Cu-Macrin and ^{19}F-HDL target macrophage-rich tissues and hematopoietic organs, while successfully minimizing off-target deposition. By engaging highly conserved lipid metabolism and transport pathways[22], these nanotracers achieved consistent hematopoietic organ biodistribution and macrophage targeting reliably across species, underscoring their strong translational potential.

An alternative and elegant approach is presented in **Chapter V** using an apolipoprotein A-I mimetic tracer. This peptide-based probe spontaneously assembles into nanoparticles *in vivo* by associating with endogenous lipoproteins, thereby harnessing the same phagocyte-nanoparticle axis without the need for pre-formed particles.

Macrophage molecular imaging as a tool for monitoring therapeutic response

Beyond their application in the descriptive mapping of pathological inflammation, molecular imaging of macrophages and their progeny (monocytes and HSPCs) can be deployed to monitor therapeutic responses[13]. This capability is particularly valuable within the rapidly evolving field of nanomedicine[23]. The complex behavior of nanotherapeutics cannot be reliably predicted from bulk pharmacokinetics alone. Incomplete knowledge regarding nanoparticle biodistribution, immune cell interactions, and organ-level kinetics remains a significant barrier to clinical translation[24]. Whole-body

molecular imaging directly addresses these gaps by revealing how nanotherapies engage immune cells over time, facilitating longitudinal studies and cross-species comparisons[23]. Macrophage burden-based imaging platforms are of distinct interest because many nanotherapies rely on macrophage uptake as their primary biological interface[25].

A key strength of this approach is its capacity to capture both the functional consequences of ongoing inflammation and its modulation by the treatment. For instance, in organ-specific diseases such as ARDS, we demonstrated that routine ^{18}F-FDG imaging can track not only the localized inflammatory response in the lungs but also its systemic ramifications, namely the consequences of circulating cytokines, myeloid cell mobilization, and bone marrow activation. Consequently, inflammation centered in a single organ can becomes detectable within the hematopoietic compartment. This reflects a coordinated systemic immune response, a mechanistic insight that is indispensable for nanotherapies engineered for delivery to bone marrow, spleen, and other immune reservoirs. Similarly, in the preclinical PET study of simvastatin-HDL (S-HDL) nanoparticles presented in **Chapter VIII**, tracer uptake in macrophage-rich atherosclerotic plaques enabled the non-invasive assessment of nanoparticle delivery and therapeutic engagement directly within the inflamed vascular wall.

Therefore, macrophage-specific PET imaging tracers can be deployed to refine novel immune interventions by monitoring macrophage burden and tracking therapeutic responses in real time. These attributes position macrophage PET not merely as a nice research tool, but as a prospective routine component of preclinical nanotherapy validation and early-phase clinical trials.

The added value of multiparametric imaging approaches

When ^{18}F-FDG data proves to be insufficient or insensitive to subtle biological shifts, complementary imaging modalities become valuable. Because single tracers inevitably collapse complex biology into a single signal[26], this thesis demonstrates how multiparametric immunoimaging can instead disentangle

the layered dynamics of tissue injury and repair. As presented herein, a combination of ^{18}F-FDG and ^{18}F-FLT PET, DCE MRI, and T2-weighted MRI for assessing vessel wall thickness enabled the longitudinal monitoring of S-HDL treatment in atherosclerotic animal models. Even with the small group sizes available for that study, subtle biological changes were successfully identified using this multiparametric approach.

Furthermore, in myocardial infarct models, we demonstrated that integrating MRI, routinely used clinically to evaluate infarct size, microvascular obstruction, and scar formation, with ^{18}F-FDG, ^{18}F-FLT, CCR2, and CD11b-nanobody PET successfully resolved distinct facets of tissue injury and the immune landscape. Beyond the metabolic insights provided by ^{18}F-FDG, ^{18}F-FLT PET yielded an upstream proliferative signal, reporting on biological activity independent of gross anatomical damage[27]. This data was complemented by CCR2 PET, which provided readouts on monocyte recruitment to the injured tissue[28], and CD11b-nanobody PET, which highlighted general myeloid cell involvement in the inflammatory response[29]. Together, these probes transition the focus from global inflammatory activation to lineage-specific cellular recruitment and accumulation, accurately reconstructing the complex inflammatory cascade that follows an infarction.

Concluding remarks and future directions

In summary, the molecular imaging of macrophages can be used to quantify inflammatory burden, track temporal dynamics, and assess both the pharmacodynamics and efficacy of therapeutics, thereby advancing basic immunology and translational medicine alike. Despite the inherent limitation of small sample sizes in large animal cohorts, our imaging findings proved reproducible across different species – an essential requisite for clinical translation.

The integration of complementary tracer combinations (e.g., ^{18}F-FDG with CCR2 or CD11b nanobodies) has demonstrably enhanced our biological insight. In the future, patients may benefit from standardized "immune

imaging panels", analogous to routine laboratory blood panels, in which a curated assortment of tracers is administered to generate multidimensional immune profiling. Such an approach could significantly refine clinical diagnosis, patient stratification, and therapy guidance.

Nevertheless, macrophage specificity remains imperfect. Many current probes exploit features shared across a broader range of cells, such as phagocytic capacity, metabolic activation, and receptor upregulation[28]. Consequently, these tracers still exhibit uptake in other myeloid compartments, including dendritic cells and neutrophils. This off-target overlap is particularly relevant in inflammatory lesions where mixed leukocyte populations coexist[30]. Therefore, future probe development must prioritize greater phenotypic resolution, enabling the distinction between inflammatory, resident, and reparative macrophage subsets.

Moreover, the next essential step is the robust translation of these novel tracers into patient cohorts. Ultimately, prospective human studies must be designed to evaluate whether such imaging data can directly inform clinical decision-making, such as guiding the intensification or de-escalation of anti-inflammatory therapies. Only then will macrophage molecular imaging evolve from a powerful preclinical research instrument into a foundational, routine component of precision medicine.

References

1. Yu, J. & Gao, B. Molecular imaging for cancer immunotherapy. *iRADIOLOGY* 1, 3–17 (2023).
2. Patel, N., Bergstrom, M., Murphy, P. S. & Maynard, J. PET in the characterization of immune diseases and development of therapeutics. *Oxf. Open Immunol.* 6, (2025).
3. Mansfield, A. S. *et al.* Heterogeneity of Programmed Cell Death Ligand 1 Expression in Multifocal Lung Cancer. *Clinical Cancer Research* 22, 2177–2182 (2016).
4. Xing, X. *et al.* Positron emission tomography molecular imaging to monitor anti-tumor systemic response for immune checkpoint inhibitor therapy. *Eur. J. Nucl. Med. Mol. Imaging* 50, 1671–1688 (2023).
5. Zhang, D. *et al.* Special Section on Pharmacokinetic and Drug Metabolism Properties of Novel Therapeutic Modalities–Minireview. *Drug Metabolism and Disposition* 47, 1122–1135 (2019).
6. Signore, A. *et al.* Current Status of Molecular Imaging in Inflammatory and Autoimmune Disorders. *Curr. Pharm. Des.* 24, 743–753 (2018).
7. Dorward, D. A., Lucas, C. D., Rossi, A. G., Haslett, C. & Dhaliwal, K. Imaging inflammation: Molecular strategies to visualize key components of the inflammatory cascade, from initiation to resolution. *Pharmacol. Ther.* 135, 182–199 (2012).
8. Bensch, F. *et al.* 89Zr-atezolizumab imaging as a non-invasive approach to assess clinical response to PD-L1 blockade in cancer. *Nat. Med.* 24, 1852–1858 (2018).
9. Minn, I. *et al.* Imaging CAR T cell therapy with PSMA-targeted positron emission tomography. *Sci. Adv.* 5, (2019).
10. Swann, J. W., Olson, O. C. & Passegué, E. Made to order: emergency myelopoiesis and demand-adapted innate immune cell production. *Nat. Rev. Immunol.* 24, 596–613 (2024).
11. van Leent, M. M. T. *et al.* Regulating trained immunity with nanomedicine. *Nat. Rev. Mater.* 7, 465–481 (2022).
12. Xia, W., Singh, N., Goel, S. & Shi, S. Molecular imaging of innate immunity and immunotherapy. *Adv. Drug Deliv. Rev.* 198, 114865 (2023).
13. Weissleder, R., Nahrendorf, M. & Pittet, M. J. Imaging macrophages with nanoparticles. *Nature Materials* vol. 13 125–138 Preprint at https://doi.org/10.1038/nmat3780 (2014).
14. Casali, M. *et al.* State of the art of 18F-FDG PET/CT application in inflammation and infection: a guide for image acquisition and interpretation. *Clin. Transl. Imaging* 9, 299–339 (2021).
15. Abikhzer, G. *et al.* EANM/SNMMI guideline/procedure standard for [18F]FDG hybrid PET use in infection and inflammation in adults v2.0. *Eur. J. Nucl. Med. Mol. Imaging* 52, 510–538 (2025).
16. Kreissl, M. C. *et al.* Influence of dietary state and insulin on myocardial, skeletal muscle and

brain [18F]-fluorodeoxyglucose kinetics in mice. *EJNMMI Res.* 1, 8 (2011).
17. Mbakaza, O. & Vangu, M.-D.-T. W. 18F-FDG PET/CT Imaging: Normal Variants, Pitfalls, and Artifacts Musculoskeletal, Infection, and Inflammation. *Frontiers in Nuclear Medicine* 2, (2022).
18. Jain, P. *et al.* Neuroinflammation PET Imaging: Current Opinion and Future Directions. *Journal of Nuclear Medicine* 61, 1107–1112 (2020).
19. Berroterán-Infante, N., Tadić, M., Hacker, M., Wadsak, W. & Mitterhauser, M. Binding Affinity of Some Endogenous and Synthetic TSPO Ligands Regarding the rs6971 Polymorphism. *Int. J. Mol. Sci.* 20, 563 (2019).
20. Kreisl, W. C. *et al.* A Genetic Polymorphism for Translocator Protein 18 Kda Affects both *in Vitro* and *in Vivo* Radioligand Binding in Human Brain to this Putative Biomarker of Neuroinflammation. *Journal of Cerebral Blood Flow & Metabolism* 33, 53–58 (2013).
21. Tarkin, J. M. *et al.* Detection of Atherosclerotic Inflammation by 68Ga-DOTATATE PET Compared to [18F]FDG PET Imaging. *J. Am. Coll. Cardiol.* 69, 1774–1791 (2017).
22. Van der Horst, D. J., Roosendaal, S. D. & Rodenburg, K. W. Circulatory lipid transport: lipoprotein assembly and function from an evolutionary perspective. *Mol. Cell. Biochem.* 326, 105–119 (2009).
23. Bernal, A., Calcagno, C., Mulder, W. J. M. & Pérez-Medina, C. Imaging-guided nanomedicine development. *Curr. Opin. Chem. Biol.* 63, 78–85 (2021).
24. Pérez-Medina, C., Teunissen, A. J. P., Kluza, E., Mulder, W. J. M. & van der Meel, R. Nuclear imaging approaches facilitating nanomedicine translation. *Adv. Drug Deliv. Rev.* 154–155, 123–141 (2020).
25. Gustafson, H. H., Holt-Casper, D., Grainger, D. W. & Ghandehari, H. Nanoparticle uptake: The phagocyte problem. *Nano Today* 10, 487–510 (2015).
26. Pratt, E. C. *et al.* Simultaneous quantitative imaging of two PET radiotracers via the detection of positron–electron annihilation and prompt gamma emissions. *Nat. Biomed. Eng.* 7, 1028–1039 (2023).
27. Peck, M. *et al.* Applications of PET imaging with the proliferation marker [18F]-FLT. *The quarterly journal of nuclear medicine and molecular imaging : official publication of the Italian Association of Nuclear Medicine (AIMN) [and] the International Association of Radiopharmacology (IAR), [and] Section of the Society of...* 59, 95–104 (2015).
28. Iking, J. *et al.* Imaging Inflammation with Positron Emission Tomography. *Biomedicines* 9, 212 (2021).
29. Rashidian, M. *et al.* Noninvasive imaging of immune responses. *Proc. Natl. Acad. Sci. U. S. A.* 112, 6146–6151 (2015).
30. Fullerton, J. N. & Gilroy, D. W. Resolution of inflammation: a new therapeutic frontier. *Nat. Rev. Drug Discov.* 15, 551–567 (2016).



10

Appendices

Summary

In **Chapter II**, DOTATATE was thoroughly evaluated as a diagnostic probe for cardiovascular inflammation. Its affinity for the somatostatin receptor type 2, which is abundantly expressed in macrophages, makes it a promising PET tracer for macrophage imaging. DOTATATE was compared side-by-side with the gold standard, ^{18}F-FDG, in preclinical models of atherosclerosis and myocardial infarction. The performance of both tracers was investigated utilizing *in vivo* SUV measurements, *ex vivo* gamma counting, flow cytometric analyses, and near-infrared imaging of macrophage burden. Finally, the potential of DOTATATE to either replace or complement ^{18}F-FDG in clinical and preclinical settings was discussed.

In **Chapter III**, we further investigated the use of immune-targeted tracers in the context of cardiovascular disease imaging, employing a diverse range of probes to non-invasively map myocardial infarct inflammation. Preclinical animal models of transient and permanent coronary occlusion were deployed and evaluated in parallel. We assessed cardiac function (MRI) and viability (FDG PET), bone marrow cell proliferation (FLT PET), metabolic activity in hematopoietic organs (FDG PET), immune cell influx and egression (CD11b nanobody PET, CCR2 PET and ^{18}F-MRI), as well as atherogenic plaque burden and inflammation (histology and flow cytometry).

In **Chapter IV**, we characterized a cell-specific, nanoparticle-based tracer to track macrophage dynamics. This probe was validated across both large and small animal models of inflammation, encompassing myocardial infarction, atherosclerosis, and pneumonia. The *in vivo* imaging data were thoroughly corroborated by flow cytometry and histological analyses.

Capitalizing on the macrophage-avidity of HDL, in **Chapter V** we labeled Apolipoprotein A1-mimetic with ^{89}Zr, developing a novel tracer for inflammation imaging in mouse models of myocardial infarction and cancer. The affinity of ^{89}Zr-ApoA1-mimetic probe for lipoproteins and its *in vivo* behavior were rigorously validated through *in vitro* and *in vivo* assays. The

tracer's biodistribution mirrored that of endogenous ApoA1 and HDL, accumulating heavily in the tumors of melanoma-bearing mice and the ischemic myocardium of infarcted animals. Macrophage-specific uptake was conclusively confirmed by CyTOF analyses.

Building upon these findings, we deployed ^{19}F-HDL and ^{89}Zr-^{19}F-HDL to comprehensively dissect systemic myeloid cell dynamics following a myocardial infarction. These data are discussed in **Chapter VI**, where multimodal approaches were harnessed to image myeloid cells in atherosclerotic and infarcted animals. We observed the timed egression of cells from the spleen and bone marrow to the damaged tissues. *Ex vivo* assays confirmed myeloid cell accumulation in atherosclerotic plaques and infarcted myocardium following the ischemic event, with imaging readouts strongly supported by flow cytometry and autoradiography.

Chapter VII explores the potential of a nanobiologic mTOR-inhibitor to tame dysregulated inflammation. First, sc-RNA sequencing analysis of a COVID-19 patient database underscored the critical role of mTOR in inflammatory pathways. Subsequently, myeloid cell-specific mTORi nanobiologics were evaluated in *in vitro* and *in vivo* models of inflammation. The mTORi nanobiologics efficiently reduced inflammatory cytokine production and dampened hematopoietic cell metabolism, demonstrating significant potential as a therapeutic strategy for innate immune cell hyperinflammation.

Finally, we present our efforts to overcome the clinical translation barriers associated with nanobiologics. In **Chapter VIII**, we scaled up the production of a nanoimmunotherapeutic drug for the treatment of atherosclerosis (S-HDL) and leveraged a comprehensive array of clinical imaging modalities to assess its *in vivo* behavior and therapeutic efficacy in large animals. We observed a marked reduction in systemic inflammation and the halting of atherosclerotic plaque progression in these cohorts, successfully establishing a proof-of-concept for clinical advancement of this targeted nanotherapy.

Nederlandse samenvatting

In **Hoofdstuk II** werd DOTATATE uitvoerig geëvalueerd als diagnostische probe voor cardiovasculaire ontsteking. Zijn affiniteit voor de somatostatine-receptor subtype 2, overvloedig aanwezig op macrofagen, maakt het een veelbelovende PET-tracer voor macrofaagbeeldvorming. DOTATATE werd zij-aan-zij vergeleken met de gouden standaard ^{18}F-FDG in preklinische modellen van atherosclerose en myocardinfarct. De prestaties van beide tracers werden onderzocht met in vivo SUV-metingen, *ex vivo* gamma-telling, flowcytometrische analyses en nabij-infraroodbeeldvorming van de macrofaagbelasting. Het potentieel van DOTATATE om ^{18}F-FDG te vervangen of aan te vullen werd besproken.

In **Hoofdstuk III** onderzochten we verder het gebruik van immuun-gebaseerde tracers in de context van cardiovasculaire ziektebeeldvorming verder. We gebruikten een breed scala aan tracers om myocardinfarctontsteking grondig niet-invasief in kaart te brengen. Preklinische diermodellen van tijdelijke en permanente occlusie werden naast elkaar ingezet en geëvalueerd ten aanzien van cardiale functie (MRI) en weefselschade (FDG PET), beenmergceldeling (FLT PET), metabole activiteit in hematopoëtische organen (FDG PET), immuuncelinflux en -egressie (CD11b nanobody PET, CCR2 PET en ^{18}F-MRI), atherogene plaque-belasting en ontsteking (histologie en flowcytometrie).

In **Hoofdstuk IV** karakteriseerden we een celspecifieke, nanodeeltjesgebaseerde tracer om macrofaagdynamiek te volgen en valideerden we deze in grote en kleine diermodellen van ontsteking, waaronder myocardinfarct, atherosclerose, sepsis en hart- en longontsteking. Deze gegevens werden gevalideerd met flowcytometrie en histologische analyse.

Gebruikmakend van de macrofaag-affiniteit van HDL, labelden we in **Hoofdstuk V** een ApoA-I-mimetica met ^{89}Zr en ontwikkelden zo een tracer

voor ontstekingsbeeldvorming in muismodellen van myocardinfarct en kanker. De affiniteit van de ^{89}Zr-ApoA-I-mimetica voor lipoproteïnen en het *in vivo*-gedrag werden zowel *in vitro* als *in vivo* gevalideerd. De tracer-biodistributie leek op die van ApoA1 en HDL, en vertoonde ook opname in tumoren van melanoomdragende muizen evenals in ischemisch myocard van geïnfarceerde dieren. Macrofaagopname werd bevestigd met CyTOF-analyses.

In lijn met deze bevindingen zetten we ook ^{19}F-HDL en ^{89}Zr-19F-HDL in om de systemische myeloïde celdynamiek na myocardinfarct uitgebreid te ontleden. Dit onderzoek wordt besproken in **Hoofdstuk VI**, waar multimodale analyses werden ingezet om myeloïde cellen in atherosclerotische en geïnfarceerde dieren in kaart te brengen. We observeerden getimede cel-egress uit milt en beenmerg naar het beschadigde weefsel. *Ex vivo*-assays toonden ophoping van myeloïde cellen in atherosclerotische plaques en geïnfarceerd myocard na een ischemisch voorval. De data werden ondersteund door flowcytometrie en autoradiografie-metingen.

Hoofdstuk VII verkent het potentieel van nanobiologic-mTOR-remming om gedysreguleerde ontsteking te temperen. Ten eerste toonde sc-RNA sequencing analyse het belang van mTOR in inflammatoire signaalroutes, gebruikmakend van materiaal uit een COVID-19-patiënten-database. Vervolgens werden myeloïde celspecifieke mTORi-nanobiologics ingezet in *in vitro*- en *in vivo*-modellen van ontsteking. mTORi-nanobiologics verminderden efficiënt de productie van pro-inflammatoire cytokinen en het metabolisme van hematopoëtische cellen, wat veelbelovend is als therapeutische strategie tegen hyperinflammatie van het aangeboren immuunsysteem.

Tot slot presenteren we ons werk om klinische vertaalslagen van nanobiologics te bewerkstellingen. In **Hoofdstuk VIII** schalen we de productie op van een nano-immunotherapeutisch middel voor de behandeling van atherosclerose (S-HDL) en benutten we een uitgebreid

pakket klinische beeldvormingsmodaliteiten om het *in vivo*-gedrag en de therapeutische respons in grote dieren te bestuderen. We observeerden vermindering van ontsteking en stilstand van atherosclerotische plaqueprogressie in deze dieren, waarmee een proof-of-concept voor klinische vooruitgang werd geleverd.

Curriculum vitae



Yohana Camila Toner was born on 18 February 1993 in Curitiba, Paraná, Brazil. After completing her secondary education at the Military Police School of Paraná, she earned a bachelor's degree in Biomedicine from the Federal University of Paraná, with an emphasis on Molecular Biology. During her undergraduate studies, she worked as an intern in Cell Biology and Microscopy at the Oswaldo Cruz Foundation (FIOCRUZ), where she researched the phagocytic mechanisms of parasitic trypanosomatids, receiving a distinction award for best trainee project in 2012.

During her studies, she received a Science Without Borders scholarship to undertake a one-year exchange program at KU Leuven in Belgium. There, she attended master's-level courses at both the Faculty of Bioscience Engineering and the Faculty of Pharmaceutical Sciences. She also worked at the Molecular Imaging Institute (moSAIC) at the Universitaire Ziekenhuizen KU Leuven, where she contributed to preclinical imaging studies.

After obtaining her bachelor's degree in 2015, she continued working at FIOCRUZ as a microscopy technician. In 2016, Yohana moved to New York City to work at Mount Sinai Hospital as a Research Associate in a CRISPR engineering laboratory. One year later, she joined Prof. Dr. Willem Mulder's Nanomedicine and Translational Imaging Lab as a Lab Manager and Senior Research Associate.

Under Prof. Dr. Mulder's supervision, Yohana developed her PhD trajectory in preclinical inflammation imaging, conducting her work across Eindhoven University of Technology and Radboud University Medical Center. She currently works as a Lab Manager and preclinical microsurgeon in Prof. Dr. Mulder's group at Radboud University Medical Center.

List of publications

1. Trines MM, Hoorn D, Hofstraat SRJ, Zwolsman RC, Anbergen T, Versteeg I, van Elsas Y, Deckers J, Hendrikx MMA, Kleuskens T, Darwish YB, Ros GWB, Dijkstra SF, Priem B, Timmers M, Fransen PM, Pouderoijen MJ, de Waal BFM, Meijer EW, Beldman TJ, **Toner YC**, Kluza E, Mulder WJM, Janssen HM, van der Meel R. Dendrimers Improve Apolipoprotein Nanoparticle mRNA Delivery to Immune Cells. Adv Mater. 2026 Jan;38(3):e04830. doi: 10.1002/adma.202504830. Epub 2025 Sep 12. PMID: 40937965; PMCID: PMC12801360.

2. Priem B, Willemsen L, Anbergen T, van Elsas Y, Deckers J, Schrijver DP, Hofstraat SRJ, Messing IV, Munitz J, Honing D, Prévot G, **Toner YC**, Morla J, Wang W, Ranzenigo A, Sirchia I, Post T, Duivenvoorden R, Kluza E, Cremers GAO, Kreijtz JHCM, Pérez-Medina C, van Leent MMT, Teunissen AJP, van der Meel R, Zhou Y, Glass C, Ochando J, Joosten LAB, Fayad ZA, Netea-Maier RT, Netea MG, de Winther MPJ, Beldman TJ, Griffioen AW, Mulder WJM. Systemically inducing trained immunity overcomes solid tumors' immunosuppressive microenvironment. Sci Adv. 2026 Jan 2;12(1):eadu0292. doi: 10.1126/sciadv.adu0292. Epub 2026 Jan 1. PMID: 41477842; PMCID: PMC12757067.

3. de Dreu A, de Bruin K, Hokke AM, Schrijver DP, Beelen DNH, Verhalle LM, Clavijo Perez MC, Anbergen T, Versteeg I, Maas R, Zwolsman RC, Grao-Roldán C, Bartelet B, Trines MM, Hoorn D, Ros G, **Toner YC**, Kluza E, Beldman T, Pérez-Medina C, Netea MG, Merkx M, van der Meel R, Mulder WJM. Engineering Fusion Proteins for Nanomedicine-Based Cytokine Therapy. Bioconjug Chem. 2025 Jul 11. doi: 10.1021/acs.bioconjchem.5c00182. Epub ahead of print. PMID: 40644562.

4. **Toner YC**, Munitz J, Prevot G, Morla-Folch J, Wang W, van Elsas Y, Priem B, Deckers J, Anbergen T, Beldman TJ, Brechbühl EES, Aksu MD, Ziogas A, Sarlea SA, Ozturk M, Zhang Z, Li W, Li Y, Maier A, Fernandes JC, Cremers GAO, van Genabeek B, Kreijtz JHCM, Lutgens E, Riksen NP, Janssen HM, Söntjens SHM, Hoeben FJM, Kluza E, Singh G, Giamarellos-Bourboulis EJ, Schotsaert M, Duivenvoorden R, van der Meel R, Joosten LAB, Cai L, Temel RE, Fayad ZA, Mhlanga MM, van Leent MMT, Teunissen AJP, Netea MG, Mulder WJM. Targeting mTOR in myeloid cells prevents infection-associated inflammation. iScience. 2025 Mar 4;28(4):112163. doi: 10.1016/j.isci.2025.112163. PMID: 40177636; PMCID: PMC11964677.

5. Hofstraat SRJ*, Anbergen T*, Zwolsman R*, Deckers J, van Elsas Y, Trines MM, Versteeg I, Hoorn D, Ros GWB, Bartelet BM, Hendrikx MMA, Darwish YB, Kleuskens T, Borges F, Maas RJF, Verhalle LM, Tielemans W, Vader P, de Jong OG, Tabaglio T, Wee DKB, Teunissen AJP, Brechbühl E, Janssen HM, Fransen PM, de Dreu A, Schrijver DP, Priem B, **Toner YC**, Beldman TJ, Netea MG, Mulder WJM, Kluza E, van der Meel R. Nature-inspired platform nanotechnology for RNA delivery to myeloid cells and their bone marrow progenitors. Nat Nanotechnol. 2025 Apr;20(4):532-542. doi: 10.1038/s41565-024-01847-3. Epub 2025 Feb 3. PMID: 39900620; PMCID: PMC12014499.

6. Wauters AC*, Scheerstra JF*, van Leent MMT*, Teunissen AJP*, Priem B, Beldman TJ, Rother N, Duivenvoorden R, Prévot G, Munitz J, **Toner YC**, Deckers J, van Elsas Y, Mora-Raimundo P, Chen G, Nauta SA, Verschuur AVD, Griffioen AW, Schrijver DP, Anbergen T, Li Y, Wu H, Mason AF, van Stevendaal MHME, Kluza E, Post RAJ, Joosten LAB, Netea MG, Calcagno C, Fayad ZA, van der Meel R, Schroeder A, Abdelmohsen LKEA, Mulder WJM, van Hest JCM. Polymersomes with splenic avidity target red pulp myeloid cells for cancer immunotherapy. Nat Nanotechnol. 2024 Nov;19(11):1735-

1744. doi: 10.1038/s41565-024-01727-w. Epub 2024 Jul 31. PMID: 39085390; PMCID: PMC11567884.

7. **Toner YC***, Prévot G*, van Leent MMT, Munitz J, Oosterwijk R, Verschuur AVD, van Elsas Y, Peric V, Maas RJF, Ranzenigo A, Morla-Folch J, Wang W, Umali M, de Dreu A, Fernandes JC, Sullivan NAT, Maier A, Mason C, Reiner T, Fayad ZA, Mulder WJM, Teunissen AJP, Pérez-Medina C. Macrophage PET imaging in mouse models of cardiovascular disease and cancer with an apolipoprotein-inspired radiotracer. Npj Imaging. 2024;2(1):12. doi: 10.1038/s44303-024-00009-3. Epub 2024 May 15. PMID: 38765879; PMCID: PMC11096117.

8. Schrijver DP*, Röring RJ*, Deckers J, de Dreu A, **Toner YC**, Prevot G, Priem B, Munitz J, Nugraha EG, van Elsas Y, Azzun A, Anbergen T, Groh LA, Becker AMD, Pérez-Medina C, Oosterwijk RS, Novakovic B, Moorlag SJCFM, Jansen A, Pickkers P, Kox M, Beldman TJ, Kluza E, van Leent MMT, Teunissen AJP, van der Meel R, Fayad ZA, Joosten LAB, Fisher EA, Merkx M, Netea MG, Mulder WJM. Resolving sepsis-induced immunoparalysis via trained immunity by targeting interleukin-4 to myeloid cells. Nat Biomed Eng. 2023 Sep;7(9):1097-1112. doi: 10.1038/s41551-023-01050-0. Epub 2023 Jun 8. PMID: 37291433; PMCID: PMC10504080.

9. Maier A, **Toner YC**, Munitz J, Sullivan NAT, Sakurai K, Meerwaldt AE, Brechbühl EES, Prévot G, van Elsas Y, Maas RJF, Ranzenigo A, Soultanidis G, Rashidian M, Pérez-Medina C, Heo GS, Gropler RJ, Liu Y, Reiner T, Nahrendorf M, Swirski FK, Strijkers GJ, Teunissen AJP, Calcagno C, Fayad ZA, Mulder WJM, van Leent MMT. Multiparametric Immunoimaging Maps Inflammatory Signatures in Murine Myocardial Infarction Models. JACC Basic Transl Sci. 2023 Apr 5;8(7):801-816. doi: 10.1016/j.jacbts.2022.12.014. PMID: 37547068; PMCID: PMC10401290.

10. Meerwaldt AE, Straathof M, Oosterveld W, van Heijningen CL, van Leent MM, **Toner YC**, Munitz J, Teunissen AJ, Daemen CC, van der Toorn A, van Vliet G, van Tilborg GA, De Feyter HM, de Graaf RA, Hol EM, Mulder WJ, Dijkhuizen RM. *In vivo* imaging of cerebral glucose metabolism informs on subacute to chronic post-stroke tissue status - A pilot study combining PET and deuterium metabolic imaging. J Cereb Blood Flow Metab. 2023 May;43(5):778-790. doi: 10.1177/0271678X221148970. Epub 2023 Jan 6. PMID: 36606595; PMCID: PMC10108187.

11. Deckers J*, Anbergen T*, Hokke AM*, de Dreu A, Schrijver DP, de Bruin K, **Toner YC**, Beldman TJ, Spangler JB, de Greef TFA, Grisoni F, van der Meel R, Joosten LAB, Merkx M, Netea MG, Mulder WJM. Engineering cytokine therapeutics. Nat Rev Bioeng. 2023;1(4):286-303. doi: 10.1038/s44222-023-00030-y. Epub 2023 Feb 16. PMID: 37064653; PMCID: PMC9933837.

12. **Toner YC***, Ghotbi AA*, Naidu S, Sakurai K, van Leent MMT, Jordan S, Ordikhani F, Amadori L, Sofias AM, Fisher EL, Maier A, Sullivan N, Munitz J, Senders ML, Mason C, Reiner T, Soultanidis G, Tarkin JM, Rudd JHF, Giannarelli C, Ochando J, Pérez-Medina C, Kjaer A, Mulder WJM, Fayad ZA, Calcagno C. Systematically evaluating DOTATATE and FDG as PET immuno-imaging tracers of cardiovascular inflammation. Sci Rep. 2022 Apr 13;12(1):6185. doi: 10.1038/s41598-022-09590-2. PMID: 35418569; PMCID: PMC9007951.

13. Teunissen AJP, Abousaway OB, Munitz J, van Leent MMT, **Toner YC**, Priem B, Senders ML, Pérez-Medina C, Mulder WJM, Rashidian M. Employing nanobodies for immune landscape profiling by PET imaging in mice. STAR Protoc. 2021 Apr 5;2(2):100434. doi: 10.1016/j.xpro.2021.100434. PMID: 33899016; PMCID: PMC8056265.

14. van Leent MMT, Beldman TJ, **Toner YC**, Lameijer MA, Rother N, Bekkering S, Teunissen AJP, Zhou X, van der Meel R, Malkus J, Nauta SA, Klein ED, Fay F, Sanchez-Gaytan BL, Pérez-Medina C, Kluza E, Ye YX, Wojtkiewicz G, Fisher EA, Swirski FK, Nahrendorf M, Zhang B, Li Y, Zhang B, Joosten LAB, Pasterkamp G, Boltjes A, Fayad ZA, Lutgens E, Netea MG, Riksen NP, Mulder WJM, Duivenvoorden R. Prosaposin mediates inflammation in atherosclerosis. Sci Transl Med. 2021 Mar 10;13(584):eabe1433. doi: 10.1126/scitranslmed.abe1433. PMID: 33692130; PMCID: PMC8209679.

15. van Leent MMT, Meerwaldt AE, Berchouchi A, **Toner YC**, Burnett ME, Klein ED, Verschuur AVD, Nauta SA, Munitz J, Prévot G, van Leeuwen EM, Ordikhani F, Mourits VP, Calcagno C, Robson PM, Soultanidis G, Reiner T, Joosten RRM, Friedrich H, Madsen JC, Kluza E, van der Meel R, Joosten LAB, Netea MG, Ochando J, Fayad ZA, Pérez-Medina C, Mulder WJM, Teunissen AJP. A modular approach toward producing nanotherapeutics targeting the innate immune system. Sci Adv. 2021 Mar 5;7(10):eabe7853. doi: 10.1126/sciadv.abe7853. PMID: 33674313; PMCID: PMC7935355.

16. Panizzi P, Krohn-Grimberghe M, Keliher E, Ye YX, Grune J, Frodermann V, Sun Y, Muse CG, Bushey K, Iwamoto Y, van Leent MMT, Meerwaldt A, **Toner YC**, Munitz J, Maier A, Soultanidis G, Calcagno C, Pérez-Medina C, Carlucci G, Riddell KP, Barney S, Horne G, Anderson B, Maddur-Appajaiah A, Verhamme IM, Bock PE, Wojtkiewicz GR, Courties G, Swirski FK, Church WR, Walz PH, Tillson DM, Mulder WJM, Nahrendorf M. Multimodal imaging of bacterial-host interface in mice and piglets with *Staphylococcus aureus* endocarditis. Sci Transl Med. 2020 Nov 4;12(568):eaay2104. doi: 10.1126/scitranslmed.aay2104. PMID: 33148623; PMCID: PMC7818516.

17. Poels K*, van Leent MMT*, Boutros C, Tissot H, Roy S, Meerwaldt AE, **Toner YCA**, Reiche ME, Kusters PJH, Malinova T, Huveneers S,

Kaufman AE, Mani V, Fayad ZA, de Winther MPJ, Marabelle A, Mulder WJM, Robert C, Seijkens TTP, Lutgens E. Immune Checkpoint Inhibitor Therapy Aggravates T Cell-Driven Plaque Inflammation in Atherosclerosis. JACC CardioOncol. 2020 Oct 6;2(4):599-610. doi: 10.1016/j.jaccao.2020.08.007. PMID: 34396271; PMCID: PMC8352210.

18. Priem B, van Leent MMT, Teunissen AJP, Sofias AM, Mourits VP, Willemsen L, Klein ED, Oosterwijk RS, Meerwaldt AE, Munitz J, Prévot G, Vera Verschuur A, Nauta SA, van Leeuwen EM, Fisher EL, de Jong KAM, Zhao Y, **Toner YC**, Soultanidis G, Calcagno C, Bomans PHH, Friedrich H, Sommerdijk N, Reiner T, Duivenvoorden R, Zupančič E, Di Martino JS, Kluza E, Rashidian M, Ploegh HL, Dijkhuizen RM, Hak S, Pérez-Medina C, Bravo-Cordero JJ, de Winther MPJ, Joosten LAB, van Elsas A, Fayad ZA, Rialdi A, Torre D, Guccione E, Ochando J, Netea MG, Griffioen AW, Mulder WJM. Trained Immunity-Promoting Nanobiologic Therapy Suppresses Tumor Growth and Potentiates Checkpoint Inhibition. Cell. 2020 Oct 29;183(3):786-801.e19. doi: 10.1016/j.cell.2020.09.059. PMID: 33125893; PMCID: PMC8074872.

19. Nahrendorf M*, Hoyer FF*, Meerwaldt AE, van Leent MMT, Senders ML, Calcagno C, Robson PM, Soultanidis G, Pérez-Medina C, Teunissen AJP, **Toner YC**, Ishikawa K, Fish K, Sakurai K, van Leeuwen EM, Klein ED, Sofias AM, Reiner T, Rohde D, Aguirre AD, Wojtkiewicz G, Schmidt S, Iwamoto Y, Izquierdo-Garcia D, Caravan P, Swirski FK, Weissleder R, Mulder WJM. Imaging Cardiovascular and Lung Macrophages With the Positron Emission Tomography Sensor ^{64}Cu-Macrin in Mice, Rabbits, and Pigs. Circ Cardiovasc Imaging. 2020 Oct;13(10):e010586. doi: 10.1161/CIRCIMAGING.120.010586. Epub 2020 Oct 20. PMID: 33076700; PMCID: PMC7583675.

20. Sofias AM, **Toner YC**, Meerwaldt AE, van Leent MMT, Soultanidis G, Elschot M, Gonai H, Grendstad K, Flobak Å, Neckmann U,

Wolowczyk C, Fisher EL, Reiner T, Davies CL, Bjørkøy G, Teunissen AJP, Ochando J, Pérez-Medina C, Mulder WJM, Hak S. Tumor Targeting by $\alpha_v\beta_3$-Integrin-Specific Lipid Nanoparticles Occurs *via* Phagocyte Hitchhiking. ACS Nano. 2020 Jul 28;14(7):7832-7846. doi: 10.1021/acsnano.9b08693. Epub 2020 May 20. PMID: 32413260; PMCID: PMC7392528.

21. Senders ML, Meerwaldt AE, van Leent MMT, Sanchez-Gaytan BL, van de Voort JC, **Toner YC**, Maier A, Klein ED, Sullivan NAT, Sofias AM, Groenen H, Faries C, Oosterwijk RS, van Leeuwen EM, Fay F, Chepurko E, Reiner T, Duivenvoorden R, Zangi L, Dijkhuizen RM, Hak S, Swirski FK, Nahrendorf M, Pérez-Medina C, Teunissen AJP, Fayad ZA, Calcagno C, Strijkers GJ, Mulder WJM. Probing myeloid cell dynamics in ischaemic heart disease by nanotracer hot-spot imaging. Nat Nanotechnol. 2020 May;15(5):398-405. doi: 10.1038/s41565-020-0642-4. Epub 2020 Apr 20. PMID: 32313216; PMCID: PMC7416336.

22. Binderup T*, Duivenvoorden R*, Fay F*, van Leent MMT, Malkus J, Baxter S, Ishino S, Zhao Y, Sanchez-Gaytan B, Teunissen AJP, **Frederico YCA**, Tang J, Carlucci G, Lyashchenko S, Calcagno C, Karakatsanis N, Soultanidis G, Senders ML, Robson PM, Mani V, Ramachandran S, Lobatto ME, Hutten BA, Granada JF, Reiner T, Swirski FK, Nahrendorf M, Kjaer A, Fisher EA, Fayad ZA, Pérez-Medina C, Mulder WJM. Imaging-assisted nanoimmunotherapy for atherosclerosis in multiple species. Sci Transl Med. 2019 Aug 21;11(506):eaaw7736. doi: 10.1126/scitranslmed.aaw7736. PMID: 31434756; PMCID: PMC7328283.

23. Kalb LC, **Frederico YC**, Boehm C, Moreira CM, Soares MJ, Field MC. Conservation and divergence within the clathrin interactome of Trypanosoma cruzi. Sci Rep. 2016 Aug 9;6:31212. doi: 10.1038/srep31212. PMID: 27502971; PMCID: PMC4977521.

24. Kalb LC, **Frederico YC**, Batista CM, Eger I, Fragoso SP, Soares MJ. Clathrin expression in Trypanosoma cruzi. BMC Cell Biol. 2014 Jun 19;15:23. doi: 10.1186/1471-2121-15-23. PMID: 24947310; PMCID: PMC4073184.

* These authors contributed equally

Dankword

In my view, the dankwoord of a PhD thesis is just as meaningful as the thesis itself. Many people have dedicated countless hours of their lives to make it all come together, directly or indirectly. That is also where all the nice feelings come into play.

My deepest gratitude goes to **God**. I always made plans, but His plans were far greater. Each and every piece of my story was put together in an orchestrated way so that I could be here today. Even in my wildest dreams, I could not have pictured a better reality for myself; it has surpassed my expectations. Therefore, I am grateful for all the closed doors and hurdles along the way, because they brought me to where I am now. I am genuinely happy with the end result: You knew better than I did, and I am thankful for that. But most importantly, I am grateful for the following people who crossed my path along the way:

Dear **Willem**, this dankwoord to you is the central piece of this thesis. I would hate to fall short of your worth at the very last moment! And just like in our conversations, I promise to keep it heavily unprofessional, and not entirely free of sentiment.
As I write this, a tourbillon of thoughts rushes through my mind and it could not be any different, because, in fairness, you are a storm. But amid your whirlwind, I have found stillness. I feel so lucky to have (almost accidentally) climbed my way into the Mulder Lab pack and to have become your "secret weapon" (a title I remain disproportionately proud of). More than a boss, you became my confidant, my "best male Dutch friend" (as I often describe you to my friends) and something of a Dutch dad, for those in the know. I embrace this opportunity to thank you for the important stuff: for fighting for this promotie, for your priceless supervision, and for introducing me to the wonders of the Kuilart. But I also want to thank you for the actual important stuff: for supporting me through dark days, for being confrontational in ways I could never be, for packing me in your suitcase when you moved to the

Netherlands, and for listening to every unsolicited detail of my personal life (deep down, I know you have fun listening to my crazy extracurricular endeavors).
To quote you, "our brains work in very different ways". But I love the way our differences make us such a power duo, and how remarkably productive our unprofessionalism can be. To me, that is the best part. We certainly do not conform to prescribed molds to maximize efficiency, but we have always managed to freestyle our way forward. Perhaps that is why your leadership works: beneath all the chaos, you foster the kind of loyalty and safety that gives people the confidence to truly thrive.
I hope one day you understand that your utmost loyalty to your people and your profound care for those around you don't go unnoticed; both are reflected in every aspect of our work. You are not an ordinary boss, and I would not have it any other way. At the end of the day, there is comfort in knowing that the storm is on your side.

Dear **Roy**, we are two columns of the same structure. Despite our different roles and positions, I feel like you, too, carry the same loyalty and sense of purpose in helping to keep the Mulder group standing. I see how much you care about our team, and I am thankful that you are there to support us. When I think about you, I remember the numerous times I reached out for help, and you made everything seem easy and smooth. Thank you for that, for our "let-it-out" talks, and for our traditional whisky at the Mulder Lab retreat. It meant more to me than you can imagine.

To the members of the doctoral committee: **Dr. Middeldorp**, **Dr. Bulte**, **Dr. Lopata**, and **Dr. Albertazzi**. Considering your busy schedules, I know that it takes effort to make time for this PhD defense. Thank you for reading my thesis and for the questions you have raised. **Saskia**, I genuinely admire your strength in leading the Internal Medicine Department with diplomacy and drive. Your leadership skills have my utmost respect. **Jeff**, I am very thankful for the opportunity I had to present at the WMIC in Alaska. You are a true legend in the field, and I feel privileged to have you in my committee. **Richard** and **Lorenzo**, although we have never met in person, I am honored that you

have accepted our invitation to be on my committee. Thank you for contributing with your expertise and for the thoughtful consideration you have given to this work.

Queridos pais, **Marco** e **Valéria**, vocês foram a base de tudo isso. Desde as noites em claro (nunca fui um bebê exemplar) até as aulas extracurriculares que a mãe preparava com tanto carinho. Vocês sempre estiveram presentes a cada conquista e não mediram esforços para garantir que eu tivesse o suporte necessário para brilhar. Além disso, vocês sempre tiveram muito orgulho de mim, o que me ajudou a acreditar no meu potencial: na mente de vocês, eu era "fora de série" e, em todos os momentos, isso me motivou a trabalhar para ser a filha que vocês acreditavam ter. Nunca tive dúvidas do seu amor por mim, e essa confiança foi inestimável em minha jornada. Mas um mero parágrafo nesta tese jamais daria conta da minha lista de agradecimentos a vocês, que cresce a cada ano. Ainda hoje, quando a coisa aperta, é pra vocês que eu corro – seja por um coração partido, um problema técnico com o carro, um pedido de oração ou um problema burocrático. Obrigada também por todos os sacrifícios ao longo dessa trajetória. Sacrifícios imensos investindo no meu futuro. Sei que as oportunidades que eu tive nesta vida tiveram um alto custo, financeiro ou pessoal. Incluindo a minha ausência, que, nesse caso, foi o preço da minha felicidade. Sei que vocês sentem a minha falta, mas saibam que tudo o que conquistei foi resultado da semente que vocês plantaram. Vocês investiram mais tempo nessa tese do que todos nós. Portanto, a vocês dedico este trabalho e a minha gratidão.

À minha avó **Wanda**, que, desde criança me encheu de mimos e palavras de afirmação. Sou muito grata por todo o tempo e amor investidos em mim. Lembro-me das visitas, quando você me levava ao parque de diversões no shopping em São Paulo, e lembro-me do nosso "quality time" na Flórida todas as vezes em que eu ia aos Estados Unidos – e das prateleiras cheias de todos os snacks e comidinhas que eu gosto e dos presentes que você guardava pra mim ao longo dos meses. Muito obrigada também pelas longas ligações de desabafo e pelo apoio incondicional. To my aunts Vania, Vera

and Andrea: we all know I would not be here without you. You have been very present in my life since my childhood. You have supported my journey not only emotionally but also financially. Thank you for literally paying for my education, music courses, sports classes, vacations and relocations to other countries. But thank you just as much for every phone call you picked up, for every "desabafo" session and for countless hours of fun we had together. **Vania**, the prodigy daughter, thank you for everything I learned from you and for always being excited to share a bit of your wisdom with me. You are such an adventurous person, a true inspiration to others. You are so adventurous that you ended up moving your entire family to the US, and I am grateful for that. Our reality would have been very different had you not done that. **Vera**, I do not think you will ever comprehend how special you are to me and how much of a difference you made in my life. I owe you a multitude of my dearest memories and some of the happiest moments I have ever had. I also know that you opened doors to many opportunities that ultimately led me here. **Andrea**, minha tia cool, some of the best days of my childhood were the ones when we went to São Paulo to visit you. I would even say that we have continued that tradition to this day - whether I visit you, we meet in Europe or we travel together in the US. You, too, made this all possible by investing in me, believing in me and keeping me alive at times.

À família Frederico, **tia Roze**, **tio Pedro**, **tio Paulo**, **tia Sonia**, **tio Eliezi**, **tia Cati**, **Sula**, **Álvaro**, **Aurelio**, **Martinha**, **Cris**, **Mauro**, **Claudinho**, **Eli**, **Eros**, **Andressa**, **Brunna**, **Hudson**, **Abner**, **Fernanda**, **Guilherme**, **Poly**, **Narah**, **Robert**, **Jean**, **Milena**, **Eduardo**, **Carol**, **Thiago**, **Mariana**, **Fernando**, **Paola**, **Pedro**, **Pablo**, **Janine**, **Pedrinho**, **Paulinho**, **Fernanda**, **Adrian**, **Rafael**, **Daniel**, **Rejane**, **Karine**, **Dora**, **Sebastiao** e **Ana** (*in memoriam*), que sempre me rodearam de muito amor. Sempre que nos encontramos, vem aquele sentimento quentinho de carinho e de acolhimento. Eu tive o privilégio de fazer parte de uma família unida e ativa. Os momentos que tivemos na chácara dos meus avós e nos churrascos de final de semana moram no meu coração. Fui abençoada com tios que me veem como extensão da própria família, primos com os quais pude conviver e compartilhar experiências e até mesmo primos de segundo grau e agregados que chegaram por último.

Com vocês, construí não apenas boas memórias, mas também vínculos e raízes que jamais serão rompidos. Mesmo distante, sinto-me parte do nosso clã. Muito obrigada pelo alicerce que vocês são na minha vida e por sempre me receberem como se eu nunca tivesse partido.

To my home away from home: Brenda, Fernanda, Natasha(o), Nina, and Renato(a). **Brenda**, my dear paranymph, I will always admire your ability to self-reflect and always improve. I aspire to one day be able to evolve and reinvent myself the way you do. Thank you for being someone I could count on, for infinite hours of listening, and for your irreplaceable friendship. I could list hundreds of situations in which you came through for me. In fact, it is possible that I hypothetically have that list hidden somewhere in my phone (which would hypothetically include cute birthday movies, rides to the hospital, celebratory cakes, company when my heart got broken, and casual stuff like spontaneous meals together). We've been through a lifetime of events together and we learned so much along the way. Thank you for walking alongside me on this journey and for the times you completely left your comfort zone to rescue me. **Nina**, my dear paranymph, you are my tag team for life. At this point I feel that our connection is so strong that it is almost in the physical realm. You are my "casca de bala", my Meredith Grey: from ski trips to karaoke, from Oktoberfest to terrasjes, from the Olympics to the World Cup. Damn, we truly live our best lives! And let's not forget the Vierdaagse. Our Vierdaagse team stories would be enough for a whole chapter of this thesis. But our friendship goes far beyond that. You have been the voice of reason, the "reality check", a shoulder to cry on, and one of the first people I want to call when I have good news. Thank you for living a life that always seems to run short on time, just to make sure we are all taken care of. You truly ground me in ways nobody can. P.S.: I am also thankful for your mom, **Berenice**. **Fernanda**, you are probably one of the funniest people I have ever met. But who you are goes far beyond that. You are a role model. The love you show for those around you and the way you care deeply for your friends will always inspire me. Your generosity is remarkable: you give yourself entirely, never asking for anything in return. Above all, you have the rare gift of making even the heaviest moments feel lighter and bearable.

Thank you for being the protagonist of some of my craziest moments and for the awesome stories that come with these events, from Albania to Barcelona, and for readily defending me from all the evils of this world. You are always there for me and what you mean to me is immeasurable. I just hope that one day I can return to you the same friendship you have given me. **Natasha**, I always say that you have no flaws. And to be honest, I am yet to find one. On top of that, you also have numerous qualities. To the outside world, you are disciplined, loving, caring, and nurturing. In my universe, you are the one who listens to me in ways nobody does (sometimes I think you understand me better than I understand myself). Your presence feels like comfort and all that makes me feel very lucky that you have accepted me into your life. **Renato**, every time you say something, I feel seen, and I understand exactly what you mean. Our brains work in a similar way, at least when it comes to humor. Besides, I adore having our man-to-man conversations, which are raw, direct and self-limiting. Also, thank you for introducing me to your wonderful family: **Julia**, **Rafael**, his amazing wife **Bruna**, **Inacio** (the best kid), and **Nina** (the cutest kid), and your Amsterdam friends: **Paula**, **Rodrigo**, **Ana** (best skier), and **Alex** (not best snowboarder). Lastly, a fun fact: you hate going out, but every time you do, you are the life of the party!

Janneke, you certainly are my third paranymph. You came into my life by surprise and, in a short period of time, became so important to me. I love our activities together, from being each other's emotional support friend to weekly gym dates. But above all, I love how easy it was to connect with you and how you make everything seem possible. You deeply care about the people you love and give yourself completely to those around you, and for that I am grateful. Thank you for choosing me, for all your support (you literally bought me flowers to celebrate the start of this PhD defense process), for investing in our friendship, and for always making sure we have fun in the process, no matter what.

Alexia, I will never understand how our paths crossed, but I feel lucky because we were an instant match. You are hardworking, but also super "parceira de rolês"; you are far younger than me, but you give the best advice. I also

appreciate how you are always eager to help whenever I need it, zero ceremony, zero drama, full commitment. Over the last few years, I have proudly watched you grow, graduate, move (up), and even get engaged and yet, you will always be one of my kids. Also, thank you for introducing me to **Alysa** and **Isa** and for all the events that followed. Speaking of kids, **Matheus**, I feel the same way about you. In my eyes, you are still a young boy from Canada, no matter how many times you tell me we are about the same age. But you are a young boy who built a life in a foreign country (twice!) and nailed it (twice!). I admire your ability to build connections through your sweetness and your never-ending patience. I am so proud of you and of everything you have accomplished.

Bryan, thank you for your kindness, for your willingness to lend an ear, for your stillness, and your wisdom. Your love for your friends is apparent in all of your actions. I am also grateful to have met **Charlotte** through you. **Rafinha**, I miss having you around. I miss your sense of humor, your unfiltered personality, and our unapologetic conversations. I still hope that one day you come back to Nijmegen so our group can be whole again.

Cullen and **Bonnie**, you were my support system many times on this journey. Thank you for holding the fort, for always cheering me up, and for enduring the most difficult days with me. Without you, I would not have made it.

Alana, thank you for the support group, for the reality checks, and for helping me keep my sanity.

I am also grateful for my Dutch friends. **Bram** (Brammys), every time we hang out, we have so much fun. You are always down for doing things outside of your comfort zone and meeting new people. Thank you for always being so understanding of me and for always being there when I call for help. **Myrthe Reiche**, I love your bubbly personality and how you always want to make sure that everyone feels included. It is also impressive how you are able to engage in a conversation with anyone about anything. Thank you for your warmth and your spontaneous visits to our office. Family Anbergen, **Brigitte**,

Gertwin, **Opa Udy**, and **Oma Deanna**, you guys showed me the real meaning of Brabantse gezelligheid. Always warm, welcoming, and ready to party (you sure party like gods). Also, **René** (for the late-night rescues, for the epic Brabants carnaval, and the lekker klussen), **Robin** (you proved to me that when people are meant to connect, they can meet at the wrong place, wrong time, under the worst circumstances, and still make it).

I am very thankful for my German friends. **Anne Wienand**, for our legendary and wild parties together, but also for the cozy and chill dinners. You have always been so sweet and kind. I miss having you around to join my spontaneous Dollars visits or to drink hot chocolate while having the most unfiltered conversations. **Marina Saade**, thank you for your visits to Nijmegen, for joining us during our ski trip and for always staying in touch. You are so much fun to be around and so easygoing. And of course, the Hamburg girls. **Alline**, my bestie's bestie who, in the end, became my bestie. You are the voice of reason, the greatest listener of all time, the wisest, and also such a great "parceria". I love you to the moon and back and am so thankful to have met you. Thank you for always being a part of my life, despite the distance. Also thank you for introducing me to such a great group of friends and to **Jonas**. In advance, I apologize for always taking his side. **Samara**, I am your number one fan. You are the definition of someone who "has it together", while always looking like a true Disney princess. Your strength and your drive are truly inspirational. **Bruna**, I love our deep and honest conversations and how much in common we have. We have different backgrounds, different stories, and different upbringings and yet, we think alike. Unfortunately, the universe made us live in different countries because I feel like I could hang out with you every day. **Anandaia**, your bubbly personality and your big heart light up the room wherever you are. Thank you for always being down to have fun with me. **Faby**, you are always so sweet and so kind. From the day we met, you were ready to make me feel welcome and loved. I am also very thankful for the fun memes.

Mury and Jean, to you go my eternal love and "saudades". Thank you for the support group "Busch gardens" on WhatsApp. Thank you for the long video

calls, and for all the visits along the years. You are some of the most extraordinary people I have ever met. Any time things happen in my life, I run to you two – for the good and bad news. **Murielly**, you are genuinely a one of the best people in this world, a great friend, and my fashion muse. **Jean**, you are one of my rocks. I admire the way you give yourself fully to your friends, how much you care about us, and how much you continue to take care of us, no matter the distance. Thank you for our yearly meetings and for being my speed dial friend for the past 13 years.

To the official buddies **Heidi**, **Mohit**, and **Agus** by proxy, for the fun picnics and birthday parties, for always making an effort to be part of my life. We did so many things together in the past few years. Thank you for being adventurous with me and for always keeping in touch. And let's not forget the epic wedding party, which was absolutely perfect.

Deep Dinner girls - **Monika**, **Ea**, **Lauren**, and **Amaris** - I am so glad I scheduled that dinner! The six of us (including Nina) were just meant to be connected. Thank you for all the epic events that followed, as well as the many dinners we scheduled afterwards. You are so much fun to be around, and I feel lucky to have met such strong and inspiring women. Every time we meet, it feels light, honest, and comforting. I love our conversations, our wild parties, and the memes I get from you girls. Thank you so much for signing up for that dinner!

To my temporary roommates: **Finja**, you are so much fun to be around. I feel like we clicked the moment I met you, and you made me miss you the first day you went away. Despite our opposite schedules and contrasting dietary preferences, it was so effortless to build a true friendship. Fun fact: sometimes I use your catch phrases, and I still hear them with your voice in my head. I will always remember your homemade bread, you protecting our pigeon, our gym dates, and our trip to Giethoorn. **Laxmi**, you made it so easy to be roommates. You were always kind and thoughtful, and always generous with your amazing food. Thank you for the sunsets we shared together in my Muldersweg apartment.

To **Aljosa**, **Koen the Barman**, and **Dollars Muziek Café**, thank you for the late-night rescues, for the gezelligheid, for the profane amount of tequila shots, and for some of the most epic nights of my life.

To the Sinai people of my previous life - Ana Borges, Ana Cristina, Chrisa, Madhura, Paola and Valentina: The bond we share was forged in fire. We supported each other on a professional and personal level. There was no competition, no favorites, only teamwork and I always felt like I could share anything with you. I miss our lunches together, our outings in NYC and our late nights at the lab. **Ana Borges**, from the very start, you were a pillar in my NYC life. Your nurturing nature somehow coexisting with your party animal side was somehow perfectly balanced. Who would have thought we would build so many memories together and that our friendship would know no borders. From Portugal to India, years later you are still part of my life. **Ana Cristina**, had it not been for you, none of this would have happened. You call me "mini-me" but to me you are a true legend, and I am still a budget version. Regardless, you saw potential in me before I could see it. Thank you for getting me this position at the Mulder Lab and for your priceless mentorship. **Chrisa**, thank you for being the "heart" in our duo and for forcing me into the hipster spots everywhere we go, from NYC to Greece and even in my own home in Nijmegen. The universe determined that we would be too powerful in the same country, but I am glad it allowed us to stay in the same continent. This way we can still hang out from time to time. **Madhura**, you showed me how Brazil is just next door to India. We were there for each other during our big moments, as well as the meaningful small ones while strolling through Central Park. I miss having you in my daily life, but I know that you are still there for me. **Paola**, you are the kindest. With your gentle way, you made the lab feel like a friendlier place - always positive and sweet. I am grateful that our paths have crossed. **Valentina**, we didn't have much time working together, but we sure had a lot of fun outside working hours. You are a brilliant individual, and I hope we meet again (academically and in our personal lives).

To the pirate ship: **Thijs**, you are probably one of the most brilliant scientists I have ever met. You have the remarkable ability to identify all the overlooked pitfalls in a project, and you ask the most insightful and incisive questions after a presentation. You have added considerable value to every project you got involved in, with your exceptional gift for interpreting data. And through all that, you still find the bandwidth to be kind and just. You listen to everyone's perspective and make a true effort to treat everyone with empathy and fairness. You have my utmost respect and admiration. **Yuri**, I still remember our first interaction, when we had a Zoom call during the COVID lockdown. Your whey protein in the background for good luck, and you pointing out halfway through the call that I was not sharing my screen with the presentation slides. During that year, you were my right-hand. While half of the planet was working from home, you and I trooped together through all the *in vivo* experiments of the lab in a hospital basement. That includes late nights eating Taco Bell in SC1, watching *EuroTrip* during long PET scans, and observing you absorb years of knowledge and experience in just a few months. You are something else, for sure, and I can't express enough my gratitude and esteem. **Jeroen**, likewise, from a young student coming to NYC for a bootcamp experience, I witnessed your growth to become one of the best presenters in our group. I am very proud of the scientist you became and of your constant drive to mentor, learn, and "do better". You genuinely deserve all the credit for that. Thank you for the spontaneous baked goods, for the heart-to-heart conversations and for your epic ability to make any party more fun. **Tom**, you are one of the most complete human beings I have ever come across. You are simply good at everything. You can be a party animal on the weekend and still return on Monday with the focus, productivity and perfectionism of someone who had a balanced diet and slept for 8 hours the night before. You can lead a project like no other, combining pristine planning skills with the ability to motivate an entire team. Did I mention you are also good at sports? Nothing seems to defeat you. Your ever-present positive mindset has influenced my perspective on things, and I am grateful for that. **Rianne**, you were also my right-hand person in the last couple of years. Your commitment to being a team player is unmatched. You always try to take over tasks to make any workload feel lighter, and that does not go

unnoticed. Thank you for your steady encouragement and for believing in me, even when I did not, and for cheering me up through every stage of our heart transplant journey. It meant the world to me. I am also grateful for the many rides home, for the celebratory cakes and gifts, and for our deep talks in the surgery room. **Iris**, you surround yourself with people who value your warmth, energy and friendship, and I love how you build such a vibrant life around you. Thank you for the awesome moments at the Qmusic Foute Party, bake-off competitions, singing karaoke, Hollandse Zomer and so many more. I am also grateful for the cute pictures you take of all of us, for our bumblebee tea times, for the collective gifts you organized, and for introducing me to the basics of Gen Z culture. You were a later addition to our team, but you completed it.

To the Brabants Mulder Lab team: **Anna-Maria** (every time we met it was so much fun), **Anne** (for that epic ski trip and for many other awesome events), **Ayla** (for your sweet personality and for being such a great listener through my crazy stories), **Bianca** (you know what I wanted to write here), **Birgit**, **Chiara**, **Daniek** (for hosting me and for always being so kind), **Fenna**, **Glenn**, **Jari**, **Joost**, **Maaike**, **Matt** (for the fun drive back to the Kuilart), **Milou**, **Mirre**, **Robby**, **Senna**, **Sjoerd** (you were always so pleasant to talk to) and **Stijn** (for the koala incident). **David**, thank you for the sharp wit, the relentless "information exchange" and the uniquely salty humor we shared and perfected over the years. Beneath all the friendly jabs lies a genuine mutual respect that I value deeply. I am grateful for your honesty, for your perspective and for always keeping things entertaining. **Ewelina**, you care so deeply for all of us. Thank you for the long and fun chats, in which I felt comfortable sharing details about my daily life. Thank you for being such a great listener, for providing me with priceless advice and also for trusting me with your own stories and thoughts. From trips to the cinema to impromptu brunches in our new homes, I have cherished our friendship and the moments we shared. **Merel**, I am secretly a big fan. I admire your cleverness, your focus and your ability to bring organization to everything you do. Recently, you involuntarily became an essential source of structure on your side of our branch, keeping things on course. I am thankful for that.

Vivienne, you were such a precious addition to our team! You stood up for me in so many instances in such a short period of time. You are so wonderfully amazing at troubleshooting and thinking outside the box. I love our conversations, our teamwork, our focaccia lunches, and our break-room tea in between surgeries. Thank you for always being so optimistic and supportive.

To the Sinai folks: First and foremost, to **Carlos**, who introduced me to the Mulder Lab, believed in my potential and hired me in NYC. I cannot imagine my life outside the Mulder Lab, and I owe it all to you. You were always a stronghold in the group, maintaining structure and peace. And I'll always admire your ability to draw good people to your inner circle. To **Jazz**, the original minion. Thank you for all the long, philosophical and heavy talks in SC1, deep into the night. I admire your drive and your enthusiasm, never letting anything come between you and your goals. Thank you for El Aguila and Mrs. An Thai, but also for the pep talks and for the emotional support. I feel like we have been through everything together and that is a bond we will always share. **Mandy**, for your outstanding mentorship but also for your friendship. Professionally, you always pushed me to be my best version, to try new protocols and techniques and to not limit myself. Personally, I loved our outings, our post-work quality time and the number of times you were there for me when I needed to open up to someone. We grabbed drinks together, we grabbed healthy smoothies together, but we also had our share of bonding time during late-night experiments, recovering specimens from a bag and quartering animals bigger than me. Somehow, in all that, we certainly managed to have fun. **Bram T**, we always had a strange connection and we used to cause much commotion because of our shared dry humor. Thank you for the many times you stood up for me, for your honest feedback and for always being my tag-team partner when staying late in the office. **Alex**, Dr. Lemoncello, we were a different breed of best friends. We mocked each other in ways that defied every HR boundary in the books but also managed to work together as a dream team would. Our friendship survived projects, distance and most importantly, our dark humor. We rarely express how much we mean to each other, but you always made sure to be there for

my birthdays and celebrations, even now that we live very far apart. I just want to say: Shakira, Shakira, enjoy your emotions, I will shut this down and SC1 for life. **Anu**, I will always admire your brilliance and how much of a powerhouse you are. You are the perfect combination of genius and drive. Amidst that, you manage to be reliable and considerate to your colleagues. Thank you for always being so mindful and thoughtful and for involving me in such enticing projects. **Max**, you challenged me outside my comfort zone. You included me in all your projects and believed in my potential. Thank you also for the fun outings after hours, buying drinks for everyone on my birthday, and for partying together in Friesland. **Bram Priem** for making the long hours of work in SC1 seem fun, for the happy-hour drinks as a reward for our hard work, and for the unmatched sense of humor. **Geoffrey**, thank you for the venting sessions, for the picnics in Central Park, for the words of encouragement and for the happiness you brought into our lives. **Jessica**, for enduring through my moving chaos, for your patience in the process, helping me transition smoothly to the Netherlands. I am also grateful for our good old days studying Biomedicine together in Brazil. Thank you for the prayers, for the company, and for your love. **François**, thank you for welcoming me to the Mulder Lab, and for teaching me everything from scratch, when I did not know much about imaging or nanomedicine. **Magda**, thank you for the wonderful friendship you provided me during my NYC stay. We had so much fun singing karaoke, having lunch together and grabbing dinner at your place. You took me ice skating, took me to Greenpoint to eat pierogis and taught me so much about Polish culture. I miss you dearly. **Alexandros**, you were my biggest fan. You believed in my potential, you encouraged me to be more ambitious, and you put in a good word for me with so many people. Thank you for making me the second author on your paper and for your trust. **Marianne**, thank you for being nurturing and enveloping us in Southern hospitality. I miss the game nights at your apartment. **Sonum** and **Letizia** for all your help and support during the endless DOTATATE nights. And to the rest of the NYC family **Judit**, **Catherine**, **Gilbert**, **Ken**, **Jordi**, **Alan Soto**, **Laila**, **George** and **Stefanie Hectors**.

To the most amazing vets and CCMS people: **Pedro**, **Ron**, **Melanie**, **Ignacio**, **Bryan**, **Jeffery**, and **Carlos Franco**. You guys put so many of our experiments in motion, often at the expense of very late work hours. Thank you for always inviting me to CCMS events and for always saving me some food during the Christmas parties.

To all the students (minions) over the years. **Francisca**, you are irreplaceable in my life. We had so many amazing adventures together. I miss you so much that I always wonder what my life would have been like had you stayed in the Netherlands. But it brings me joy to see how happy you are in Belgium and how much you have achieved. **Cristina**, thank you so much for all the outings, the salsa and bachata nights - and days - and for always being so sweet. You came into my life during a turbulent period and made it seem much lighter. **Anna Vera** (you were a true hero taking over my internet bill when I moved to the Netherlands. Thank you for always being such a sweet friend), **Eliane** (for the fun times during COVID and in Switzerland), **Gijs** (for always being so proactive and kind), **Anthony** (I will never forget the mouse cookies you made for my birthday), **Pepijn** (for spotting me at the bench press machine and for bench-pressing me), **Esther van Leeuwen** (for the fun Utrecht escapades), **Danyel** (for introducing me to the Dyson world and for being such a true trooper), **Scott** (for surviving my sense of humor), **Branca** (for the snacks), **Fleur** and **Myrte** (for always being so sweet), **Shequoia** (thank you for the karaoke and sushi days), **Roderick**, **Sanne**, **Willem**, **Nathaniel**, **Emma**, **Chetan**, **Alexandre Berchouchi**, **Ana**, **Daniel** and **Haruki**.

Adriana, **Ajie** (for the BBQ in The Hague), **Aline**, **Alisa**, **Anaisa**, **Anca** (for the fun parties and the unforgettable farewell dinner), **Andra**, **Andy** (the best DJ! I will never forget how amazing our birthday party was and it was all because of you. You were also such a great friend in times of need), **Berend**, **Bruna** (we go waaay back, since you were a freshman in college, and I love that you ended up staying in Nijmegen; thank you for the epic bake-off competition), **Busra**, **Cas**, **Charles** (the king), **Chon-Kit** (thank you for introducing me to the stairmaster), **Collins**, **Corlinda**, **Daniela** (February babies, kayak buddy and tequila from our trio), **Diletta** (for hosting the most epic house parties, which

are dearly missed), **Dineke** (for always organizing fun events for the lab), **Dorien**, **Dulfer**, **Eleen**, **Esther** (for the SUP days and Oktoberfest), **Ezio**, **Flavia**, **Gizem** (for feeding me life-saving crackers in Cluj. You are one of the friendliest people I have ever met), **Hanneke** (and our inside jokes), **Harsh** (thank you for introducing me to the squat mafia and for the fun times partying, and at the gym), **Heidi**, **Helga**, **Helin** (I always remember our heart-to-heart conversations and your advice), **Ilayda**, **Ilse**, **Ilyas**, **Jasmijn**, **Jelle**, **Jelmer**, **Jessica**, **Job**, **Jorge** (for sharing the IvD burdens with me), **Julia B** (for all the trips together), **Julia v H** (for always being so kind), **Julia v Tuijl**, **Kai**, **Krystallenia**, **Laura** (for all the parties), **Laszlo**, **Leonie** (for the absolute best PhD defense advice), **Lieke**, **Liesbeth**, **Lisa K**, **Lisa T** (for the golden year of 2022), **Lisanne** (for always being so cheerful and for partnering with me at the Mulder Lab retreat 2025), **Lorenzo**, **Lotte**, **Lucinda**, **Maaike**, **Maartje**, **Malin** (for the KISS idea), **Manon** (for the funny portrait of me that sits on my desk), **Marc**, **Margo**, **Marijn**, **Mariolina** (I still remember our talks about learning Dutch), **Martin Jager** (my dearest Jager bomb! For always helping me), **Mihai** (for being such a great team player during bake-offs and carpools), **Mike**, **Missy** (by proxy; every time we meet I have so much fun! Thank you for always being down to sing karaoke, dinner parties and more. You are a real delight!), **Mumin** (for the BBQs and analyses), **Nick** (for the (not so) deep talks and for the fun lunches), **Nils** (for the Hanos tips), **Nils Rother**, **Noriko**, **Orsi** (for the awesome video of Leo twerking down to the floor), **Ozlem**, **Patricia** (for your unquestionable loyalty as a friend, for always being down to join us at parties, trips and Brazilian events, for working so hard, and for always being on our side), **Pau**, **Peng**, **Pepijn**, **Prashant**, **Rosanne**, **Robbin**, **Ruiqi**, **Rutger** (for squat mafiaaa), **Siroon** (for that epic tompouce recipe, for the warm welcome to the lab and for teaming up with me during grant season), **Suzanne**, **Thanasis** (for the pep talks, for the party talks and for the parking tips), **Tijmen**, **Titus**, **Tomas** (for stealing that liquor bottle that one time, hypothetically), **Twan**, **Wieteke**, **Yavor**, **Yutaka**, **Zara**.

To the CDL people who support our work on a daily basis: **Saskia** (for your friendship and sharing the murine heart transplant struggles with me), **Karin Mulder** (for being so sweet and such an amazing teammate), **Manon** (for

always supporting us), **Floor** (for being so amazing at work and outside of work alike), **Liz**, IvD (J**eannette**, **Alinde**, **Pieter** and **Miriam**), **Otto**, **Charlene**, **Denise**, **Alex**, **Maikel**, and **Marielle**.

To the PIs along this journey: **Leo Joosten**, **Musa Mhlanga** (and your epic parties), **Rapha Duivenvoorden** (o holandês mais brasileiro), **Mihai Netea**, **Esther Lutgens** (and for the wonderful opportunity to be part of the Leducq consortium), **Niels Riksen**, **Amanda Killian**, **Sandra Heskamp**, **Youssef Wadghiri** (and your legendary dance moves), and **Zahi Fayad**, for the mentorship, support, and the many enjoyable moments we shared in this process.

To the Mulders: Marielle, Janneke and Juultje. **Marielle**, thank you for being such a strong mother figure in my life. You are always loving, caring, and nurturing. I always felt welcome in your family: surprisingly, not because of Willem's invitations but because of your gezellig nature. **Juultje**, I always admire your strength and how well put-together you are, especially for your age. Also, thank you for sharing your dad with the Mulder group. **Janneke**, thank you for always being so sweet, kind, and approachable.

Aos amigos no Brasil: **Angélica** e família, por toda a sua positividade e acolhimento. Por sempre me apoiar em todas as minhas decisões. Pela companhia agradável e pelo amor incondicional. **Talita**, minha amiga de faculdade. Te amei à primeira vista, contra sua vontade. Ao longo dos anos, aprendi muito contigo. No começo, éramos verdadeiros polos opostos e hoje em dia, somos muito semelhantes. Amo conversar com você, amo nossos encontros no Brasil e amo nossa conexão. Ainda hoje, sinto que faço parte da sua vida e você da minha e me considero uma pessoa de sorte por ter você. Amigos do Orkut **Milena**, **Alejandro** e **Patrícia**, obrigada por todos os encontros quando vou ao Brasil, por todas as mensagens tradicionais de aniversário e por cultivarem a nossa amizade. **Beggiato**, você surgiu na minha vida de uma forma muito inconvencional. Mas a amizade se desenvolveu de forma natural. Você e o tipo de pessoa que todo mundo quer ter por perto. Muito obrigada por todo o apoio virtual e pelas visitas

ocasionais, tanto no Brasil quanto na Europa. **Kamyla**, minha prima do coração, mas também da vida real. Muito obrigada por todo o carinho e pelo acolhimento. Ao povo do Erasto e companhia: **Ananda**, **Ivy**, **Pedro** e **Victor**. Especialmente à **Dafne**, minha melhor amiga de infância, que me sustentou em momentos difíceis e que me ligou várias vezes pra se certificar de que eu estava bem. Te admiro muito pela pessoa que você é, e sinto falta de tê-la no meu dia a dia. Muito obrigada pelos conselhos, pelo apoio, por sempre se lembrar de mim, por sempre me tirar da minha zona de conforto e por manter a nossa amizade viva. E ao **Rodney**, meu irmão de coração e melhor amigo. Pela linda amizade que nutrimos ao longo desses anos.

Povo do ICC: **Ligia Kalb**, muito obrigada por acreditar em mim antes de qualquer outra pessoa. Você viu meu potencial e me moldou completamente do zero para me tornar a cientista que sou hoje. Até hoje aplico muito do que aprendi com você na minha vida profissional, desde a organização e planejamento ao controle do estoque de reagentes "reserva". Muito obrigada por ter me resgatado, pela confiança, por me incluir em seus projetos e por todo o apoio ao longo dessa jornada. **Claudia**, obrigada por ser essa pessoa sem defeitos. Você ama as pessoas à sua volta e faz todo mundo se sentir bem-vindo. Seu coração é enorme, doce e fiel aos seus amigos. Ser sua colega foi um verdadeiro privilégio. **Camila**, obrigada por toda a parceria dentro e fora do laboratório, pelas inúmeras caronas, pelas risadas e pelas nossas conversas a caminho do Uberaba. **Bia**, sem você eu não estaria aqui. Iniciamos juntas o nosso processo de nos candidatar a vagas fora do país. Nossas vidas seguiram caminhos diferentes, mas mesmo assim, tenho muito carinho pela nossa amizade, pelo seu companheirismo e por tudo o que você fez por mim. Tenho muitas saudades do nosso ano de 2016, das suas piadas e das nossas idas ao YaGe e ao Suprema. **Ligia Ceole**, sempre muito amável e gentil. Muito obrigada pelo seu apoio, pelas melhores empadinhas do mundo e pelo exemplo de pessoa que você foi pra mim. **Cassy (Cassinger)**, você sempre foi muito querido com todos nós, justo e amável. Sempre ajudando a todos e celebrando as nossas vitórias. **Jaque**, pela amizade, pelas risadas e pelos conselhos. **Maurilio**, obrigada por me

dar a oportunidade de fazer parte do Lab de Biologia Celular e por todos os aprendizados.

Priscila, my best friend from high school, we shared a lifetime of events, from graduations to weddings to professional achievements and everything in between. Through all that, thank you for always being present, despite the distance, the time zone gap, and the demands of our adult lives. Thank you for always making an effort to stay in touch, to visit each other and to support me through the good and the bad times. I have missed you dearly for all these years, but I am also grateful for that, because it reflects how much you mean to me.

À família Vergara e Shalon: **Sinora** e **Odilon**, **Leonor**, **Tito** e **Rose**, **Damaris** e **Reinaldo**, **Rebeca**, **Midi**, **Talitah**, **Manu**, **Liliane**, **Deisy** e **Manfred**. Também aos meus avos de coração: **Lori** e **Vendelino**, *in memoriam*.

Dear Hamersmas, **Hans**, **Brigitte**, **Niels**, and **Katya**, thank you for welcoming me into your family and making me feel so at home. I am also grateful to you for raising, shaping, and surrounding one of the most wonderful people I know with love (and for sharing him with me). You give us your full support for our adventures, ideas, travel plans, and dreams wholeheartedly, and I am truly grateful for that.

I am also very grateful for the proxy friendship group, who took me in without reservation: **Caner**, **Els** and **Benny**, **Tijs** and **Lottje** (also thank you for the life-saving air conditioner), **Rick** and **Marjolein** (who also helped me so much with organizing my defense party), and **Remco**.

My dear **Thomas**, as you know, I am a person of many lists. Naturally, I had a list of every quality I was looking for in a partner. In fact, there were even subcategories: some were deemed "essential", others "a big plus", and many merely "nice additions". You effortlessly tick every box. So much so that I sometimes wonder whether you are a figment of my imagination because you are genuinely surreal. It is surreal how compatible we are; how

easily you befriend everyone; how supermarket trip ends with you bringing home something that made you think of me; and how, when the entire world is in chaos, you remain attentive to the little things (in this case, I mean the insects and plants, but the pun is intended). Your heart is so beautiful that it was impossible not to fall in love with you. In all your modesty, you told me that you should not be part of this acknowledgment section, because you were not there for most of my PhD journey. And you are right, in the sense that our paths crossed only "in the last minute of the second half". Yet somehow you have done so much in such a short period of time. Thank you for every gym date, for every time you (almost supernaturally) sensed that I needed to decompress, for every call, for every massage, for every time you "rescued" me, and for bringing a sense of calm to my often busy and overthinking mind. Most importantly, thank you for filling my heart with so much gratitude, the feeling with which I choose to end this thesis. I have lived in many countries in search of a safe haven, but no place, and no one, has ever made me feel as at home as you do.

